DEPARTMENT OF MECHANICAL & AEROSPACE ENGINEERING

SHIELDING GAS PARAMETER OPTIMISATION IN ARC WELDING PROCESSES

STUART WILLIAM CAMPBELL M.Eng

2015

A thesis submitted in the fulfilment of the requirements for the degree of Doctor of Philosophy

This thesis is the result of the author's original research. It has been composed by the author and has not been previously submitted for examination, which has led to the award of a degree.

Signed: Date:

Abstract

This thesis is focussed on shielding gas optimisation in gas shielded arc welding processes, and has been conducted along two themes; deriving conditions in which the shielding gas flow rate can be safely reduced, and through the highly novel process of alternating shielding gases.

The correct shielding gas flow rate is essential for providing adequate protection to the weld metal during the heating, liquid and solidification stages. Hence, there is an optimum shielding gas flow rate, but this is difficult to define and is often decided on the basis of preference or experience.

A multi-disciplined, systematic study has been conducted, which has shown that there is considerable scope to reduce the shielding gas flow rate. Experimental trials have shown that the shielding gas flow rate can be reduced, in a draft-free environment, to 6 l/min, with no degradation in weld quality for the worst draft conditions measured in a typical shipyard fabrication hall, at 10 l/min.

This study has resulted in shielding gas flow controllers, preset at 12 l/min, being installed in a large shipyard environment, removing the welding operatives ability to increase the shielding gas flow rate.

The application of alternating shielding gases offers clear manufacturing cost reduction benefits which arise from measurable increases in productivity, improved distortion control and re-work reduction, and overall improvements to the mechanical properties of the weld.

Arc pressure measurements, and the subsequent derivation of forces acting on the liquid weld metal, have indicated that flow vectors for helium are opposite in direction to that produced by argon, creating a dynamic action within the weld pool.

Schlieren visualisation has shown that there is a greater degree of helium entrainment in the primary jet due to a constriction of its flow in the secondary jet, influencing the arc's behaviour and inferring more of the associated benefits.

Acknowledgements

Firstly, I would like to express my sincere gratitude to my supervisor, Dr Alexander Galloway, for his continued assistance, advice and guidance throughout this research. In addition, I would like to thank Dr Norman McPherson for his guidance, support and input from both a technical and industrial perspective.

I gratefully acknowledge the funding provided by BAE Systems and the Engineering and Physical Sciences Research Council, which made this research possible. I would also like to thank BAE Systems for the wealth of experimental samples and apparatus provided throughout.

I am indebted to the departmental technical staff, in particular Mr Steven Black for his assistance and expertise throughout the experimentation, and Mr James Kelly for his guidance in the preparation and interpretation of the metallurgical analysis. I would also like to acknowledge the support of Mr Andrew Crockett and Dr Fiona Sillars during mechanical and thermal property analysis, respectively.

The computational modelling support and guidance provided by Professor Duncan Camilleri and Dr Daniel Micallef, during my time at the University of Malta, has proved invaluable.

I extend my thanks to Dr Vivien Beyer and Mr Ioannis Bitharas, Heriot Watt University, for their knowledge and expertise in supporting and conducting the shielding gas visualisation studies.

I would like to express my appreciation for the continued willingness of Mrs Aileen Petrie to assist in the reprographic content.

My colleagues in the department have been very supportive, and I thank them for their input on a wide range of issues, which has proved extremely valuable.

Finally, I would like to thank my family for their continued support throughout my time at University, and Kirsty Watson, for her encouragement throughout this research.

Contents

General Introduction

Background

Introduced in the early-mid twentieth century, gas metal arc welding (GMAW) and gas tungsten arc welding (GTAW) were initially developed for the joining of aluminium and other non-ferrous metals but were later developed for a broad range of metallic materials.

Shielding gases are a fundamental component of each process; their primary purpose to protect the metal transfer stream and molten weld pool from contamination by atmospheric gases. In addition to preventing contamination, the shielding gas is a critical variable in gas shielded welding processes, with each gas having its own unique set of thermodynamic and transport properties, which influence various arc characteristics including temperature distribution and electrical fields. Consequently, the shielding gas alters the geometry, microstructure and integrity of the solidified weld metal.

The shielding gas flow rate is also known to influence the quality of the solidified weld; too low a flow rate can lead to inadequate coverage of the weld pool which often leads to porosity and excess spatter development, whilst too high a flow rate can result in poor penetration. Hence, there is an optimum flow rate for weld shielding gases, but this is difficult to define and is often decided on the basis of preference or experience.

The correct shielding gas flow rate is essential for providing adequate protection to the welding region; drafts therefore present a significant problem to the welding process from both a technical and economic viewpoint. Cross drafts potentially remove the shielding gas, adversely affecting its ability to protect the welding region from contamination by atmospheric gases such as nitrogen and oxygen.

Alternating shielding gases is a method of discretely supplying two shielding gases to the weld region in order to take advantage of the beneficial properties of each gas, and the dynamic action that the alternating gas process produces. This dynamic action is a result of alternate fluid flow vectors being present within the liquid weld pool, and is reported to be a result of three independent phenomena: arc pressure

variation, variation of weld pool fluidity and arc pressure peaking, which combine to produce a stirring action within the weld pool.

Fluid flow and heat flow are key factors in determining the final weld shape, and the arc pressure distribution allows for the numerical derivation of various forces acting on the liquid weld metal. Although studies have reported on the arc pressures produced when using argon, and to a limited extent for helium and argon–helium mixtures, there is no previous data for the arc pressure produced during the alternating shielding gas process. Therefore, the phenomena occurring during the process of alternating shielding gases are based solely on theoretical assumptions.

Although the shielding gas changes the mechanical integrity of the welded joint, the effect that alternating shielding gases has on the mechanical and thermal properties of the weld metal in relation to a conventional supply is unknown. Due to a lack of experimental data, the difference in material properties between the parent plate and weld metal are often neglected, and many computational modelling simulations make the assumption that the properties of the weld metal are the same as those for the parent plate. However, particularly in cases where a filler material is used, the chemical composition and mechanical property data is generally different to that of the parent material, hence it can be inferred that the thermal properties will also differ.

Artificial neural networks (ANNs) are mathematical or computational models that are able to capture and represent complex input-output relationships, and can be used to predict any process so long as sufficient data is generated to accurately train and validate the model. ANN networks benefit from being bidirectional, i.e. they have the ability to predict the input variables required to produce a given output. This type of computational model can be effectively applied to the arc welding processes, in which extremely complex relationships and interactions between several nonlinear welding variables exist.

In addition to preventing contamination, the shielding gas is a critical variable for gas shielded arc welding processes as a result of the extreme temperatures of the electrical arc. The properties of a GTAW arc, and the corresponding weld, are strongly dependent upon the shielding gas used. GTAW is a highly complex process

and involves a solid, liquid, gas and plasma in close proximity. Simulations of the arc characteristics are based on the governing equations of computational fluid dynamics (CFD), with modifications to account for electromagnetism.

The application of the schlieren technique to gas shielded arc welding processes (with the electrical arc present) is somewhat limited. The schlieren technique, when applied to the welding process is generally used as a validation tool for CFD models and to assess the effect of shielding gas flow rates. Other studies have necessitated around the development of schlieren apparatus parameters (light source, and source aperture geometry and orientation) to enhance the schlieren image during arc welding.

Aims and objectives

The aims of this research study will be to derive conditions in which the shielding gas flow rate can be safely reduced, without detriment to weld quality, and investigate the novel process of alternating shielding gases. The main objectives will therefore be to:

- Ascertain the effects of implementing a lower shielding gas flow rate, and derive conditions in which the flow rate can safely be reduced when drafts are present in the welding area.
- Implement methods to visualise the experimental shielding gas flow, and develop a CFD model to predict the flow profile.
- Conduct arc pressure measurements to validate/disprove the previous theoretical assumptions that the benefits of alternating shielding gas process are founded upon, i.e. arc pressure variation and arc pressure peaking.
- Derive the arc forces acting upon the liquid weld metal when using a shielding gas composition of argon or helium.
- Investigate the effect that the shielding gas configuration has on the thermal cycles and induced distortion.

- Determine the effect of the shielding gas configuration on the mechanical integrity of the welded joint.
- Determine the effect of the shielding gas configuration on the thermal expansion coefficient, specific heat capacity, thermal conductivity and thermal diffusivity of the weld metal.
- Develop ANN computational models to accurately predict the weld geometry when implementing alternating shielding gases, weld quality when alternating shielding gases are subjected to cross drafts, and distortion as a function of the welding parameters, with the subsequent transient induction heating parameters required to rectify it.
- Develop a CFD model to simulate the arc characteristics as a function of the shielding gas composition, and investigate the effects of individual thermophysical properties.
- Apply the schlieren optical visualisation technique to the alternating shielding gas process in order to depict the flow vectors created using this novel supply method.

The approach taken in terms of the complimentary aspects of computational modelling, optical visualisation and experimental validation are highly novel, and the above objectives will significantly enhance the state of the art in the research field of shielding gas optimisation for advanced joining and manufacture.

Structure of thesis

This study focuses on the optimisation of shielding gas parameters in GMAW and GTAW, and investigates the effects of both reducing the shielding gas consumption and the application of alternating shielding gases. This thesis is subdivided into different chapters; the first two detailing the background and experimental apparatus, with subsequent chapters investigating the effects of reducing the shielding gas flow rate and various aspects of the alternating shielding gas process.

In chapter one, a general review of shielding gases and alternating shielding gases applied in both GMAW and GTAW are discussed. An introduction to the various modelling techniques used throughout this thesis is also given, namely the application of CFD and ANNs.

In addition, a general description of the experimental setup, measurement systems and the theory of the techniques implemented throughout this thesis are given in chapter two.

The first stage in the analysis involved developing conditions in which the shielding gas flow rate could be reduced without detriment to weld quality for a conventional argon / 20% carbon dioxide shielding gas supply. Chapter three describes the multi-discipline approach taken to reduce shielding gas consumption and consisted of a series of both experimental and computational studies, and was conducted along two themes; a techno-economic evaluation, and the optimisation of nozzle geometry through experimental shadowgraphy measurements and CFD simulations.

The techno-economic evaluation comprised of a comprehensive series of experimental trials in a variety of welding scenarios in order to ascertain the true effects of reducing the shielding gas flow rate and determine the optimum shielding gas flow rate without detriment to weld quality.

A systematic study was conducted to visualise (shadowgraphy) and simulate (CFD) the effect that the shielding gas flow rate, cross draft velocity and weld nozzle design have on the quality of the solidified weld.

In chapter four an experimental investigation was conducted to determine the effect that shielding gas composition and alternating shielding gases have on arc pressure distribution at the workpiece. The arc pressure distribution allows for the numerical derivation of various forces acting on the liquid weld metal including arc force, plasma shear and Lorentz force.

Chapter five assesses the effects that alternating shielding gases have on the mechanical properties of the welded joint in both steel and aluminium workpieces. In addition, the effect that alternating shielding gases have on various thermal property data including the linear thermal expansion coefficient, specific heat capacity,

thermal conductivity and thermal diffusivity, within the weld material itself and for the parent plate is presented.

The development, and subsequent application, of ANN models to predict various weld aspects are discussed in chapter six. This involved the construction and optimisation of several ANN models to predict weld geometry when implementing alternating shielding gases, weld quality when alternating shielding gases are subjected to cross drafts, with the additional aim of generating a safe criteria for reducing the shielding gas consumption, distortion as a function of the welding parameters, and the subsequent transient induction heating parameters required to rectify it.

Chapter seven focuses on the development of a CFD model to simulate the effects of an argon and helium shielding environment, and examines the effects of individual thermophysical shielding gas properties. The model generated will form the initial stage of development of a transient CFD model to simulate the effects of alternating between shielding gases.

The shielding gas flow vectors present when implementing the alternating shielding gas process are transient in nature. Chapter eight therefore focuses on the application of the schlieren method to the GTAW process in order to visualise the flow regimes present when implementing this novel process, due to its ability to focus on a plane within the flow region.

A summary of the results obtained throughout this thesis, and their application in an industrial setup are given in the final chapter. In addition, this section also details new challenges and areas for future work, which have arisen as a result of this study.

1 Literature review

1.1 Shielding gases

1.1.1 Purpose

The primary functions of the shielding gas in gas shielded welding processes are to protect the weld area, i.e. the molten metal, electrode and arc, from contamination by atmospheric gases, and to provide a medium for the electrical current to flow.

Atmospheric gases, absorbed into the molten weld metal, can result in defects in the solidified weld. Shielding gases are either inert or active; inert gases do not combine chemically with any other elements, whereas active gases do and will react with the molten metal.

In addition to its shielding function, the arc plasma generated acts as a medium for the electrical current to flow. Each gas has unique thermophysical properties that can have a major effect on welding speed, penetration, mechanical properties, weld appearance and geometry, fume generation and arc stability.

1.1.2 Inert, active and mixed gases

There are a number of shielding gases commonly used for GMAW and GTAW, which can be classified by one of three categories: inert, active and mixed. A selection of gases and their respective properties are shown in Table 1.1.

The reactivity of a shielding gas, from a welding perspective, is a comparative measurement of how readily a given shielding gas will react with the molten weld pool.

There are only six naturally occurring inert gases: helium, neon, argon, krypton, xenon and radon. However, only argon and helium are used as shielding gases due to the rarity and expense associated with the other four. Both argon and helium are completely unreactive and therefore have no chemical reactions with the weld pool. Nitrogen is an inert gas at room temperature, however, at temperatures experienced in arc welding processes it's behaviour varies with different materials.

Active gases are either oxidising or reducing. Oxidising gases include any gas that contains oxygen, and will react to form oxides within the solidified weld pool. Reducing gases are gases that attract oxygen, preventing the formation of oxides in the molten weld metal.

In addition to using shielding gases in their pure form, combinations of different gas blends are also used to protect the welding region.

Table 1.1: Properties of shielding gases (Adapted from BS EN ISO 14175:2008)

	Argon	**Helium**	**Carbon Dioxide**	**Hydrogen**	**Nitrogen**	**Oxygen**
Chemical Symbol	Ar	He	CO_2	H_2	N_2	O_2
Type of Gas	Inert	Inert	Active oxidising	Active reducing	Unreactive[a]	Active oxidising
Atomic Number	18	2	-	1	7	8
Molecular Weight	39.95	4.00	44.01	2.016	28.01	32.00
Density[b] (kg m^{-3})	1.784	0.178	1.977	0.090	1.251	1.429
Specific Gravity[b]	1.380	0.138	1.529	0.070	0.968	1.105
Purity (% vol. min.)	99.99	99.99	99.70	99.50	99.50	99.50
Moisture (p.p.m. max)	40	40	200	40	40	200
Ionisation Potential (eV)	15.760	24.587	13.780	13.598	14.534	13.618

[a] The behaviour of nitrogen varies with different materials and applications.
[b] Specified at 0 °C and 0.101 MPa (1.013 bar)

1.1.3 Shielding gas thermodynamic and transport properties

Each shielding gas has its own unique set of thermodynamic and transport properties (density, molar mass, specific heat capacity, dynamic viscosity, thermal conductivity and electrical conductivity as well as radiation properties and diffusion coefficients), which influence various arc characteristics including temperature distribution, and both electrical and magnetic fields.

Although it is experimentally possible to estimate the transport coefficients and the thermodynamic properties of gases, the most reliable method of obtaining the required data is through calculation [1.1]. However, transport coefficients are difficult to calculate, and due to uncertainties in the values of the intermolecular potentials, large variations in their values remain. Calculations are simplified by the assumption that the plasma is in local thermodynamic equilibrium (LTE), which is generally the case for computational modelling of atmospheric plasmas. Derived material properties for various shielding gases are given in Figure 1.1.

The peaks in specific heat capacity at approximately 3,500 and 7,000 K correspond to the energy required to dissociate the molecules for hydrogen and nitrogen respectively, while the remaining peaks on the graph correspond to the energy required to ionise the respective atoms (approximately 15,000 K for argon, hydrogen and nitrogen, and 22,000 K for helium).

The viscosity for argon, helium and nitrogen is similar up to approximately 10,000 K and then helium is considerably higher. The viscosity is proportional to the square root of the atomic mass, and inversely proportional to the collision integral [1.3]. Hydrogen is lower at all temperatures due to its lower mass.

All of the gases, with the exception of helium, have similar electrical conductivities. Helium has very low values at temperatures up to about 15,000 K, which makes it difficult to initiate an arc, however the electrical conductivity above 20,000 K is higher for helium. This is because the electrical conductivity is related to the electron density, and explains the phenomenon of helium ionising at higher temperature [1.3].

The thermal conductivity of each gas has peaks corresponding to the dissociation and ionisation temperatures in each case.

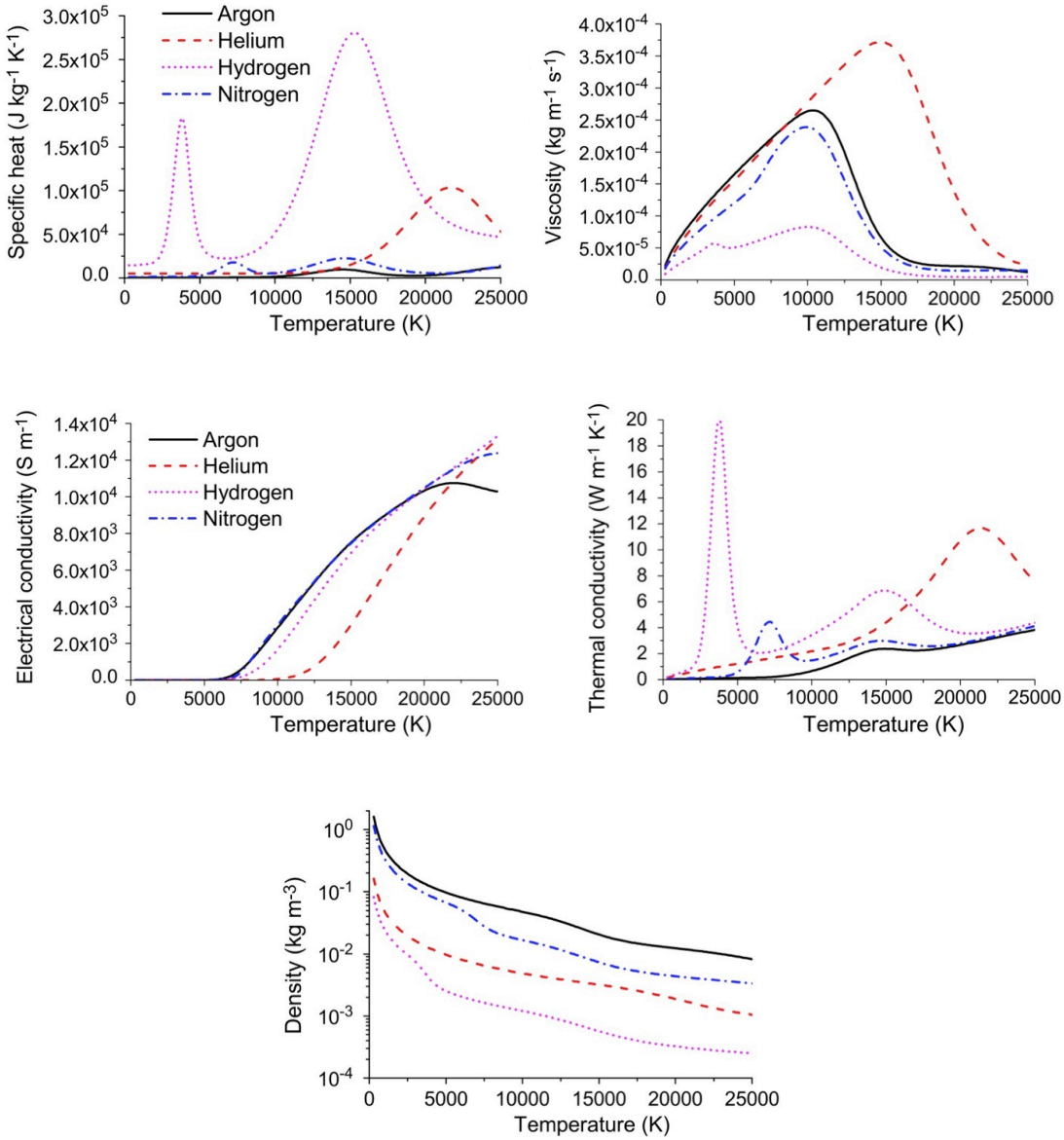

Figure 1.1: Dependence of specific heat at constant pressure, viscosity, electrical conductivity, thermal conductivity and density for argon, helium, hydrogen and nitrogen at 1 atm [1.2].

The density is largely determined by the atomic or molecular weight of the gas. The densities of each gas decreases with increasing temperature because the molecules move further apart as the kinetic energy increases. The density is also reduced upon dissociation and ionization.

The radiative source term for the energy lost from the plasma can be determined through various methods depending upon the fundamental property data available and computational time. Menart [1.4] and Menart et al. [1.5] performed a detailed radiative transport analysis simulation, which utilised a line-by-line radiative analysis, however computation times are large. The method of partial characteristics uses tabulated data of Som (representing the radiation from X and reaching the point O) and ΔSim (the difference between the radiation emitted from ξ and absorbed in X, and, the radiation emitted from X and absorbed in ξ) to calculate the radiative transfer in a given direction [1.6]. The net emission coefficient, ε_N, takes into account the self-absorption of the arc plasma and can be used to estimate the amount of radiant energy lost from the plasma.

Computational modelling allows for the simulation of the effects of various welding parameters. Tanaka et al. [1.3] presented the temperature fields and velocity vectors for 150 A GTAW welding arcs in the presence of argon, helium, hydrogen and nitrogen. It was shown that the argon arc produced the lowest voltage potential and the lowest maximum plasma temperature, anode temperature and plasma velocity. It was also stated that the helium arc did not posses the typical bell shape profile that the other gases exhibited, as shown in Figure 1.2. This was attributed to a higher thermal conductivity increasing the rate of heat transfer from the high-temperature central arc region to the outer arc. In addition, electrical conductivity increases with temperature, which consequently results in a flatter current density profile, further contributing to the distributed temperature profile.

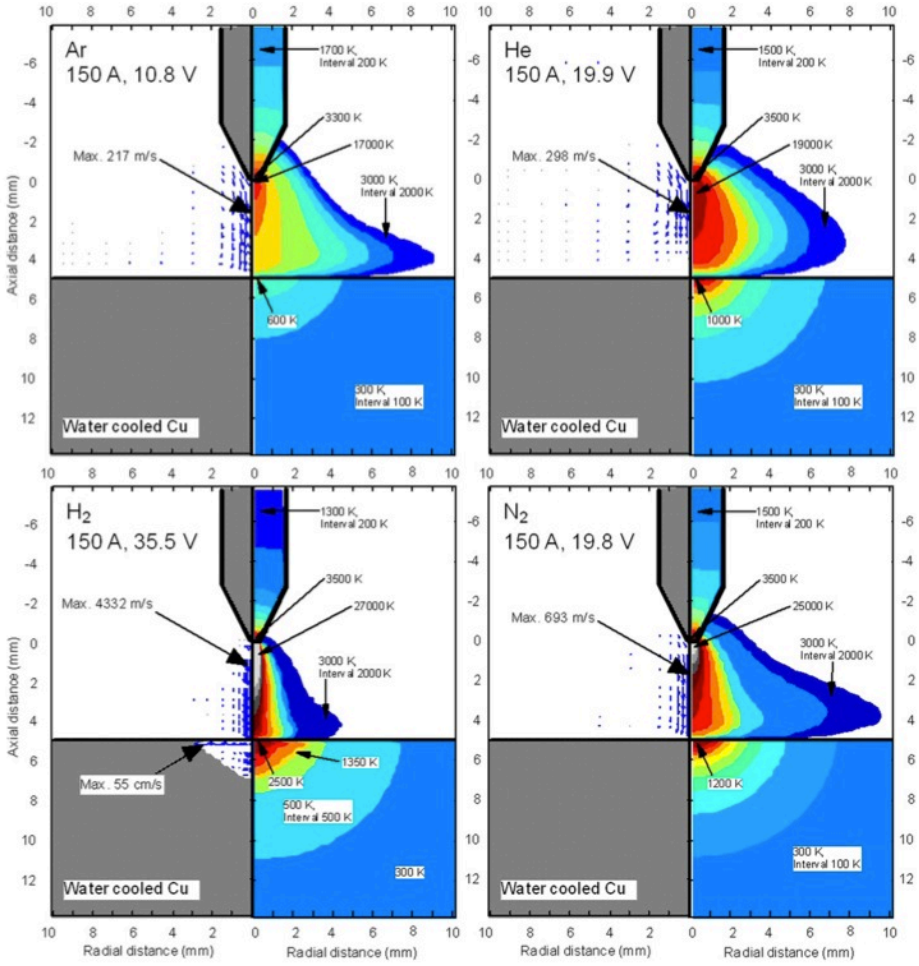

Figure 1.2: Temperature fields and velocity vectors for 150 A arcs in argon, helium, hydrogen and nitrogen [1.3]

Since most thermophysical properties of a given gas differ greatly from all other gases, it is difficult in a practical setup to isolate the property responsible for a particular effect in the arc plasma [1.2]. Computational modelling is not restricted to real gases and therefore allows for the analysis that individual thermophysical properties have on the arc plasma characteristics. Murphy et al. [1.2] used a method of 'imaginary gases' in which one thermophysical property is replaced with that of another gas. This particular study used the thermophysical properties of argon and substituted those for helium systematically, thus allowing the effects of individual thermophysical properties to be evaluated, Figure 1.3.

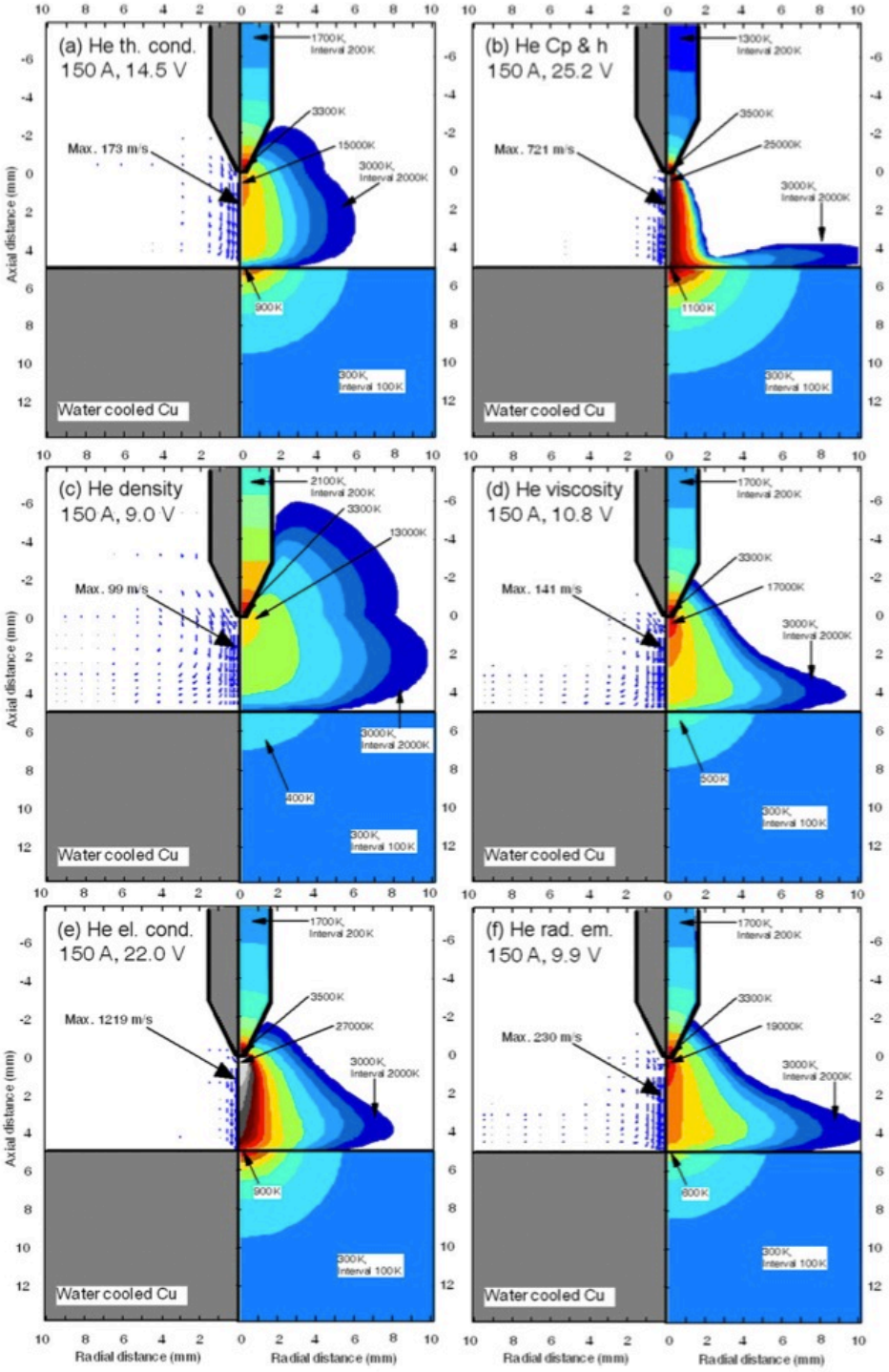

Figure 1.3: Temperature fields and velocity vectors for 150 A arcs in imaginary gases. Thermophysical properties of argon with (a) thermal conductivity, (b) composite value of specific heat and enthalpy, (c) density, (d) viscosity, (e) electrical conductivity and (f) net radiative emission coefficient, altered to that of helium [1.2]

The thermodynamic and transport properties of the shielding gas are modified by the presence of metal vapour in the plasma medium as a result of evaporation from the weld pool surface, and in the case of GMAW, the molten metal droplets. Traces of metal vapour in the plasma medium can have a strong impact on the properties and behaviour of the arc [1.7].

Metal vapours have a significant effect on the electrical properties of the plasma medium; particularly at low temperatures, i.e. below approximately 10,000K, the radiative emission coefficient of the shielding gas has been found to increase by more than an order of magnitude [1.8-1.12]. The electrical conductivity of the medium has been found to increase by a similar magnitude for low temperatures, i.e. below approximately 15,000K, and decrease for higher temperatures [1.2, 1.7], [1.13-1.14].

As a result of the metal vapour in GMAW being concentrated in the central arc column, the radiative emission increases causing greater energy losses from the plasma core. This results in low temperatures occurring at the centre of the arc plasma as presented in Figures 1.4 and 1.5, which show experimental spectroscopy measurements and numerical simulations respectively.

The electrical conductivity has a very small influence on the arc temperature distribution [1.10]. Conversely, simulations [1.2, 1.15] have indicated that the electrical conductivity has a greater influence on the GTAW process than the radiative emission; this is because the metal vapour originates from the relatively low temperature weld pool and is concentrated in the low temperature regions near the workpiece surface as shown in Figure 1.6.

The other thermodynamic properties have been found to have a small effect on the temperature distribution in the arc [1.10]. However, while metal vapour has been shown to influence the thermophysical properties of the plasma, and consequently the arc properties, there have been no experimental measurements to determine the actual percentage of the metal vapour present within the arc plasma.

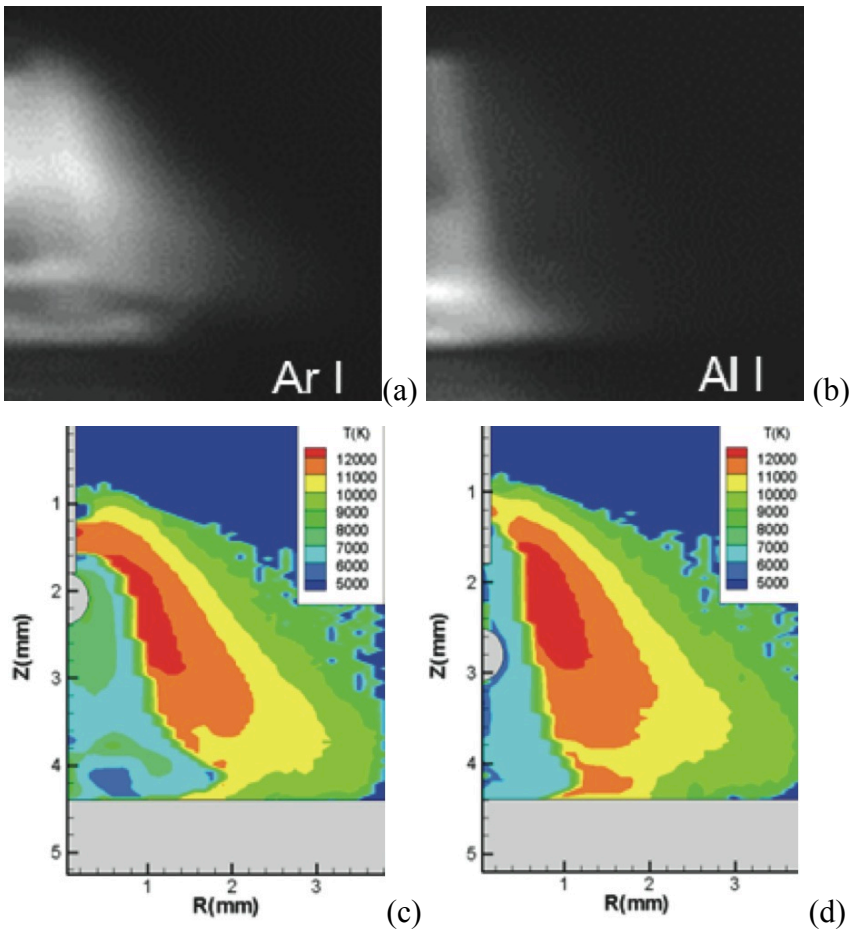

Figure 1.4: GMAW Line spectrum images of (a) Ar I at 696 nm and (b) Al I at 669 nm, converted to temperature distribution by Fowler-Milne method after Abel conversion for (c) 0 ms and (d) 1.5 ms [1.16]

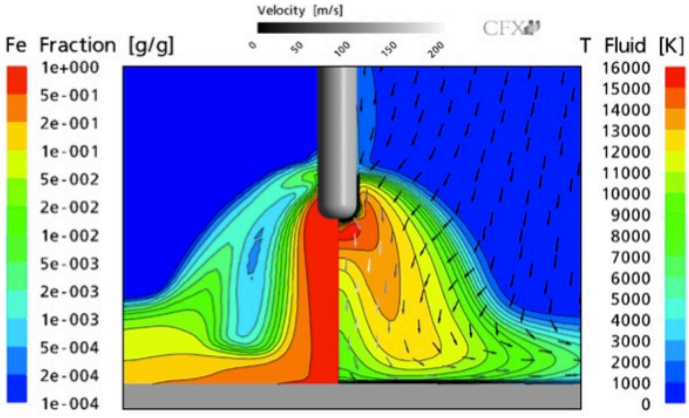

Figure 1.5: Calculated values of iron vapour mass fraction (left), temperature (right) and gas flow (vectors) for a 250A arc with a vaporisation rate of 1% relative to the 10 m/min wire feed rate [1.12]

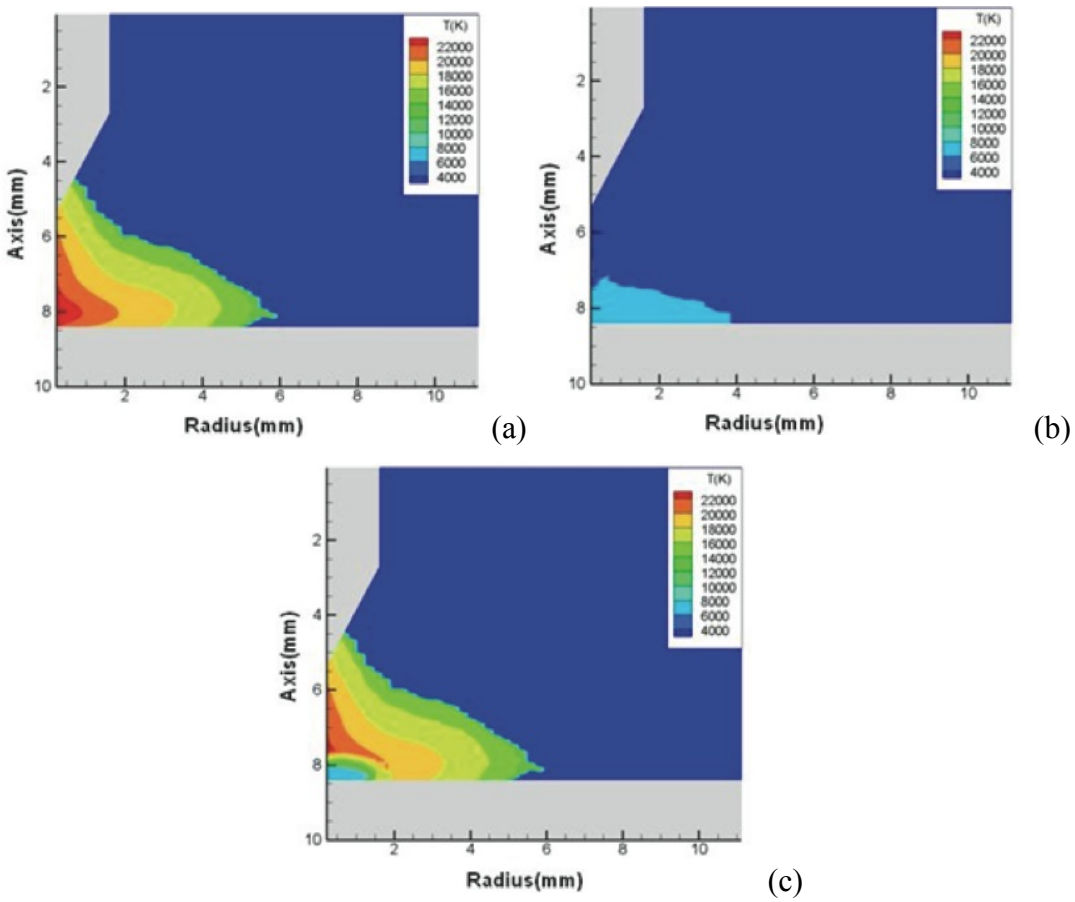

Figure 1.6: GTAW temperature distribution of (c) arc plasma by superimposing (b) metal vapour temperature onto (a) shielding gas temperature [1.17]

1.1.4 Shielding gas efficiency

The efficacy of the shielding gas can either be related to how efficiently the atmospheric gases are displaced from the arc area, or how efficient the arc plasma is in transmitting the electrical energy to the workpiece.

1.1.4.1 Atmospheric gas displacement efficiency

There are a number of factors that influence the shielding efficiency including: shielding gas density, flow rate and purity, defects in the shielding gas delivery system, nozzle geometry and stand-off distance, and drafts in the working region.

The density is the mass per unit volume of shielding gas, while the specific gravity is the density of shielding gas to density of air ratio. Therefore a shielding gas with a specific gravity greater than one is more effective in displacing air in the flat position

than that with a specific gravity lower than one, and vice versa for the overhead position, thus a lower shielding gas flow rate is required. It has been reported [1.18] that a shielding gas flow rate of between 2 and 2.5 times that of pure argon is required when using pure helium in the flat position when using GTAW process, primarily due to differences in the shielding gas densities.

The correct shielding gas flow rate is essential for providing adequate protection to the weld metal during the heating, liquid and solidification stages. Hence, there is an optimum flow rate for weld shielding gases, but this is difficult to define and is often decided on the basis of preference or experience. It is known that too low a flow rate can lead to inadequate coverage of the arc area, which often leads to porosity and excess spatter development. Conversely, too high a flow rate can result in poor penetration [1.19] and/or porosity due to turbulence in the gas column. In the case of the latter, the turbulence effect results in atmospheric gases being drawn into the arc [1.20], which promotes the formation of entrapped gas (porosity) during the solidification phase.

The minimum shielding gas purity for each shielding gas is specified in Table 1.1. However, the parent and filler materials used also influence the quality of the solidified weld for a varying degree of shielding gas impurity [1.18]; carbon steels have a relatively high tolerance for weld region contaminants, others including aluminium, copper and magnesium are fairly sensitive to impurities, whereas others such as titanium and zirconium have extremely low tolerances.

Leakage in the shielding gas delivery system can account for 50-75% of the total losses in a bulk system or plant [1.21]; this includes leaks in piping and hoses, malfunctioning solenoid valves, defective pressure regulators etc. A single leak, with a diameter of a pin needle, can account for gas losses of approximately £6,700 ($10,000) per annum [1.21]. In addition, leaks in the gas delivery system can have greater implications than the monetary losses, as a result of inadequate shielding of the arc area; defects in the solidified weld could arise.

In addition to over-estimating the correct steady state flow rate, a surge of gas is also known to occur at the arc initiation stage with flow rates of up to 60 l/min reported [1.19, 1.22] due to a build up of pressure in the gas line. This initial surge is

deleterious to the properties at the start of the weld due to the turbulence effect described previously and is also cost ineffective. In such cases, it is widely understood that this initial surge of gas results in moisture-ladened air being drawn into the shielding gas column [1.19, 1.20], which is detrimental to the weld quality. Concurrently, it is recognised that some additional shielding gas is required at the arc initiation stage [1.20, 1.23] in order to purge the gas supply line and weld region of atmospheric gases.

Although it has been reported [1.24, 1.25] that the cost of the shielding gas is minimal in relation to the overall welding costs, Standifer [1.21] stated that a typical welding plant with 300 workstations, each operating with a shielding gas flow rate of approximately 21 l/min (45 CFH), at 50% efficiency and 30% arc time will consume more than £1 million ($1.5 million) of argon annually. In addition to this, Standifer also determined that an additional £112,000 ($168,000) is accrued by the initial surge at weld ignition. Furthermore, these calculations are based upon argon shielding gas costs that were generated a decade ago, and consequently, the unit cost is likely to have increased substantially due to inflation and other economic drivers. Additionally, the calculations assumed ideal conditions, which included each workstation having the recommended gas flow rate pre-set, which is reported [1.19] to be no more than 12 times the filler wire diameter. As predicted, it was found that less than 20% of workstations did so, and the majority were found to exceed the recommended pre-set flow rate.

Okada et al. [1.26] conducted chromatography measurements for an argon shielding gas, both with and without an electrical arc (Figure 1.7), although the results were used for comparison with visualisation techniques rather than weld quality. It was found that the electrical arc causes a contraction in the high concentration shielding gas boundary, an effect that was found to increase for higher arc currents.

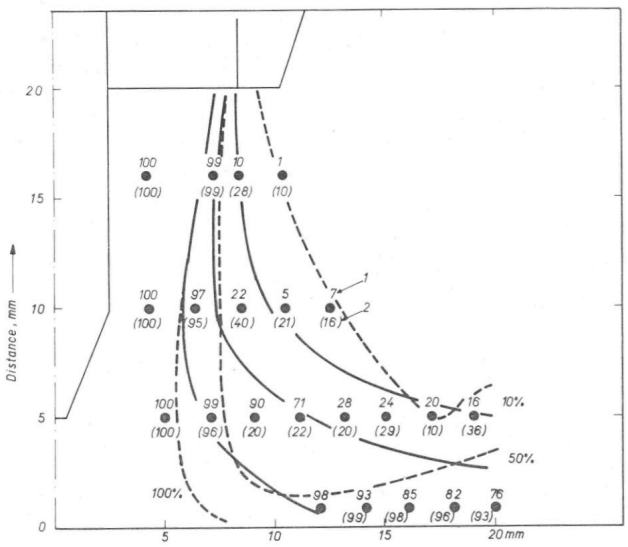

Figure 1.7: Chromatography measurements for GTAW with 20 l/min argon gas flow; no arc (solid lines, top values), and with arc (dashed lines, bottom values) [1.26]

The nozzle geometry, i.e. the outlet diameter, and stand-off distance (the distance from the nozzle exit to the workpiece surface), when subjected to the adverse effects of cross drafts also influence the shielding efficiency. A larger outlet diameter nozzle results in the shielding gas exiting the nozzle at a lower velocity, and consequently, takes longer to reach the surface of the liquid weld pool. A similar case applies to the stand-off distance where a larger distance increases the time taken for the gas to reach the weld, thus making the shielding gas column vulnerable to any draft in the arc region.

Tamaki et al. [1.27] made shielding gas concentration measurements in the absence of an arc (Figure 1.8) and correlated this with radiographic examination to conclude that the minimum CO_2 concentration required to prevent harmful porosity in the weld was 95% by volume in the core region. The effect of cross drafts was also studied, and a value of the ratio Vs/Vw (where Vs is shielding gas speed and Vw is the draft speed) was determined below which harmful porosity occurred in the weld.

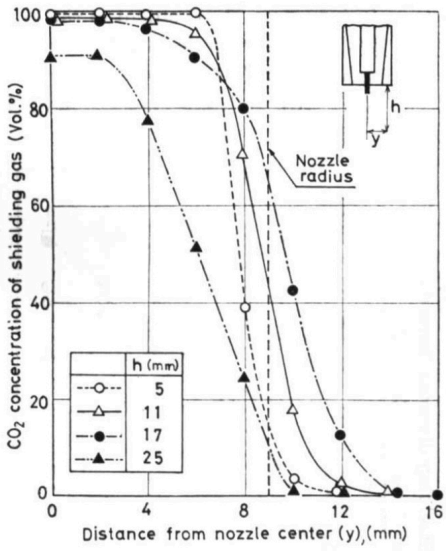

Figure 1.8: CO_2 shielding gas concentration with respect to the nozzle exit [1.27]

The shielding gas flow rate is normally controlled through the use of conventional flow meters attached either directly to the gas cylinder, on the gas line prior to the welding unit, or built into the unit itself. Despite the importance of the shielding gas to the GMAW process, there is a lack of knowledge among welding operatives as to how the shielding gas flow rate should be established and controlled in practice. An industrial survey has shown [1.28] that the welding operative often adjusts the shielding gas flow rate to as high as 30 l/min, with the belief that a higher shielding gas flow rate means better protection for the weld region.

Various mechanical and electromagnetic gas-saving devices have been developed to regulate the gas flow rate and minimise shielding gas consumption, and have been reported to produce gas savings in the region of 60% [1.29-1.32].

The wastage of shielding gas can be controlled through the installation of a mechanical anti-surge device. This device aims to reduce the initial surge of gas at weld initiation and deliver a controlled flow rate throughout welding.

Some electromagnetic units have been developed to implement a feedback control loop that synchronises the flow rate according to a correlation between shielding gas flow rate and the welding current used. A theoretical relationship between welding current and shielding gas flow rate has been derived [1.22], which, in principle, means that, the higher the welding current used, the greater the shielding gas flow

rate required. In doing so, the theoretical optimum shielding gas flow rate is continuously supplied to the weld zone. The conventional method of manually setting the shielding gas flow rate by welding operatives often becomes a permanent setting regardless of the welding current being used, often accounting for the maximum estimated welding current, thus resulting in a gross over usage of gas.

A reduction in shielding gas consumption provides additional benefits, as a consequence of having less down-time due to cylinder changeovers; an increase in productivity is promoted. In addition, cylinders are never completely empty at changeover; nevertheless, this is commonly overcome through the use of bulk storage shielding gases, which negates these issues. Moreover, a reduction in carbon emissions [1.19] is achieved through a culmination of a reduction in CO_2 gas mixture consumption and a decrease in energy required for gas production and delivery.

1.1.4.2 Arc thermal efficiency

The arc thermal efficiency plays an important role in various aspects of the welding process, and provides a quantitative measure of the fraction of the total arc energy delivered to the workpiece [1.33]. The gross power generated by the arc is given by the product of the welding current and voltage. The net power transmitted to the workpiece is the gross power minus process losses, which are a result of radiation, convection, electrode heating and heat conduction to the welding torch [1.34]. The ratio of the net to gross power input is the arc thermal efficiency, which is shown in Figure 1.9 for various arc welding processes.

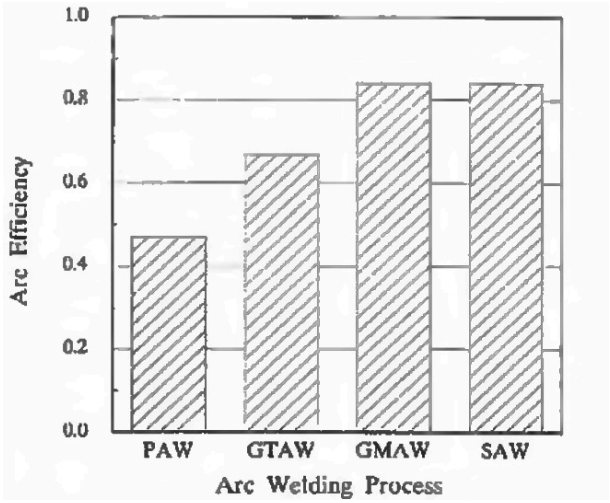

Figure 1.9: Arc efficiency for arc welding processes [1.33]

1.1.5 Shielding gas flow visualisation

A number of studies have been conducted to visualise the shielding gas flow in GMAW and GTAW. These have primarily been conducted in 'cold' flow conditions, i.e. with no welding arc, although limited visualisations have been conducted for 'hot' flow conditions, i.e. with a welding arc. The 'hot' flow measurements are more complex due to the high emissions from the electrical arc, and due to the heating of both the arc and the plate, which in turn heats the surrounding air, making it visible.

Gibson [1.35] measured the shielding gas coverage using aluminium and titanium GTAW spot welds for various weld conditions, including shielding gas composition, stand-off distance and cross drafts. Useful guidelines on the extent of gas coverage were determined, but these were not related to adequate weld quality. Schlieren optical visualisation was used to qualitatively show the shielding gas flow profile both with and without a welding arc, generating some of the first images of this type for arc welding (Figure 1.10).

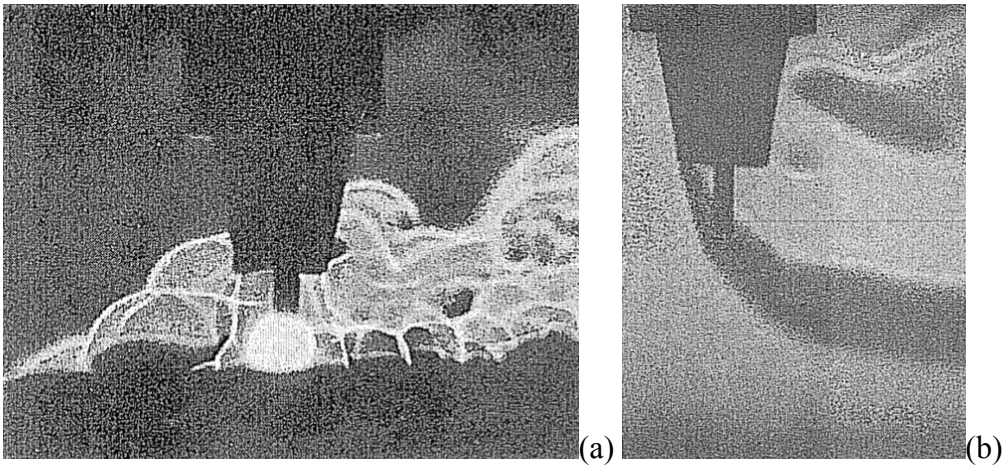

Figure 1.10: Schlieren images for (a) 'hot', and (b) 'cold' flow [1.35]

More recently, Siewert et al. [1.36] investigated the effect of various schlieren parameters on the image quality obtained for arc welding. The effect of the slit geometry and orientation was evaluated, determining that a vertical rectangular source slit (2 x 6 mm) produced optimum results, as shown in Figure 1.11. The orientation of the slits dictates the direction of the density gradients visualised, while the iris aperture visualised the flow in all directions at a reduced brightness.

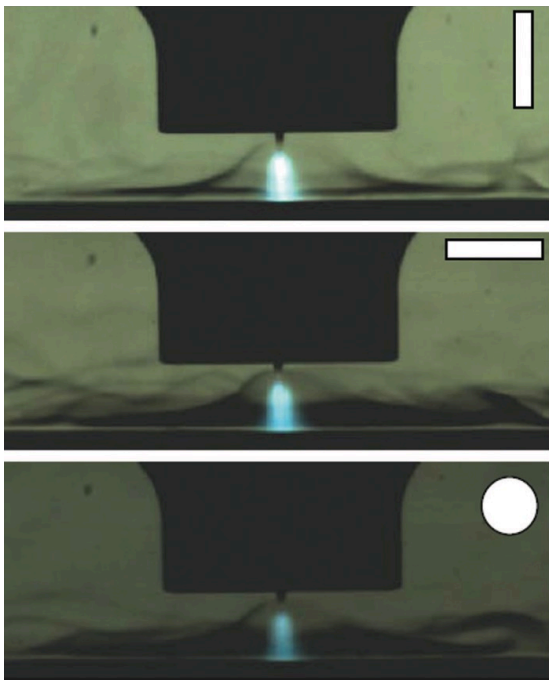

Figure 1.11: Schlieren images for an argon / 50% helium mixture, highlighting the effect of aperture geometry; vertical rectangle (top), horizontal rectangle (middle), and iris (bottom) [1.36]

The schlieren technique has been implemented as a validation method for computational modelling of the welding arc. The images generated for GTAW (Figure 1.12) show the effects of increasing the shielding gas flow rate for an argon / 50% helium mixture, with a progressive level of turbulence present.

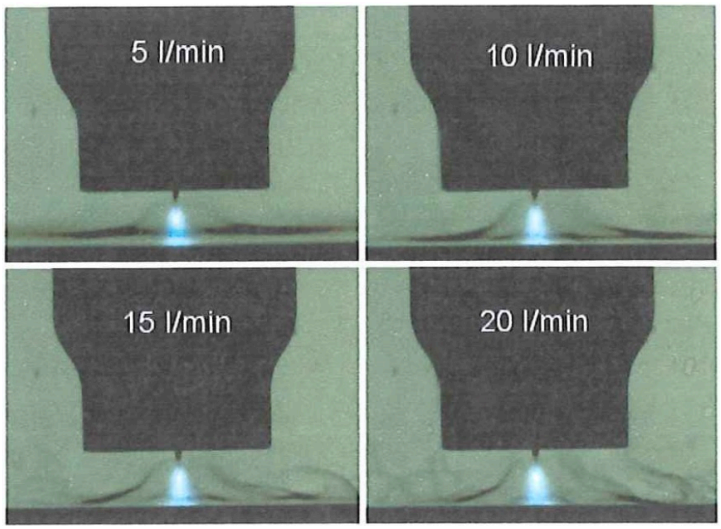

Figure 1.12: Schlieren images for varying shielding gas flow rate in GTAW [1.37]

Okada et al. [1.26] implemented a combination of shadowgraphy with a laser source to visualise the shielding gas flow, and chromatography to measure the shielding gas concentration in the arc region. The boundary of the laminar flow area below the nozzle was found to coincide with 90–99% lines of equiconcentration of the argon shielding gas measured by gas chromatography. The shielding gas was shown to contract towards the arc centre, with a greater contraction occurring for lower shielding gas flow rates, Figure 1.13. This contraction effect was also observed when the arc length and/or current increased; the shielding gas coverage for a 20 l/min flow rate was found to decrease from 12 to 4 mm radius, for no arc and a 500 A arc respectively. Where the outer boundary of the shielding gas column comes into contact with the arc periphery, the final weld bead was found to be unacceptable. Skovfo and Jørgensen [1.22] also reported that a higher welding current required a higher shielding gas flow rate to provide adequate protection.

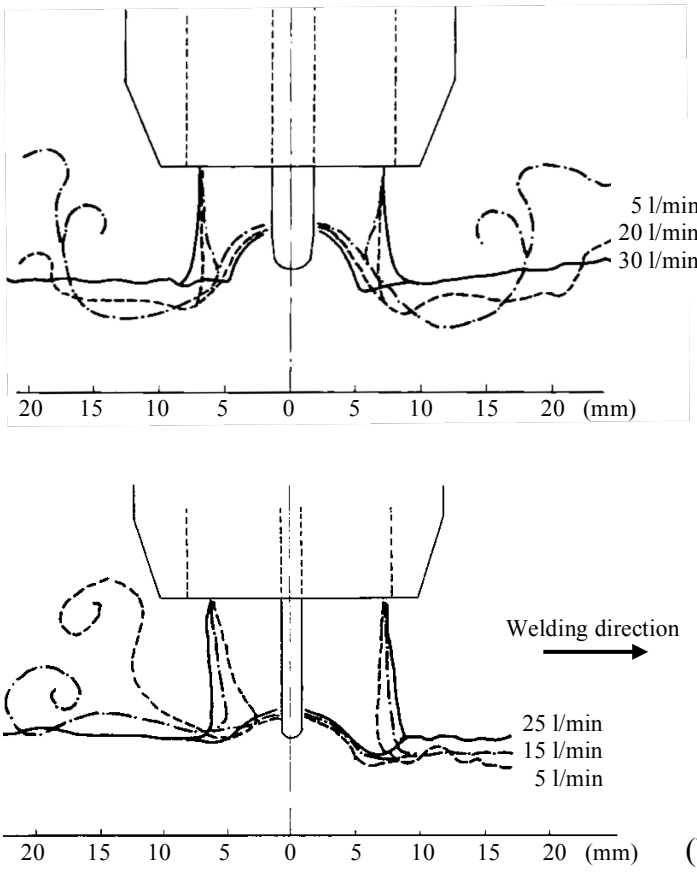

Figure 1.13: Influence of flow rate on shielding gas flow based on schlieren imaging for (a) GTAW, and (b) GMAW [1.26]

Flow visualisation techniques such as gas seeding, and particle image velocimetry (PIV) have also been used to characterise the behaviour of the shielding gas flow [1.38-1.40]. PIV is a non-intrusive optical method, in which a laser light illuminates tracer particles twice within a defined, short time interval while following the flow.

Johnson et al. [1.38] conducted 'cold' flow visualisation of the 'shielding gas' through smoke seeding of air, and PIV measurements for a range of Reynolds numbers for the gas. As can be seen in Figure 1.14, higher Reynolds number flows increase the turbulence present at the shielding gas boundary, drawing the atmospheric gases towards the arc region. The results presented confirms prior statements that increasing the shielding gas flow rate will not improve the shielding effect, and may instead cause deterioration of the weld quality. Although air was used, it was assumed that for similar Reynolds numbers, the findings would apply to other shielding gases commonly used.

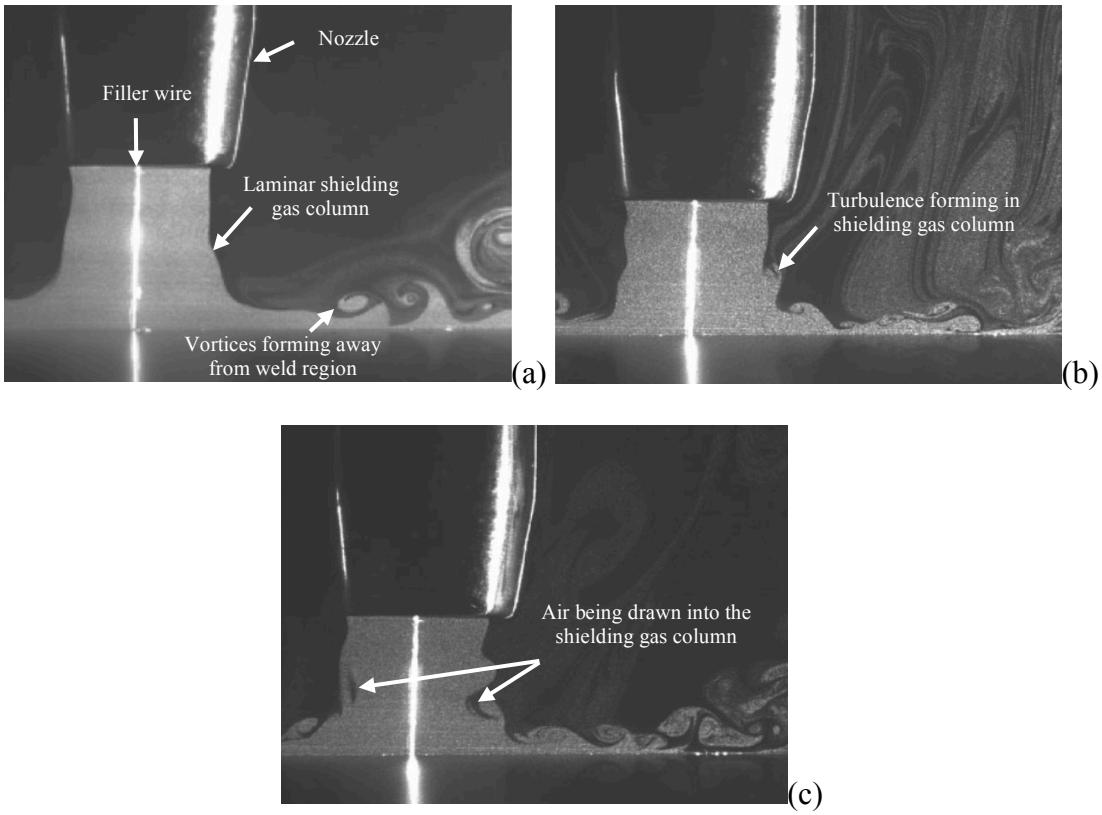

Figure 1.14: Images of air seeded with smoke exiting a conventional nozzle at (a) Re 1260 (~15 l/min), (b) Re 1680 (~20 l/min), and (c) Re 2100 (~25 l/min) [1.38]

Schnick [1.40] conducted PIV measurements for different orientations of the welding torch, Figure 1.15. It was stated that the flow analysis is only reliable in the free jet where particles are present, and an unsteady back flow region was present between the wire tip and the work piece for the example with no welding arc. During welding, the PIV analysis showed an immediate expansion of the shielding gas in the arc region, and a large increase of the velocity adjacent to the arc and above the workpiece. A vortex formed on the left hand side of the arc, its velocity and diameter is dependant upon the pulse time and current.

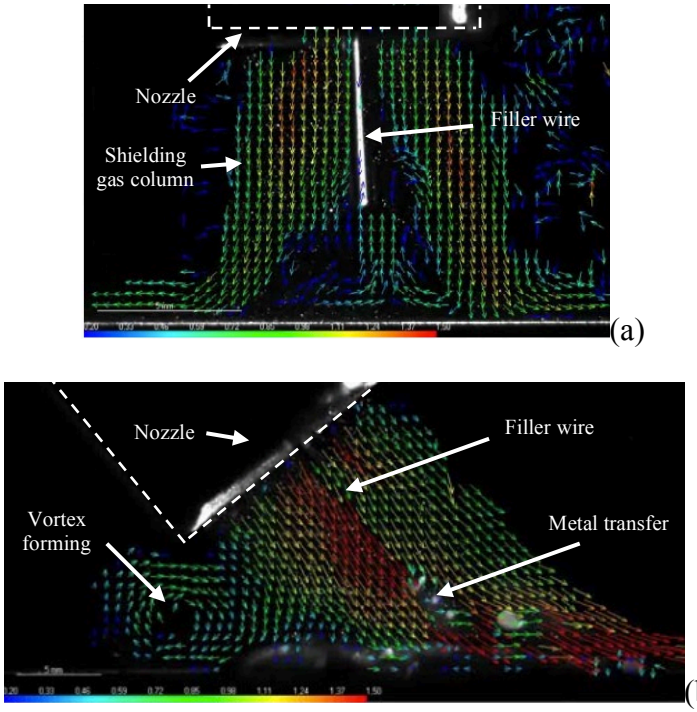

Figure 1.15: Calculated vector field for (a) vertical torch (no arc), and (b) 45° torch in pushed position (with arc) [1.40]

1.1.6 Arc pressure and weld metal fluid flow

The pressure produced as a result of the arc plasma impinging on the weld pool surface is one of the major contributing factors influencing the depth of penetration and the size and shape of the weld bead. A high welding current is desirable for increasing productivity; however, high welding currents increase the possibility of weld defects such as humping, undercutting, split bead, parallel humping and tunnel porosity [1.41].

A number of experimental and computational studies have been conducted [1.42-1.48], to investigate the effect that various parameters (including welding current, shielding gas composition and pressure, tungsten electrode tip geometry, arc length and nozzle outlet diameter) have on the peak pressure and the pressure distribution in the arc column.

It has been shown that the welding current has a significant effect on the maximum arc pressure recorded, with Lin and Eagar [1.42] reporting a linear relationship between the maximum arc pressure and the welding current, which was in agreement with other data they presented. Studies [1.43-1.45] have shown that the current density increases approximately linearly with increasing current, while Fan and Shi [1.46] stated that the electromagnetic force is the driving force for fluid flow in the arc plasma and increases with increasing current density; thus the electromagnetic force will increase with increasing arc pressure.

A number of studies have been conducted to investigate the effect of the GTAW tungsten electrode geometry [1.42, 1.44, 1.46], predominantly looking at the effects of the vertex angle. Data have been presented for vertex angles of 30–120°: a narrower angle increasing the peak pressure, with Fan and Shi [1.46] showing a peak pressure of ~1150 and ~200 Pa for a 60° and 120° vertex angle respectively, both for a 200 A welding current. Fan et al. [1.47] investigated the effect of varying the size of a flat surface (truncation diameter) at the electrode tip, showing that the smaller the truncation diameter, the higher the arc pressure.

The shielding gas composition is known to have a substantial effect on the arc pressure, argon producing a considerably higher maximum pressure than helium [1.42, 1.45]. Lin and Eagar [1.42] found that the arc length has a negligible effect on the peak arc pressure when using argon as a shielding gas. However, when using helium, as the arc length increased, the peak pressure decreased linearly. This was attributed to the lower density and higher viscosity of helium at high temperatures when compared to argon. Oh et al. [1.45] reported that a shielding gas mixture of argon / 33% helium reduced the maximum pressure by a factor of approximately three when compared to a pure argon shielding gas for a 5 mm arc length.

Ham et al. [1.48] reported on the effects that the shielding gas pressure and nozzle diameter have on the arc shape, arc pressure and gas pressure measurements. It was determined that a higher shielding gas pressure or narrower nozzle diameter decreased the diameter of the arc plasma due to a thermal pinch effect. They also concluded that the shielding gas pressure did not affect the arc pressure measurement but did influence the gas stagnation pressure.

Fluid flow and heat flow are key factors in determining the final weld shape [1.49], with the direction of the liquid weld metal fluid flow being estimated based upon the various body forces acting upon it. A schematic diagram of the GTAW process and the forces acting on the liquid weld metal is shown in Figure 1.16. As can be seen, the arc force and Lorentz force are opposite in direction to the plasma shear and buoyancy force, while the direction of flow due to Marangoni convection is dependent upon the surface tension gradient.

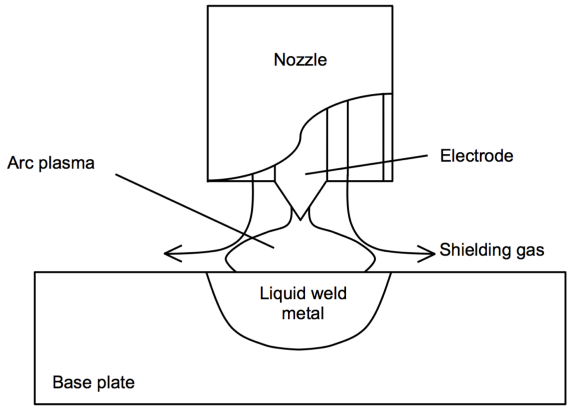

(a)

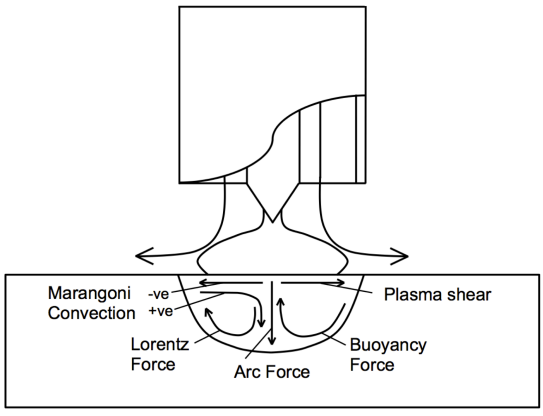

(b)

Figure 1.16: Schematic diagram of (a) GTAW process, and (b) forces acting on liquid weld metal

Plasma shear is due to the arc plasma moving radially outwards on the weld pool surface, causing a drag force, and is therefore a function of the dynamic viscosity and radial velocity of the shielding gas. Lee and Na [1.44] used numerical modelling to simulate the GTAW process and presented results for the plasma shear over a range of welding currents and electrode vertex angles. They determined that a maximum shear force occurred between 1 and 2 mm from the arc centreline, which, for a 60° vertex angle, they found to be ~15, 75 and 155 N/m^2 for a 100, 200 and 300 A welding current respectively. Hu and Tsai [1.50] also used numerical modelling to simulate a GMAW arc and found that a plasma shear of ~90 N/m^2 was produced for a welding current of 220 A.

The arc force is defined as the force of the arc plasma impinging upon the weld pool surface for which there are several methods of determining: experimentally measure the arc force using a torsion bar and displacement transducer [1.51], or numerically integrate the arc pressure over the impingement area of the arc [1.42]. Lin and Eagar [1.42] presented arc force data for a range of welding currents and electrode vertex angles while using argon, showing that the arc force is proportional to the square of the current.

The Lorentz (or electromagnetic) force is one of the driving forces for fluid flow in the weld pool [1.52-1.55]. Kou and Wang [1.52] demonstrated using three-dimensional mathematical modelling, and by considering various driving forces individually (electromagnetic, buoyancy and surface tension), that the electromagnetic force produced deeper penetration than those attributed to the buoyancy force or surface tension effects.

Computational simulations generally include the effect of buoyancy and surface tension on the weld metal; however, modelling has only been used to simulate the driving forces individually or as part of a combination of driving forces, and the effect of the shielding gas has never been considered. Kou and Sun [1.53] demonstrated experimentally using alternative heat sources that the buoyancy force produced shallower penetration in the central location but was radially wider than the Lorentz force.

1.2 Alternating shielding gases

1.2.1 Background

Alternating shielding gases is the process of periodically supplying two different shielding gases to the welding region in order to take advantage of the beneficial properties of each shielding gas. In doing so, the arc plasma exhibits transient thermophysical properties, thus allowing for the manipulation of arc characteristics and consequently solidified weld properties.

1.2.2 Invention

Although the majority of research publications regarding the use of alternating shielding gases have been produced within the last 5-10 years, the process of periodically varying shielding gas composition was first suggested in 1967 [1.56] as a means to alternate the arc current between two values.

Cunningham [1.56] suggested a method and apparatus that generated pulsations in the current through a welding or cutting arc, similar to that of a pulsed power supply, produced by periodic variations in the composition of the shielding gas in which the arc operates. The primary objective of the invention being to reduce the average arc current, whilst retaining the advantageous properties of a higher peak current that helium would provide.

1.2.3 Shielding gases

The first recorded use of alternating shielding gases [1.56] proposed a shielding gas combination of argon and carbon dioxide, although it was acknowledged at this stage that other shielding gases could equally be used. This combination was later applied to narrow gap welding [1.57] in which the variation in thermophysical properties caused the arc length to oscillate. More recently [1.58-1.59], the alternating shielding gas process has necessitated around the use of argon and helium gases.

1.2.4 Experimentally derived process benefits

The alternating shielding gas process has been applied as a shielding gas supply method in GMAW and GTAW; particularly for aluminium alloys [1.60-1.65], carbon [1.65] and stainless [1.61, 1.66-1.67] steels, and narrow gap welding [1.57].

Studies regarding the use of alternating shielding gases have identified the potential for an increased travel speed, as well as several interrelated secondary benefits, when compared to conventional shielding gas supply methods:

- Improved pre-weld efficiency
    - Reduced edge preparation requirement
- Increase in productivity (weld travel speed)
    - Reduced weld heat input
        - Reduced distortion
        - Reduction in residual stresses
    - Reduced electrical energy consumption
    - Reduced shielding gas consumption
- Improved mechanical properties
    - Increased yield and ultimate tensile strength (UTS)
    - Increased bend angle
    - Improved impact toughness
    - Increased low-cycle fatigue strength
    - Reduced fatigue crack propagation rate
- Improved macro- and microstructural properties
    - Reduction in porosity
    - Refined structure of the weld metal
    - Increased cracking resistance
    - Reduction in lack of fusion defects and undercutting
- Increased post-weld efficiency
    - Increased accuracy of manufacture
    - Reduction in post-weld examination
    - Fewer rejected components
    - Less post-weld refit work

Thus the alternating shielding gas process has been found to produce an array of benefits throughout the processes; from reducing weld edge preparation to improving the mechanical properties of the welded joint.

1.2.5 Theoretical weld pool phenomena and fluid flow

The benefits achieved through the use of alternating shielding gases have been attributed to three independent phenomena occurring in the process:

- Arc pressure variation
- Arc pressure peaking
- Variation in weld pool fluidity

Kang et al. [1.62] proposed a schematic diagram of arc pressure vs. time, as shown in Figure 1.17. It was suggested based on previous publications that since argon results in a higher arc current (for a constant voltage power source), it would produce a greater arc pressure than helium. It was also stated that a pressure impulse would occur whenever there is a change in gas supply from argon to helium or vice versa.

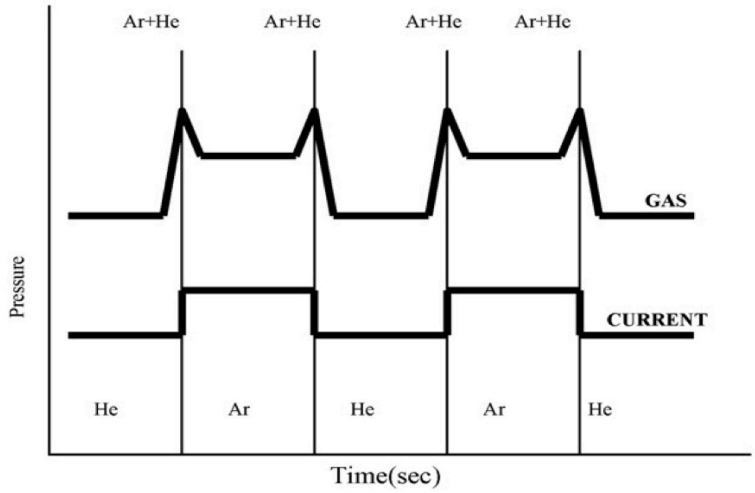

Figure 1.17: Schematic diagram showing variation in arc pressure and welding current when using alternating shielding gases [1.66]

Tazetdinov et al. [1.65] stated that the arc pressure in the arc column is equal to the sum of the static and dynamic pressures. The oscillograms presented indicated that

the arc current when using alternating shielding gases is approximately constant throughout the alternating cycle, and due to the static pressure being primarily governed by the arc current [1.42], the static pressure will remain constant throughout. Contrariwise, Tazetdinov et al. [1.65] stated that the dynamic pressure would vary as a function of the gas density, and specified a dynamic pressure for argon being approximately 24 times higher than that for helium.

Kang et al. [1.62] speculated that as a result of the variation in arc pressure, the high arc pressure produced using argon causes the weld pool to move downwards in the central location, whereas the relatively low pressure produced using helium produced the opposite flow vectors as shown in Figure 1.18.

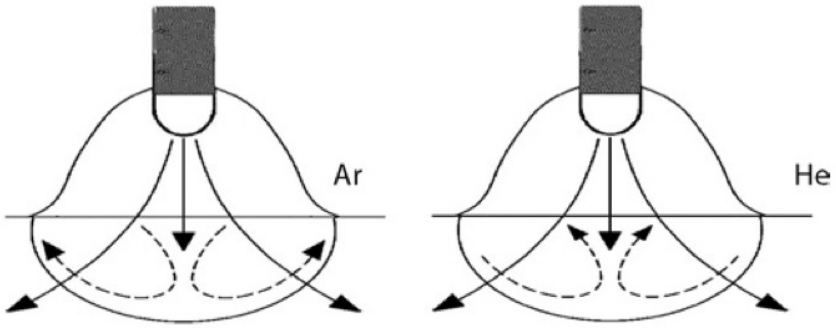

Figure 1.18: Schematic diagram of weld pool fluid flow when using alternating shielding gases [1.62]

The flow vectors for argon and helium have been simulated through the use of CFD [1.67], which found that there are two vortices near the top of the free surface. As can be seen in Figure 1.19, the simulated fluid flow is considerably more complex than that suggested by Kang et al. [1.62], but is also opposite in direction in the central region of the weld pool. This is primarily due to the surface tension gradient, which has an important impact on the flow direction and is material dependent, thus different flow vectors will be present for different metals.

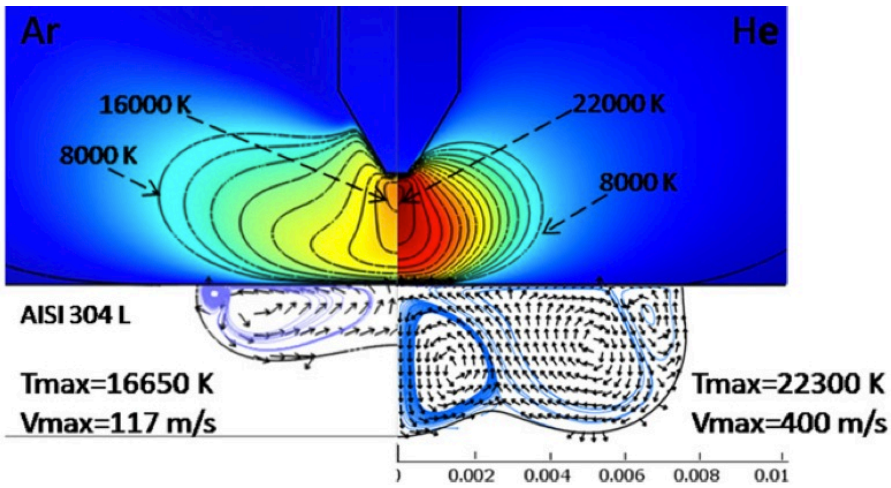

Figure 1.19: Temperature fields, weld pool velocity and streamlines for argon (left) and helium (right) [1.67]

The surface tension gradient is generally discussed as a function of the surface-active elements, such as sulphur or oxygen [1.68, 1.69]. For pure metals and those containing surface-active elements below a critical content, the surface tension gradient is negative and results in an outward thermocapillary flow from low to high surface tension. Conversely, for those containing surface-active elements above the critical content, a positive surface tension gradient exists and results in an inwards surface flow. In addition, the surface tension gradient is temperature dependent, thus a temperature gradient across the weld pool surface could result in the gradient changing from positive to negative as indicated in Figure 1.20.

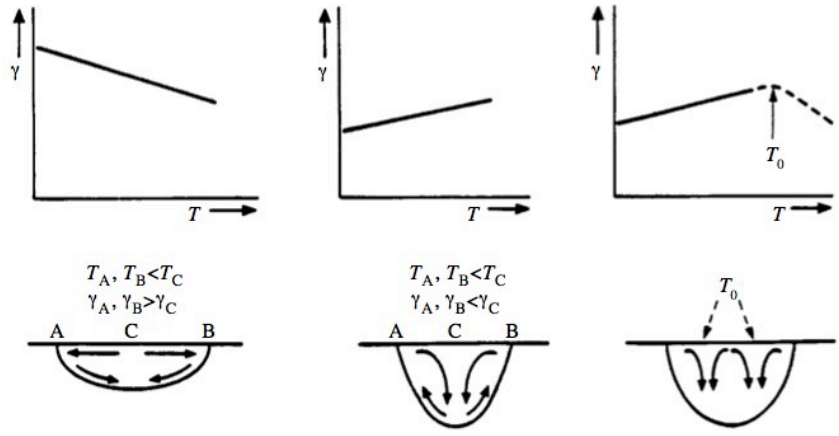

Figure 1.20: Schematic diagram illustrating the Heiple-Roper theory for variable weld penetration [1.68]

1.3 Distortion

1.3.1 Introduction

Distortion is a problem that occurs in many manufacturing processes and is particularly prevalent in the shipbuilding industry due to the non-uniform expansion and contraction cycles present in the arc welding processes implemented.

Distortion is an increasing problem when structures are constructed using a unit assembly process, and consequently distortion can be detrimental when the welded sub-structures have to be aligned and joined together. For example, fillet welds are commonly used in the shipbuilding industry to attach stiffener bars to larger flat sections to improve the rigidity of the structure, Figure 1.21. However, as observed, fillet welded configurations generally lead to out-of-plane distortion, which is particularly troublesome when joining the previously mentioned flat sections to one another to form part of a larger structure [1.70, 1.71].

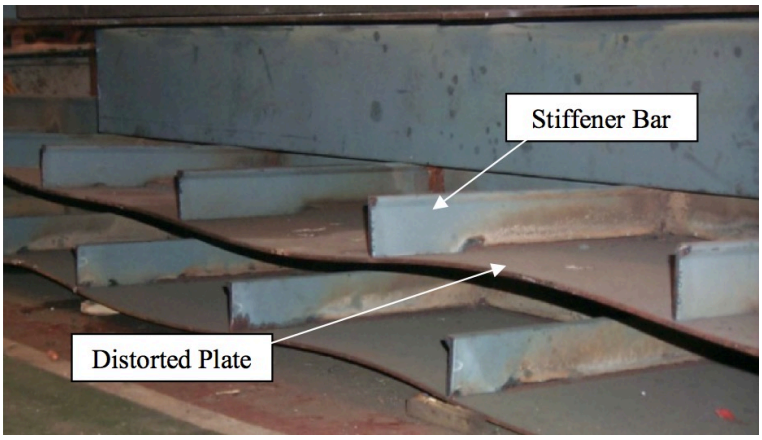

Figure 1.21: Distorted plate with welded stiffeners

1.3.2 Distortion evolution

During the welding process, the workpiece is locally heated by what is essentially a point source. The temperature distributions along its length and across its width are non-uniform and change as the process progresses [1.72].

A schematic diagram of the thermal and stress cycles present during the welding process are shown in Figure 1.22. A weld bead is deposited along the x-axis at a travel speed, v, and origin, O. The welding speed is normally fast in comparison to

the heat conduction and therefore thermal gradients ahead of the arc (A-A) are usually neglected. The location of the arc (B-B) exhibits extremely high temperature gradients, while behind the arc (C-C) the cooling cycle prevails. Far away from the arc location (D-D), the temperature of the weld bead and surrounding material has reached equilibrium and hence no thermal gradients exist.

As there are no thermal gradients ahead of the welding position, the material at this position is not subjected to any thermal strains and consequently no deformation.

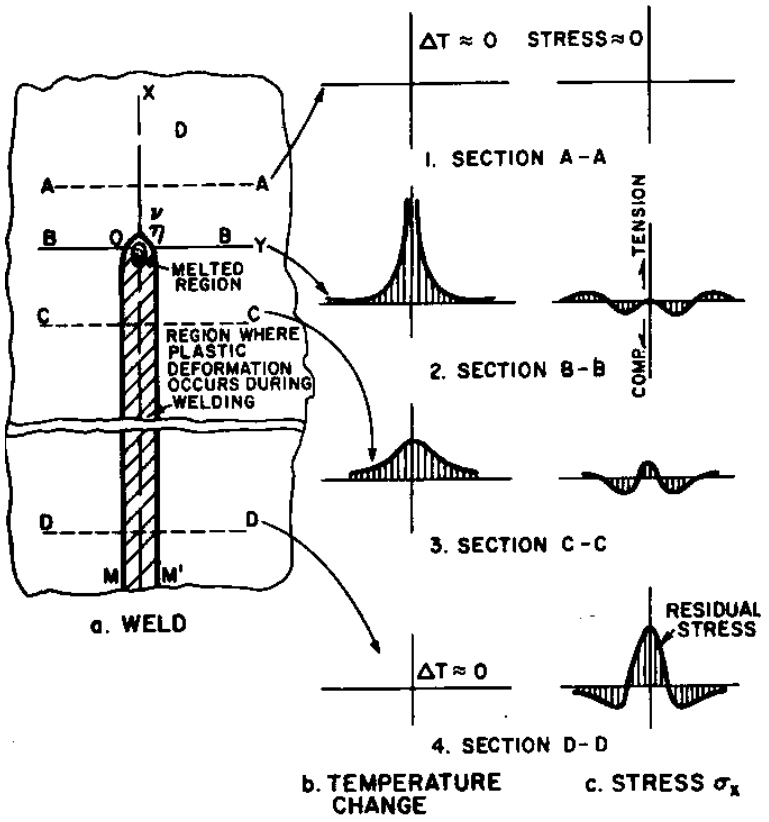

Figure 1.22: Schematic representation of changes in temperature and stresses during welding [1.72]

The temperature is highest at the welding location (B-B) and, consequently, localised thermal expansion occurs. As the welding torch passes, the surrounding material is at a considerably lower temperature and therefore large thermal gradients exist. As a result of the surrounding material, which acts to restrain the weld metal expansion, compressive stresses are introduced to the structure.

The liquid weld metal does not support any load, and therefore does not exhibit any thermal strains. Further away from the weld bead the stresses are tensile to balance the compressive stresses adjacent to the weld.

At location C-C, i.e. after the welding torch has passed, the weld metal and adjacent workpiece regions are in the cooling cycle and will try to contract to maintain equilibrium. The colder material adjacent to the weld bead will act to restrict contraction and will introduce tensile stresses to the weld bead.

As the material cools, the weld bead and surrounding material will reach thermal equilibrium, and the remaining cooling will take place by convection. At this point, the material will undergo almost uniform thermal contraction; however, the weld metal has already produced a net in-plane contraction.

Once the workpiece has returned to room temperature, i.e. no thermal gradients present, high tensile stresses are produced in regions near the weld while corresponding compressive stresses are produced further away. If the thermal stresses imparted on the material due to the thermal gradients exceed the yield stress then permanent deformations will occur.

As a result of welds having non-uniform geometry, i.e. generally wider at the weld surface than the weld root, the overall contraction will be non-uniform through the thickness of the plate. This therefore leads to residual stress fields being produced; tensile stresses forming within the heated zone and compressive stresses on the opposite side of the plate to balance these. The combination of these stresses results in bending and a permanent deformation of the plate [1.73]. Figure 1.23 depicts the key stages of weld induced distortion.

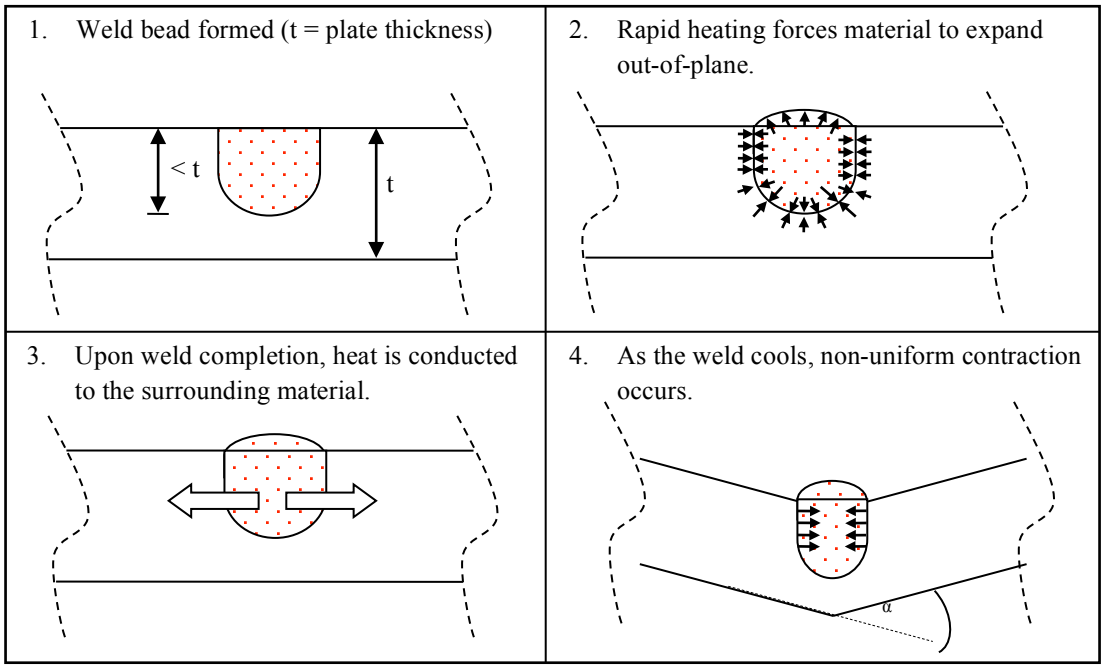

Figure 1.23: Schematic diagram of weld induced distortion

1.3.3 Modes of distortion

The distortion modes experienced by a welded structure are dependent upon a number of factors including the welding sequence, heat input, material properties and mechanical restraint. An Ishikawa diagram, Figure 1.24, details factors that contribute to weld induced distortion.

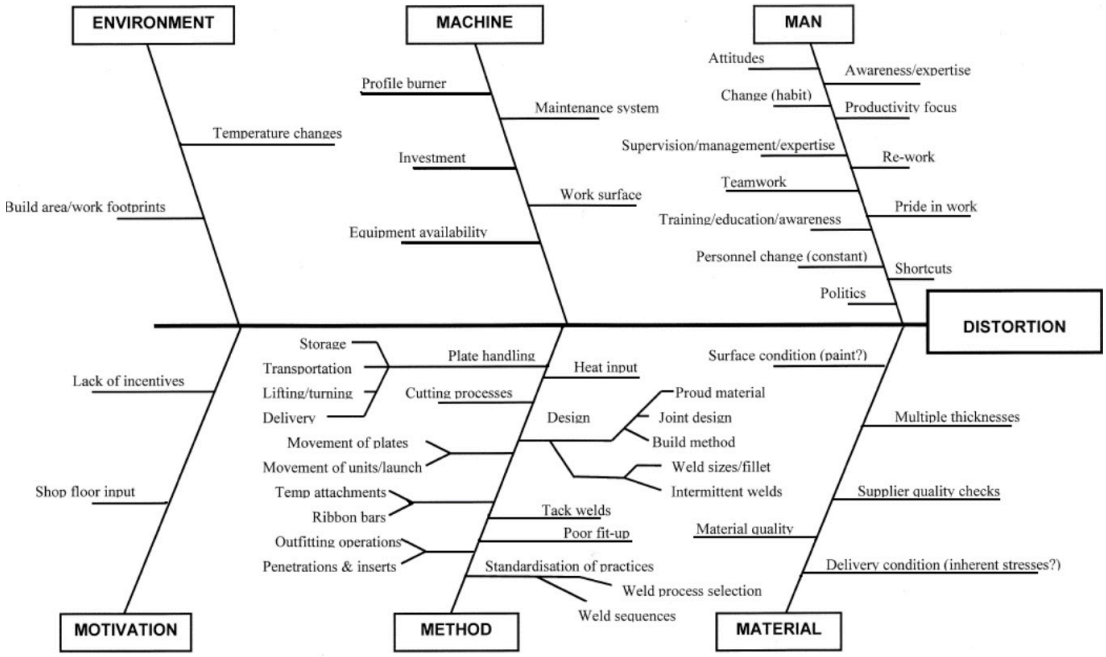

Figure 1.24: Ishikawa diagram on factors related to thin plate distortion [1.74]

Deformation has been reported [1.75] to occur according to six distinct modes (Figure 1.25) and can be classified into two categories: in-plane and out-of-plane. The modes of distortion are categorised as follows:

- In-plane distortion
    - Transverse deformation is the result of in-plane transverse shrinkage
    - Longitudinal deformation is the result of in-plane longitudinal shrinkage
    - Rotational deformation occurs due to change in the weld gap ahead of the welding torch as a result of the heating-cooling cycle
- Out-of-plane distortion
    - Angular distortion occurs due to non-uniform heating through the thickness of the workpiece resulting in asymmetrical residual stresses
    - Longitudinal distortion is caused by uneven longitudinal shrinkage in the neutral axis
    - Buckling distortion is the result of the longitudinal residual stresses exceeding the critical buckling load, and is therefore particularly prevalent in thin plate structures

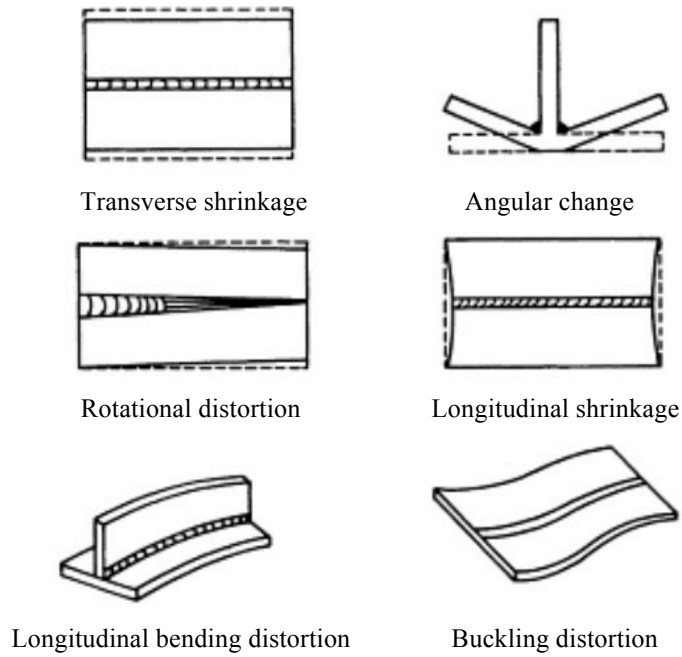

Figure 1.25: Distortion modes [1.75]

1.3.4 Distortion mitigation

There are a variety of methods for dealing with the issue of weld induced distortion; understand the distortion mechanisms so that the deformation can be accounted for in the design (predictive), minimise distortion by optimising the welding procedure (preventative), and implement techniques to reduce the distortion to acceptable levels (corrective).

1.3.4.1 Predictive measures

Computational modelling techniques, such as finite element analysis and ANNs, have previously been implemented to predict the out-of-plane distortion experienced by a structure due to the welding process and have shown the ability to predict the final distortion with a reasonable degree of accuracy [1.71, 1.76]. The ability to predict the distortion that will occur due to the welding process is extremely important as it allows the engineer to factor this into the design, i.e. the unit will deform to a position that will allow accurate fit-up to the preceding unit.

1.3.4.2 Preventive measures

Distortion in the final structure can be minimised through a combination of effective design, i.e. optimising process and weld sequencing, mechanical restraint, fit-up improvement, and thermal tensioning [1.77].

It is important to optimise the welding procedure, i.e. tack welding, deposit sequence, weld bead size, and heat input.

Tack welding is essential for setting and maintaining positioning of the panels to be welded. The size, number and location of tack welds are an important consideration; too few can result in the workpiece not being sufficiently restrained, whereas too many will induce unnecessary thermal strains.

The sequence of tack welds is important in maintaining the joint gap; there are three main options [1.78]:

- Tack from one end to the other (Figure 1.26a)
- Tack the ends, then use a back stepping technique from the centre out (Figure 1.26b)
- Tack from centre out in both directions (Figure 1.26c)

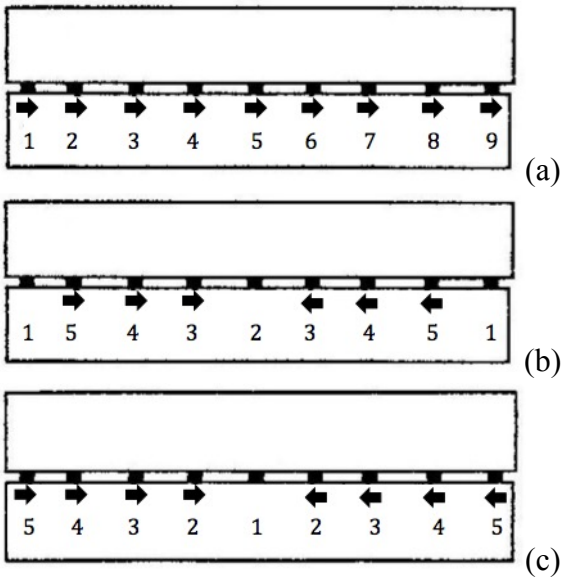

Figure 1.26: Tack welding sequence [1.78]

Weld induced distortion can be minimised by using as few weld passes as possible [1.78]. Balancing the weld bead about the neutral axis can also reduce deformation;

rather than weld entirely from one side, perform a double sided weld (preferably at the same time). As is shown schematically in Figure 1.27, where multiple passes are used in a double sided weld, the sequence of deposition can be tailored to minimise distortion.

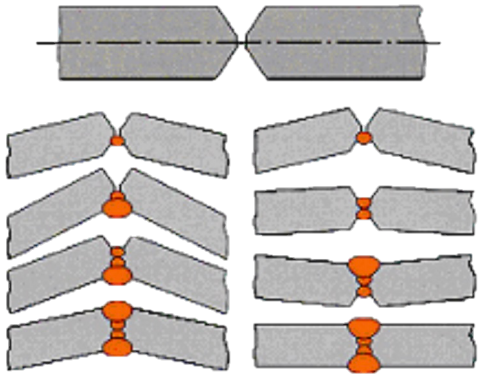

Figure 1.27: Correct edge preparation [1.79]

Over welding results in larger weld geometry than required for a particular application [1.80]. Larger welds result in greater shrinkage effects, hence it is important to deposit the correct weld bead size. For example, if the specified leg length in a fillet weld is 4 mm, and a 5 mm leg length is produced, this equates to 56% over welding (by volume). For thinner plate (4-5 mm thick), a 3.5 mm leg length is acceptable; hence the 5 mm leg length now results in 100% over welding.

It is well known that the heat input in welding is one of the major contributors to weld induced distortion. As discussed previously, distortion is a result of the non-uniform expansion and contraction of the material, which gives rise to thermal stresses. The magnitude of the thermal stresses is a factor of the heat input, and consequently, greater heat input leads to greater distortion.

The sequence of welding is an important factor in minimising the distortion present in the final structure [1.74, 1.77, 1.81]. The fabrication process normally involves a series of welds being completed, i.e. longitudinal and transverse stiffeners, and it is important to balance the effects of the expansion-contraction cycle. For example, for long welds, the whole weld should not be completed in one direction, and it is shown

in Figure 1.28 that welding from the middle out in both directions reduces the maximum distortion.

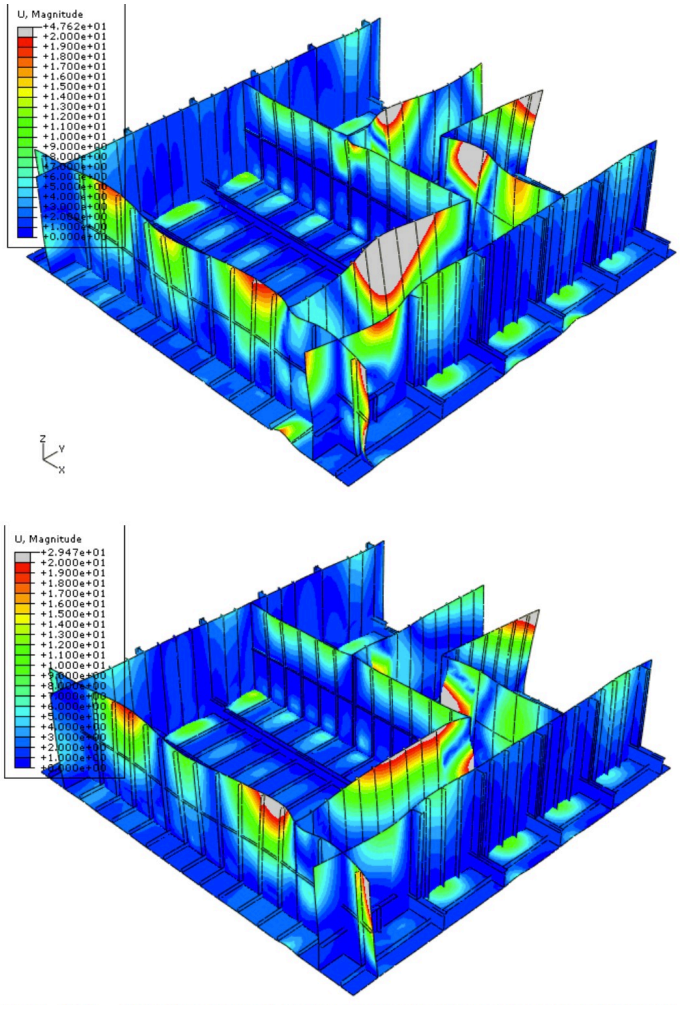

Figure 1.28: 3D modelling of a segment for an aircraft carrier, welded from (a) end to end, and (b) centre out, showing a reduction in maximum deformation [1.74]

Mechanical restraint through clamps, jigs and fixtures are essential to prevent movement in the structure during the welding process. Clever design can also implement the restraints as a heat sink to reduce the heat affected zone size [1.77]. Once the restraints are released, some deformation will occur due to the elastic strain energy being released, resulting in some welding distortion. The distortion can be minimised by using a small amount of pre-bending and/or stress relieving prior to the removal of the restraints. Conrady et al. [1.77] showed the distortion introduced to a structure as a result of inadequate restraint, Figure 1.29.

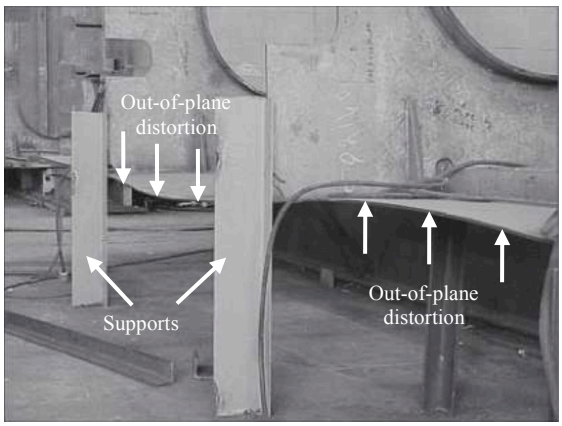

Figure 1.29: Out-of-plane distortion due to inadequately restrained structure [1.77]

Accurate fit-up is essential for minimising distortion; excessive gaps require larger than necessary welds to join the sections, which will increase the distortion present in the structure. Non-uniform joint gap is also detrimental to the final structure; a uniform joint gap will allow for predictable and consistent shrinkage along the length of the weld.

Thermal tensioning is the application of additional heat to the workpiece, with the aim of altering the residual stress pattern [1.82]. In static thermal tensioning (STT), the peak residual tensile stress is reduced. STT involves simultaneously heating either side of the weld using resistive heating bands, and cooling the weld using quenching techniques such as water spray on the bottom of the workpiece. Transient thermal tensioning (TTT) alters the residual stress pattern by adding regions of tensile stress using local heat sources. This creates bands of tensile stresses, in opposition to the compressive stress induced by the welding process (Figure 1.30), reducing the tendency of the plates to buckle [1.83].

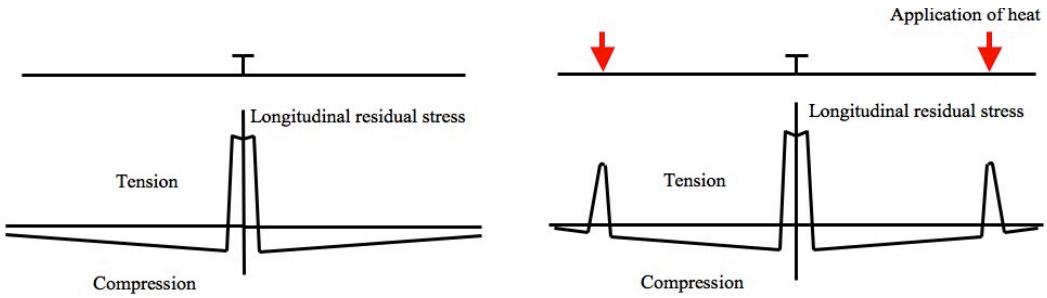

Figure 1.30: Schematic illustration of residual stresses without (left), and with thermal tensioning (right) (adapted from [1.77])

1.3.4.3 Corrective measures

Traditionally, flame straightening and mechanical straightening have been used to reduce distortion in welded structures to within tolerance. Flame straightening relies on localised expansion–contraction effects due to the heating–cooling cycle to generate bending within the structure. The process is dependent on the thermal contraction of the material, during the cooling phase, inducing tensile residual stresses within the structure. As a result of the constraints imposed by the unheated surrounding material, this tensile stress generates bending of the plate. The magnitude of bending is controlled by the depth of heat penetration through the plate; insufficient heat input levels do not generate the required contraction on the heated surface, whilst excessive heat input levels result in through thickness heating, which has the adverse effect of generating tensile stresses on the opposite side of the plate, with an overall reduction in distortion rectification due to inadequate bending. Hence, there is an optimum level of heat input, with the results obtained from flame straightening heavily dependent on the skill of the operator, which in turn limits the consistency, and repeatability of the process [1.84]. Consequently, the process is difficult to control when the plate thicknesses is less than 6 mm [1.70] as there is a tendency for the applied heat to rapidly penetrate through the entire plate.

Mechanical straightening can be used to rectify distortion by the application of a force to cause plastic deformation of the work piece. This is typically achieved by inserting the structure into a press, or using a series of hydraulic jacks to apply a force, and is therefore limited by the size of the press and the geometry of the component that requires rectification. Further, it has been reported [1.85] that additional residual stresses will be produced within the material when using this method, which has the potential to cause problems later in the assembly process.

Induction heating has been used for a number of years for the correction of plate distortion and has been shown to have a number of advantages over using flame straightening including improved repeatability, increased productivity and the potential for process optimisation [1.84, 1.86]. The induction heating process uses a coil that, when supplied with a high-frequency current, induces eddy currents within the workpiece, and the electrical resistance of the material causes heat to be generated within the area where the eddy currents form [1.87, 1.88]. As a result of

the heating within this area, localised thermal expansion occurs. The material surrounding the heated zone is effectively at ambient temperature, as the rapid rate of heating does not allow sufficient time for heat to be conducted to the surrounding material.

The conventional method of induction heating involves using a stationary induction coil to strategically heat the plate in a pre-defined pattern to correct the distortion present. This method heats the plate through the entire plate thickness to cause a transverse contraction of the material. For this method to straighten the plate, the edges must be constrained so that the material contraction will result in overall tensile residual stresses in the plate, which will straighten any bends present [1.86].

More recently, research has shown that a travelling induction coil can also be used to bend steel plate in a forming process [1.73, 1.89]. These studies determined that the bending distortion caused in the process is predictable and, similar to welding, the bending effect is primarily influenced by the travel speed of the coil (the heat input) and the thickness of the plate.

However, distortion rectification is a major expenditure for manufacturing companies; Camilleri [1.90] estimated that the BAE Systems shipyard in Govan spends approximately 12,000 hours per annum on distortion rectification. Therefore, a reduction in distortion at source will reduce the amount of rework required, consequently leading to productivity savings.

1.4 Computational fluid dynamics

1.4.1 Introduction

CFD is the application of numerical methods and algorithms to solve and analyse fluid flow. The range of applications for CFD modelling is very broad and includes the aerodynamics of vehicles and structures, wind and wave energy, medical applications such as blood flow, and plasma physics.

1.4.2 Governing equations of fluid dynamics

The physical phenomena of any fluid flow are governed by three fundamental equations:

- Conservation of mass
- Conservation of momentum
- Conservation of energy

CFD involves the numerical solution of the governing equations in space and/or time, and advancing through the solution to obtain a final numerical description of the fluid flow.

1.4.3 Application of CFD to the welding process

CFD simulations have been used extensively in the prediction of gas shielded arc welding processes. As has previously been shown, CFD has been used in the prediction of thermal fields for pure gases, gas mixtures and 'imaginary' gases [1.2, 1.3]. CFD has also been used to predict the flow within the welding nozzle and optimise the design of the diffuser [1.91, 1.92], the percentage of shielding gas (or oxygen content) present in the weld region [1.39, 1.91], and the fluid flow within the liquid weld metal [1.93].

Dreher et al. [1.91, 1.92] used CFD modelling to simulate the shielding gas flow within the welding nozzle. As shown in Figure 1.31, turbulence is induced in the shielding gas flow, even at low flow rates (10 l/min), when exiting the diffuser. This turbulence is then transported downstream and affects the gas shield, indicating that there is an optimum mass flow rate for the torch design evaluated.

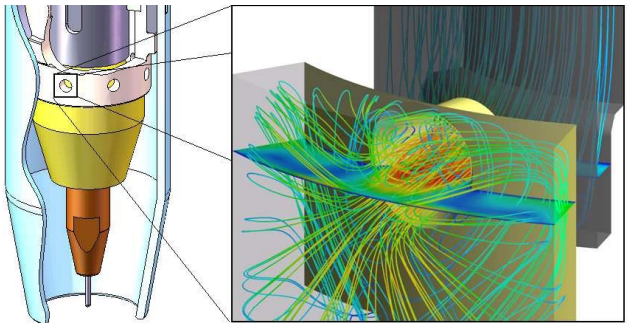

Figure 1.31: Gas distribution in the upper section of the welding nozzle [1.91]

The function of the gas diffuser is to produce equal flow at the whole circumference of the gas nozzle. In order to achieve this, the boreholes are quite small, which consequently results in high velocities and induces turbulence in the flow. Larger boreholes would produce steady flow field inside the lower part of the welding nozzle but the flow can be out of rotational symmetry.

The CFD model was subsequently implemented in the design process that would result in laminar flow across the entire area of the nozzle. The two options proposed were the addition of slots in the gas supply prior to the diffuser, or a sinter material insert to distribute the shielding gas flow, as shown in Figure 1.32.

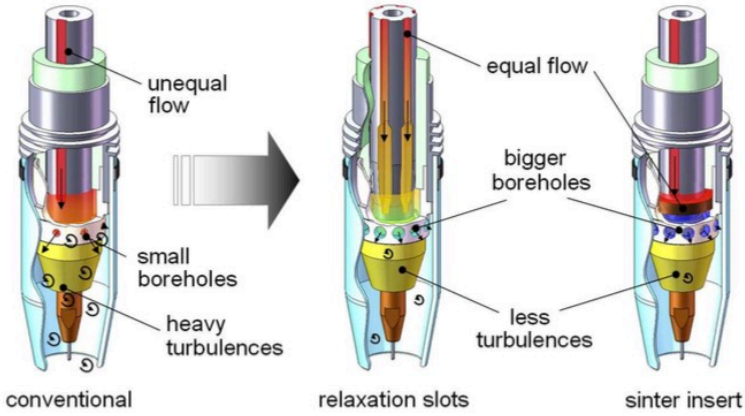

Figure 1.32: Design alterations to optimise shielding gas flow [1.91]

Simulations have also been conducted to determine the effect of the electrical arc on the shielding gas coverage. The results of Dreher et al. [1.91], Figure 1.33, show that the presence of the electrical arc draws the shielding gas towards the arc axis, this is in agreement with the experimental chromatography measurements of Okada et al. [1.26]. It can also be observed that the electrical arc accelerates the shielding gas towards the axis of the arc, in particular near the arc attachment at the wire. The axial plasma jet subsequently changes direction and flows outwards, parallel to the workpiece surface.

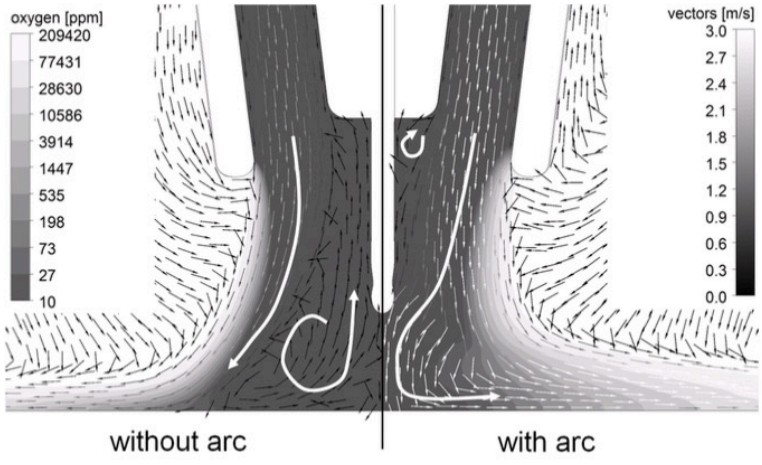

(a)

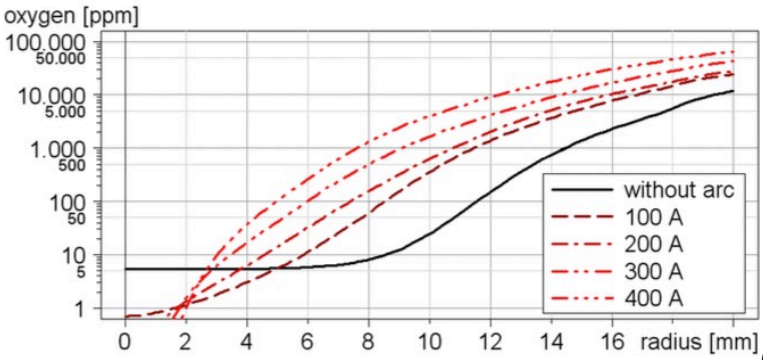

(b)

Figure 1.33: Simulation of (a) the effect of the electrical arc on the shielding gas, and (b) oxygen content at the workpiece for 10 l/min shielding gas flow [1.91]

Schnick et al. [1.39] developed a computational model and investigated the effect of various turbulence models on the prediction accuracy of shielding gas concentration at the workpiece surface, Figure 1.34. The model was subsequently developed to include the welding arc; the results presented in agreement with other studies that the arc causes a constriction in the shielding gas column.

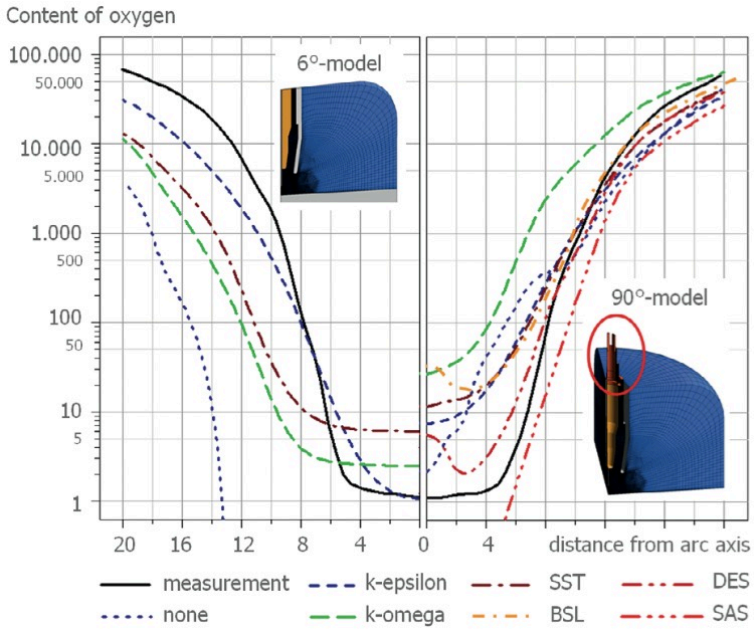

Figure 1.34: Oxygen concentration (PPM) at the workpiece surface without an arc for different turbulence models [1.39]

The computational model developed by Traidia [1.93] simulated the fluid flow in the weld pool for argon, helium and argon-helium mixtures as a result of the arc characteristics, Figure 1.35. The argon arc temperature field has the typical bell-shape commonly observed in other experimental and computational studies. As the helium fraction is increased, the arc plasma becomes progressively more constricted. It was also found that the maximum velocity in the plasma jet increases with helium mole fraction; the velocity for the helium arc being a factor of four greater than the corresponding argon arc.

In the weld pool for the argon arc it can be observed that two vortices occur near the free surface; an inward flow near the edge of the weld pool and an inward flow near the centre of the weld pool. The vortex direction is a function of the surface tension gradient, $\partial t/\partial T$. The addition of helium resulted in a third vortex forming near the arc axis, which contributes to an increase in weld penetration. This third vortex was attributed to the electromagnetic forces present; helium increases, and causes a constriction in both the axial and radial electromagnetic force.

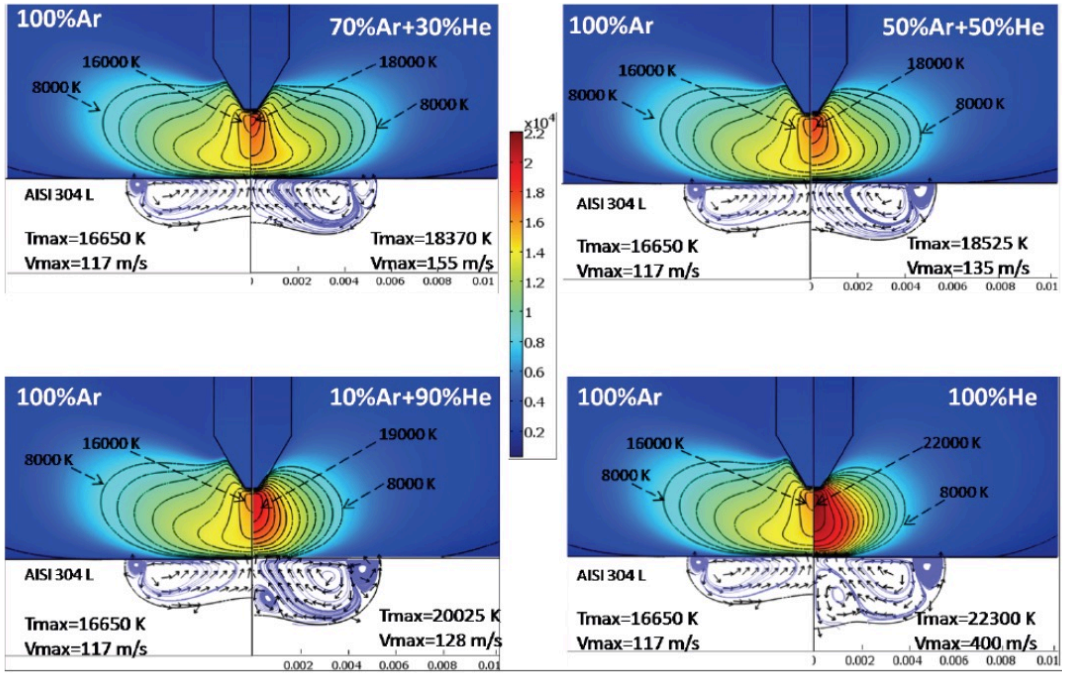

Figure 1.35: Temperature fields, normalized weld pool velocity and streamlines for different argon-helium mixtures [1.93]

1.5 Artificial neural networks

1.5.1 Introduction

ANNs are mathematical or computational models that are able to capture and represent complex input-output relationships. They are distributed, adaptive, generally nonlinear learning machines built from many different processing elements (PEs) [1.94]. McCulloch and Pitts [1.95] developed the first neural networks in 1943 based upon their understanding of neurology; this operated using simple and/or logic functions and made several assumptions as to the operation of biological neurons. Major advances were made around 1960 when Rosenblatt [1.96] designed and developed the perceptron, which was constructed by multiple layers and allowed the system to learn to associate a given input to an output. Around the same time, Widrow and Hoff [1.97] developed the ADALINE (ADAptive LINear Element) system, an analogue electronic device that operated on the least mean square (LMS) learning rule. Werbos [1.98] developed the backpropagation learning method in the early 1970s and although this learning method took a number of years to gain

popularity, it is now probably the best known, and most commonly applied learning method used today.

ANNs can be used to predict any process as long as sufficient data is generated to accurately train and validate the model. They have adaptability in that they can be applied in a variety of ways, that is, pattern recognition (also known as classification) in which the model produces a binary result, or function approximation (also known as regression) in which the model predicts the magnitude and direction of the result.

1.5.2 Basic architecture

The basic element of the ANN model is the processing element, and its design and functionalities are based upon those of a biological neuron. The ANN network consists of layers of interconnected PEs that communicate by sending signals to one another. A general ANN model consists of the following layers:

- Input layer - raw data that are fed into the system
- One or more hidden layers - the output is determined by the activities of the inputs and the weights of the connections
- Output layer - conveys the signals to the environment

A schematic diagram of both the biological and artificial neurons are shown in Figure 1.36. In the case of the biological neuron, data enters via a dendrite, is processed in the soma, and exits via an axon. Similarly, data enters the artificial neuron via weighted inputs, the processing element sums the inputs and bias, and processes the sum with a transfer function, the value then exits via the output connection. The relative weighting of each input affects the impact of that input, and consequently, some inputs have a greater influence than others.

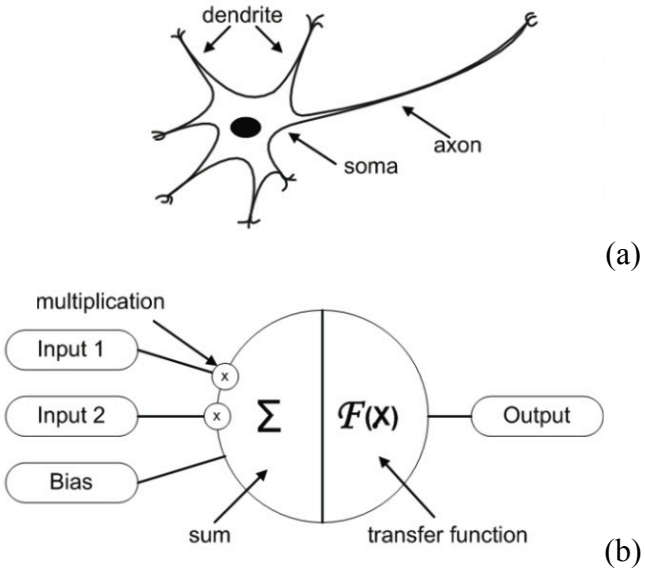

Figure 1.36: Schematic diagram of (a) a biological neuron, and (b) an artificial processing element [1.99]

The transfer function defines the properties of the artificial neuron and, theoretically, can be any mathematical function. The transfer function can be either step, linear or non-linear (i.e. sigmoid and hyperbolic tangent).

1.5.3 Topologies of artificial neural networks

The interconnectivity of the PEs defines the topology of the network. There are many different ANN architectures; multi layer feed-forward (MLF) neural networks, trained with a backpropagation learning algorithm, are the most popular networks, and the three main network topologies commonly implemented are:

1.5.3.1 Multilayer perceptron (MLP)

MLPs are feed-forward ANNs, and are generally trained using a standard backpropagation algorithm [1.100]. They are supervised networks, and trained with error correction learning, meaning that the desired response for each data set is required. They learn how to transform input data into a desired response, and are widely used for pattern classification.

Two important characteristics of the MLP are: its nonlinear PEs has a nonlinearity that must be smooth (i.e. log function and hyperbolic tangent etc.), and their massive interconnectivity (i.e. any PE of a given layer feeds all PEs of the subsequent layer).

The main advantage of MLP networks is that they are easy to use, however, they train slowly and require a large amount of training data [1.101]. An example of the network topology is shown in Figure 1.37.

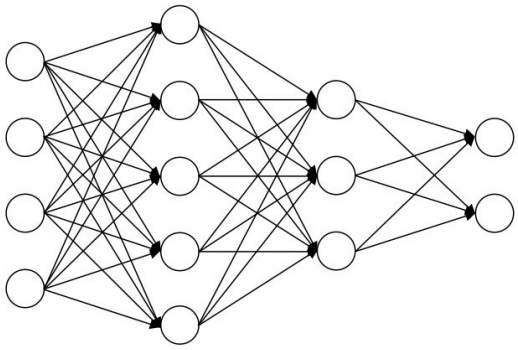

Figure 1.37: MLP network topology

1.5.3.2 Generalized feed-forward (GFF)

GFF networks are a special case of MLP, in that connections can bypass one or more layers (Figure 1.38). Therefore, theoretically speaking, a MLP can solve any problem that a GFF network can. However, in reality, GFF networks are often able to solve the problem much more efficiently, requiring hundreds of times less training epochs than the MLP network of the same structure due to its ability to bypass layers [1.101].

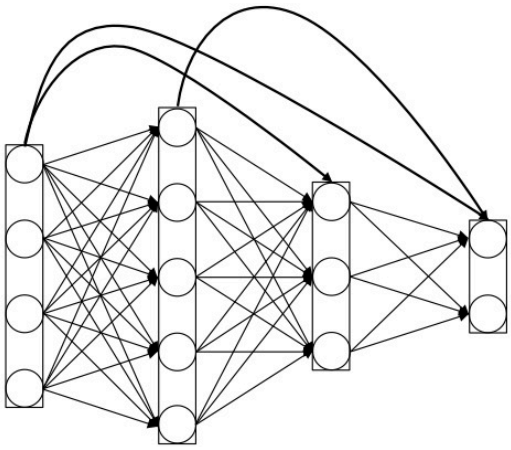

Figure 1.38: GFF network topology

1.5.3.3 Modular feed-forward (MFF)

MFF networks are a variation of MLP, such that the network is segmented into two or more parallel MLPs, the outputs from which will combine to yield the results (Figure 1.39). This tends to create some structure within the topology, and reduces the interconnectivity between layers, reducing the complexity of the network. Thus, a smaller number of weights are required for the same size network, which generally speeds up training and reduces the number of data sets required [1.102].

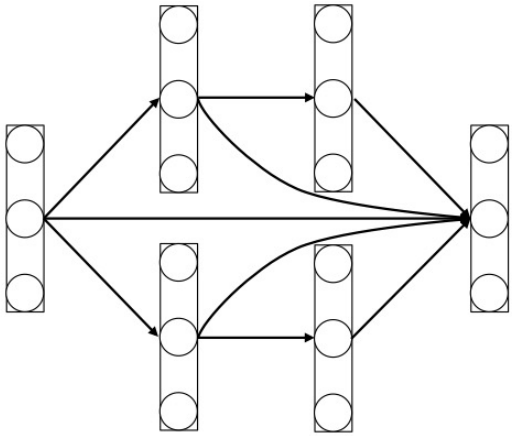

Figure 1.39: MFF network topology

1.5.4 Application of ANNs to the welding process

ANNs were first applied to the welding process around the early 1980s [1.103, 1.104]. Ever since, they have been used extensively in the prediction of key weld characteristics such as mechanical properties [1.105-1.108], weld quality [1.109, 1.110], weld-induced deformation [1.76, 1.111] and weld geometry [1.80, 1.112-1.113].

1.5.4.1 Mechanical properties

Numerous models have been developed to predict the mechanical properties of a welded joint; some examples of this are the models generated by Ates [1.106] and Pal et al. [1.107].

Ates [1.106] developed an MLP ANN with three inputs, two hidden layer and four outputs to predict the hardness, tensile strength, elongation and impact strength as a function of the shielding gas composition. The model was capable of accurately

predicting the results of the verification data, with a percentage error of 0.76, 2.25, 1.60 and 4.40%, respectively, as shown in Figure 1.40.

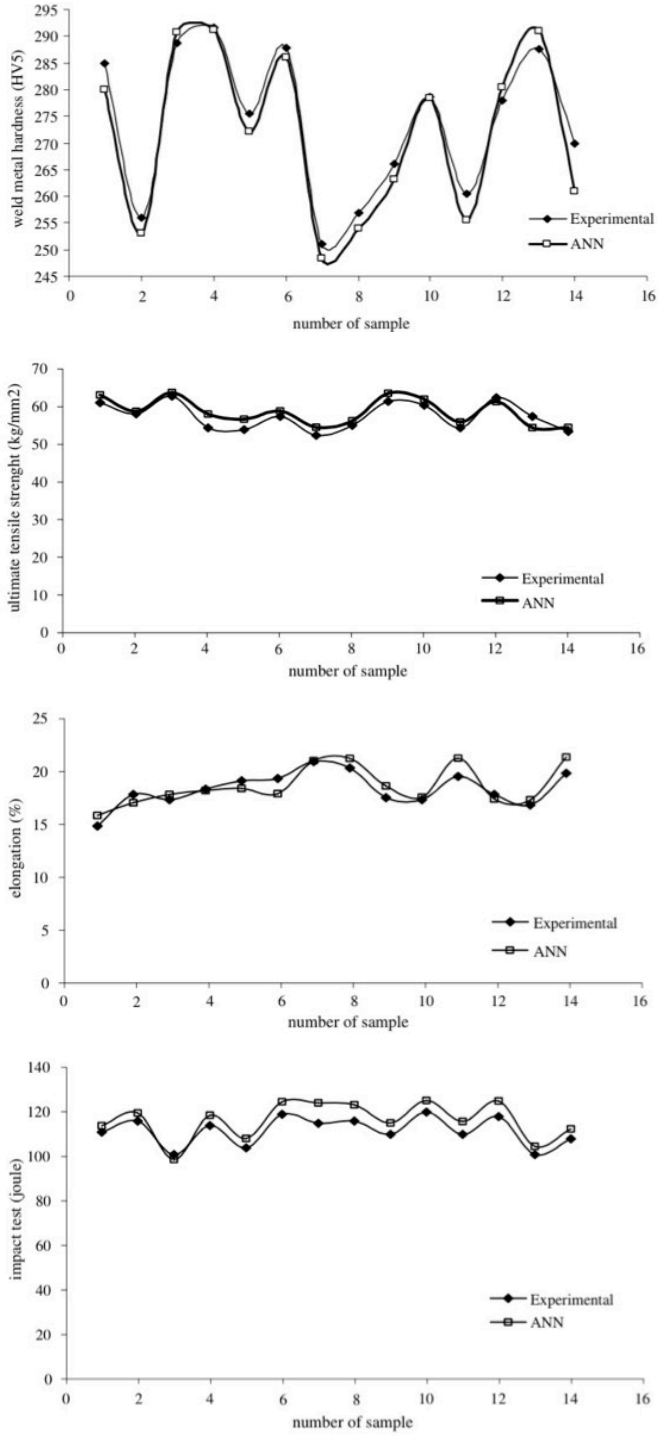

Figure 1.40: Comparison of experimental data and ANN predictions for (a) hardness, (b) UTS, (c) elongation, and (d) impact strength [1.106]

Pal et al. [1.107] implemented a fully connected multi-neuron, multi-hidden layer ANN architecture for the prediction of the ultimate tensile strength (UTS) of welded plates based upon the arc signals for pulsed metal inert gas welding (PMIGW). The model generated was capable of predicting the UTS within 8% of the experimental values, as shown in Figure 1.41.

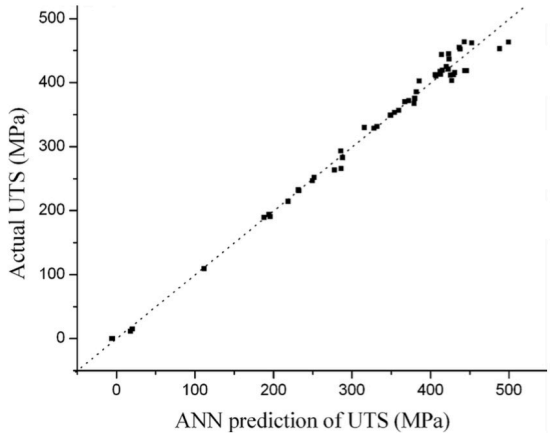

Figure 1.41: Comparison of experimental data and ANN predictions [1.107]

1.5.4.2 Weld quality

A major challenge in welding is the prediction of weld quality without the need for destructive testing. The model developed by Zeng et al. [1.109] predicted the quality of GTAW welded joints, using penetration measurements and profile appearance as the model outputs, with an acceptable quality achieved when both thresholds are met simultaneously. The predictions of the model are shown in Figure 1.42.

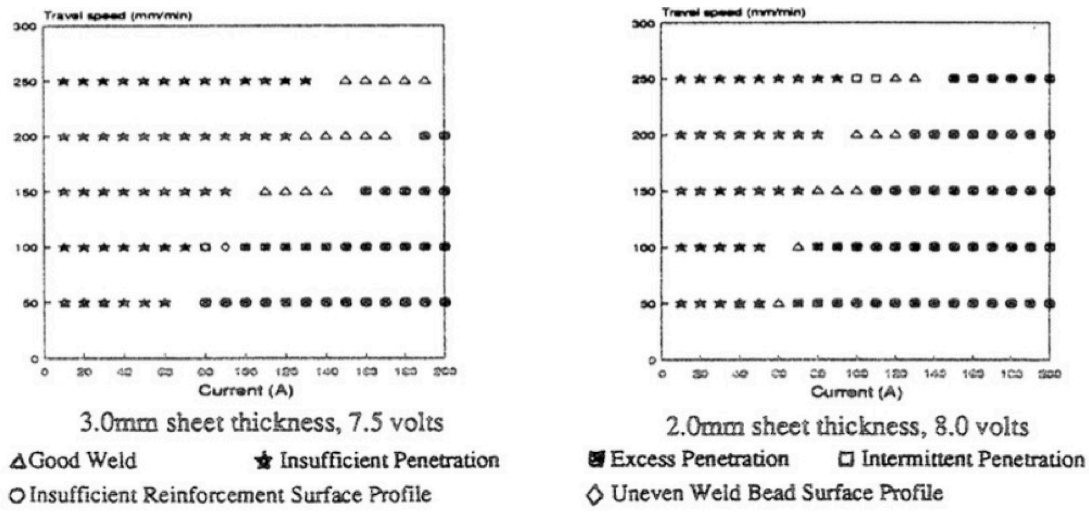

Figure 1.42: ANN predictions of weld quality for autogenous GTAW [1.109]

Pal et al. [1.110] developed ANN models for the prediction of weld quality; a combination of UTS, weld bead geometry, distortion and deposition efficiency, based upon arc signals. Two different models were developed, and optimised, for comparison; a backpropagation neural network (BPNN) and a radial basis function network (RBFN).

It was found that the prediction performance of BPNN models are more accurate than the RBFN model for weld strength, bead geometry and deposition efficiency parameters. Contrariwise, the RBFN model is better than the BPNN model for prediction of weld distortion.

1.5.4.3 Weld-induced distortion

Lightfoot et al. [1.76, 1.111] implemented ANN modelling as a prediction tool for the weld-induced distortion of DH36 grade steel plates. The comprehensive model included the workpiece mechanical properties, material properties, treatments, dimensions and initial surface topology, as well as the welding parameters as model inputs. While the model output is the predicted distortion at 72 locations.

Two models were generated; a MLP network with three hidden layers was found to produce the greatest accuracy of prediction in 6 mm thick plate, while a GFF network with two hidden layers was found to produce the greatest accuracy in 8 mm thick plate. Typical errors of approximately 15% were achieved, and an example of the prediction is shown in Figure 1.43.

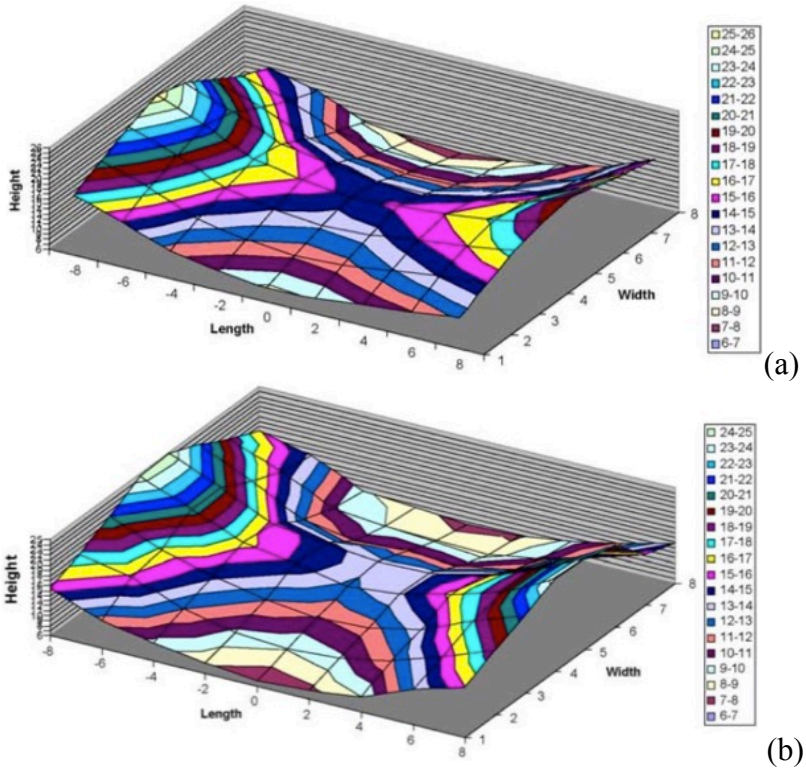

Figure 1.43: Comparison of (a) measured distortion, and (b) ANN prediction [1.76]

A sensitivity analysis was conducted in the study, which allows for factors contributing to distortion to be evaluated, and their significance identified. Although variations in other input variables (i.e. heat input, yield strength / tensile strength ratio and the carbon content) had a higher sensitivity on the distortion output, the identification of the carbon equivalent value (CEV) having a high sensitivity was deemed extremely significant. Within the CEV there are a number of sub factors, the main ones being carbon and manganese. The sensitivity analysis was subsequently rerun with carbon and manganese as input variables, with the carbon content having a more significant effect than manganese.

1.5.4.4 Weld geometry

A number of studies have applied ANNs for the prediction of weld geometry [1.80, 1.112-1.113]. As heat input is one of the key influencing parameters in the weld-induced distortion, there is a constant drive to minimise the heat transmitted to the workpiece. Over welding results in unnecessary heat input and, consequently, larger deformations will occur. Thus, there is a requirement to optimise the weld parameters in order to produce the smallest acceptable weld bead geometry.

The model generated by Nagesh and Datta [1.113] consisted of a MLP with two hidden layers. The input parameters were the welding speed, wire feed speed, cleaning percentage, welding current and arc gap. The model outputs were weld geometry measurements, i.e. front height, back height, front width and back width, as indicated in Figure 1.44.

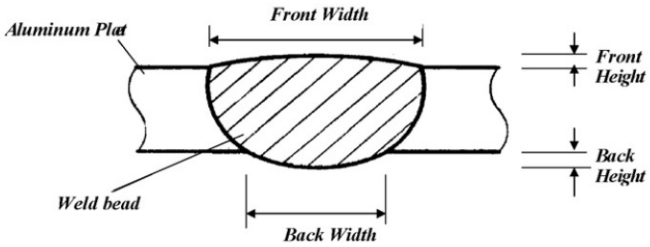

Figure 1.44: Schematic diagram of weld geometry measurements [1.113]

The predictions of the model are shown in Figure 1.45. The model was able to accurately predict the weld geometry with the exception of approximately 7.8% of the outputs, which exceeded 20% error.

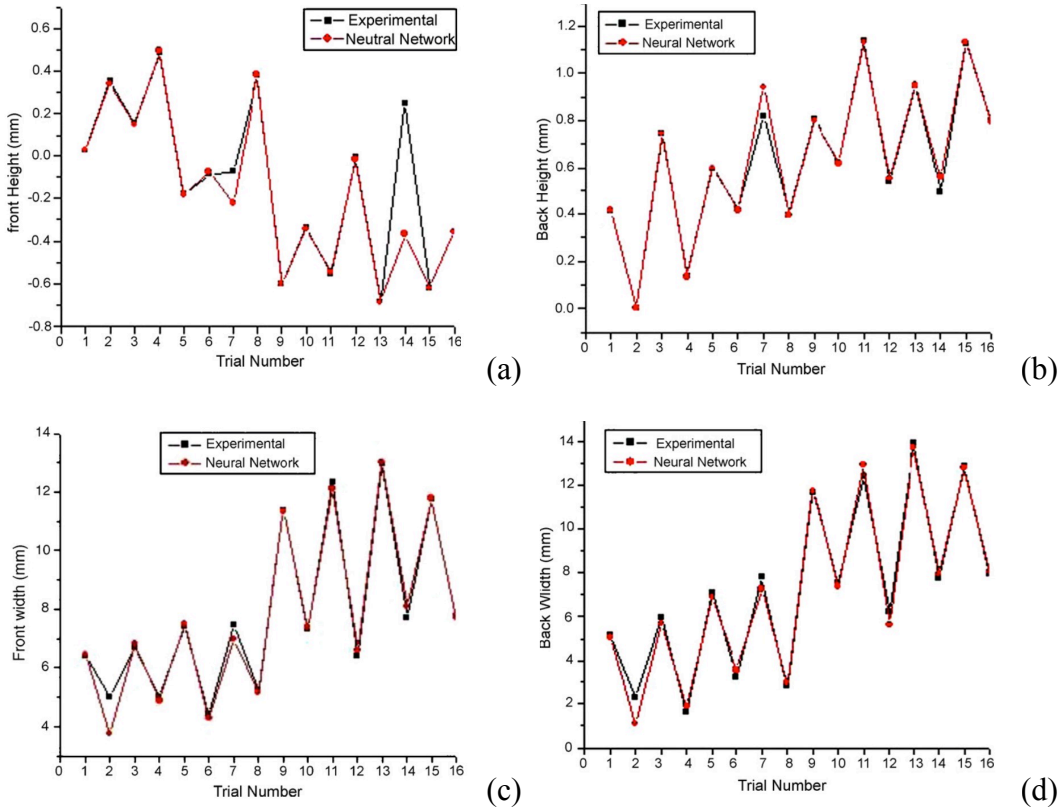

Figure 1.45: Comparison of experimental data and ANN predictions for (a) front height, (b) back height, (c) front width, and (d) back width [1.113]

1.6 References

[1.1] Murphy, A. B. and Arundell, C. J., 'Transport coefficients of argon, nitrogen, oxygen, argon-nitrogen, and argon-oxygen plasmas', *Plasma Chemistry and Plasma Processing*, Vol. 14, No. 4, pp. 451-490, 1994.

[1.2] Murphy, A. B., Tanaka, M., Yamamoto, K., Tashiro, S., Sato, T. and Lowke, J. J., 'Modelling of thermal plasmas for arc welding: the role of the shielding gas properties and of metal vapour', *Journal of Physics D: Applied Physics*, Vol. 42, No. 19, Article No. 194006 (20pp), 2009.

[1.3] Tanaka, M., Tashiro, S., Satoh, T., Murphy, A. B. and Lowke, J. J., 'Influence of shielding gas composition on arc properties in arc welding', *Science and Technology of Welding and Joining*, Vol. 13, No. 3, pp. 225-231, 2008.

[1.4] Menart, J., 'Radiative transport in a two-dimensional axisymmetric thermal plasma using the S-N discrete ordinates method on a line by line basis', *Journal of Quantitative Spectroscopy & Radiative Transfer*, Vol. 67, No. 4, pp. 273-291, 2000.

[1.5] Menart, J., Malik, S. and Lin, L., 'Coupled radiative, flow and temperature field analysis of a free-burning arc', *Journal of Physics D: Applied Physics*, Vol. 33, No. 3, pp. 257-269, 2000.

[1.6] Raynal, G. and Gleizes, A., 'Radiative transfer calculation in SF6 arc plasmas using partial characteristics', *Plasma Sources Science and Technology*, Vol. 4, No. 1, pp. 152-160, 1995.

[1.7] Mostaghimi-Tehrani, J. and Pfender, E., 'Effects of metallic vapor on the properties of an argon arc plasma', *Plasma Chemistry and Plasma Processing*, Vol. 4, No. 2, pp. 129-139, 1984.

[1.8] Ton, H., 'Physical properties of the plasma-MIG welding arc', *Journal of Physics D: Applied Physics*, Vol. 8, No. 8, pp. 922-933, 1975.

[1.9] Zielińska, S., Musioł, K., Dzierżęga, K., Pellerin, S., Valensi, F., Izarra, Ch de. and Briand, F., 'Investigations of GMAW plasma by optical emission spectroscopy', *Plasma Sources Science and Technology*, Vol. 16, No. 4, pp. 832-838, 2007.

[1.10] Schnick, M., Füssel, U., Hertel, M., Spille-Kohoff, A. and Murphy, A. B., 'Metal vapour causes a central minimum in arc temperature in gas–metal arc welding through increased radiative emission', *Journal of Physics D: Applied Physics*, Vol. 43, No. 2, Article No. 022001 (5pp), 2010.

[1.11] Lowke, J. J., Murphy, A. B. and Tanaka, M., 'Metal vapour in MIG arcs can cause (1) minima in central arc temperatures and (2) increased arc voltages', *Welding in the World*, Vol. 54, No. 9-10, pp. R292-R297, 2010.

[1.12] Schnick, M., Fuessel, U., Hertel, M., Haessler, M., Spille-Kohoff, A. and Murphy, A. B., 'Modelling of gas-metal arc welding taking into account metal vapour', *Journal of Physics D: Applied Physics*, Vol. 43, No. 43, Article No. 434008 (11pp), 2010.

[1.13] Dunn, G. J. and Eagar, T. W., 'Metal vapors in gas tungsten arcs: part II. Theoretical calculations and transport properties', *Metallurgical and Materials Transactions A*, Vol. 17, No. 10, pp. 1865-1871, 1986.

[1.14] Tashiro, S., Tanaka, M., Nakata, K., Iwao, T., Koshiishi, F., Suzuki, K. and Yamakazi, K., 'Plasma properties of helium gas tungsten arc with metal vapour', *Science and Technology of Welding and Joining*, Vol. 12, No. 3, pp. 202-207, 2007.

[1.15] Tanaka, M., Yamamoto, K., Tashiro, S., Nakata, K., Ushio, M., Tamazaki, K., Yamamoto, E., Suzuki, K., Murphy, A. B. and Lowke, J. J., 'Metal vapour behaviour in thermal plasma of gas tungsten arcs during welding', *Welding in the World*, Vol. 52, No. 11-12, pp. 82-88, 2008.

[1.16] Tsujimura, Y., Nakanishi, S., Kodama, S., Murphy, A. B. and Tanaka, M., 'Dynamically plasma diagnostics of MIG welding of Aluminium', *Quarterly Journal of the Japan Welding Society*, Vol. 31, No. 4, pp. 5s-8s, 2013.

[1.17] Nakanishi, S., Tsujimura, Y., Kodama, S., Murphy, A. B. and Tanaka, M., 'Dynamic behaviour metal vapor during gas tungsten arc welding', *Quarterly Journal of the Japan Welding Society*, Vol. 31, No. 4, pp. 1s-4s, 2013.

[1.18] Praxair Technology, Inc., 'Shielding gases selection manual', Danbury: Praxair Technology, Inc., 1998.

[1.19] Loxton Industries, ‘New welding gas innovation’, *Australasian Welding Journal*, Vol. 55, No. 1, pp. 10-11, 2010.

[1.20] Uttrachi, G. D., ‘GMAW shielding gas flow control systems’, *Welding Journal*, Vol. 86, No. 4, pp. 22-23, 2007.

[1.21] Standifer, L. R., ‘Shielding gas consumption efficiency’, *The Fabricator*, Vol. 30, No. 6, 2000.

[1.22] Skovfo, J. L. and Jørgensen, A. H., ‘Optimizing gas usage in arc welding’, Presented at 16th International Conference on the Joining of Materials Conference (JOM-16), May 2011, Tisvildeleje, Denmark.

[1.23] Goldberry, C., ‘Preventing shielding gas waste can boost the bottom line’, *Welding Design and Fabrication*, Vol. 81, No. 1, pp. 22-23, 2008.

[1.24] Gillies, A., Galloway, A. M. and McPherson, N. A., ‘Helium addition to MIG shielding gas – an economic option’, *Welding and Cutting*, Vol. 10, No. 2, pp. 118-121, 2011.

[1.25] Weber, R., ‘How to save 20% on welding costs’, *Trailer-Body Builders*, Vol. 44, No. 3, 2003.

[1.26] Okada, T., Yamamoto, H. and Harada, S., ‘Observation of the shielding gas flow pattern during arcing by the use of a laser light source’, in ‘Arc Physics and Weld Pool Behaviour’, Lucas, W. (ed), Vol. 1, pp. 203-213, Cambridge: The Welding Institute, 1980.

[1.27] Tamaki, K., Masumoto, I. and Takahashi, Y., ‘Some observation on the gas shielding conditions of CO_2 arc welding by the application of a television system’, *Journal of the Japan Welding Society*, Vol. 47, No. 5, pp. 37-42, 1978.

[1.28] McPherson, N. A., Unpublished work, BAE Systems, Glasgow, 2011.

[1.29] Stauffer, H. V., ‘Apparatus and method for reducing the waste of welding gas’, US Patent no. 4,341,237, 1982.

[1.30] Hanby, S. K., ‘Apparatus and method for preventing gas-surge in a welding gas delivery system’, US Patent no. 6,390,134,B1, 2002.

[1.31] Uttrachi, G. D., 'Welding shielding gas saver device', US Patent no. 6,610,957,B2, 2003.

[1.32] Uttrachi, G. D., 'Welding shielding gas saver flow-control device', US Patent no. 7,015,412,B1, 2006.

[1.33] DuPont, J. N. and Marder, A. R., 'Thermal efficiency of arc welding processes', *Welding Journal*, Vol. 74, No. 12, pp. 406s-416s, 1995.

[1.34] Stenbacka, N., Choquet, I. and Hurtig, K., 'Review of arc efficiency values for gas tungsten arc welding', Presented at IIW Commission IV-XII-SG212 Intermediate Meeting, April 2012, Berlin, Germany.

[1.35] Gibson, G. J., 'Gas flow requirements for inert-gas-shielded arc welding', *Welding Journal*, Vol. 34, No. 4, pp. 198s-208s, 1953.

[1.36] Siewert, E., Wilhelm, G., Hässler, M., Schein, J., Hanson, T., Schnick, M. and Füssel, U., 'Visualisation of gas flows in welding arcs by the schlieren measuring technique', *Welding Journal*, Vol. 93, No. 1, pp. 1s-5s, 2014.

[1.37] Dreher, M., Füssel, U., Schnick, M. and Hertel, M., 'Numerical simulation of the shielding gas flow with GMA welding and options of validation by diagnositics' Presented at 4th International Doctoral Seminar, May 2009, Trnava, Slovakia.

[1.38] Johnson, D. A., Orakwe, P. and Weckman, E., 'Experimental examination of welding nozzle jet flow at cold flow conditions' *Science and Technology of Welding and Joining*, Vol. 11, No. 6, pp. 681-687, 2006.

[1.39] Schnick, M., Dreher, M., Zschetzsche, J., Fuessel, U. and Spille-Kohoff, A., 'Visualization and optimization of shielding gas flows in arc welding', *Welding in the World*, Vol. 56, No. 1-2, pp.54-61, 2012.

[1.40] Schnick, M., 'PIV measurements of shielding gas flow in gas metal arc welding (GMAW) with a Cavilux® HF diode laser', Cavitar Ltd.

[1.41] Mendez, P. F. and Eagar, T. W., 'Penetration and defect formation in high-current arc welding', *Welding Journal*, Vol. 82, No. 10, pp. 296-306, 2003.

[1.42] Lin, M. L. and Eagar, T. W., 'Pressures produced by gas tungsten arcs', *Metallurgical Transactions B*, Vol. 17, No. 3, pp. 601-607, 1986.

[1.43] Choo, R. T. C., Szekely J. and Westhoff, R. C., 'On the calculation of the free surface temperature of gas–tungsten–arc weld pools from first principles. Part 1: modeling the welding arc', *Metallurgical Transactions B*, Vol. 23, No. 3, pp. 357-369, 1992.

[1.44] Lee, S. Y. and Na, S. J., 'Analysis of TIG welding using boundary-fitted coordinates', *Proceedings of the Institution of Mechanical Engineers, Part B: Journal of Engineering Manufacture*, Vol. 209, No. 2, pp. 153-164, 1995.

[1.45] Oh, D.-S., Kim, Y.-S. and Cho, S.-M., 'Derivation of current density distribution by arc pressure measurement in GTA welding', *Science and Technology of Welding and Joining*, Vol. 10, No. 4, pp. 442-446, 2005.

[1.46] Fan, H. G. and Shi, Y. W., 'Numerical simulation of the arc pressure in gas tungsten arc welding', *Journal of Materials Processing Technology*, Vol. 61, No. 3, pp. 302-308, 1996.

[1.47] Fan, D., Ushio, M. and Matsuda, F., 'Numerical computation of arc pressure distribution', *Transactions of the Joining and Welding Research Institute*, Vol. 15, No. 1, pp. 1-5, 1986.

[1.48] Ham, H.-S., Oh, D.-S. and Cho, S.-M., 'Measurement of arc pressure and shield gas pressure effect on surface of molten pool in TIG welding', *Science and Technology of Welding and Joining*, Vol. 17, No. 7, pp. 594-600, 2012.

[1.49] Cho, M. H., Lim, Y. C. and Farson, D. F., 'Simulation of weld pool dynamics in the stationary pulsed gas metal arc welding process and final weld shape', *Welding Journal*, Vol. 85, No. 12, pp. 271-283, 2006.

[1.50] Hu, J. and Tsai, H. L., 'Heat and mass transfer in gas metal arc welding. Part 1: The arc', *International Journal of Heat and Mass Transfer*, Vol. 50, No. 5, pp. 833-846, 2007.

[1.51] Burleigh, T. D. and Eagar, T. W., 'Measurement of the force exerted by a welding arc', *Metallurgical Transactions A*, Vol. 14, No. 6, pp. 1223-1224, 1982.

[1.52] Kou, S. and Wang, Y. H., 'Weld pool convection and its effect', *Welding Journal*, Vol. 65, No. 3, pp. 63-70, 1986.

[1.53] Kou, S. and Sun, D. K., 'Fluid flow and weld penetration in stationary arc welds', *Metallurgical Transactions A*, Vol. 16, No. 1, pp. 203-213, 1985.

[1.54] Oreper, G. M., Eagar, T. W. and Szekely, J., 'Convection in arc weld pools', *Welding Journal*, Vol. 62, No. 11, pp. 307-312, 1983.

[1.55] Matsunawa, A., Yokoya, S. and Asako, Y., 'Convection in weld pool and its effect on penetration shape in stationary arcs', *Transactions of the Joining and Welding Research Institute*, Vol. 16, No. 2, pp. 229-236, 1987.

[1.56] Cunningham, J. W., 'Pulsed welding and cutting by variation of composition of shielding gas', US Patent no. 3,484,575, 1969.

[1.57] Nakamura, T., Hiraoka, K., Takahishi, M. and Sasaki, T., 'Gas metal arc welding with periodic control of shielding gas composition', *Science and Technology of Welding and Joining*, Vol. 10, No. 2, pp. 131-138, 2005.

[1.58] Kim, I. S., Son, J. S., Kim, H. J. and Chin, B. A., 'A study on variation of shielding gas in GTA welding using finite element method', *Journal of Achievements in Materials and Manufacturing Engineering*, Vol. 17, No. 1-2, pp. 249-252, 2006.

[1.59] Kim, I. S., Son, J. S., Kim, H. J. and Chin, B. A., 'Development of a mathematical model to study on variation of shielding gas in GTA welding', *Journal of Achievements in Materials and Manufacturing Engineering*, Vol. 19, No. 2, pp. 73-80, 2006.

[1.60] Barabokhin, N. S., Bushuev, Y. G., Shulgina, E.V. and Kazakov, V. A., 'Technological special features of welding 1460 high-strength aluminium alloy', *Welding International*, Vol. 14, No. 6, pp. 468-470, 2000.

[1.61] Chang, Y. H., 'Improve GMAW and GTAW with alternating shielding gases', *Welding Journal*, Vol. 85, No. 2, pp. 41-43, 2006.

[1.62] Kang, B. Y., Prasad, Y. K. D. V., Kang, M. J., Kim, H. J. and Kim, I. S., 'Characteristics of alternate supply of shielding gases in aluminium GMA welding', *Journal of Materials Processing Technology*, Vol. 209, No. 10, pp. 4716-4721, 2009.

[1.63] Novikov, O. M., Persidskii, A. S., Rad'ko, E. P., Baranovskii, A. V. and Khasyanov, B. A., 'Effect of the composition of the shielding gas on the properties

of arc welded joints in aluminium alloys', *Welding International*, Vol. 26, No. 5, pp. 384-387, 2012.

[1.64] Novikov, O. M., Persidskii, A. S., Rad'ko, E. P., Baranovskii, A. V. and Khasyanov, B. A., 'Effect of changes in the composition of the gas shielding medium on the properties of arc welded joints in aluminium alloys', *Welding International*, Vol. 27, No. 3, pp. 222-225, 2013.

[1.65] Tazetdinov, R. G., Novikov, O. M., Persidskii, A. S., Khasyanov, B. A., Ivanov, E. N. and Plaksina, L. T., 'Arc welding in shielding gases with alternate pulsed supply of dissimilar gases', *Welding International*, Vol. 27, No. 4, 2013.

[1.66] Kang, B. Y., Prasad, Y. K. D. V., Kang, M. J., Kim, H. J. and Kim, I. S., 'The effect of alternate supply of shielding gases in austenite stainless steel GTA welding', *Journal of Materials Processing Technology*, Vol. 209, No. 10, pp. 4722-4727, 2009.

[1.67] Traidia, A. and Roger, F., 'A computational investigation of different helium supplying methods for the improvement of GTA welding', *Journal of Materials Processing Technology*, Vol. 211, No. 9, pp. 1553-1562, 2011.

[1.68] Mills, K. C., Keene, B. J., Brooks, R. F. and Shirali, A., 'Marangoni effects in welding', *Philosophical Transactions of the Royal Society A*, Vol. 356, pp. 911-925, 1998.

[1.69] Aidun, D. K. and Martin, S. A., 'Effect of sulphur and oxygen on weld penetration of high-purity austenitic stainless steel', *Journal of Materials Engineering and Performance*, Vol. 6, No. 4, pp. 496-502, 1997.

[1.70] McPherson, N. A., 'Thin plate distortion – the ongoing problem in shipbuilding', *Journal of Ship Production*, Vol. 23, No. 2, pp. 94-117, 2007.

[1.71] Camilleri, D., Comlekci, T. and Gray, T. G. F., 'Computational prediction of out-of-plane welding distortion and experimental investigation', *Journal of Strain Analysis for Engineering Design*, Vol. 40, No. 2, pp. 161-176, 2005.

[1.72] Masubuchi, K., 'Models of stresses and deformation due to welding - a review', *JOM*, Vol. 33, No. 12, pp. 19-23, 1981.

[1.73] Bae, K. L., Yang, Y. S., Hyun, C. M. and Cho, S. H., 'Derivation of simplified formulas to predict deformations of plate in steel forming process with induction heating', *International Journal of Machine Tools and Manufacture*, Vol. 48, No. 15, pp. 1646-1652, 2008.

[1.74] McPherson, N. A., Galloway, A. M. and McGhie, W., 'Thin plate buckling distortion and reduction challenges for naval ships', *Journal of Marine Engineering and Technology*, Vol. 12, No. 2, pp. 3-10, 2013.

[1.75] Masubuchi, K., 'Analysis of welded structures', USA: Massachusetts Institute of Technology, Pergamon Press Ltd, 1980.

[1.76] Lightfoot, M. P., McPherson, N. A., Woods, K. and Bruce, G. J., 'Artificial neural networks as an aid to steel plate distortion reduction', *Journal of Materials Processing Technology*, Vol. 172, No. 2, pp. 238-242, 2006.

[1.77] Conrady, C., Huang, T. D., Harwig, D., Fong, P., Kvidahl, L., Evans, N. and Treaster, A., 'Practical welding techniques to minimise distortion in lightweight ship structures', *Journal of Ship Production*, Vol. 22, No. 4, pp. 239-247, 2006.

[1.78] Lightfoot, M., 'Prediction of weld distortion using artificial neural networks', Ph.D. Thesis, Newcastle University, 2008.

[1.79] Yuliadi, M. Z., 'A study on the topology of ship plate by neural networks', Ph.D. Thesis, Newcastle University, 2000.

[1.80] Beckett, S., MacPherson, M. J. and McPherson, N. A., 'Improved welding control of automated fillet welding for ship structures using artificial neural networks (ANN)', Presented at 16th International Conference on the Joining of Materials Conference (JOM-16), May 2011, Tisvildeleje, Denmark.

[1.81] Tsai, C. L., Park, S. C. and Cheng, W. T., 'Welding distortion of a thin-plate panel structure', *Welding Journal*, Vol. 78, No. 5, pp. 156s-165s, 1999.

[1.82] Gray, T., Camilleri, D. and McPherson, N., 'Control of Welding Distortion in Thin-Plate Fabrication: Design Support Exploiting Computational Simulation', Cambridge: Woodhead Publishing Limited, 2014.

[1.83] Dull, R. M., Dydo, J. R., Russell, J. J. and Shanghvi, J., 'Method of reducing distortion by transient thermal tensioning', US Patent no. US 6861617 B2, 2005.

[1.84] McPherson, N. A., 'Correcting thin plate distortion in shipbuilding', *Welding Journal*, Vol. 89, No. 1, pp. 30-34, 2010.

[1.85] Pattee, H. E., Evans, R. M. and Monroe, R. E., 'Effect of flame and mechanical straightening on material properties of weldments', Summary report to the Ship Structure Committee, Project SR-185 straightening distorted weldments. Battelle Memorial Institute, Columbus, Ohio, USA, 1970.

[1.86] McPherson, N. A., Coyle, A. and Wells, M., 'Induction heat straightening – a distortion rework reduction tool for thin plate', *Welding and Cutting*, Vol. 7, No. 3, pp. 162-166, 2008.

[1.87] Lee, J. H., Lee, K. and Yun, J. S., 'An electromagnetic and thermo-mechanical analysis of high frequency induction heating for steel plate bending', *Key Engineering Materials*, Vol. 326-328, pp. 1283-1286, 2006.

[1.88] Sadeghipour, K., Dopkin, J. A. and Li, K., 'A computer aided finite element/experimental analysis of induction heating process of steel', *Computers in Industry*, Vol. 28, No. 3, pp. 195-205, 1996.

[1.89] Ngyuyen, T. T., Yang, Y. S., Bae, K. Y. and Choi, S. N., 'Prediction of deformations of steel plate by artificial neural network in forming process with induction heating', *Journal of Materials Science and Technology*, Vol. 23, No. 4, pp. 1211-1221, 2009.

[1.90] Camilleri, D., 'Support tools for the prediction of distortion in the design and manufacture of thin plate welded structures', Ph.D. Thesis, University of Strathclyde, 2005.

[1.91] Dreher, M., Füssel, U. and Schnick, M., 'Numerical optimisation of gas metal arc welding torches using ANSYS CFX', Presented at 63rd Annual Assemble & International Conference of the International Institute of Welding, July 2010, Istanbul, Turkey.

[1.92] Dreher, M., Füssel, U. and Schnick, M., 'Simulation of shielding gas flow inside the torch and in the process region of GMA welding', Presented at Mathematical Modelling of Weld Phenomena 9, September 2009, Graz, Austria.

[1.93] Traidia, A., 'Multiphysics modelling and numerical simulation of GTA weld pools', Ph.D Thesis, Ecole Polytechnique, 2011.

[1.94] Principe, J. C., Euliano, N. R. and Lefebvre, W.C., 'Neural and adaptive systems: fundamentals through simulations', New York: John Wiley & Sons, Inc., 2000.

[1.95] McCulloch, W. S. and Pitts, W., 'A logical calculus of the ideas immanent in nervous activity', *Bulletin of Mathematical Biophysics*, Vol. 5, pp. 115-133, 1943.

[1.96] Rosenblatt, F., 'The perceptron: a probabilistic model for information storage and organization in the brain', *Psychological Review*, Vol. 65, No. 6, pp. 386-408, 1958.

[1.97] Widrow, B. and Hoff, M. E., 'Adaptive switching circuits', *IRE Wescon Convention Record*, Vol. 4, pp. 96-104, 1960.

[1.98] Werbos, P. J., 'Beyond regression: new tools for prediction and analysis in the behavioural sciences', Ph.D. Thesis, Harvard University, 1974.

[1.99] Krenker, A., Bešter, J. and Kos, A., 'Introduction to the artificial neural networks', In: Suzuki, K., (Ed.) 'Artificial neural networks – methodological advances and biomedical applications', Rijeka: InTech, 2011.

[1.100] Rumelhart, D. and McClelland, J., (eds.) 'Parallel Distributed Processing'. Cambridge: MIT Press, 1987.

[1.101] Principe, J., Lefebvre, C., Lynn, G., Fancourt, C. and Wooten, D., 'NeuroSolution User Manual', Florida: NeuroDimension, Inc., 2014.

[1.102] Tahmasebi, P. and Hazarkhani, A., 'Application of a modular feedforward neural network for grade estimation', *Natural Resources Research*, Vol. 20, No. 1, pp. 25-32, 2011.

[1.103] Dornfield, D. A., Tomizuka, M. and Langari, G., 'Modeling and adaptive control of arc welding processes', ASME Special Publication: *Measurement and Control for Batch Manufacturing*, 1982.

[1.104] McGlone, J. C., 'Weld bead geometry prediction – a review', *Metal Construction*, Vol. 14, No. 7, pp. 378-384, 1982.

[1.105] Sterjovski, Z., Nolan, D., Carpenter, K. R., Dunne, D. P. and Norrish, J., 'Artificial neural networks for modelling the mechanical properties of steels in various applications', *Journal of Materials Processing Technology*, Vol. 170, No. 3, pp. 536-544, 2005.

[1.106] Ates, H., 'Prediction of gas metal arc welding parameters based on artificial neural networks', *Materials and Design*, Vol. 28, No. 7, pp. 2015-2023, 2007.

[1.107] Pal, S., Pal, S. K. and Samantaray, A. K., 'Artificial neural network modeling of weld joint strength prediction of a pulsed metal inert gas welding process using arc signals', *Journal of Materials Processing Technology*, Vol. 202, No. 1-3, pp. 464-474, 2008.

[1.108] Lakshminarayanan, A. K. and Balasubramanian, V., 'Comparison of RSM with ANN in predicting tensile strength of friction stir welded AA7039 aluminium alloy joints', *Transactions of Nonferrous Metals Society of China*, Vol. 19, No. 1, pp. 9-18, 2009.

[1.109] Zeng, X. M., Lucas, J. and Fang, M. T. C., 'Use of neural networks for parameter prediction and weld quality inspection in TIG welding', *Transactions of the Institute of Measurement and Control*, Vol. 15, No. 2, pp. 87-95, 1993.

[1.110] Pal, S., Pal, S. K. and Samantaray, A. K., 'Prediction of the quality of pulsed metal inert gas welding using statistical parameters of arc signals in artificial neural network', *International Journal of Computer Integrated Manufacturing*, Vol. 23, No. 5, pp. 453-465, 2010.

[1.111] Lightfoot, M. P., Bruce, G. J., McPherson, N. A. and Woods, K., 'The application of artificial neural networks to weld-induced deformation in ship plate', *Welding Journal*, Vol. 84, No. 2, pp. 23s-26s, 2005.

[1.112]Nagesh, D. S. and Datta, G. L., ‘Modeling of fillet welded joint of GMAW process: integrated approach using DOE, ANN and GA’, *International Journal on Interactive Design and Manufacturing*, Vol. 2, No. 3, pp. 127-136, 2008.

[1.113]Nagesh, D. S. and Datta, G. L., 'Genetic algorithm for optimization of welding variables for height to width ratio and application of ANN for prediction of bead geometry for TIG welding process', *Applied Soft Computing*, Vol. 10, No. 3, pp. 897-907, 2010.

2 Experimental apparatus and procedures

2.1 Nomenclature

I - Current

Q - Heat input

$t.s.$ - Travel speed

V - Voltage

2.1 Welding units

Experimental trials were conducted using a combination of GMAW and GTAW units, to evaluate various aspects of the alternating shielding gas process, and assess the effects of reducing the shielding gas consumption.

2.1.1 Gas metal arc welding

The GMAW process is a welding technique whereby an electrical arc forms between a consumable electrode, which is continuously fed by a wire feed unit, and the workpiece surface. The electrical arc causes the electrode and workpiece to melt, and are subsequently fused upon solidification. A shielding gas is also supplied through the welding torch in order to displace atmospheric gases from the welding region, additional information on shielding gases can be found in Chapter 1.

GMAW trials were conducted using a 3-phase Miller® XMT® 304 Series DC inverter arc welder with a 60% duty cycle rating of 300 A at 32 VDC. The inverter was connected to a Miller® 20 Series 24V wire feeder.

The experimental welding trials were conducted using an Abicor Binzel® ABIMIG® 350 TM welding torch, mounted to the automated welding rig discussed later. The torch handle is constructed using high performance, reinforced plastic, with a rotational swan neck allowing greater flexibility for the welding setup. Conventional welding consumables including M8 contact tips and diffusers, along with gas nozzles with an outlet diameter of 16 mm (alternative nozzles were used in

specific trials and will be detailed in latter sections). Gas nozzles had a coating of anti-spatter applied prior to welding to prevent spatter build up.

GMAW trials were conducted using two independent shielding gas supplies for each base material; argon / 20% carbon dioxide and helium were used for studies conducted on DH36 steel, while argon and helium were used when welding 6082T6 aluminium, further details on the specifications for weld shielding gases are documented in Chapter 1. The shielding gas flow rate was pre-set using conventional flow meters, and monitored and recorded using a Regula® EWR® welding monitor. Shielding gas flow was also controlled using a dedicated alternating gas control unit, and will be discussed later in this chapter.

The filler wire used was dependent upon the base material being welded; a combination of metal cored 1 mm diameter MC-1 and 1.2 mm diameter flux cored SF-1A filler wires were used for trials conducted on DH36 steel and 1.2 mm diameter Alumig Si5 4043 for trials conducted on 6082T6 aluminium. The filler wire feed speed was dependent upon the welding setup.

2.1.2 Gas tungsten arc welding

GTAW is a welding process in which an electrical arc is formed between a non-consumable tungsten electrode and the workpiece surface. The electrical arc causes the workpiece surface to melt, and can be performed with or without a consumable filler wire. As with the GMAW process, a shielding gas is used to protect the welding region from contamination by atmospheric gases.

GTAW trials were conducted using a 3-phase Miller® Dynasty® 300DX power source with a 40% duty cycle rating of 200 A at 28 VDC, and a Miller® Invercool® cooling unit.

A water-cooled Parweld® WP18 welding torch, with a 350A rating for 60% duty cycle was used throughout GTAW experimental trials. A 2.4 mm diameter, 2% thoriated tungsten electrode was used throughout, with a 45° vertex angle. The electrode was machined using an ULTIMA-TIG wet grinder to ensure accuracy and

repeatability of the vertex angle. GTAW welding trials were conducted autogenously, i.e. without the addition of a filler wire.

Two shielding gas supplies were used for the GTAW trials, argon and helium. As with GMAW trials, shielding gas flow rates were set with conventional flow meters, monitored and recorded using a Regula® welding monitor and controlled using a dedicated alternating gas unit. In addition, shielding gas mixtures were created using a manifold block with numerous internal meshes.

2.2 Rig setup

Experimental welding trials were conducted upon an automated welding rig; a schematic diagram of the control system is shown in Figure 2.1.

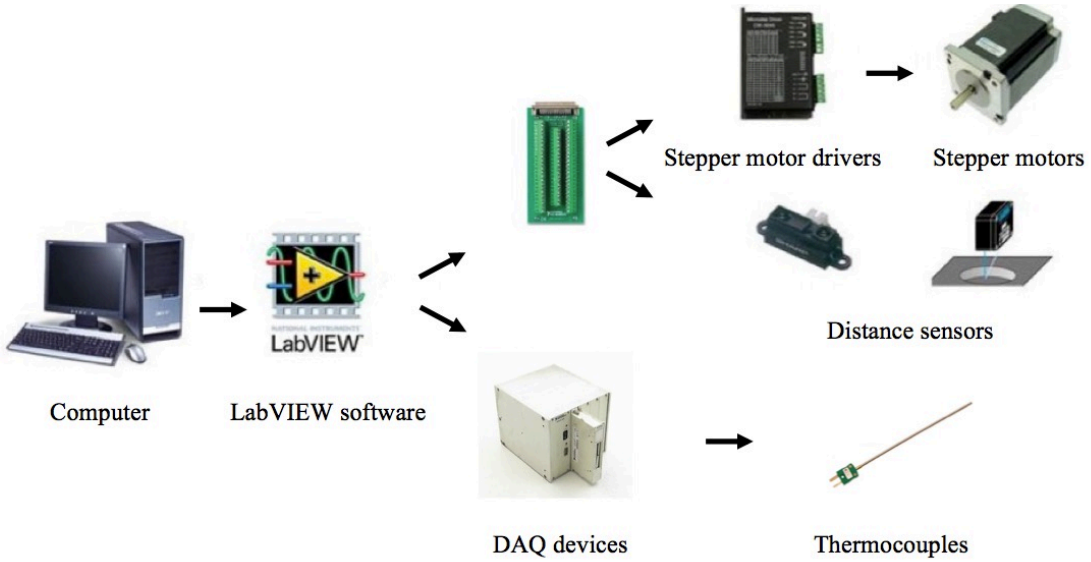

Figure 2.1: Schematic diagram of welding rig control system

2.2.1 Welding system

The control system for the experimental rig consists of three computer systems; the first controls the movement of the workpiece and distortion measurements, the second acquires data from thermocouples, and the third, records data from a thermographic camera.

The automated welding rig held the workpiece rigid upon a traversing frame, which moves at a constant speed under a stationary welding torch, Figure 2.2. The workpiece is supported on the frame by four corner locating points so that no restrictions are applied to the in-plane and out-of-plane deformation, each of which are calibrated to a zero reference plane using an optical distance sensor to ensure the plate is level prior to experimental trials.

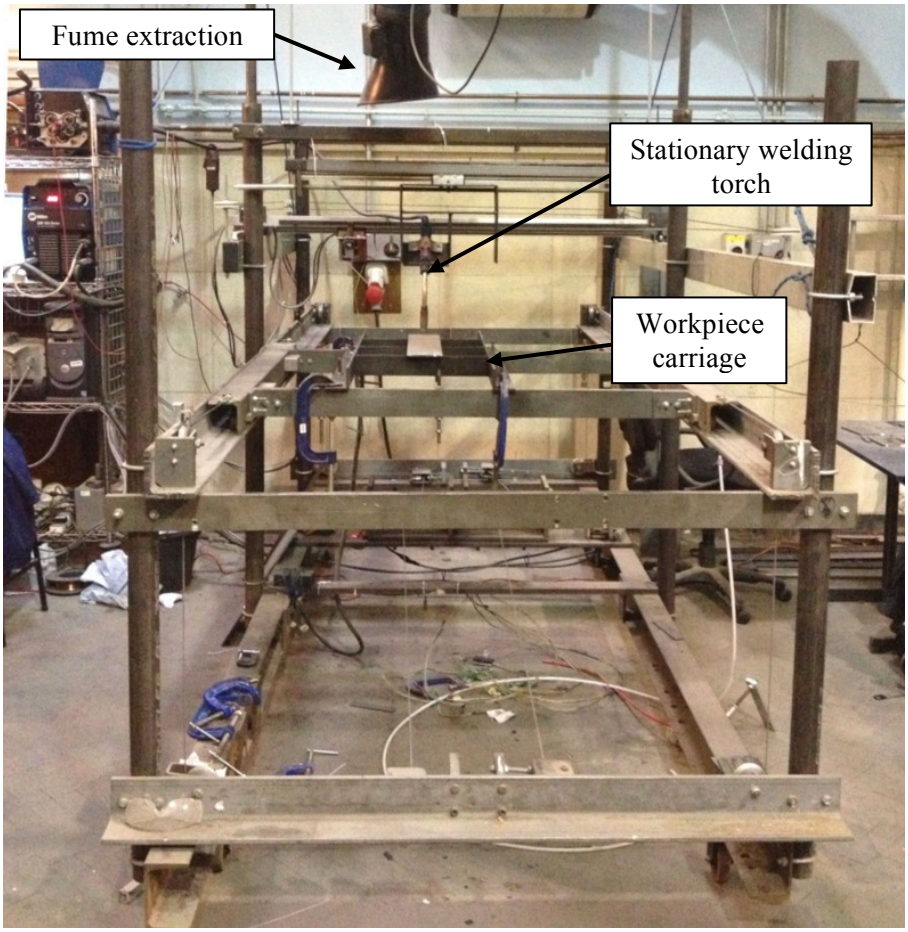

Figure 2.2: Automated welding rig with stationary welding torch

The welding rig can accommodate a maximum plate size of approximately 1 x 1 m for welding trials, and approximately 1 x 2.5 m for distortion measurement (requires the removal of the welding torch mounting).

The position of the welding torch relative to the workpiece can be changed by adjusting the welding torch carriage position along a threaded bar (y-axis), and by raising/lowering the carriage (z-axis). Plate movement was achieved (x-axis) by

means of the frame traversing along parallel angle sections, driven by two bipolar stepper motors using a cable pulley system. The motion of the frame is controlled using a LabVIEW operating system that converts the specified travel speed into a stepping frequency, and is transmitted to the stepper motor using a stepper motor driver.

2.2.2 Distortion measurement system

An essential component of the welding rig is the distortion measurement system, which scans the workpiece surface in two dimensions (x- and y-axis), whilst recording the third dimension (z-axis), thus allowing for the out-of-plane distortion to be measured.

The welding rig configured for distortion only measurements, i.e. with the welding torch mounting removed, is shown in Figure 2.3.

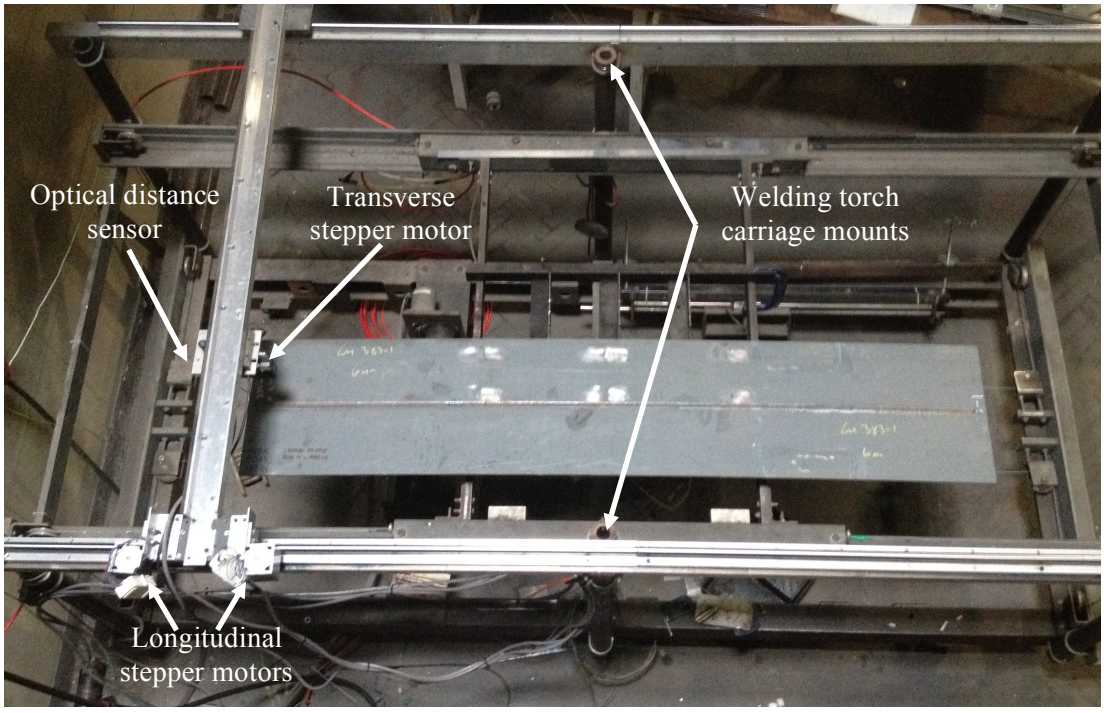

Figure 2.3: Welding rig configured for distortion measurements

A M5L/100 optical distance sensor, which uses a triangulation method, was used to measure the distance from the sensor to the plate surface. The sensor has the ability

to measure displacements ±50 mm at a stand off distance of 220 mm, with a linearity and resolution of 0.3 and 0.03 mm respectively.

The position of, and data acquisition from, the optical distance sensor was controlled through a LabVIEW program. The longitudinal (x-axis) and transverse (y-axis) movement of the sensor was controlled via a rack and pinion system in order to eliminate as much vibration as possible, with the drive provided by two stepper motors in the longitudinal direction and one stepper motor in the transverse direction. The measurement path taken by the sensor is shown in Figure 2.4.

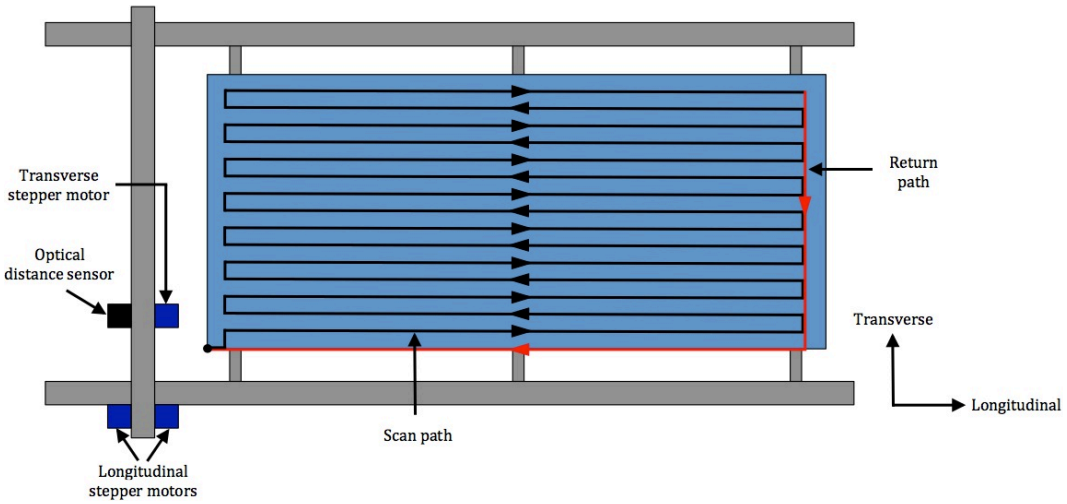

Figure 2.4: Optical distance sensor measurement path (adapted from [2.1])

Distortion measurements were conducted prior to welding (but after tack welding) and after welding (with a cooling period of 45 minutes), the difference between the two measurements being the distortion induced by the welding process.

2.2.3 Temperature measurement systems

The temperature distribution within the workpiece, and thermal history, during the welding process and subsequent cooling, was obtained through a combination of thermocouple arrays and a thermographic camera.

2.2.3.1 Thermocouple arrays

The thermocouple arrays served two purposes; provide thermal history data at specified positions and index the emissivity of the workpiece.

There are a variety of thermocouples available, with the selection based upon temperature measurement range, sensitivity and cost. The most common, general-purpose thermocouple, belonging to the nickel – chromium – aluminium group is Type K. This group of thermocouple was used throughout experimentation, which have a short-term temperature range of -180 to 1350 °C, and conform to a minimum of class two tolerance error, i.e. ±2.5 °C (-40 to 333 °C) and ±0.0075T (333 to 1200 °C) [2.2].

Owing to the destructive nature of the welding process, i.e. the extreme temperatures generated by the electrical arc and spatter emission, thermocouples were mounted on the underside of the workpiece. Thermocouples were inserted to the mid thickness of the workpiece, with the specific location being defined in the experimental setup section of each chapter.

2.2.3.2 Thermographic camera

A thermographic camera, ThermaCAM™ SC500, manufactured by FLIR systems was used to measure the temperature at the workpiece surface. The thermographic camera measures and images the infrared radiation emitted from an object, the fact that the radiation is a function of the surface temperature allows the ThermaCAM™ Researcher software to display the objects temperature.

The infrared radiation measured by the thermographic camera is not only a function of the temperature of the object, but also of its emissivity. In addition to the radiation emitted by the specimen, radiation generated by surroundings and reflected by the specimen will also be captured. The radiation measured by the thermographic camera will also be influenced by radiation absorbed by the atmosphere, and by any external optics. Thus, in order to accurately measure the temperature of the specimens surface, it is necessary to quantify:

- Specimen emissivity
- Ambient temperature
- Atmospheric temperature
- The distance between the specimen and the thermographic camera
- The relative humidity of the atmosphere
- Transmittance and temperature of external optics

Emissivity

The emissivity is a measure of how much radiation is emitted from the specimen compared to that of a perfect black body, i.e. a perfect radiator that emits and absorbs the maximum amount of radiation for any given wavelength.

Real objects never attain black body properties, and are known as grey bodies. The total incident radiation is the sum of the radiation absorbed, reflected and transmitted by a specimen. For opaque materials, the transmittance component is zero and therefore the total incident radiation is the sum of absorbed and reflected radiation. Kirchoff's law states that the radiation absorbed is equal to that emitted by a specimen, which is quantified via the emissivity.

The emissivity is therefore a measure of how much radiation is emitted from the specimen compared to that of a perfect black body.

The emissivity of a body is directly related to its surface conditions; a highly polished specimen will exhibit low emissivity, whereas specimen with a 'dull' surface finish will exhibit relatively high emissivity.

As will be discussed, the surface of the workpiece is coated with a paint primer consisting of ZnO in a silicate binder. Camilleri [2.1] previously conducted emissivity readings for the current setup and primer, he found that within the surface temperature range 25 – 525 °C, the emissivity was generally within the range 0.9 – 0.95, as shown in Figure 2.5.

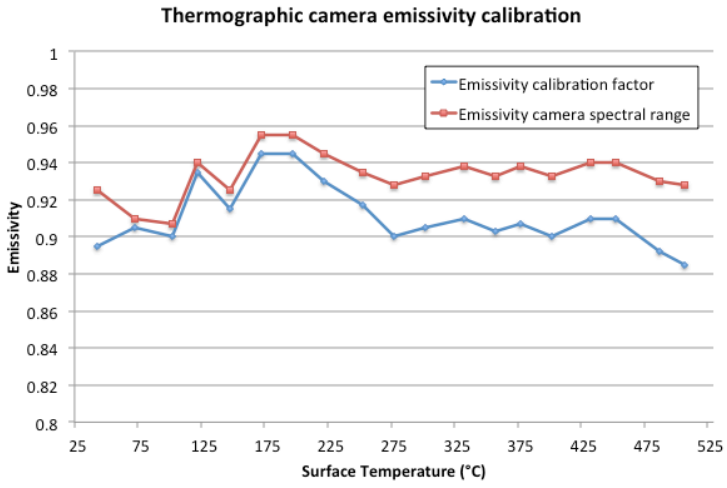

Figure 2.5: Surface emissivity and calibration emissivity factor of primed plate at different temperatures (adapted from [2.1])

Ambient temperature

The ambient temperature is required to compensate for the radiation reflected by a specimen. This is critically important for the camera/software to be able to compensate for when the emissivity is low and the specimen temperature is close to that of the ambient.

Atmospheric temperature, humidity and distance to the specimen

These parameters are required in order for the camera/software to determine the actual temperature of the specimen by accounting for the absorption of infrared radiation by the atmosphere.

Transmittance and temperature of external optics

If the radiation has to pass through optics prior to reaching the thermographic camera, the optics will absorb some of the radiation. Hence the transmittance and temperature data for the optics have to be accounted for by the camera/software.

2.3 Weldycar® NV

The Weldycar® NV is a lightweight (11 kg), battery powered, 4 wheel drive portable carriage system designed to automate various welding operations, Figure 2.6. The welding torch is mounted onto the carriage, and the manual trigger on the torch wired into the units control system, allowing the Weldycar® NV to be programmed to perform a series of automated welds making it ideal for tack/stitch welding.

The unit is powered by a 14 V battery and is capable of autonomous welding for up to 6 hours, with a travel speed of 5-70 cm/min. The carriage incorporates a magnetic attraction system (25 kg force) in order ensure the unit maintains traction in all orientations.

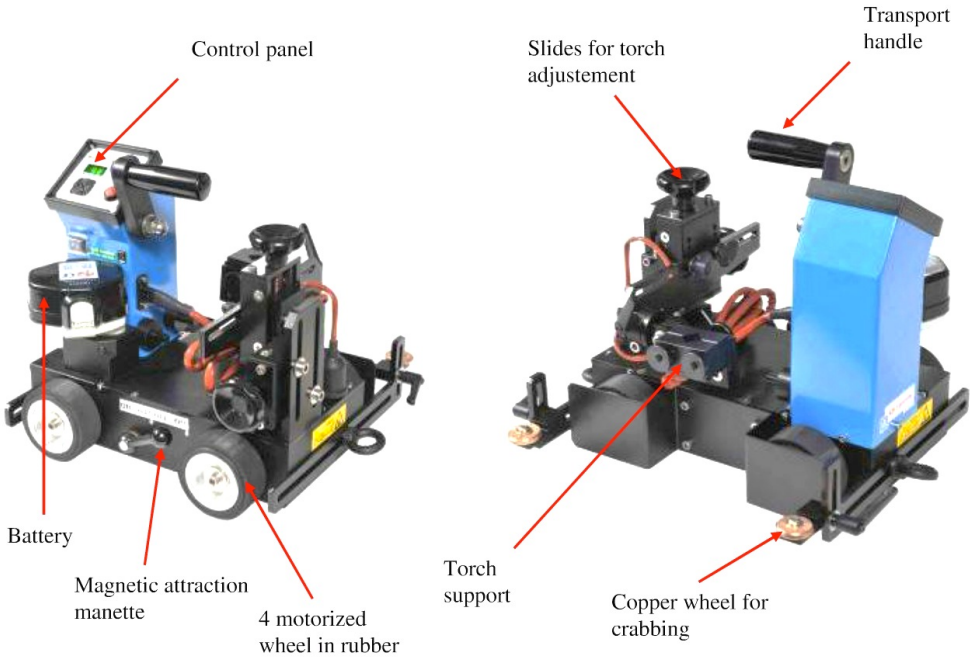

Figure 2.6: Weldycar® NV

2.4 Alternating gas control unit

In order to regulate the flow of shielding gases in the alternating shielding gas process, a dedicated electronic gas control unit, Figure 2.7, was designed that would allow for two shielding gas supplies to be connected to the welding unit.

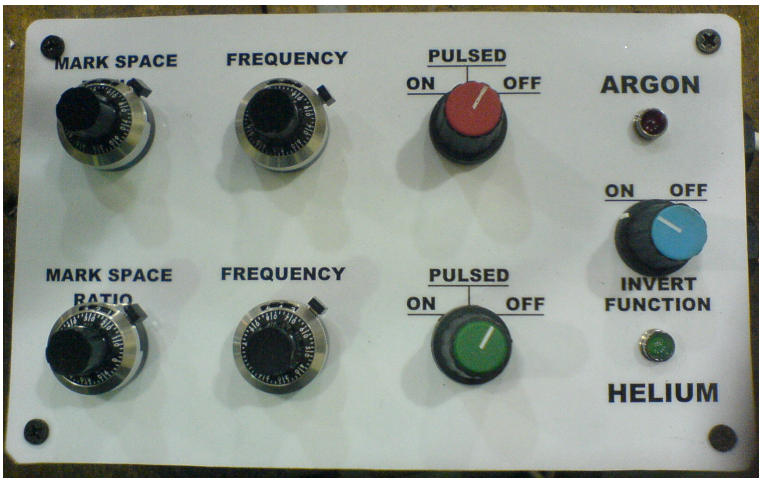

Figure 2.7: Alternating gas control unit

The functionality of the unit relied on two, eight pin, triple five (555) timing circuits that would supply a control signal to a solenoid valve on each gas supply line, thus regulating the flow of each gas. Details of the internal circuitry and solenoid valve selection are given in Appendix A.

The flow rate of each gas was preset when flowing continuously, and as a result of the on/off functionality of the control unit, the overall gas consumption remained the preset value, independent of the frequency used. A schematic diagram of the shielding gas control system is shown in Figure 2.8.

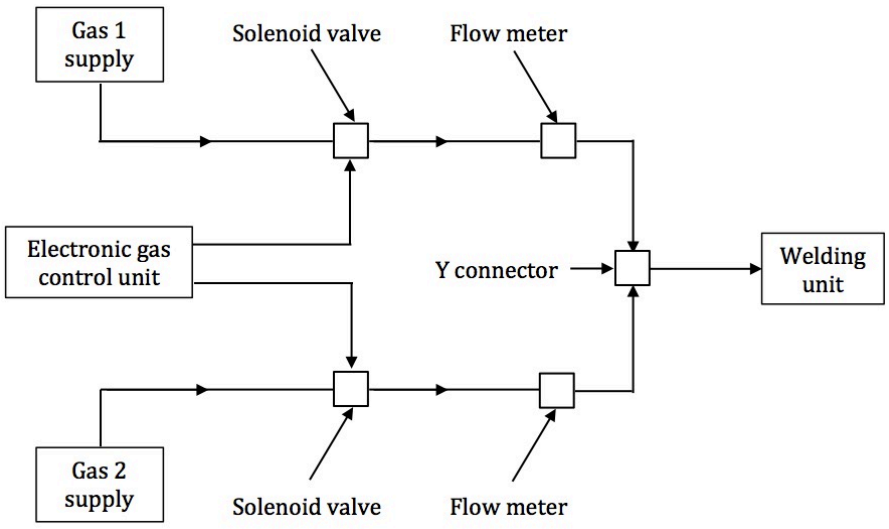

Figure 2.8: Schematic diagram of shielding gas control system for alternating shielding gases

2.5 Welding parameter measurement equipment

2.5.1 Portable arc monitoring system

A state of the art, pre-calibrated AMV3500 portable arc monitoring system (P.A.M.S. unit), Figure 2.9, was used to monitor and record various welding parameters. The system is capable of recording and analysing 6 data channels at a rate of 5000 samples per second per channel. The default channels and their respective ranges are shown in Table 2.1.

The A/D converter has a 14-bit resolution, which means that the measured arc voltage is accurate to approximately 0.012 V and the arc current is accurate to approximately 0.12 A.

Figure 2.9: AMV3500 portable arc monitoring system

Table 2.1: AMV3500 data channel specification

Channel Number	Channel Name	Input Range	Maximum Sensor Input Voltage
1	Arc Voltage	-100 V to +100 V	±100 V
2	Arc Current	-1000 A to +1000 A	±5 V
3	Wire Feed Rate	-25 m/min to +25 m/min	±10 V
4	Temperature	0 °C to 300 °C	±10 V
5	Channel 5	-10 V to +10 V	±10 V
6	Channel 6	-10 V to +10 V	±10 V

The welding parameters detailed in each experimental section are those obtained using the P.A.M.S. unit, with the heat input being calculated according to equation (2.1). A thermal efficiency factor of unity is assumed throughout in order to produce a comparator solely for the effect of shielding configuration. However, it is appreciated that, in reality, the thermal efficiency factor would take into account a number of variables (wire stick-out, voltage, current, shielding gas, etc.) and these would have a cumulative effect on the true thermal efficiency factor of the system.

$$Q = \frac{V\ x\ I}{t.s.} \tag{2.1}$$

2.5.2 Shielding gas welding monitor

A calibrated, in-line Regula® welding monitor (Figure 2.10) was used to monitor and record the shielding gas consumption throughout the shielding gas optimisation welding trials. The system also monitors the welding current using a secondary probe.

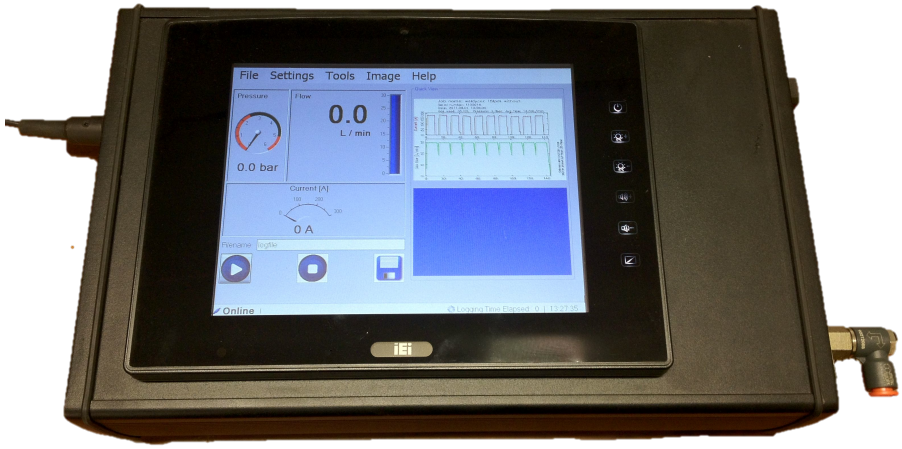

Figure 2.10: Regula® welding monitor

2.6 Material properties

2.6.1 Parent material

Two parent materials were used throughout experimental trials, DH36 shipbuilding grade steel and 6082T6 grade aluminium. In each case, the typical chemical compositions are presented in Table 2.2.

Table 2.2: Typical chemical composition of parent materials (%) (max. value unless stated)

Chemical Element	**Parent Material**	
	DH36	AA6082T6
C	0.180	-
Si	0.500	0.700 – 1.300
Mn	0.900 – 1.600	0.400 – 1.000
P	0.035	-
S	0.030	-
Cr	0.020	0.250
Mo	0.008	-
Ni	0.040	-
Cu	0.035	0.100
Nb	0.020 – 0.050	-
V	0.113 – 0.118	
Ti	0.020	0.100
Zn	-	0.200
Mg	-	0.600 – 1.200
Fe	Balance	0.500
Al	0.015 min.	Balance

The DH36 grade steel plate was shot blasted using steel grit with a particle size of 0.6 – 1.0 mm, prior to a coating of Interplate 937 primer being applied. The primer, typically used by ship building companies, consists of ZnO in a silicate binder and

has a typical film thickness of 17 μm. The primer is heat resistant, and does not interfere with welding and cutting operations, and has good corrosion resistance, preventing the formation of oxides on the plate surface.

The parent materials used throughout have typical mechanical property specification as detailed in Table 2.3.

Table 2.3: Typical mechanical property specification of parent material

Mechanical Property	**Parent Material**	
	DH36	AA6082T6
Yield strength (MPa)	> 355	310
Tensile strength (MPa)	490 – 620	340
Elongation (%)	> 21	11
Charpy impact toughness[a] (J)	> 34 (longitudinal) > 24 (transverse)	-

[a]Charpy impact toughness conducted at -20°C

2.6.2 Filler wire material

Three filler wires were used in the experimental trials; metal cored MC-1 and flux cored SF-1A for experimental welds conducted on DH36 grade steel and Alumig Si5 4043 for those conducted on AA6082T6 aluminium.

The typical chemical composition and mechanical property specification for each wire are detailed in Table 2.4 and 2.5 respectively.

Table 2.4: Typical chemical composition of filler wires (%)

Chemical Element	**Filler Wire**		
	MC-1	SF-1A	Alumig Si5
C	0.050	0.040	-
Si	0.500	0.410	5.000
Mn	1.300	1.000	0.010
P	<0.015	0.010	-
S	<0.015	0.008	-
Cu	-	-	0.030
Ti	-	-	0.010
Zn	-	-	0.010
Mg	-	-	0.010
Fe	Balance	Balance	0.200
Al	-	-	Balance

Table 2.5: Filler wire mechanical property specifications

Mechanical Property	**Filler Wire**		
	MC-1	SF-1A	Alumig Si5
Yield strength (MPa)	> 470	530	≥ 40
Tensile strength (MPa)	560-650	590	≥ 120
Elongation (%)	> 24	28	≥ 8
Charpy impact toughness[a] (J)	> 60	95	-
Charpy impact toughness[b] (J)	> 100	129	-

[a]Charpy impact toughness conducted at -40°C
[b]Charpy impact toughness conducted at -20°C

2.7 Shielding gas visualisation techniques

Many fluids are transparent in nature and therefore require special visualisation methods in order to make the flow regimes visible. Flow patterns can be detected using a variety of techniques including optical methods due to variations in their optical refractive index distorting the path of the light source, or particle tracer methods in which the transparent fluid is seeded with particles that can be illuminated by a light source. Details on the theory of the optical visualisation techniques are given in Appendix B.

2.7.1 Shadowgraphy

A shadowgram is not a focussed optical image; it is, as the title suggests, a shadow. The illuminance level of the shadowgram responds to the second spatial derivative (or Laplacian) of the refractive index field in the transparent medium, e.g. $\delta^2 n/\delta x^2$.

2.7.2 Schlieren

A schlieren image on the other hand is a focussed optical image. The illuminance level corresponds to the variations in the refractive index gradient of the transparent medium, e.g. $\delta n/\delta x$.

2.8 Metallographic analysis

By studying the character, quantity and distribution of macro and microstructural features, it is possible to predict and explain physical properties of a given specimen.

2.8.1 Sample preparation

2.8.1.1 Cutting

When removing a specimen from the test piece, methods must be used to prevent change to the microstructure of the specimen, for example through heating, chemical

attack, or mechanical damage. Specimens were cut to size using abrasive discs with coolant to minimise disturbance to the microstructure.

2.8.1.2 Mounting

Mounting of specimens allows for samples to be easily handled, whilst minimising the amount of damage that could be caused to the specimen.

The mounting material and technique should not influence the chemical composition of the specimen or induce/relax mechanical stresses.

Steel specimens were hot mounted in a Struers ProntoPress-10 mounting press using Struers MultiFast thermosetting, phenolic resin. Hot mounting offers high preparation quality, uniform size and shape, and short process times. However, for specimens that are sensitive to heat or pressure, cold mounting systems must be used, e.g. epoxy, acrylic or polyester resin. Consequently, aluminium specimens were mounted in a Struers EpoFix epoxy resin, which is a thermosetting polymer that cures irreversibly with low shrinkage.

The thickness of a mounted specimen is typically half its diameter, in order to prevent rocking during grinding and polishing. The edges of the mounted specimen should be rounded to minimise damage to grinding and polishing discs.

2.8.1.3 Grinding

Surface damage, as a result of the cutting process, is removed by grinding using progressively finer grades of silicon carbide (SiC) abrasive paper; each grinding stage removing the damage caused by the previous stage. Water was used as a coolant during grinding stages, and to remove grinding debris.

The number of SiC grains per square inch indicates the coarseness of the grinding paper; 120, 220, 500 (first grade used for aluminium specimens), 800, 1200, 2400 grit papers were used.

2.8.1.4 Polishing

Polishing pads, covered with soft cloth, with abrasive particles suspended in lubricant that can roll or slide across the cloth and specimen. Three polishing stages were used; two coarse stages, 6 and 3 μm diamond suspension and blue DP-lubricant

(alcohol based with high cooling and low smearing) with DP-MOL pads, and fine 0.05 μm colloidal silica polishing suspension used with an OP-CHEM pad.

2.8.1.5 Etching

To analyse features such as grain boundaries, a metallic sample must be polished to a mirror finish. However, under a microscope, such a highly polished surface appears as a plain white field. Etching is a chemical process used to highlight features of metals at microscopic levels. Chemical solutions known as etchants are selected to corrode some of those elements, which show up as darker regions. Etching can be used to expose grain boundaries, highlight different phases, and identify inclusions.

Two etching agents were used in this study: Nital solution and Keller's reagent. Nital solution (2 ml nitric acid and 98 ml ethanol) is used to reveal austenite grain boundaries and other phases in steel. Keller's reagent (5 ml nitric acid, 3 ml hydrochloric acid, 2 ml hydrofluoric acid and 190 ml distilled water) is used to highlight common features of aluminium alloys including grain boundaries.

2.8.2 Optical microscopy

All light optical microscopy (LOM) was carried out using an Olympus GX51 inverted microscope with a UIS2 infinity-corrected optical system. A built-in depolarizer lens removes spot flare and produces a clear, high contrast image by combining a set of polariser and analyser plates.

The Olympus GX51 has differential interference contrast (DIC), and uses a simple switching slider type single prism system. It encompasses three DIC prisms: U-DICR for all imaging applications, high resolution U-DICRH, and high contrast U-DICRHC, so that the excellent resolution and contrast matched to the state of the sample are obtained, as shown in Figure 2.11.

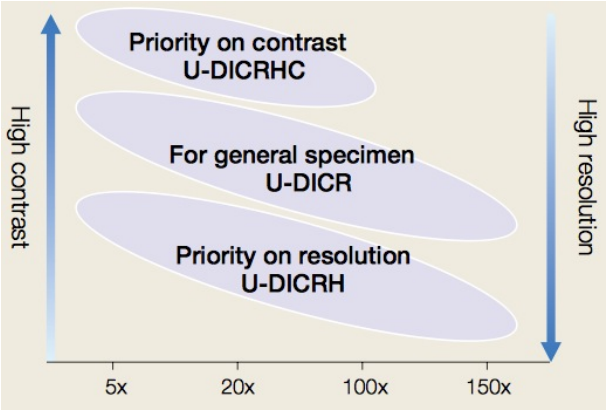

Figure 2.11: DIC prism selection trade-off for contrast vs. resolution

2.8.2.1 Microstructure

LOM was conducted in a systematic manner with specific regions of the weld sections being imaged in order to characterise the entire weld area whilst maintaining an objective approach.

2.8.2.2 Inclusion percentage

As with the microstructural analysis, the weld defect inclusion percentage was determined by systematically analysing images from around the weld pool. Image analysis software (ImageJ) was used to determine the percentage of each image that exhibited a shade contrast to that of the bulk material; these contrasts are a combination of micro-porosity, metallic and non-metallic inclusions. Therefore allowing the 'cleanliness' of the weld to be quantified as a function of the welding parameters.

2.8.2.3 Geometry

The weld geometry, as detailed in Figure 2.12, was measured using ImageJ image analysis software. Thus allowing for the effect of weld parameters on geometry to be determined. Measurement errors were minimised by measuring the geometry at three cross sections along the weld, with the average values being reported in each case.

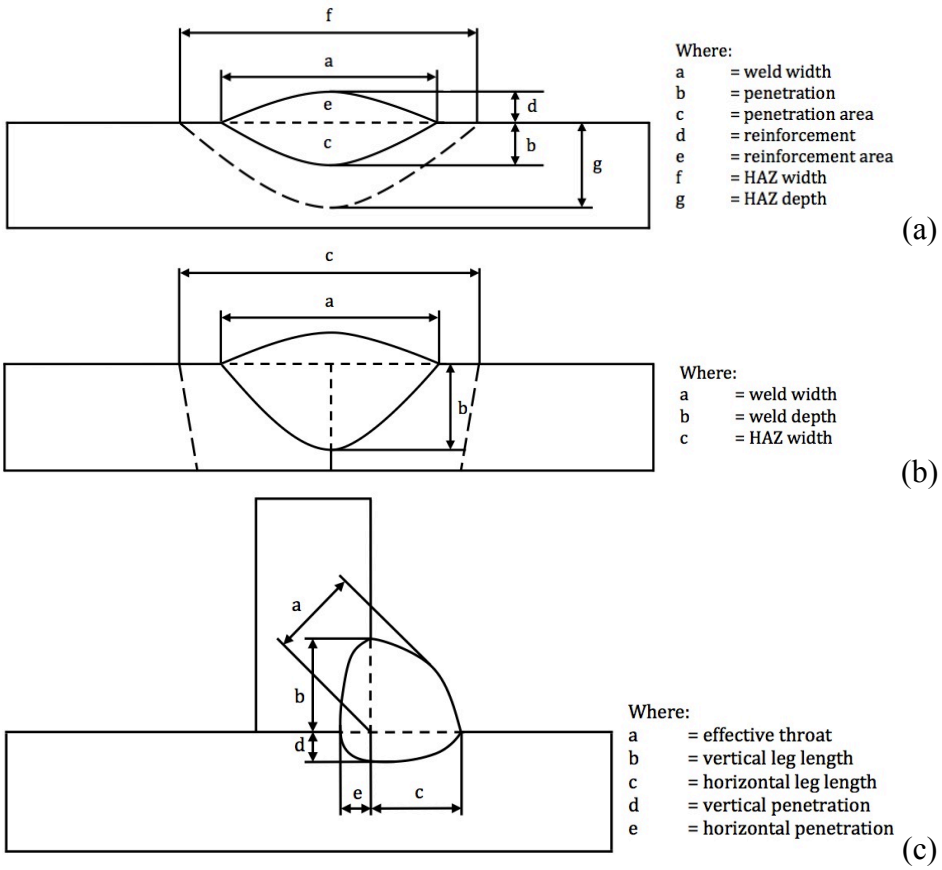

Figure 2.12: Schematic diagram of weld geometry measurements for (a) bead on plate, (b) butt weld and (c) fillet weld, configurations

2.8.3 Microhardness

Specimens had macro sections removed from the weld and were subjected to the grinding and polishing sequence, detailed previously. Microhardness measurements were conducted using a Mitutoyo MVK-G1 microhardness tester with a 200 g load and 10 s dwell time. The distance between each indentation was large enough to eliminate the effects of work hardening influencing subsequent indents.

2.9 Mechanical analysis

Mechanical analysis of the welded joint was conducted in order to ascertain the effect that changing weld parameters, more specifically shielding gas parameters, have on the mechanical integrity of the structure. Three specimens were generated for each mechanical assessment, with the mean average being reported in each case.

2.9.1 Tensile testing

Transverse and longitudinal specimens were prepared in accordance with BS EN ISO 10002-1:2001, as shown in Figure: 2.13, and followed the testing procedures therein. An Instron 8802 Servo-hydraulic tensile testing system with a maximum capacity of 250 kN was used, with a constant strain rate of 0.5 mm/min up to 1.25 mm extension, and 5 mm/min thereafter until fracture occurred.

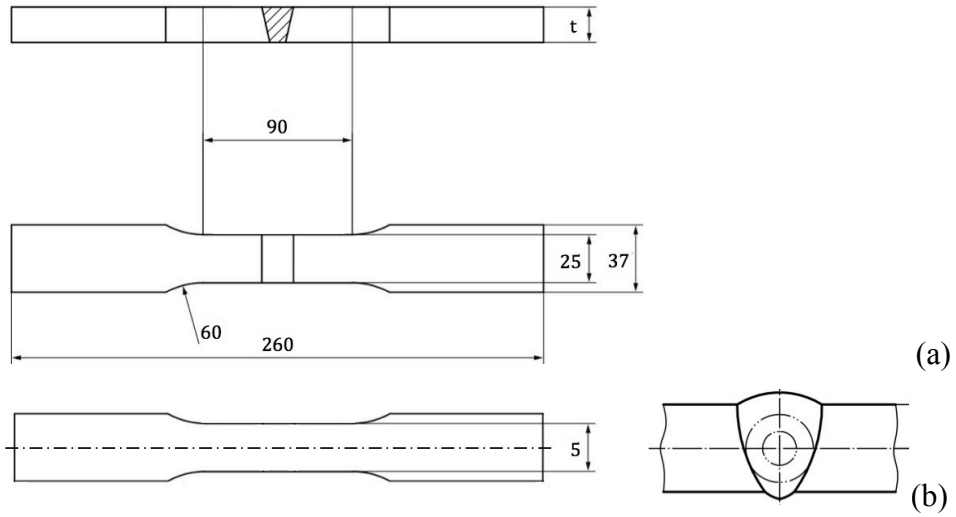

Figure 2.13: Schematic diagram of tensile specimen for (a) transverse, and (b) longitudinal testing, (adapted from [2.3])

2.9.2 Bend testing

Face and root bend tests were conducted according to BS EN 910:1996, using a three-point loading method, with a distance of 150 mm between rollers and 4T former diameter.

2.9.3 Charpy impact toughness testing

Charpy impact toughness was assessed in accordance with EN 10045-1:1990, to determine the effect that the shielding gas configuration has on the impact toughness of the weld and the HAZ. Due to the thickness of the parent material, sub-size specimens were required (5 x 10 x 55 mm).

The Charpy V-notch impact test is often regarded as the accepted method of toughness assessment for welded joints due to complications in conventional fracture toughness methods as a result of the fusion zone and HAZ exhibiting a heterogeneous microstructure that can have widely varying strength and toughness values.

2.10 Thermal property analysis

Thermal property analysis of the solidified weld and parent material was conducted in order to ascertain the effect that shielding gas parameters have on the thermal properties of the structure. Three specimens were generated for each thermal property assessment, with the data reported for the specimen midway along the weld.

2.10.1 Thermal expansion coefficient

The linear thermal expansion coefficient was evaluated through the use of a push-rod dilatometer (NETZSCH DIL 402C®), as shown in Figure 2.14, according to ASTM E228-11. Dilatometer specimens were taken in the longitudinal weld direction, and were 25.5 mm long, 4 mm diameter cylindrical rods. A linear variable differential transformer (LVDT) allows the displacement to be measured by means of a voltage difference, which can then be converted to a displacement signal. As the temperature is recorded by a thermocouple within the chamber, the information can provide the linear thermal expansion characteristics of the specimen. The change in length of the specimen with respect to temperature allowed for the linear thermal expansion coefficient to be calculated; data was measured from a reference temperature of 25 to 1200 °C.

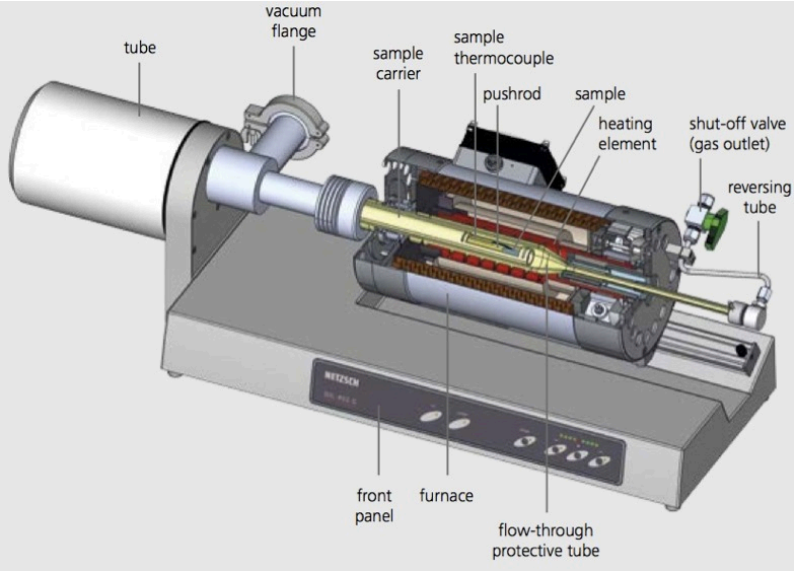

Figure 2.14: Dilatometer 3-dimensional sectional view

2.10.2 Specific heat capacity

The specific heat capacity was analysed by simultaneous thermal analysis (STA) using a NETZSCH STA 449 F1 Jupiter®, as shown in Figure 2.15, according to ASTM E1269-11. Simultaneous thermal gravimetric analysis (TGA), differential thermal analyser (DTA) and differential scanning calorimeter (DSC) allows for weight change during heating or cooling cycles to be analysed, including phase transition temperature determination such as crystallisation, melting and sublimation, and specific heat capacity. Specimens, 2 mm thick, 4 mm diameter discs, were placed in a platinum sample pan with an alumina liner and lid. Nitrogen was used to provide a protective atmosphere and heating was conducted from a reference temperature of 25 to 1200 °C.

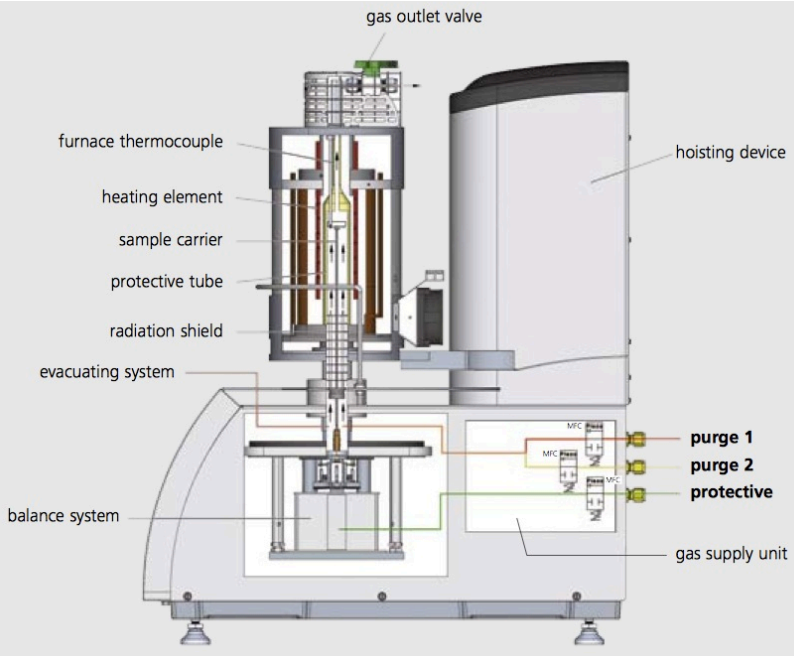

Figure 2.15: STA sectional view

2.10.3 Thermal conductivity / thermal diffusivity

Laser flash analysis (LFA) was conducted using a NETZSCH LFA 427® in order to determine both the thermal diffusivity and thermal conductivity of the specimens. The specific heat data gathered from the STA was imported to the LFA to increase the accuracy of the analysis, in accordance with ASTM E1461-11. Specimens, 3 mm thick, 12.5 mm diameter discs, were mounted in a furnace via a carrier system, and heated. At predetermined temperature steps (100 °C) a high intensity short duration radiant energy laser pulse is fired at the samples top surface, and the time taken for a temperature increase to be measured on the opposite surface recorded, as shown in Figure 2.16. The thermal diffusivity measurements allow for the thermal conductivity to be calculated over a temperature range, as with the other analysis, LFA was performed from a reference temperature of 25 to 1200 °C.

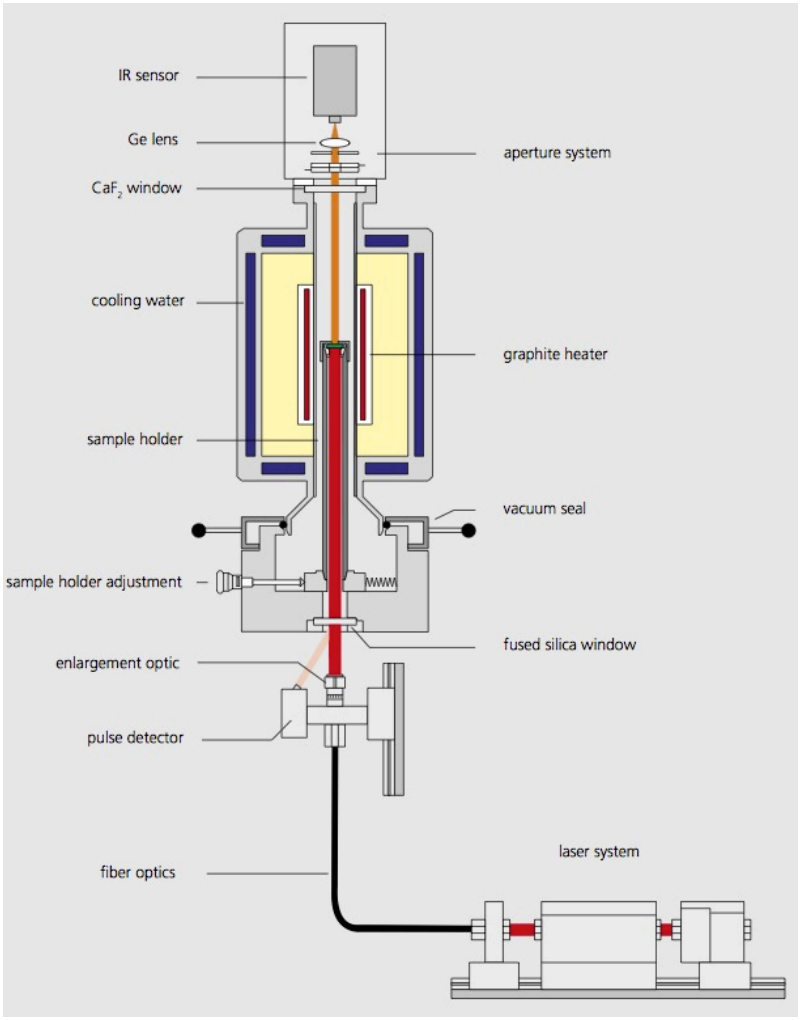

Figure 2.16: Schematic diagram of LFA

2.11 Radiographic assessment

Radiographic examination was performed due to its' ability to detect discontinuities through the thickness of the weld. Weld quality was assessed using Smart Andrex 200 X-ray equipment, in accordance with BS EN 1435:1997, with the basic setup shown in Figure 2.17.

A source to object distance of 800 mm was used throughout, and a source power of 145 kV and 4.5 mA for 50 seconds duration, with focal point size of 1.3 x 1.3 mm. Structurix AGFA D7 radiographic film was used as its fine grain film produced high contrast results at high speed, with 0.125 mm thick lead screens surrounding the film.

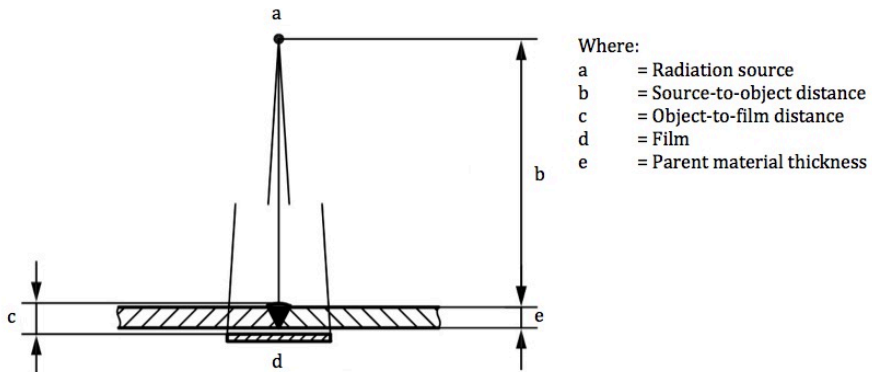

Figure 2.17: Schematic diagram of radiographic assessment (adapted from [2.4])

2.12 Trial specific setup

In order to more fully evaluate the alternating shielding gas process, and assess the effects that reducing the shielding gas consumption have on arc welding processes, some elements of the experimental setup had to be tailored in order to conduct various experiments. Consequently, an experimental setup description is given at the outset of each chapter.

2.13 References

[2.1] Camilleri, D., 'Support tools for the prediction of distortion in the design and manufacture of thin plate welded structures', Ph.D. Thesis, University of Strathclyde, 2005.

[2.2] British Standard Institution, 'BS EN 60584-1:2013. Thermocouples. Part 1: EMF specifications and tolerances', London: BSI, 2013.

[2.3] British Standard Institution, 'BS EN ISO 10002-1:2001. Metallic materials - tensile testing. Part 1: Method of test at ambient temperature', London: BSI, 2013.

[2.4] British Standard Institution, 'BS EN 1435:1997. Non-destructive testing of welds – Radiographic testing of welded joints', London: BSI, 2013.

3 Study of GMAW shielding gas flow rate for a conventional gas supply

3.1 Nomenclature

β	- Thermal expansion coefficient
$C_{1\varepsilon}, C_{2\varepsilon}, C_{3\varepsilon}$	- Constant
C_{μ}	- Constant
ε	- Rate of dissipation
ε_{ext}	- Emissivity of the external wall surface
g	- Gravity
Gr	- Grasholf number
G_b	- Turbulent kinetic energy due to buoyancy
G_k	- Turbulent kinetic energy due to mean velocity gradient
h_f	- External heat transfer coefficient
h_{ext}	- Fluid-side local heat transfer coefficient
k	- Turbulent kinetic energy
L	- Characteristic length
μ	- Viscosity
μ_t	- Turbulent viscosity
q	- Heat flux
q_{rad}	- Radiative heat flux
ρ	- Fluid density
Re	- Reynolds number
σ	- Stefan-Boltzmann constant
σ_{ε}	- Turbulent Prandtl number for rate of dissipation
σ_k	- Turbulent Prandtl number for turbulent kinetic energy
S_{ε}, S_k	- User defined source terms
ΔT	- Temperature differential between the wall surface and bulk fluid
T_{ext}	- External heat sink temperature
T_f	- Local fluid temperature
T_w	- Wall surface temperature

T_∞ - Temperature of the radiation source/sink

v - Kinematic viscosity

Y_m - Dilation dissipation

3.2 Introduction

Effective shielding of the molten metal in any fusion welding process is a prerequisite for good quality welds. There is an ongoing drive to improve the efficiency of the GMAW process and/or any other conventional processes that require a gas shield to be present during welding. The primary purpose of the shielding gas is to shield the metal transfer stream and molten weld pool from the effects of atmospheric re-oxidation.

The correct flow rate is essential for providing adequate protection to the weld metal during the heating, liquid and solidification stages, with a shielding gas flow rate of 15-20 l/min typically specified for GMAW. Despite the importance of the shielding gas to the GMAW process, there is a lack of knowledge among welding operatives as to how it should be applied and controlled in practice. Surveys showing that the welding operative often adjusts the shielding gas flow rate to as high as 30 l/min [3.1], with the belief that a higher shielding gas flow rate means better protection for the weld region.

It is known that too low a flow rate can lead to inadequate coverage of the weld pool which often leads to porosity and excess spatter development, whilst too high a flow rate can result in poor penetration [3.2] and/or porosity due to turbulence in the gas column. In the case of the latter, the turbulence effect results in atmospheric gases being drawn into the arc [3.3], which promotes the formation of entrapped gas (porosity) during the solidification phase. Hence, there is an optimum flow rate for weld shielding gases, but this is difficult to define and is often decided on the basis of preference or experience. Nevertheless, the issues associated with over estimating the optimum flow rate are often preferred to those of insufficient flow. Consequently, a higher flow rate is normally selected albeit at a substantial and unnecessary cost to the process and a risk to the weld integrity.

Various mechanical anti-surge and electromagnetic gas-saving devices have been developed to regulate the gas flow rate and minimise shielding gas consumption [3.4-3.7]. Mechanical anti-surge devices are developed with the aim of reducing shielding gas surge at arc initiation and delivering a controlled flow rate throughout the welding process. Electromagnetic gas-saving devices have been developed to implement a feedback control loop that automatically synchronises the shielding gas flow rate according to a correlation between shielding gas flow rate and the welding current used. In doing so, the theoretical optimum flow rate of shielding gas is continuously supplied to the weld region. In addition, some electromagnetic units take advantage of an extremely fast response valve that is used to create a pulsing effect of the shielding gas flow allowing for optimal flow to be maintained. This creates the added benefit of providing a near-instantaneous shielding gas shut-off at the weld termination.

Cross drafts present a significant problem to the welding process from both a technical and economic viewpoint, potentially adversely affecting the shielding gas's ability to protect the welding region from contamination by atmospheric gases such as nitrogen and oxygen. To counteract the detrimental effects of cross drafts, welding operatives generally use shielding devices to prevent the draft reaching the welding region and/or increase the shielding gas flow rate, with the mindset that more shielding gas means better protection. However, as previously stated excessive flow rates can induce turbulence in the shielding gas column, thus encouraging intermixing with atmospheric gases.

There is therefore a need to understand and control the minimum shielding gas flow rate needed in practical welding conditions where drafts may affect the coverage.

3.3 Experimental setup

In order to ascertain the true effects of reducing the shielding gas flow rate with a conventional shielding gas supply of argon / 20% carbon dioxide, i.e. a single supply of shielding gas, both with and without the aid of 'gas saving devices' installed, a multi-discipline approach was taken consisting of a series of systematic experimental and computational studies.

This section details the experimental setup used to conduct each series of experimental trials, with reference to Experimental Apparatus, Chapter 2.

3.3.1 Techno-economic evaluation

A comprehensive series of trials have been conducted in a variety of welding scenarios, including butt, fillet and bead-on-plate configurations, to ascertain the true effects of reducing the shielding gas flow rate to determine the optimum shielding gas flow rate without detriment to weld quality.

Trials were conducted upon an automated welding rig (butt and fillet weld trials) and using the Weldycar NV (stitch/tack weld trials) in order to ensure repeatability of the trials conducted.

The study was conducted using both a conventional shielding gas flow meter and an electromagnetic gas-saving device installed. The electromagnetic gas-saving device implements a feedback loop to synchronise the shielding gas flow rate to the welding current used; a higher current requiring a greater flow rate. In addition, it has an extremely responsive valve that opens/closes (50 Hz) throughout the welding process to further optimise gas delivery. Latterly, a gas consumption study was undertaken to determine the impact of implementing a mechanical anti-surge device in conjunction with a conventional flow meter. The shielding gas control mechanisms are shown in Figure 3.1.

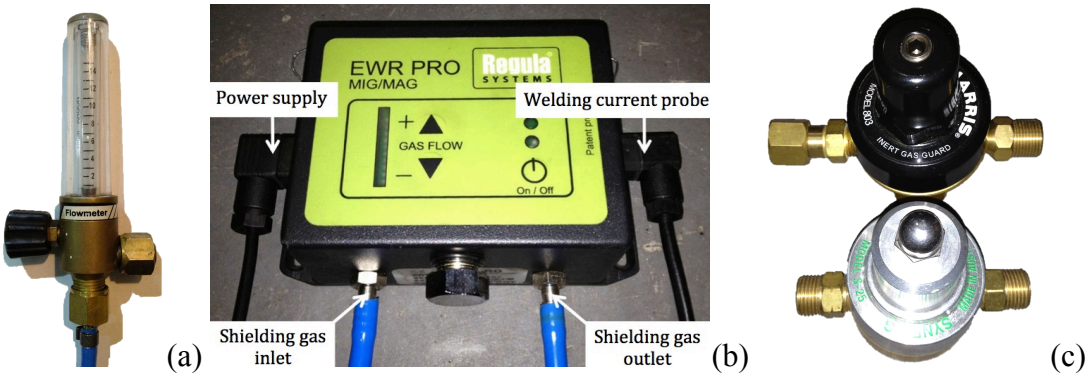

Figure 3.1: Shielding gas control methods; (a): conventional flowmeter, (b) electromagnetic gas-saving device, and (c) mechanical anti-surge device

Welding parameters were analysed using an AMV3500 portable arc monitoring system (P.A.M.S. unit), and shielding gas flow rate monitored and recorded using a Regula® welding monitor.

3.3.1.1 Butt weld trials

Butt welds were performed to join two 500 x 250 x 4 mm (length x breadth x thickness) DH36 grade steel plates, with a square edge preparation and 3 mm root gap as shown in Figure 3.2. Trials were conducted using 1.2 mm diameter SF-1A filler wire and a 6 mm diameter ceramic backing strip applied to the underside of the workpiece to provide support to the weld root.

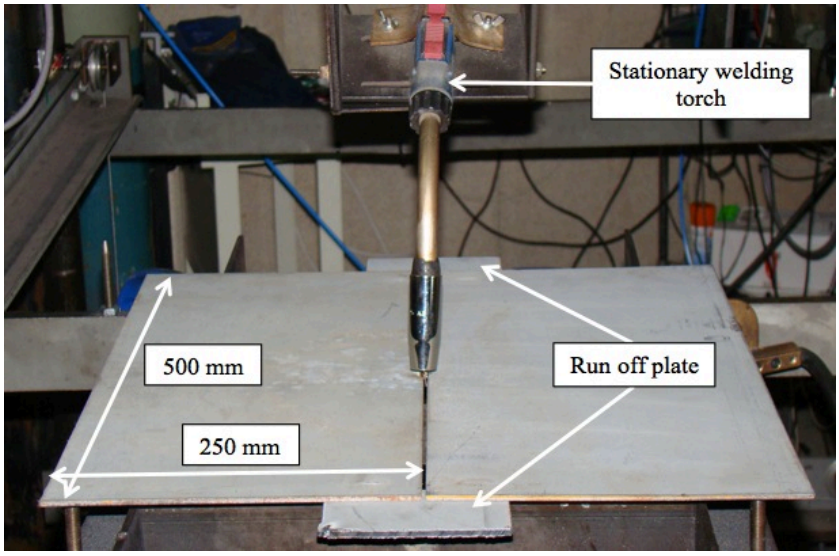

Figure 3.2: Weld setup for butt configuration shielding gas optimisation trials

Thermal data was captured using thermocouples, located at the mid-length of the plate, between 10 and 50 mm from the weld centreline, in 10 mm increments. A symmetrical temperature distribution was assumed, and therefore, thermocouples were located on one side of the weld centre line only.

Distortion data was captured using an optical distance sensor, with measurements taken every 10 mm in both longitudinal and transverse directions. The workpiece was scanned before welding (after tack welding of run off plates) and after a cooling period of 45 minutes.

A travel speed of 5 mm/s, 10 mm stand-off distance and nominal average weld parameters of 24.8 V and 196 A were used throughout, Table 3.1 shows the average parameters used for each configuration.

Table 3.1: Parameters for butt configuration shielding gas optimisation trials

Shielding Gas Flow Rate (l/min)	Electromagnetic Gas Saving Device	Voltage (V)	Current (A)	Travel Speed (mm/s)
15	No	24.9	196	5
15	Yes	24.9	191	5
12	No	24.7	198	5
12	Yes	24.8	196	5
9	No	24.8	198	5
9	Yes	24.9	197	5
6	No	24.8	196	5
6	Yes	24.7	199	5

3.3.1.2 Fillet weld trials

Fillet weld trials were performed using 1000 x 60 x 6 mm DH36 grade steel bar and 1.0 mm diameter MC-1 filler wire. The bar was tacked together in the form of an inverted ‘T’ fillet weld, i.e. horizontal vertical position, as shown in Figure 3.3.

A travel speed of 5 mm/s, 10 mm stand-off distance and nominal average weld parameters of 26.0 V and 202 A were used throughout. The average welding parameters, for this section of investigation are documented in Table 3.2.

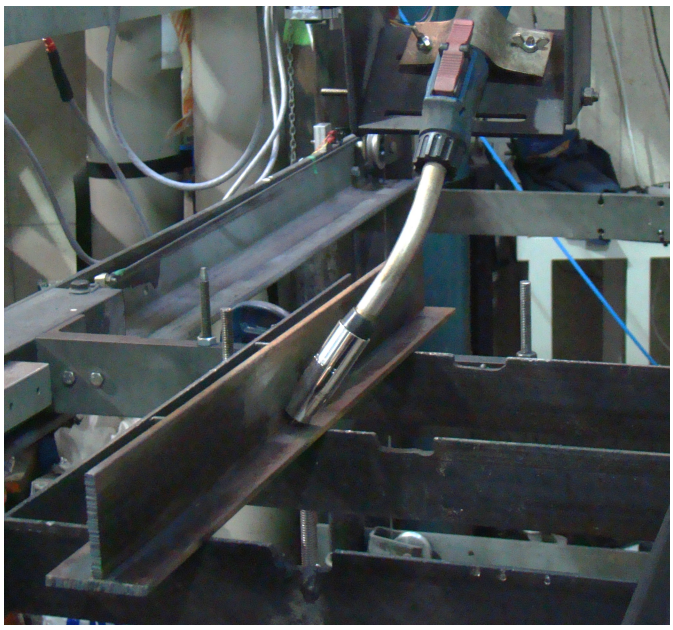

Figure 3.3: Weld setup for fillet configuration shielding gas optimisation trials

Table 3.2: Parameters for fillet configuration shielding gas optimisation trials

Shielding Gas Flow Rate (l/min)	Electromagnetic Gas Saving Device	Voltage (V)	Current (A)	Travel Speed (mm/s)
15	No	26.0	203	5
15	Yes	25.9	201	5
12	No	26.1	206	5
12	Yes	26.0	197	5
9	No	26.0	201	5
9	Yes	26.1	200	5
6	No	26.0	203	5
6	Yes	26.1	205	5

3.3.1.3 Stitch/tack weld trials

A Weldycar NV was used in order to automate the welding process and to simulate the process of performing numerous stitch/tack welds. The Weldycar NV was programmed to travel at a pre-set speed and perform a series of 50 mm welds with a 50 mm gap, over a 1 m length. These took place in the form of bead-on-plate trials using 1.2 mm diameter flux cored SF-1A filler wire on 1000 x 100 x 10 mm DH36 grade steel bar, as shown in Figure 3.4.

Figure 3.4: Weld setup for stitch/tack configuration shielding gas optimisation trials

To replicate the conditions likely to occur in construction yards, a light cross draft of approximately 0.7 mph was introduced, which was measured using a hot-wire anemometer in the welding region.

A travel speed of 6 mm/s, 10 mm stand-off distance and nominal average weld parameters of 23.6 V and 185 A were used throughout. The average welding parameters, for this section of trials are shown in Table 3.3.

Table 3.3: Parameters for stitch/tack configuration shielding gas optimisation trials

Shielding Gas Flow Rate (l/min)	Electromagnetic Gas Saving Device	Voltage (V)	Current (A)	Travel Speed (mm/s)
15	No	23.7	189	6
15	Yes	23.4	186	6
12	No	23.7	188	6
12	Yes	23.6	180	6
9	No	23.7	181	6
9	Yes	23.6	183	6
6	No	23.7	186	6
6	Yes	23.6	189	6

3.3.2 Welding nozzle optimisation

Many fluids, including shielding gas flow in arc welding, are transparent in nature and are essentially invisible to the naked eye. Therefore, in order to make the flow regimes visible, special visualisation methods have to be implemented. Flow patterns can be detected using a variety of techniques including optical methods due to variations in their optical refractive index distorting the path of the light source, or particle tracer methods in which the transparent fluid is seeded with particles that can be illuminated by a light source.

A systematic study was conducted to visualise (shadowgraphy) and simulate (CFD) the effect that the shielding gas flow rate, cross draft velocity and weld nozzle design have on the quality of the solidified weld. Experimental trials were conducted on an automated welding rig, which moved a DH36 grade steel plate workpiece, of dimensions 500 x 250 x 8 mm, under a stationary welding torch. Bead-on-plate welds were conducted using 1.2 mm diameter SF-1A flux cored filler wire, a welding speed of 3.2 mm/s, with nominal welding parameters of 24.7 V and 210 A as recorded using the P.A.M.S. unit. The welding nozzle was positioned with a stand-off distance of 10 mm to the workpiece for all tests.

The shielding gas flow rate was measured using a Regula® welding monitor. Shielding gas flow rates of 5, 10, 15 and 18 l/min were evaluated with independent checks made to validate the shielding gas flow rate exiting the welding torch using a simple flow meter placed over the end of the torch.

Cross drafts were introduced through a custom-made laminar flow device, comprising a diffuser and a flow-straightener, connected to a compressed air line. The device was placed 300 mm from the centre of the weld bead and the steady, uniformly distributed, laminar output was directed at the weld nozzle. The cross draft velocity in the welding arc region, which was measured using a hot-wire anemometer, was adjustable by varying the air inlet pressure. Cross draft velocities of 0–8 mph (0–3.6 m/s) in 1 mph (0.45 m/s) increments were used.

The effect of nozzle geometry was assessed through the modification of conventional 16 mm diameter nozzles. Initially, uncoated brass inserts were soldered to the nozzle exit to simulate the effect of cylindrical spatter build up. Three outlet diameters were

evaluated; 16 mm (unrestricted), 14 mm and 11 mm. Latterly, the effect of insert geometry was considered; an end plate, with a series of eight 2.5 mm diameter holes, with a central hole to allow for the filler wire to pass through, an internal plate, positioned 6 mm from the nozzle outlet, and had a series of twelve 1.5 mm diameter holes, with a central hole for the contact tip, and a double helix on the internal surface of the nozzle. All geometries, with the exception of the internal double helix, which was omitted due to manufacturing issues, were evaluated experimentally and are shown in Figure 3.5.

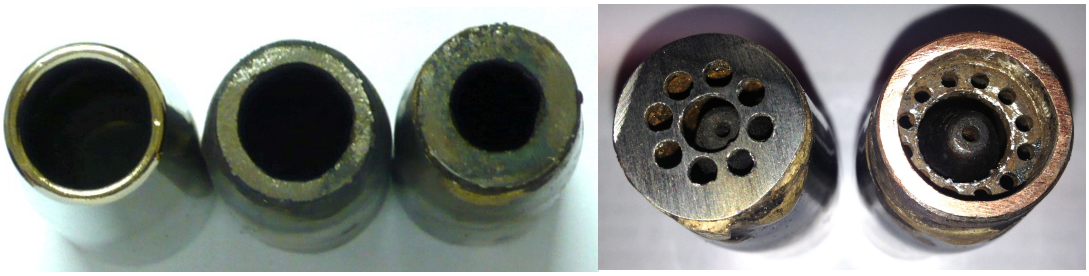

Figure 3.5: Nozzle geometry. Left to right: 16 mm (unrestricted) nozzle, 14 mm circumferential restriction, 11 mm circumferential restriction, end plate restriction, and internal plate restriction.

3.3.2.1 Shadowgraphy

The stationary welding torch setup allowed for shadowgraphy equipment to be sited in line with the welding torch. The shadowgraphy setup followed the 'focussed' shadowgraphy theory as detailed in Appendix B. The shielding gas flow was visualised using a portable shadowgraphy system, which used a 35 mm diameter collimated 12 mW helium-neon laser beam (1 mm divergence on the beam diameter over 3 m length); directed across the weld-region, perpendicular to the weld direction, Figure 3.6. The beam was focussed to a high-speed camera. Broad band-pass (10 nm) and narrow band pass (1 nm) optical filters centred on the laser wavelength (633 nm) and absorptive neutral density attenuating filters were used in order to match the laser illumination power to the dynamic range of the camera. This allowed the unwanted light from the welding arc to be effectively eliminated with respect to the laser light. Camera images were recorded at 9,000 frames per second and resolution of 256(H) × 128(V) pixels.

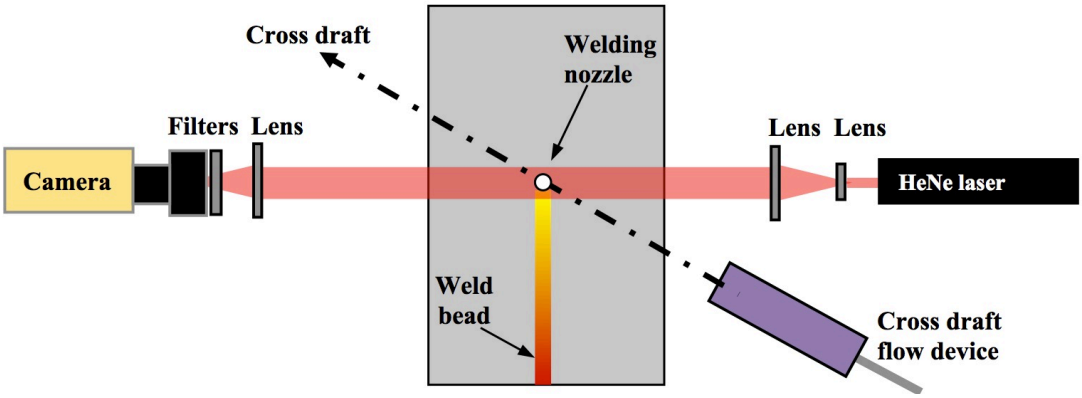

Figure 3.6: Schematic diagram of the shadowgraphy setup

As shown in Figure 3.6, the flow device used to create a cross draft in the weld region was positioned 300 mm from the centre of the welding nozzle, at an angle of 60° to the weld bead. The flow device was unable to be located perpendicular to the welding direction due to the positioning of the shadowgraphy equipment.

The shadowgraphy visualisation technique was applied to three nozzle geometries; 16 mm unrestricted nozzle, and the 14 and 11 mm circumferentially restricted nozzles.

3.3.2.2 Computational fluid dynamics model generation

A simplified, multi-physics, 3D transient state model was developed to analyse several nozzle geometry changes using the CFD software Fluent. The model geometry was constructed in Gambit, in which, the welding nozzle is positioned with a 10 mm gap directly above the surface of a 500 mm × 250 mm × 8 mm thick workpiece. The nozzle and plate are situated within a defined volume of fluid, of dimensions 600 x 1000 x 200 mm, to ensure that all flow development was captured, although the main area of interest which was the 10 mm between the tip of the nozzle and the plate surface. The overall model consisted of approximately 190,000 tetrahedral elements, the density of which was greatly increased in the volume surrounding the nozzle outlet. Figure 3.7 shows the welding nozzle, arc plasma plate and fluid surface mesh.

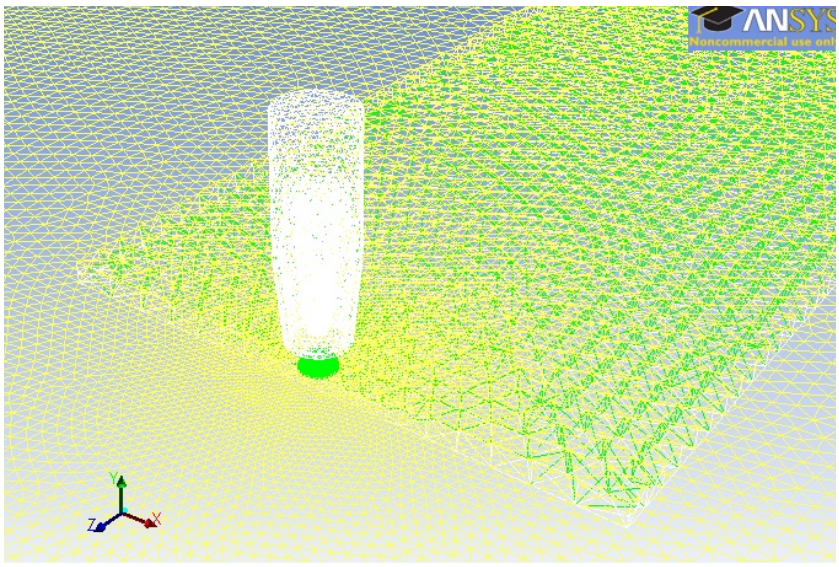

Figure 3.7: CFD model mesh

A simplification of the welding arc plasma was applied in the model geometry, this involved a 12 mm diameter hemisphere being positioned adjacent to the plate surface, directly beneath the welding nozzle, as shown in Figure 3.8. The hemisphere fluid was detached from the surrounding fluid, thus enabling it to be assigned independent properties.

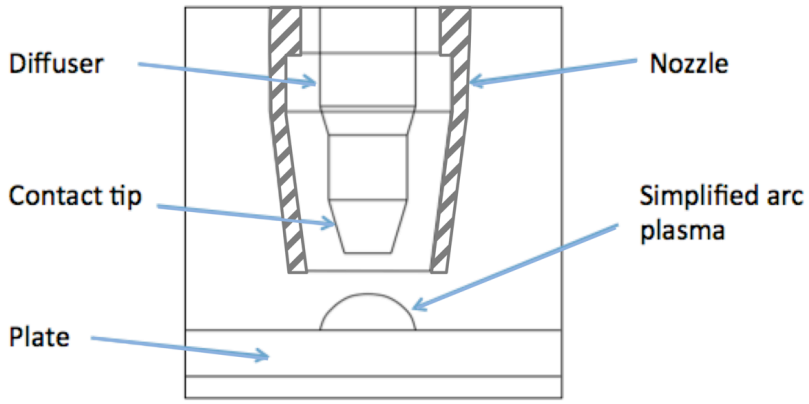

Figure 3.8: CFD model geometry showing simplified arc plasma assumption

This arc plasma simplification was justified by several studies conducted in the GTAW process, which showed that the shielding gas composition, welding current, arc length and electrode geometry were the dominant factors influencing the arc

pressure distribution [3.8, 3.9]; all of which are constants in the present study. Furthermore, it has also been reported that the shielding gas pressure has negligible effect on the arc pressure distribution [3.10]. As a result, this led to the assumption that the arc pressure distribution can be assumed constant from which various forces (e.g. arc force, arc shear stresses and Lorentz magnetic forces) can be numerically derived [3.11]. While it is acknowledged that this simplification of the arc plasma may be inadequate for the accurate modelling of certain weld aspects, for the case of shielding gas flow simulation it is shown to be sufficiently accurate through validation with shadowgraphy and radiographic examination of the solidified weld.

The mesh generated using Gambit was imported into the CFD solver, Fluent, where the physics of the model were defined. Heat transfer through the fluid and workpiece was analysed through a combination of convection and external radiation, according to the energy equation:

$$q = h_f\left(T_w - T_f\right) + q_{rad} = h_{ext}(T_{ext} - T_w) + \varepsilon_{ext}\sigma\left({T_\infty}^4 - {T_w}^4\right) \tag{3.1}$$

The gravitational acceleration components were input enabling buoyancy effects to be considered. The importance of buoyancy forces in a mixed convection flow can be measured by the ratio of the Grashof and Reynolds numbers, equation (3.2). Both are dimensionless parameters used in the correlation of heat and mass transfer due to thermally induced natural convection and forced convection, respectively, at a solid surface. The Grashof number represents the ratio of the buoyancy force due to special variation in fluid density to the restraining force due to the fluid viscosity, while the Reynolds number represents the ratio of the momentum to viscous shear force of the fluid.

$$\frac{Gr}{Re} = \frac{g\beta\Delta\mathrm{T}L}{\nu^2} \tag{3.2}$$

Thus, the ratio of the Grashof number to the Reynolds number gives an indication of the importance of natural and forced convection in determining heat transfer. Natural convection effects are dominant when Gr/Re >> 1, whereas forced convection dominates when Gr/Re << 1.

The k-epsilon turbulence model was used to simulate the flow regimes due to its good convergence rate and relatively low memory requirements. The k-epsilon model is the simplest of the two equation turbulence models, it is a semi-empirical model based on model transport equations and solves for two variables: k, the turbulent kinetic energy, and epsilon, the rate of dissipation of kinetic energy. The semi-empirical equations that govern the k-epsilon model are:

$$\frac{\partial}{\partial t}(\rho k) + \frac{\partial}{\partial x_i}(\rho k v_i) = \frac{\partial}{\partial x_j}\left[\left(\mu + \frac{\mu_t}{\sigma_k}\right)\frac{\partial k}{\partial x_j}\right] + G_k + G_b - \rho\varepsilon - Y_M + S_k \tag{3.3}$$

$$\frac{\partial}{\partial t}(\rho \varepsilon) + \frac{\partial}{\partial x_i}(\rho \varepsilon v_i) = \frac{\partial}{\partial x_j}\left[\left(\mu + \frac{\mu_t}{\sigma_\varepsilon}\right)\frac{\partial \varepsilon}{\partial x_j}\right] + C_{1\varepsilon}\frac{\varepsilon}{k}(G_k + C_{3\varepsilon}G_b) - C_{2\varepsilon}\rho\frac{\varepsilon^2}{k} + S_\varepsilon \tag{3.4}$$

The value of ε can be obtained from the turbulent viscosity ratio, μ_t/μ, and k using equation (3.5). The turbulent viscosity ratio is directly proportional to the turbulent Reynolds number, $Re_t \equiv k^2/(\varepsilon\nu)$.

$$\varepsilon = \rho C_\mu \frac{k}{\mu}\left(\frac{\mu_t}{\mu}\right)^{-1} \tag{3.5}$$

The cross draft of air was modelled as a 25 x 40 mm (height x width) inlet on the surface of the 3D domain, to replicate the experimental setup. As such, the cross draft was supplied at 60° to the weld bead in order for validation through shadowgraphy, and at 90°, i.e. perpendicular, to the weld bead for all other simulations. This generated a uniform, laminar airflow as this best correlated with the conditions produced during experimental validations, the velocity of which was measured in the region between the nozzle and workpiece surface.

The shielding gas was simulated to be argon / 20% carbon dioxide, as used in the experimental trials. This was achieved by selecting argon and carbon dioxide within Fluent's material database, specifying the ratio of the required gas and applying the rule of mixtures. The shielding gas was supplied through a mass flow inlet inside the welding nozzle, which allowed various shielding gas flow rates to be applied (5, 10, 15 and 18 l/min).

An interface boundary condition was defined on the surface between the hemisphere fluid and workpiece surface, hemisphere fluid and surrounding fluid, and the surrounding fluid to the workpiece. Thus enabling Fluent to compute across the boundary of each volume.

Following each solution iteration, the residual sum of each variable is computed, which will tend to zero as the solution converges. However, the residual sum will never reach zero but will reduce to a small value then remain constant. The convergence criteria for each residual of the simulation were set at $1e^{-5}$, when each residual reduces to within this criterion simultaneously, the solution is considered to have solved.

The temperature of the simplified arc plasma hemisphere was selected using an iterative approach to replicate the temperature distribution within an experimental workpiece, as determined through a combination of K-type thermocouples and thermographic imaging. The hemisphere temperature that provided the correct temperature distribution within the workpiece was 32,000 K.

3.3.2.3 Computational fluid dynamics model validation

In order to more fully validate the CFD model simulations, additional experimental trials were conducted for the end plate and internal plate restrictions. The experimental setup was identical to that of the shadowgraphy study with the exception of the flow device positioning. The flow device was positioned perpendicular to the weld bead, again at a distance of 300 mm as shown in Figure 3.9.

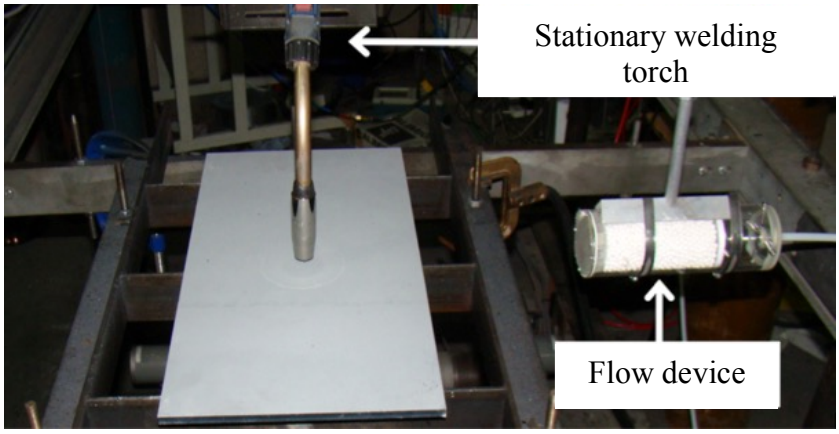

Figure 3.9: Experimental setup for CFD model validation

3.4 Results and discussion

3.4.1 Techno-economic evaluation

In order to assess the effects of reducing the shielding gas flow rate and determine the optimum shielding gas flow rate without detriment to weld quality, various aspects of each welding setup have been analysed.

3.4.1.1 Butt weld trials

Butt welds were performed to assess the effect that the shielding gas flow rate and controlling method (conventional flow meter or electromagnetic gas-saving device) have on the thermal transients during the heating-cooling cycle and the distortion present in the final structure.

The thermal data for each configuration during the heating-cooling cycle due to the welding process are shown in Figures 3.10-3.13.

It can be observed that the shielding gas flow rate and supply method considerably affect the peak temperature and thermal distribution within the workpiece. It was found that the peak temperature increases with reducing shielding gas flow rate; an increase of more than 100 °C was observed when the flow rate was reduced from 15 to 6 l/min. This increase in peak temperature with a reduction in shielding gas flow rate could be attributed to a reduced forced convection cooling effect due to less heat transfer away from the weld. The use of the electromagnetic gas-saving device has also resulted in approximately 30 °C increase in peak temperature when compared with a conventional flow meter at an equivalent gas flow rate. This may therefore give rise to other issues, in particular, a lower shielding gas flow rate could have a detrimental heating affect on the welding torch and nozzle, as the forced convection generated by the shielding gas is responsible for the cooling mechanism of each component.

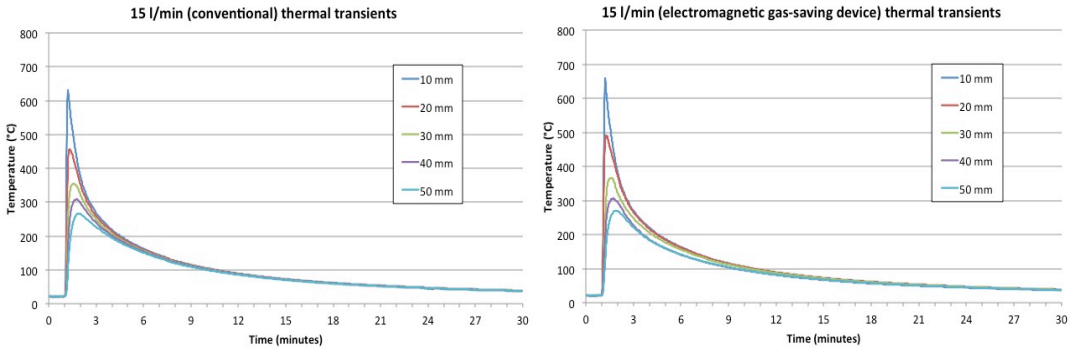

Figure 3.10: 15 l/min butt weld thermal transients

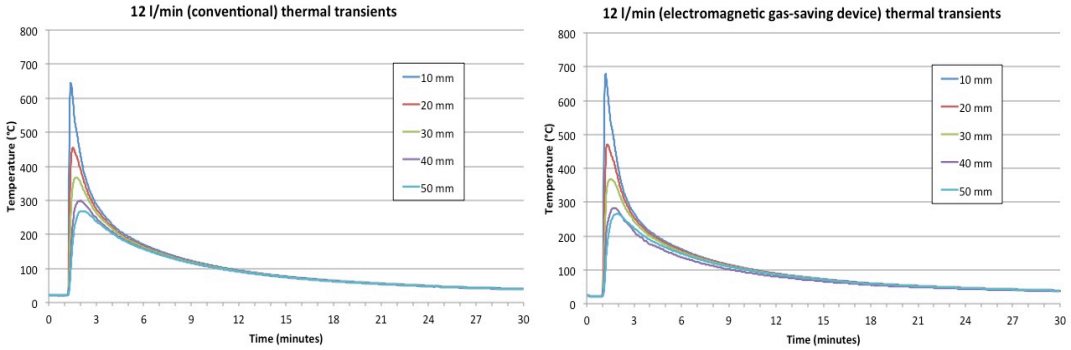

Figure 3.11: 12 l/min butt weld thermal transients

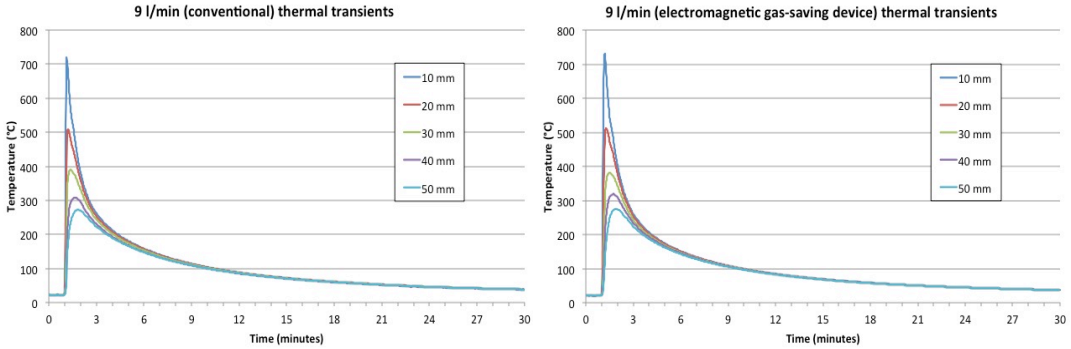

Figure 3.12: 9 l/min butt weld thermal transients

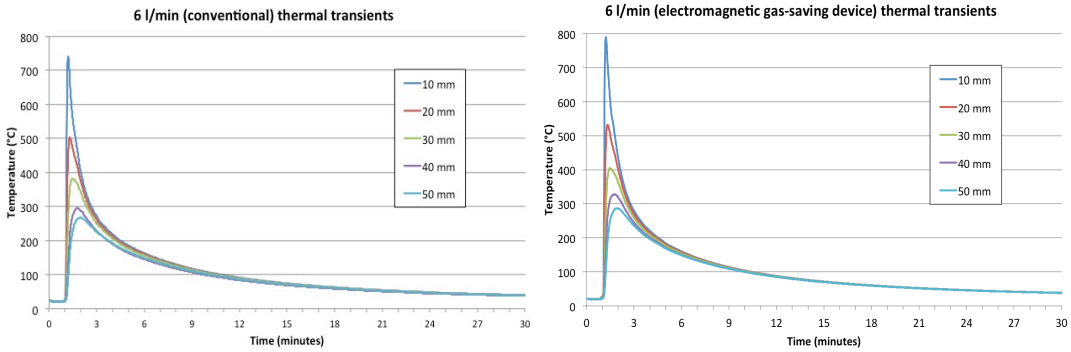

Figure 3.13: 6 l/min butt weld thermal transients

Table 3.4 details the peak temperature 10 mm from the weld centreline and the resultant temperature gradient between 10 mm and 50 mm from the weld centreline. The temperature gradient is higher for a lower shielding gas flow rate; this is primarily due to the increase in peak temperature.

Table 3.4: Butt weld thermal data

Shielding Gas Flow Rate (l/min)	Electromagnetic Gas Saving Device	Peak temperature (°C)	Temperature Gradient (10 – 50 mm) (°C/mm)
15	No	630	9.075
15	Yes	659	9.725
12	No	646	9.425
12	Yes	680	10.350
9	No	720	11.175
9	Yes	732	11.425
6	No	743	11.875
6	Yes	789	12.550

The highly localised transient heat source results in non-linear temperature fields, resulting in non-uniform expansion and contraction of the material due to the heating and cooling cycle. This introduces residual stresses into the structure, which, if they exceed the yield strength of the material, result in plastic deformation and consequently deformation in the final structure.

All welded plates distorted according to a classic saddle-like shape due to longitudinal and transverse out-of-plane distortion as illustrated in Figure 3.14. Longitudinal distortion, results in bowing of the welded structure, whereas transverse shrinkage, i.e. shrinkage perpendicular to the weld, results in angular distortion along the weld.

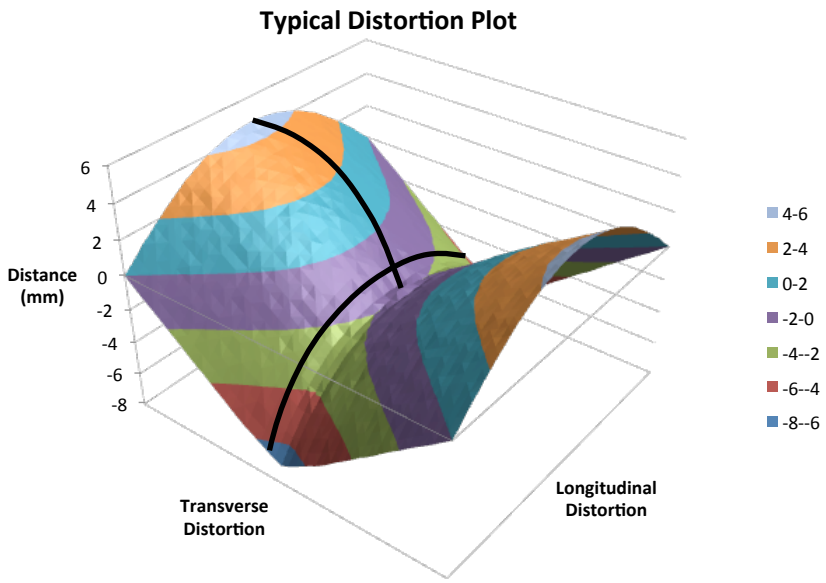

Figure 3.14: Typical distortion plot (not to scale)

The distortion plot for each shielding gas flow rate and supply method is shown in Figures 3.15-3.18. It can be observed that a lower shielding gas flow rate results in a greater level of distortion when compared to higher shielding gas flow rates.

A correlation can therefore be drawn between the peak temperature and thermal gradient, and the distortion in the butt-welded structure. As a consequence, this implies that the travel speed would need to be increased to obtain an equivalent level of distortion to the 15 l/min conventional structure. Such an increase in travel speed would also reduce the exposure time to the extreme temperature of the arc column and therefore bring the peak temperature and temperature gradient back into line with the 15 l/min case.

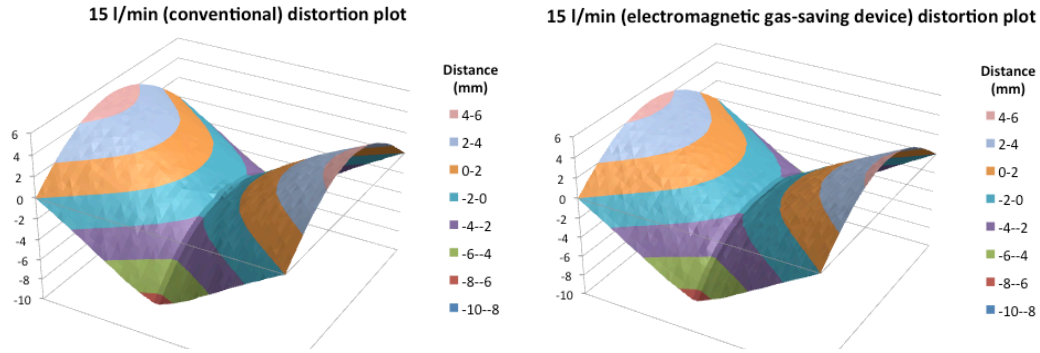

Figure 3.15: 15 l/min butt weld distortion plots

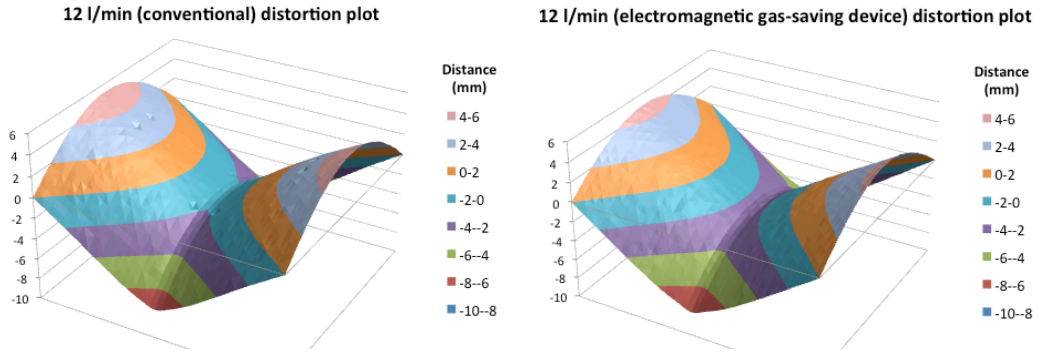

Figure 3.16: 12 l/min butt weld distortion plots

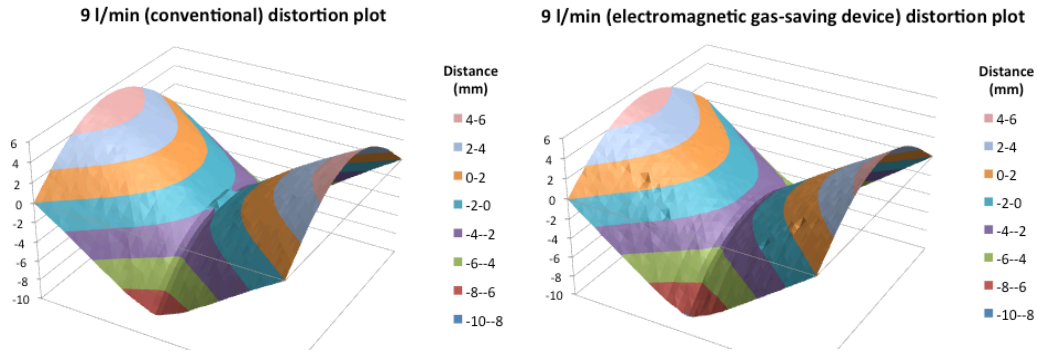

Figure 3.17: 9 l/min butt weld distortion plots

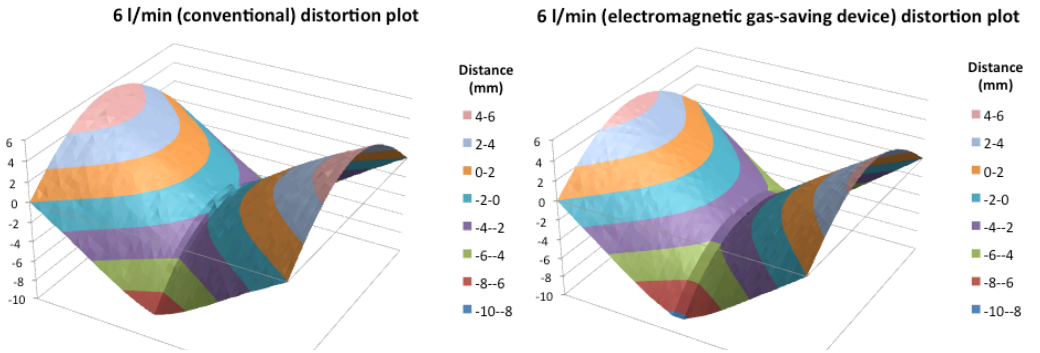

Figure 3.18: 6 l/min butt weld distortion plots

In order to accentuate the deformation of the workpiece, the distortion has been broken down into its transverse (angular) and longitudinal components. Transverse distortion data is presented at the mid-length of the workpiece, perpendicular to the weld bead, while longitudinal distortion data is parallel to the weld bead. The location for each is illustrated on Figure 3.14.

The transverse distortion, averaged for shielding gas flow rate, is shown in Figure 3.19. Although the centre line of the workpiece has moved downwards with respect to the four corner locating points due to angular distortion, in order to create a direct comparison between the distortion measurements, the mid-point of the workpiece has been taken as the zero reference.

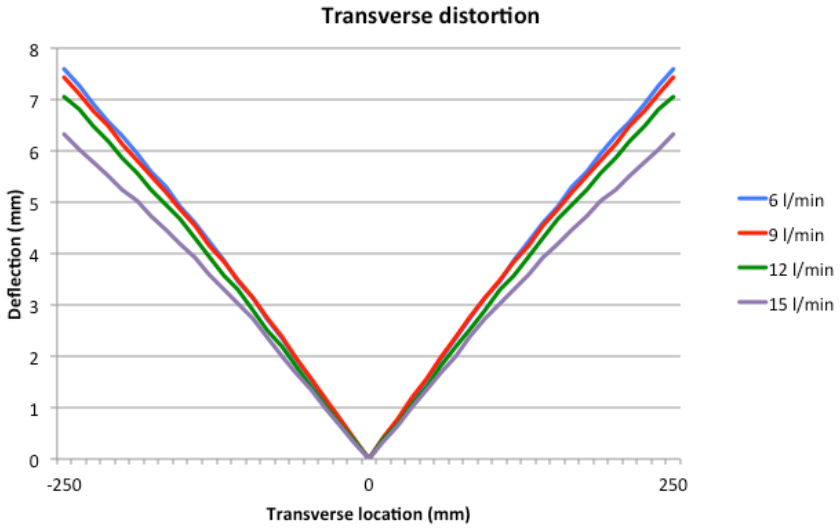

Figure 3.19: Transverse distortion (averaged for shielding gas flow rate)

As can be noted, a reduction in shielding gas flow rate results in an increase in angular deflection, an increase of 1.27 mm (20%) between the 6 l/min and 15 l/min cases. The average angle of deflection was measured to be 1.45° (15 l/min), 1.62° (12 l/min), 1.71° (9 l/min) and 1.74° (6 l/min).

Similarly, the transverse distortion, averaged for shielding gas supply method, is shown in Figure 3.20. It was found that using a conventional flow meter resulted in a lower degree of angular distortion when compared to the electromagnetic gas-saving device; the average angle of deflection for each method was measured to be 1.57° and 1.68° respectively.

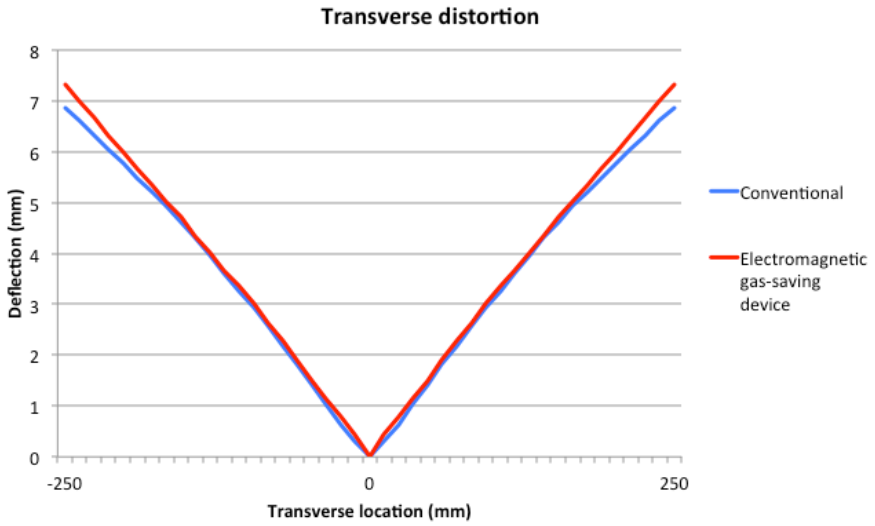

Figure 3.20: Transverse distortion (averaged for shielding gas supply method)

The longitudinal distortion, averaged for shielding gas flow rate, is shown in Figure 3.21. The centreline of the workpiece has moved downwards with respect to the four corner locating points due to angular distortion, consequently the entire longitudinal distortion plot is below the zero deformation line. It can be observed that the 15 l/min cases produced a lesser degree of longitudinal distortion than the 6 l/min cases, i.e. higher shielding gas flow rates produce distortions closer to the zero deformation line.

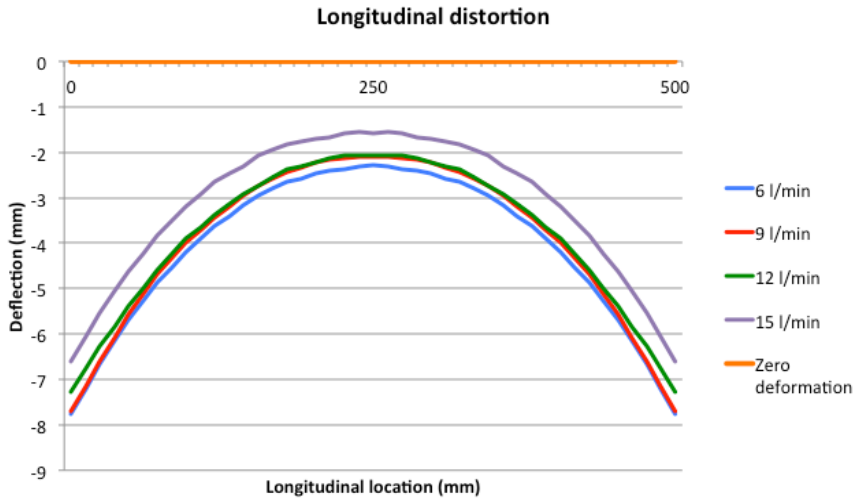

Figure 3.21: Longitudinal distortion (averaged for shielding gas flow rate)

Similarly, the longitudinal distortion, averaged for shielding gas supply method, is shown in Figure 3.22. As with transverse distortion, the longitudinal distortion plot has shown that a conventional flow meter results in a lower degree of distortion and consequently results in a flatter plate.

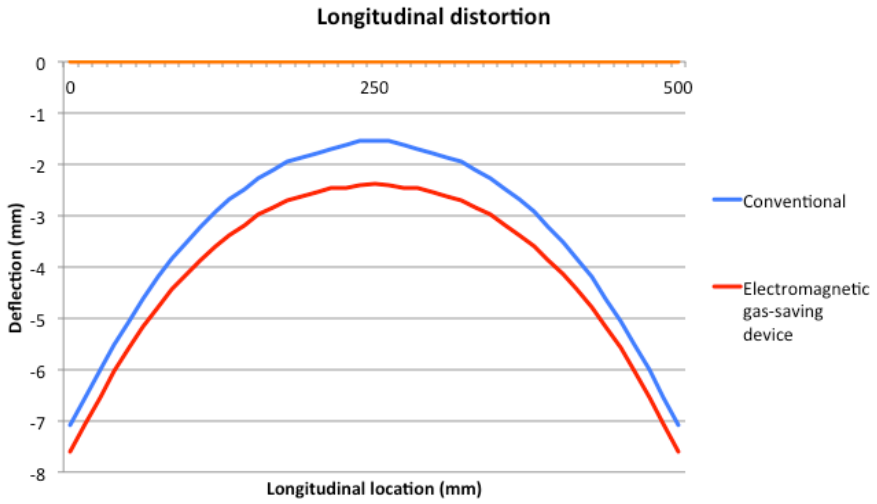

Figure 3.22: Longitudinal distortion (averaged for shielding gas supply method)

Therefore, it is implied that for lower shielding gas flow rates, and when using the electromagnetic gas-saving device, the travel speed may be increased to produce equivalent temperatures within the workpiece and comparable levels of deformation.

The potential shielding gas savings compared with a conventional flow meter manually set to a flow rate of 15 l/min is depicted in Figure 3.23. Savings of approximately 60% can be obtained by reducing the shielding gas flow rate to 6 l/min. The difference in gas consumption for welds produced with and without the electromagnetic gas-saving device is approximately 3–4%; the additional savings generated using the electromagnetic gas-saving device are attributed to the faster shut off of gas at weld termination.

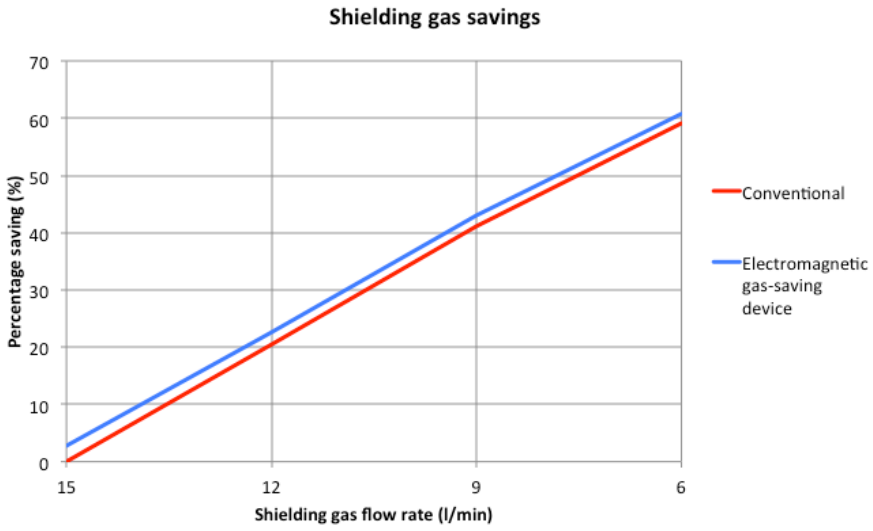

Figure 3.23: Butt weld shielding gas savings

3.4.1.2 Fillet weld trials

Fillet welds were performed in order to assess any effects the shielding gas flow rate and control method (conventional flow meter or electromagnetic gas-saving device) have on the weld quality and geometry. A metallographic analysis was performed on three transverse cross-sections from each set of weld parameters.

The defect percentage was determined through the analysis of numerous images from around the weld metal at locations indicated on Figure 3.24. Image analysis software (ImageJ) was used to determine the percentage of the image that exhibited a shade contrast to that of the bulk material, the contrasting areas are a combination of micro-porosity, metallic and non-metallic inclusions, therefore allowing the 'cleanliness' of the weld to be quantified. A weld micrograph is shown in Figure 3.25, which shows the typical 'clean' nature of the solidified weld.

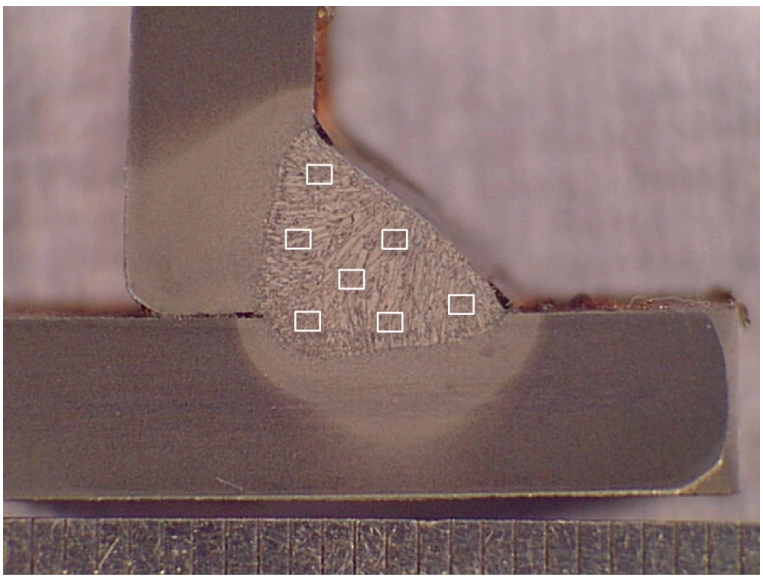

Figure 3.24: Weld macrograph showing approximate location of analysed micrographs

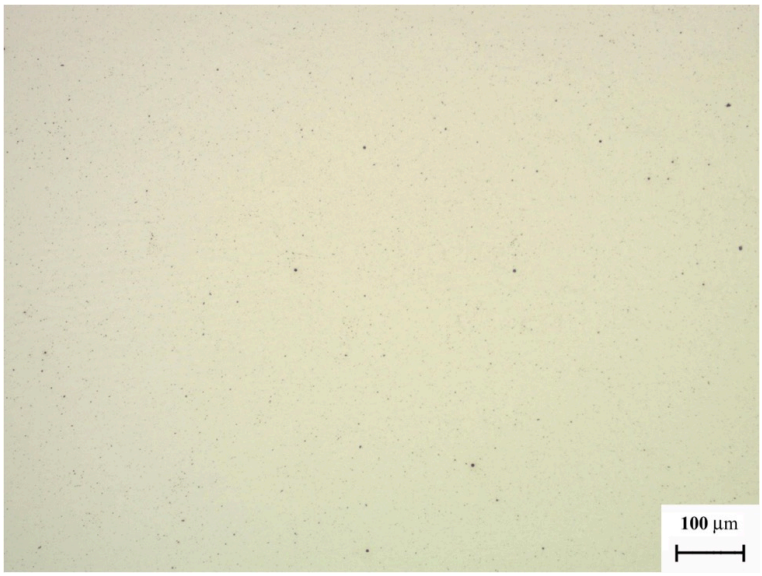

Figure 3.25: Weld micrograph (x100) showing typical defect level found throughout the weld pool

The defect percentage, as determined through image analysis, is depicted in Figure 3.26. It can be noted that all shielding gas flow rates trialled produced ‘clean’ welds, i.e. welds in which the defect levels present would not be detrimental to the overall weld integrity. These low levels of impurities can be attributed to the near-perfect

welding conditions in the absence of drafts and the fact that the upright of the fillet joint prevents the shielding gas drifting from the weld region. Shielding gas flow rates of 9 and 12 l/min have been shown to generate the lowest impurity percentage.

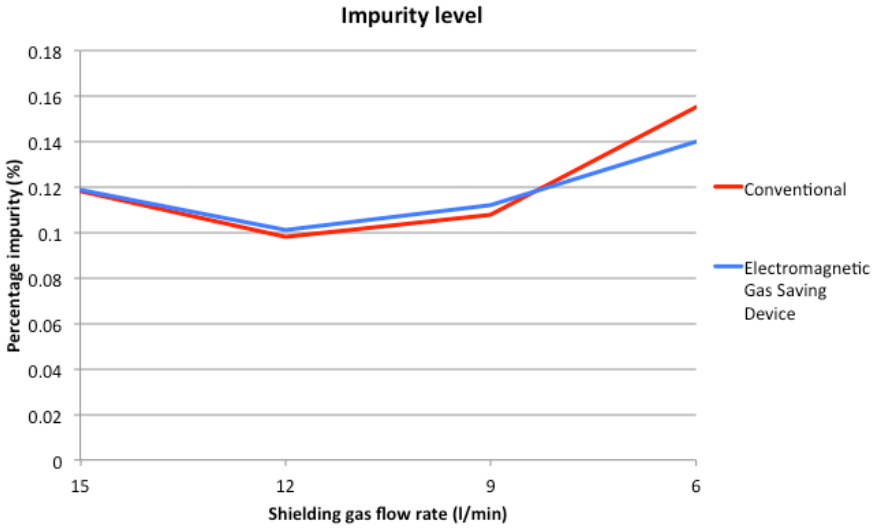

Figure 3.26: Weld metal impurity level

As stated in other publications [3.2, 3.3], excessive shielding gas flow can result in poor weld quality as a result of atmospheric gases being drawn into the shielding gas column. This was in relation to a surge of gas at weld initiation, reported to be up to 60 l/min. In addition, it was stated that the optimum shielding gas flow rate should not be greater than 12 times the filler wire diameter [3.2]. Therefore, the increase in porosity percentage above 12 l/min is in line with other published data and indicates the onset of turbulence in the shielding gas column. The extent to which the shielding gas flow rate can be reduced without adversely affecting weld quality has not previously been reported. Therefore, the increase in percentage impurity level at 6 l/min can be attributed to the beginning of a transition from good to incomplete coverage of the welding region.

Figure 3.27 indicates that the shielding gas flow rate has a marginal effect on the depth of penetration and leg length, again measured using image analysis software. An increase in both is found with a reduction in flow rate; a flow rate of 6 l/min has been shown to increase penetration and leg length by approximately 5 and 8%, respectively when using a convectional flow meter, and by 17 and 15% respectively

when using the electromagnetic gas saving device, when compared with the 15 l/min conventional base case. This is in agreement with a similar study [3.2], in which excessive shielding gas surge at weld initiation resulted in poor weld penetration; flow rates in excess of 30 and 50 l/min were reported depending upon the gas supply method. As can be noted, these flow rates are far higher than the maximum flow rate implemented in these trials (15 l/min), which has been shown to produce adequate penetration. Therefore, as a result of convective cooling, the shielding gas flow rate has the ability to influence how much heat is transmitted to the weld metal, the geometry measurements correlating with the thermal and distortion measurements reported in Section 3.4.1.1, therefore indicating that the welding travel speed could be increased while maintaining specific weld geometries when using lower shielding gas flow rates.

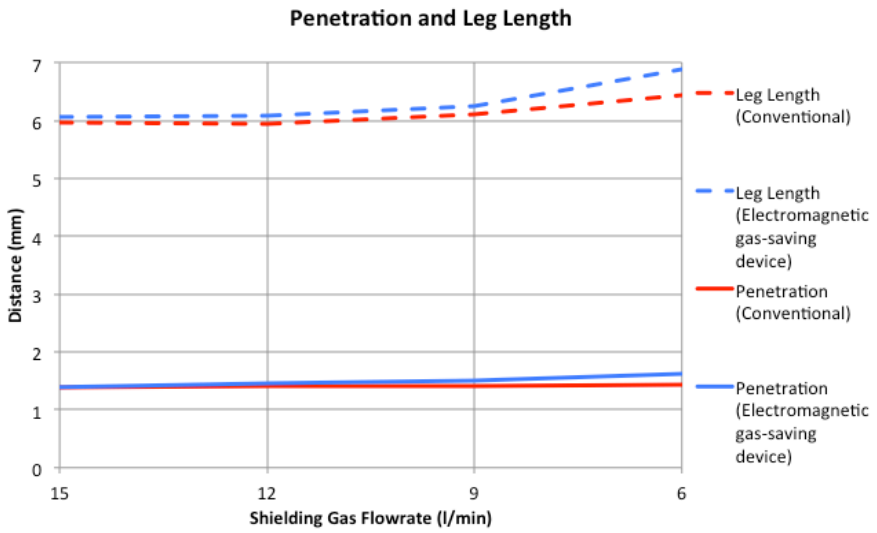

Figure 3.27: Fillet weld penetration and leg length dimensions

The electromagnetic gas-saving device has been shown to increase the level of penetration and leg length when compared with manually setting the gas flow rate with a conventional flow meter. The penetration has been increased by up to 11%, whilst leg length has been increased by between 2 and 6% when compared with using a conventional flow meter to control the gas flow rate; a comparison can be seen in Figure 3.28 and shows a visual difference in penetration. The depth of the heat affected zone (HAZ), as annotated ‘a’ on the images, in the base plate has increased by approximately 15% when using the electromagnetic gas-saving device.

In addition, the area of penetration, as annotated 'b' on the images, produced using a conventional flow meter was 13.3 mm^2, and increased to 15.0 mm^2 when implementing the electromagnetic gas-saving device. Again, this indicates that a further increase in travel speed could be permitted.

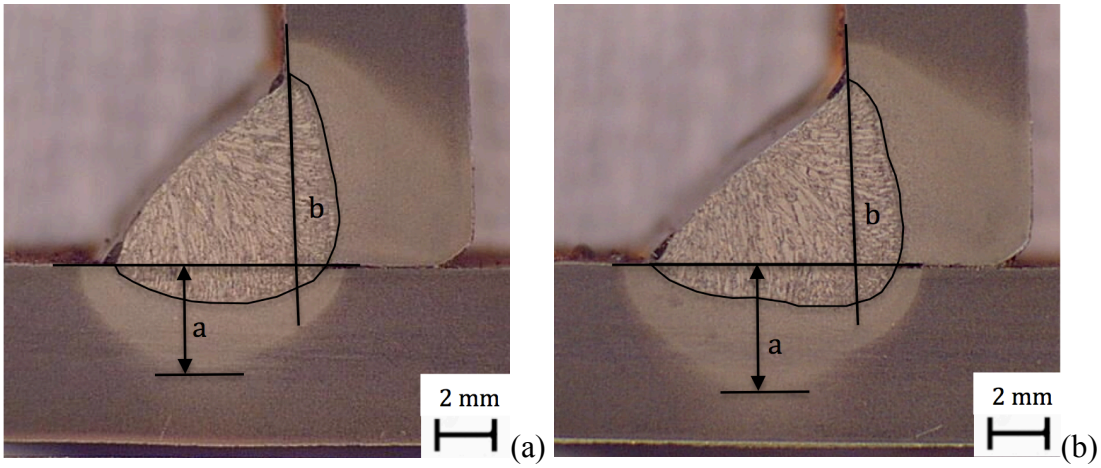

Figure 3.28: Weld geometry variation at 6 l/min using (a) a conventional flow meter and (b) an electromagnetic gas-saving device

Micro-hardness tests were performed on each sample using a 200 g weight and 10 s dwell time. Measurements were taken on two axes from the weld cap, vertically through the base plate and horizontally through the upright plate, in 1 mm increments to ensure local work hardening does not influence the determined hardness. In doing so, a direct comparison between shielding gas flow rate and also the effect of using an electromagnetic gas-saving device could be obtained.

The effect of the shielding gas flow rate is insignificant on the hardness of both the weld metal and heat affected zone (HAZ); the weld metal has a mean hardness of 209 Hv with a standard deviation of 5.44 (2.6%), whilst the HAZ has a mean hardness of 215 Hv with a standard deviation of 6.01 (2.8%).

The potential shielding gas savings, compared with a conventional flow meter, manually set to a flow rate of 15 l/min, is depicted in Figure 3.29. The analysis has shown that the weld quality has been maintained for shielding gas flow rates down to 6 l/min, which produced savings of approximately 54% using a conventional flow meter. In addition, the implementation of the electromagnetic gas-saving device has

been shown to further reduce the shielding gas consumption; savings of approximately 5–7% have been found when compared to a conventional flow meter. Again, the additional savings associated with the electromagnetic gas-saving device appears to be primarily linked to the quicker response of the valve resulting in less shielding gas being consumed at weld initiation and termination.

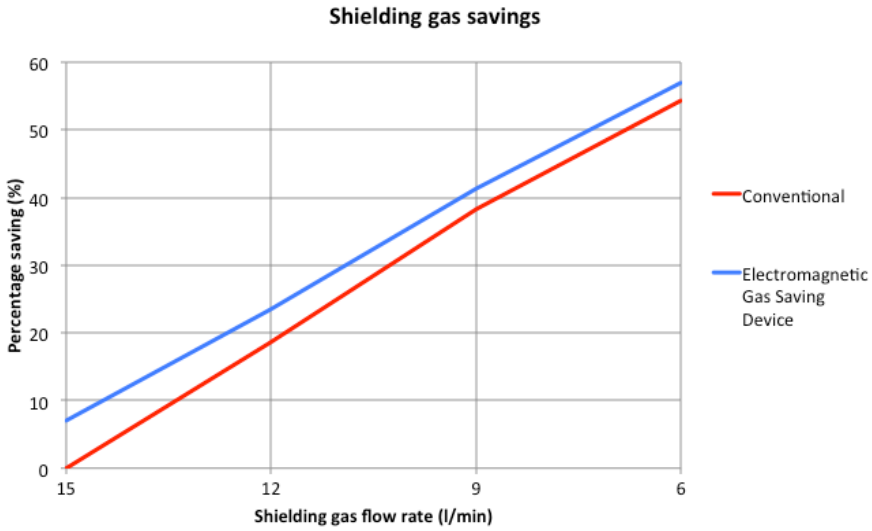

Figure 3.29: Fillet weld shielding gas savings

3.4.1.3 Stitch/tack weld trials

Bead-on-plate stitch/tack welds were performed in order to assess any effects the shielding gas flow rate and control method (conventional flow meter or electromagnetic gas-saving device) have on the weld quality and shielding gas consumption.

Radiographic examination was performed on each experimental weld due to its ability to detect discontinuities through the thickness of the weld. A grading system was developed to categorise the quality levels of the weld deposit; the system allowed clean welds, or those free from harmful imperfections to pass, whilst welds containing harmful defects would fail. The results of the radiographic examinations are shown in Table 3.5; with examples of pass and fail radiographic films are shown in Figure 3.30. As can be seen, all welds with a shielding gas flow rate of 9 l/min or greater produced defect-free welds, which would pass industrial testing. The 6 l/min

case failed both with and without the electromagnetic gas-saving device; this has been attributed to the 0.7 mph induced cross draft.

Table 3.5: Stitch/tack weld radiographic assessment

Shielding Gas Flow Rate (l/min)	Electromagnetic Gas Saving Device	Radiographic Assessment
15	No	Clear (Pass)
15	Yes	Clear (Pass)
12	No	Clear (Pass)
12	Yes	Clear (Pass)
9	No	Clear (Pass)
9	Yes	Clear (Pass)
6	No	Heavy porosity (Fail)
6	Yes	Heavy porosity (Fail)

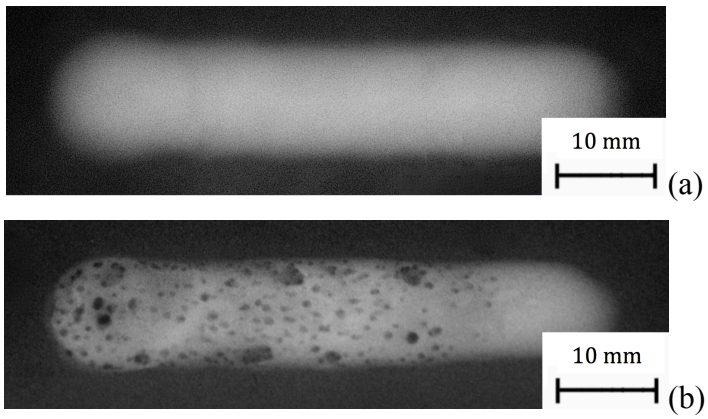

Figure 3.30: Typical radiographic film for (a) pass (9 l/min) and (b) fail (6 l/min)

The potential savings compared with a conventional flow meter manually set to a flow rate of 15 l/min is depicted in Figure 3.31. As a result of the extremely fast response of its internal valves, the electromagnetic gas-saving device has been shown to further reduce the shielding gas consumption; savings of approximately 20% have been found whilst maintaining a shielding gas flow rate of 15 l/min compared with the conventional flow meter supply.

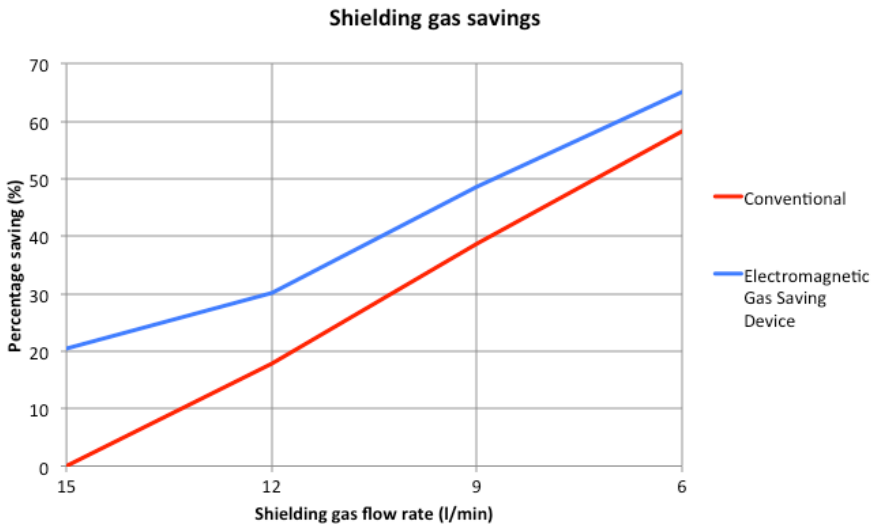

Figure 3.31: Stitch/tack weld shielding gas savings

Plots of current vs. time and shielding gas flow rate vs. time are shown in Figure 3.32. The period of time when the current falls to zero (Figure 3.32 (a)) correspond to the weld down-time between stitch welds and is a constant regardless of the shielding gas control method. The primary reason for the savings produced using the electromagnetic gas-saving device has again been linked to the more rapid response of the valve. Using a conventional flow meter (Figure 3.32 (b)), the shielding gas flow never completely degrades to zero between welds and therefore consumes unnecessary gas, i.e. whilst no welding is taking place. Conversely, with the electromagnetic gas-saving device installed (Figure 3.32 (c)), the rapid response of the valve meant that the unit was able to purge the line ready to start welding again before shutting off completely. The aforementioned mechanical anti-surge device was also subjected to the stitch weld trials, and, in this case, the performance was found to be equivalent to that of the conventional flow meter (Figure 3.32 (b)) in that the shielding gas does not shut off between welds.

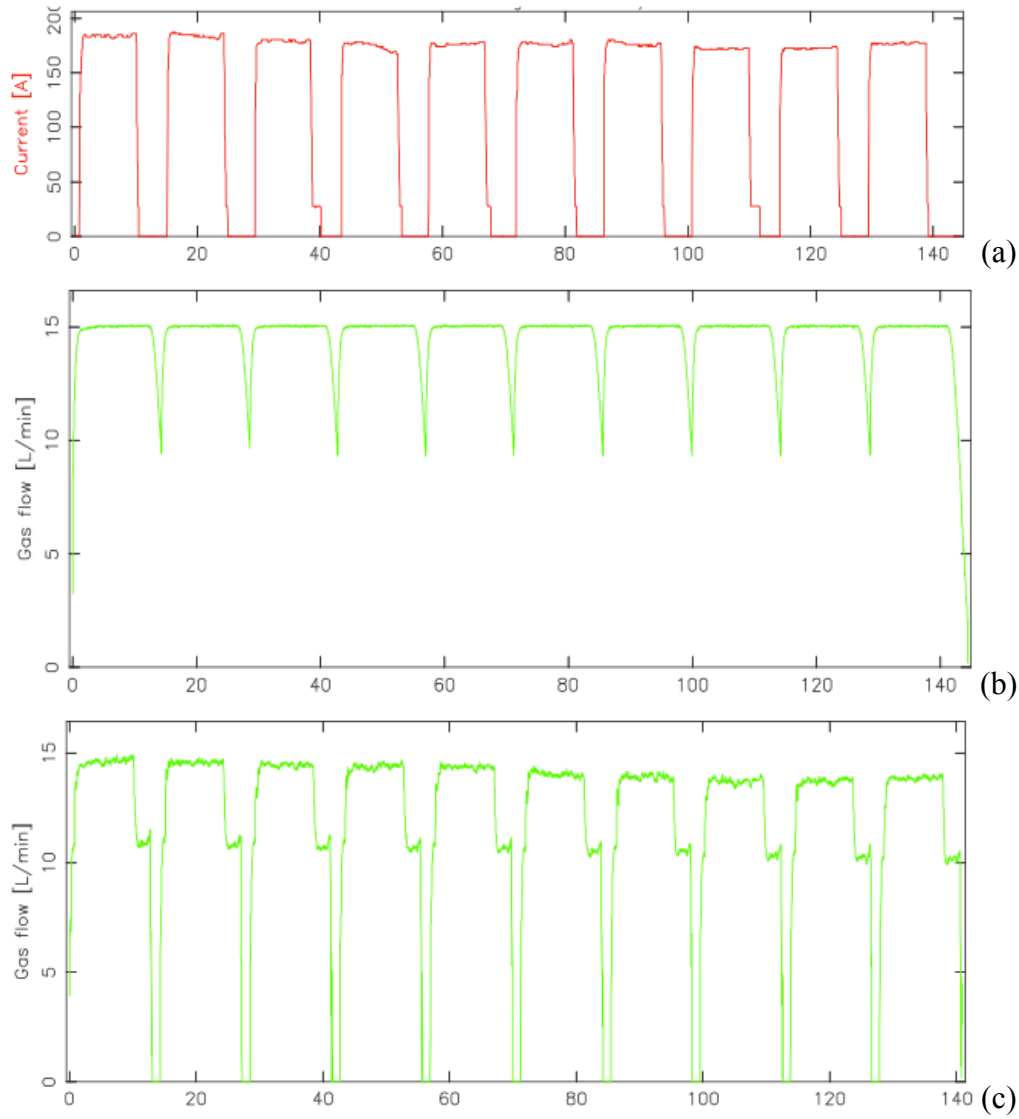

Figure 3.32: Welding monitor plots of (a) current vs. time, (b) shielding gas vs. time (conventional) and (c) shielding gas vs. time (electromagnetic gas-saving device)

3.4.2 Welding nozzle optimisation

In order to generate practical scenarios in which the shielding gas flow rate could be reduced whilst retaining weld quality, a systematic study was conducted in the form of bead-on-plate welds to investigate combinations of cross drafts velocities, shielding gas flow rates and welding nozzle design.

The cross draft speed was calibrated at 1, 3, 5 and 7 mph with the velocity of the flow being measured using a hot-wire anemometer at a height of 5 mm above a reference plate at 55 different locations around the welding nozzle.

The cross draft calibration plots are shown in Figure 3.33, with the flow passing from left to right. The edges of the flow are clearly visible and the flow speed drops to negligible values at approximately ±40 mm from the axis of the flow. The flow is uniform in the test region under the weld nozzle. Some disturbance in the flow due to the nozzle is apparent, but this occurs away from the weld region. For example, a 'buffer' region where the flow speed decreases slightly due to compression in front of the conical nozzle can be seen (particularly in Figure 3.33 (a) and (b)), and a slightly turbulent region past the weld area is apparent for higher cross-drafts speeds (for example Figure 3.33 (d)).

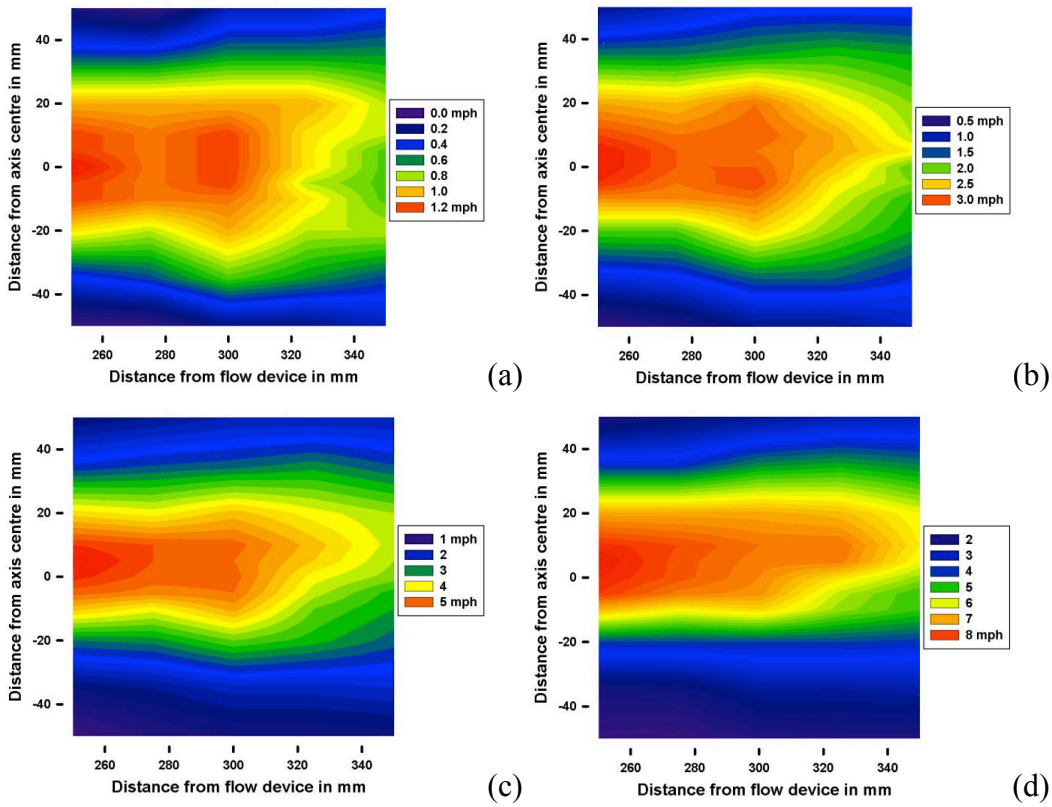

Figure 3.33: Cross draft validation measurements for (a) 1 mph, (b) 3 mph, (c) 5 mph and (d) 7 mph.

Radiographic assessment was used to evaluate the extent of defects at a position 60 mm from the start of the weld, to weld termination. A grading system, similar to that previously described, was developed according to the level of defects present: a clear weld free from harmful imperfections would produce a pass, whilst welds containing detrimental defect levels would fail.

3.4.2.1 Shadowgraphy

The shielding gas flow was visualised using shadowgraphy over the full range of shielding gas flow rates, cross draft speeds and circumferential nozzle restrictions. Measurements were conducted before welding, i.e. 'cold' measurements (shielding gas and cross drafts but with no welding arc), and during welding, i.e. 'hot' measurements. The measurements during welding were made on the same specimens that were subsequently radiographed.

Prior to all shadowgraphy measurements, a reference (or 'tare') image without any shielding gas flow was recorded. The tare image was subtracted from every measurement image in order to produce the absolute difference, and the result divided by the tare image, in order to normalise the Gaussian illumination intensity profile from the measurement images. Hence, changes in the recorded shadowgraphy intensity were proportional to the second spatial derivative of the refractive index. The image sequences obtained in this way were averaged to reveal time-invariant features in the flow, i.e. the flow profile.

For the hot measurements, the flow is more complex due to heating and spatter, and averaging the image sequence revealed fewer time-invariant features. Thus, a pixel-wise filtering approach was implemented to enhance the visibility of the shielding gas. The variation in intensity at each pixel through the time sequence gives an indication of the turbulence in the flow at that point. Hence, the intensity in the shadowgraph fluctuates with greater amplitude and frequency close to the weld (where the interaction of the cross draft and the hot weld gases produce fluctuations in the refractive index) than in regions well away from the weld region. One way to quantify this intensity fluctuation is to calculate the frequency content of the time-varying signal from a sequence of images at each pixel. A fast Fourier transform (FFT) was applied to the intensity signal at each pixel from a sequence of images, and filtered to eliminate low frequencies (0 to 252 Hz) and high-frequencies (1512 to 4500 Hz). This frequency range was chosen empirically to exclude the DC component (i.e. the flow profile) and tuned to turbulence in the shielding gas and the surrounding air. The area under the FFT magnitude in the remaining frequency band was calculated at each pixel, in order to produce a processed image indicating the turbulence at each pixel.

Radiographic analysis

The results of the radiographic assessment are shown in Figure 3.34, where green indicates a pass and red indicates a fail. For each nozzle outlet diameter, it is apparent that as the shielding gas flow rate increases the weld quality is less susceptible to cross drafts. In addition, it is also evident that a narrower welding nozzle outlet diameter is less susceptible to cross drafts than a larger nozzle.

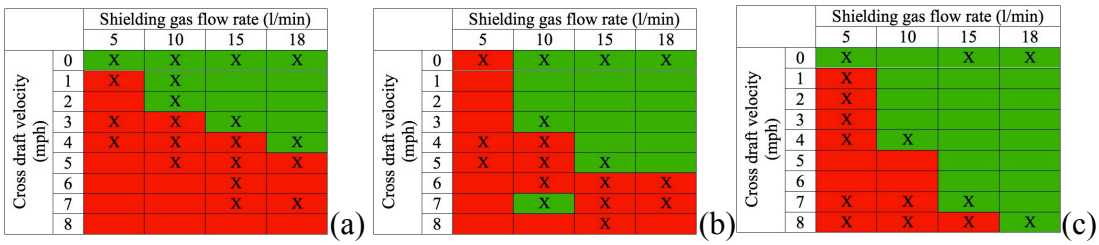

Figure 3.34: Experimental radiography and shadowgraphy measurements indicated by X, for (a) 16 mm nozzle, (b) 14 mm nozzle and (c) 11 mm nozzle. Table coloured according to radiographic assessment: pass = green and fail = red

Cold shadowgraphy measurements

The purpose of the cold measurements was to determine critical characteristics of the weld geometry that would allow a prediction of weld quality, without having to acquire weld data. Measurements were made in the same geometrical configuration as for the hot experiments but with no welding being performed, i.e. shielding gas and cross draft present but with no welding arc. In preliminary studies, no difference was observed in the results recorded for stationary or moving plate due to the slow speed of the plate in relation to the shielding gas flow, so results were recorded with the plate stationary.

Figure 3.35 shows a selection of intensity images, produced by the procedure described previously and averaged to reveal time invariant flow profile. The extent of the shielding gas, defined by two lines at the edge of the nozzle (i.e. turbulence), with a steady, laminar flow covering the weld region between them. For reduced nozzle internal diameters, the width of the shielding gas flow is reduced, and the edge turbulence increases due to the nozzle restriction. The cross draft, travelling from right to left, introduces turbulence to the weld region and deviates the shielding

gas flow away from the weld region. For reduced nozzle internal diameters, particularly 11 mm, less turbulence and deviation of the shielding gas are caused at a given cross draft speed.

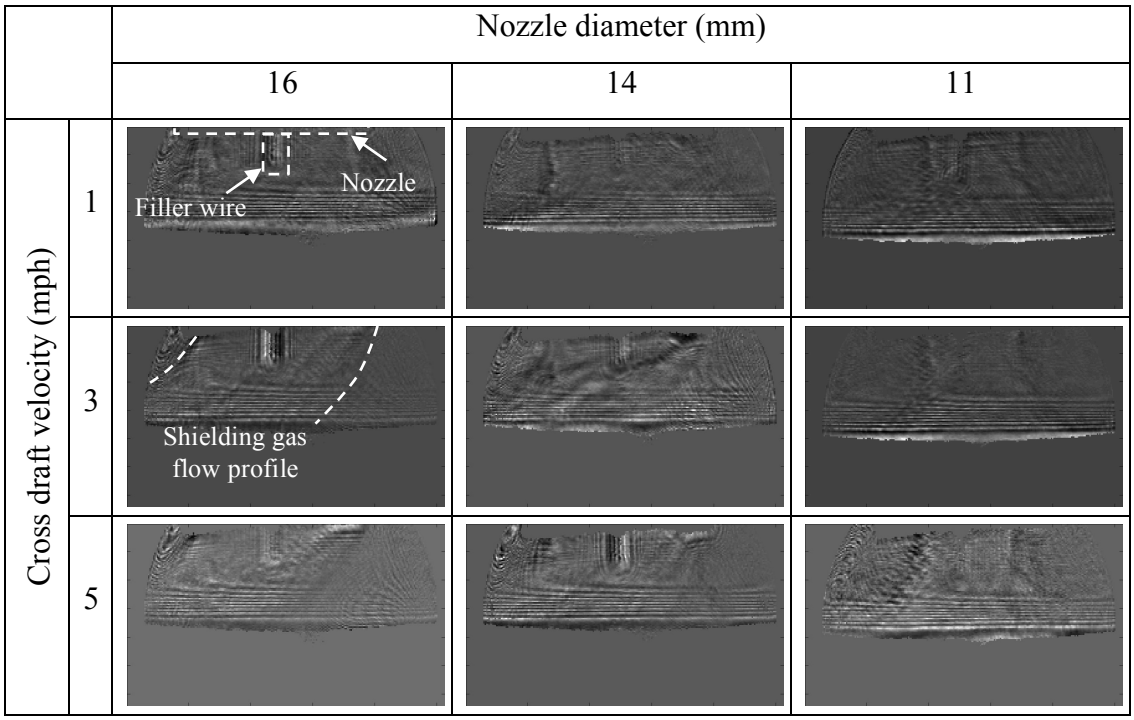

Figure 3.35: Selection of 'cold' shadowgraphy images showing average intensity

The small difference in refractive index between the shielding gas and the surrounding air at room temperature limits the visibility of shielding gas flow. Therefore, the cold measurement image sequences were also processed with the FFT technique to qualitatively show regions of turbulence (Figure 3.36). The shielding gas flow is revealed more clearly, and the position where the flow boundary impinges on the plate surface can be observed. This impingement position was determined from the largest gradient in the FFT signal along the plate surface. The impingement distance, i.e. the distance from the centre of the nozzle to the impingement position, gives a measure of shielding gas coverage in the presence of cross drafts. The measured impingement distances are shown in Figure 3.37 for the full range of tests, where positive values indicate points to the right of the nozzle centre. The table is shaded green for impingement distances >5 mm, and red for

smaller values, chosen empirically to obtain consistent agreement in the predicted weld quality with the radiography results.

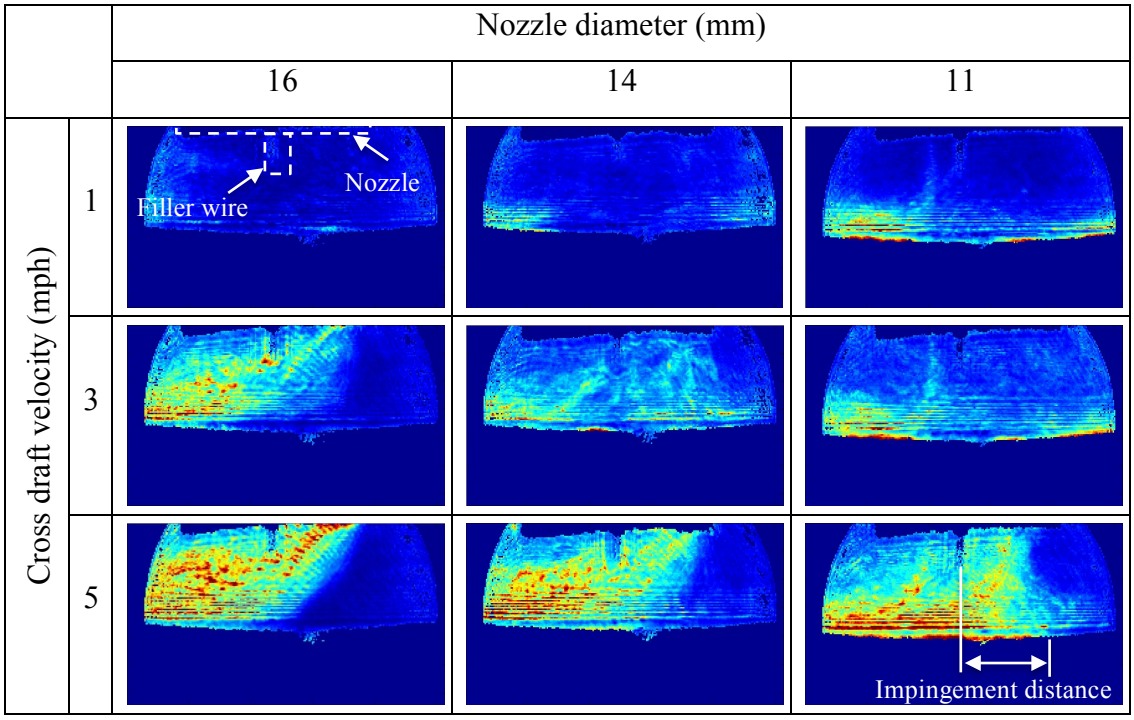

Figure 3.36: Selection 'cold' shadowgraphy images processed by FFT technique from blue (low turbulence) through to red (high turbulence)

Cross draft velocity (mph)	Shielding gas flow rate (l/min) 5	10	15	18
0	9	12	9	10
1	0	11		
2	-5	8		
3	-2	-2	9	9
4		-4	4	8
5			2	6
6			2	4
7	-5	-3	-2	3
8				

(a)

Cross draft velocity (mph)	Shielding gas flow rate (l/min) 5	10	15	18
0	11	13	8	6
1	5	10	7	8
2	1	9	6	6
3	-4	10	9	9
4	-5	4	7	7
5	-2	-2	7	8
6	-7	-1	5	6
7		-2	5	5
8			1	3

(b)

Cross draft velocity (mph)	Shielding gas flow rate (l/min) 5	10	15	18
0	8	7	7	7
1	4	7	7	7
2	0	7	7	7
3	0	7	7	7
4	1	6	7	7
5	-1	5	6	6
6	-4	0	5	5
7	-6	0	5	5
8	-8	0	2	5

(c)

Figure 3.37: Impingement distance measured from FFT images for (a) 16 mm nozzle, (b) 14 mm nozzle and (c) 11 mm nozzle. Table coloured according to impingement distance: >5 mm = green (acceptable) and ≤5 mm = red (not acceptable). Impingement distances in white font are discrepancies with respect to radiography assessment results.

Figure 3.38 shows the dimensionless ratio of cross draft to shielding gas velocity for the full range of tests. This is equivalent to the parameter suggested by Tamaki *et al*. [3.12], but the inverse ratio to avoid infinite values at zero cross draft. The table is shaded green for ratios <1.25, and red for larger values, chosen empirically to obtain consistent agreement in the predicted weld quality with the radiography results. The ratio of the cross draft to shielding gas velocity provides a simple prediction as to whether a weld will fail for the geometry tested.

Cross draft velocity (mph)	Shielding gas flow rate (l/min) 5	10	15	18
0	0.00	0.00	0.00	0.00
1	1.08	0.54	0.36	0.30
2	2.16	1.08	0.72	0.60
3	3.24	1.62	1.08	0.90
4	4.31	2.16	1.44	1.20
5	5.39	2.70	1.80	1.50
6	6.47	3.24	2.16	1.80
7	7.55	3.78	2.52	2.10
8	8.63	4.31	2.88	2.40

(a)

Cross draft velocity (mph)	Shielding gas flow rate (l/min) 5	10	15	18
0	0.00	0.00	0.00	0.00
1	0.83	0.41	0.28	0.23
2	1.65	0.83	0.55	0.46
3	2.48	1.24	0.83	0.69
4	3.30	1.65	1.10	0.92
5	4.13	2.06	1.38	1.15
6	4.95	2.48	1.65	1.38
7	5.78	2.89	1.93	1.61
8	6.61	3.30	2.20	1.84

(b)

Cross draft velocity (mph)	Shielding gas flow rate (l/min) 5	10	15	18
0	0.00	0.00	0.00	0.00
1	0.51	0.25	0.17	0.14
2	1.02	0.51	0.34	0.28
3	1.53	0.76	0.51	0.42
4	2.04	1.02	0.68	0.57
5	2.55	1.27	0.85	0.71
6	3.06	1.53	1.02	0.85
7	3.57	1.78	1.19	0.99
8	4.08	2.04	1.36	1.13

(c)

Figure 3.38: Cross draft to shielding gas velocity ratio for (a) 16 mm nozzle, (b) 14 mm nozzle and (c) 11 mm nozzle. Table coloured according to impingement distance: <1.25 mm = green (acceptable) and ≥1.25 mm = red (not acceptable).

Ratios in white font are discrepancies with respect to radiography assessment results. The cold measurements are summarised in Figure 3.39, which shows the ratio of cross draft to shielding gas velocity plotted against the impingement distance. The two criteria for a successful weld from Figures 3.37 and 3.38 are marked, namely impingement distance >5 mm and ratio of cross draft speed to shielding gas velocity of <1.25. The data points are coloured from the radiography measurements, showing no porosity (green) and unacceptable porosity present (red).

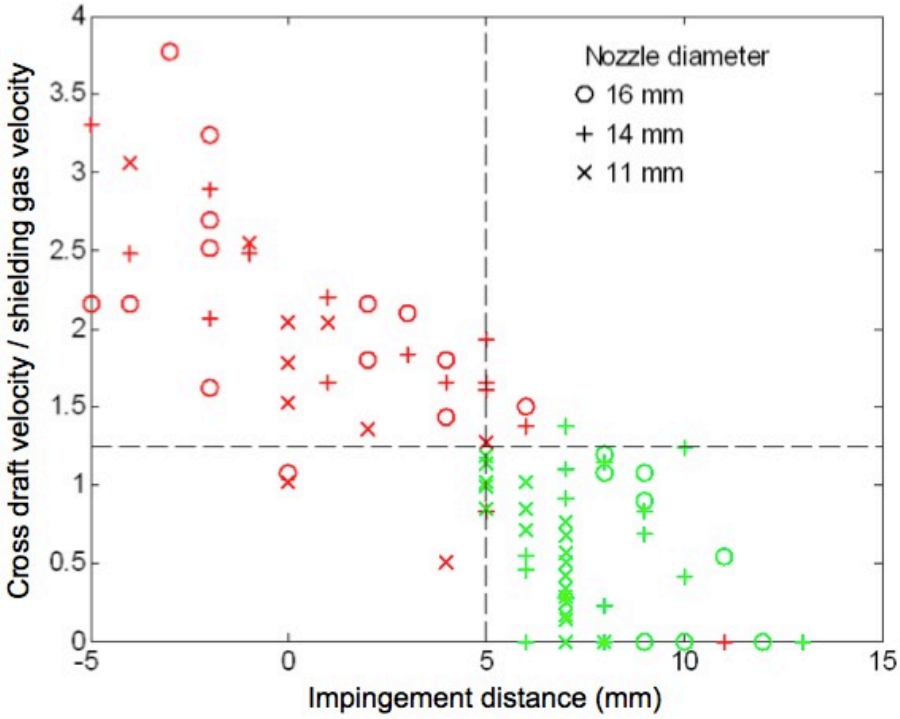

Figure 3.39: Comparison of impingement distance (Figure 3.37), cross draft to shielding gas velocity ratio (Figure 3.38) and radiographic assessment (Figure 3.34)

Hot shadowgraphy measurements

The shadowgraphy measurements were recorded from the same weld runs as the radiography results shown in Figure 3.34.

Figure 3.40 shows a selection of images produced by the pixel-wise FFT filtering to reveal regions of disturbance in the shielding gas and the surrounding air. These plots do not show as much detail as for the corresponding cold measurements due to the highly turbulent nature of the flow, particularly in the region of the weld bead. However, it can be seen that as the nozzle diameter decreases, the extent of flow reduces and the edge turbulence due to the nozzle restriction increases. The droplet transfer region is visible as a dark region, and the area above the weld pool shows a relatively low signal due to the more stable flow in that region.

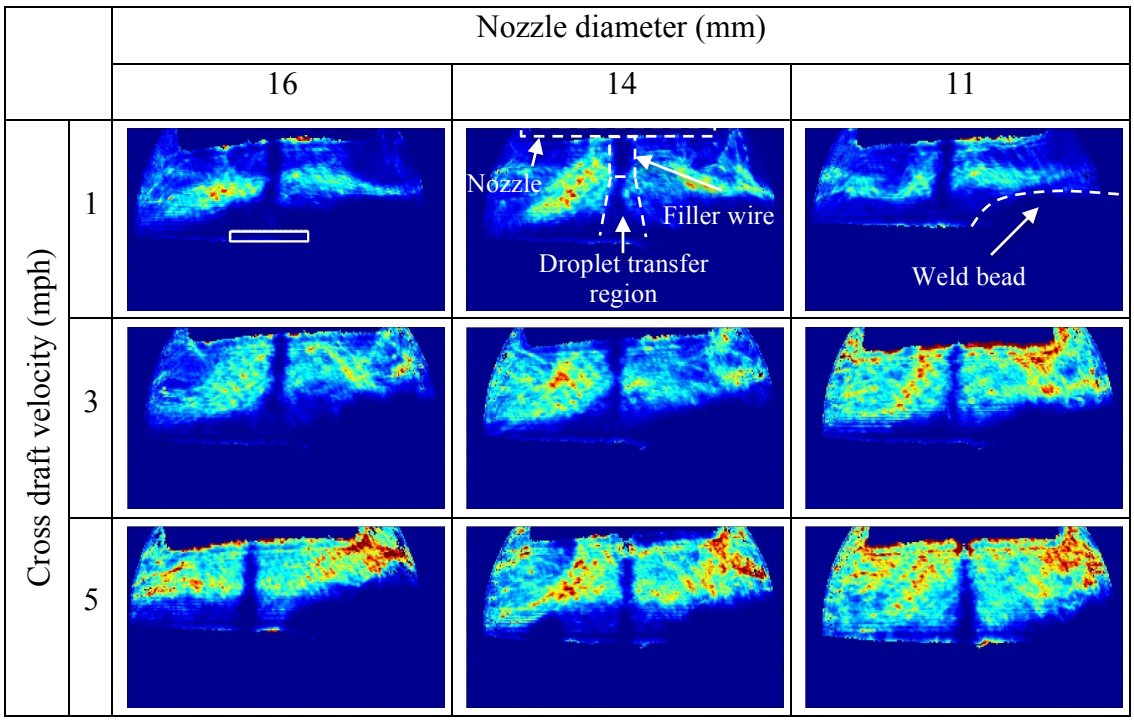

Figure 3.40: Selection 'hot' shadowgraphy images processed by FFT technique from blue (low turbulence) through to red (high turbulence)

It is proposed that the low FFT signal in the region of the weld indicates reduced disturbance to the shielding gas and therefore a reduced entrainment of air. Air entrainment into the shielding gas around the weld was estimated by summing the FFT magnitude at each pixel in a rectangular area 9.76 x 1.12 mm above the weld pool. The rectangular region is indicated in the first image of Figure 3.40. A lower signal qualitatively denotes lower turbulence and hence lower entrainment of air and so better resulting weld quality. The summed FFT values are shown in Figure 3.41 for the full range of tests. The table is shaded green for values <95 (in arbitrary units) and red for larger values, chosen empirically to obtain reasonable agreement in the predicted weld quality with the radiography results. Some discrepancies occur particularly for the 5 l/min shielding gas flow due to the general unpredictability and turbulence of the flow.

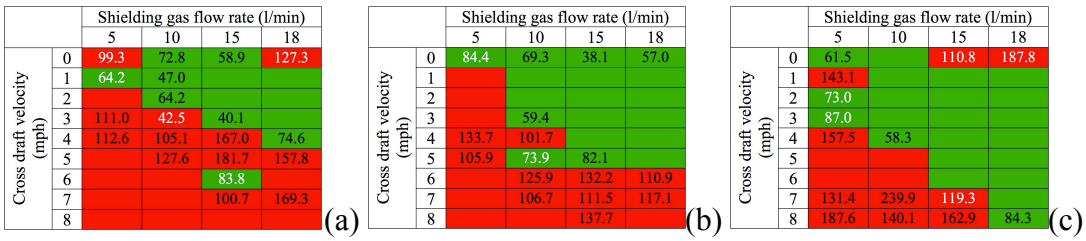

Cross draft velocity (mph)	Shielding gas flow rate (l/min) 5	10	15	18
0	99.3	72.8	58.9	127.3
1	64.2	47.0		
2		64.2		
3	111.0	42.5	40.1	
4	112.6	105.1	167.0	74.6
5		127.6	181.7	157.8
6			83.8	
7			100.7	169.3
8				

(a)

Cross draft velocity (mph)	Shielding gas flow rate (l/min) 5	10	15	18
0	84.4	69.3	38.1	57.0
1				
2				
3		59.4		
4	133.7	101.7		
5	105.9	73.9	82.1	
6		125.9	132.2	110.9
7		106.7	111.5	117.1
8			137.7	

(b)

Cross draft velocity (mph)	Shielding gas flow rate (l/min) 5	10	15	18
0	61.5		110.8	187.8
1	143.1			
2	73.0			
3	87.0			
4	157.5	58.3		
5				
6				
7	131.4	239.9	119.3	
8	187.6	140.1	162.9	84.3

(c)

Figure 3.41: FFT magnitude in the weld region (in arbitrary units). Table coloured according to FFT magnitude: <95 mm = green (acceptable) and 95 mm = red (not acceptable). FFT magnitude in white font are discrepancies with respect to radiography assessment results.

3.4.2.2 Computational fluid dynamics model simulations

Each of the models generated were subjected to the full range of experimental variables, i.e. shielding gas flow rate (5, 10, 15 and 18 l/min) and cross draft velocity (0 to 8 mph), resulting in 36 simulations for each nozzle configuration (conventional 16 mm nozzle, 14 and 11 mm circumferential restrictions, internal and external plate restrictions and a double helix nozzle insert). The flow profile in each case was analysed using contour plots of mass concentration of argon; since the shielding gas modelled was argon / 20% carbon dioxide, this meant that a contour of 80% argon was equal to 100% shielding gas coverage. A grading system for the flow profile was chosen based on the nominal weld width of 15 mm: profiles with 100% shield gas concentration on the plate surface to a distance of >8 mm on both sides of the weld/nozzle centreline would provide adequate shielding gas coverage and produce a good quality weld.

Figures 3.42 and 3.43 show a selection of shielding gas profiles generated by the CFD model. As expected, as the cross draft velocity increases, the shielding gas column drifts, removing the protection provided. An arrow on the images indicates the grading systems criterion.

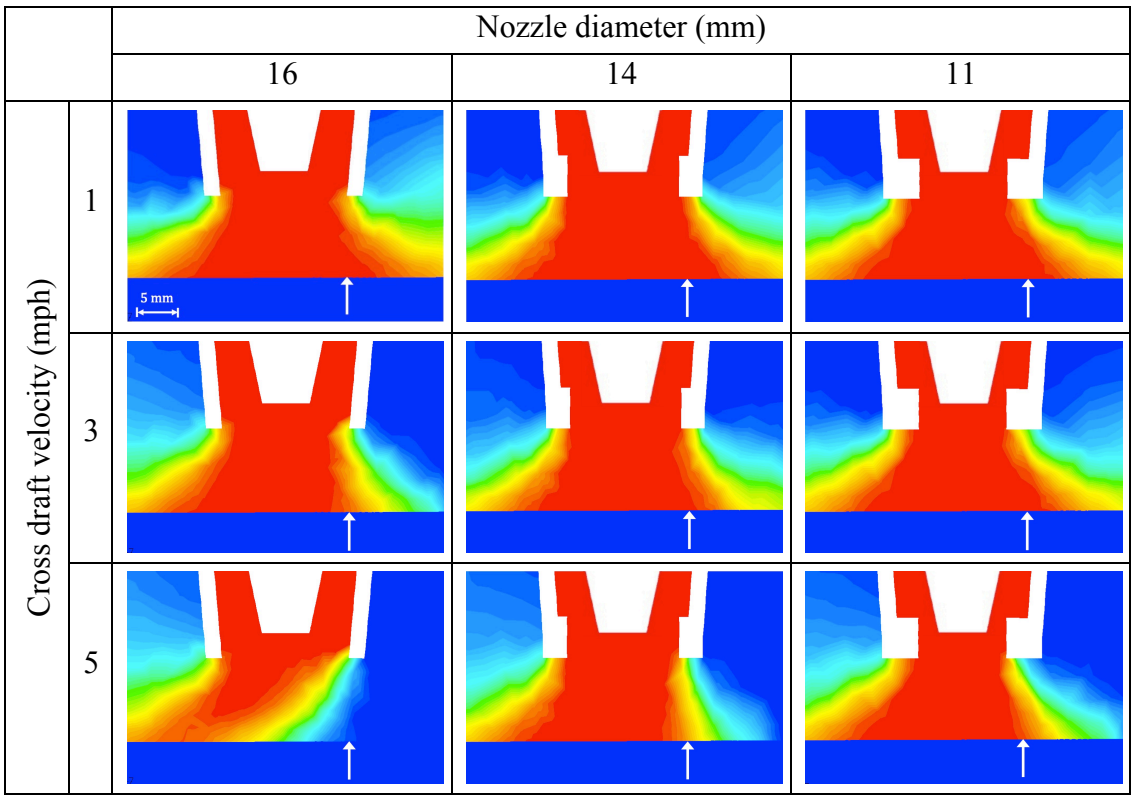

Figure 3.42: Selection of CFD results with shielding gas flow rate of 10 l/min

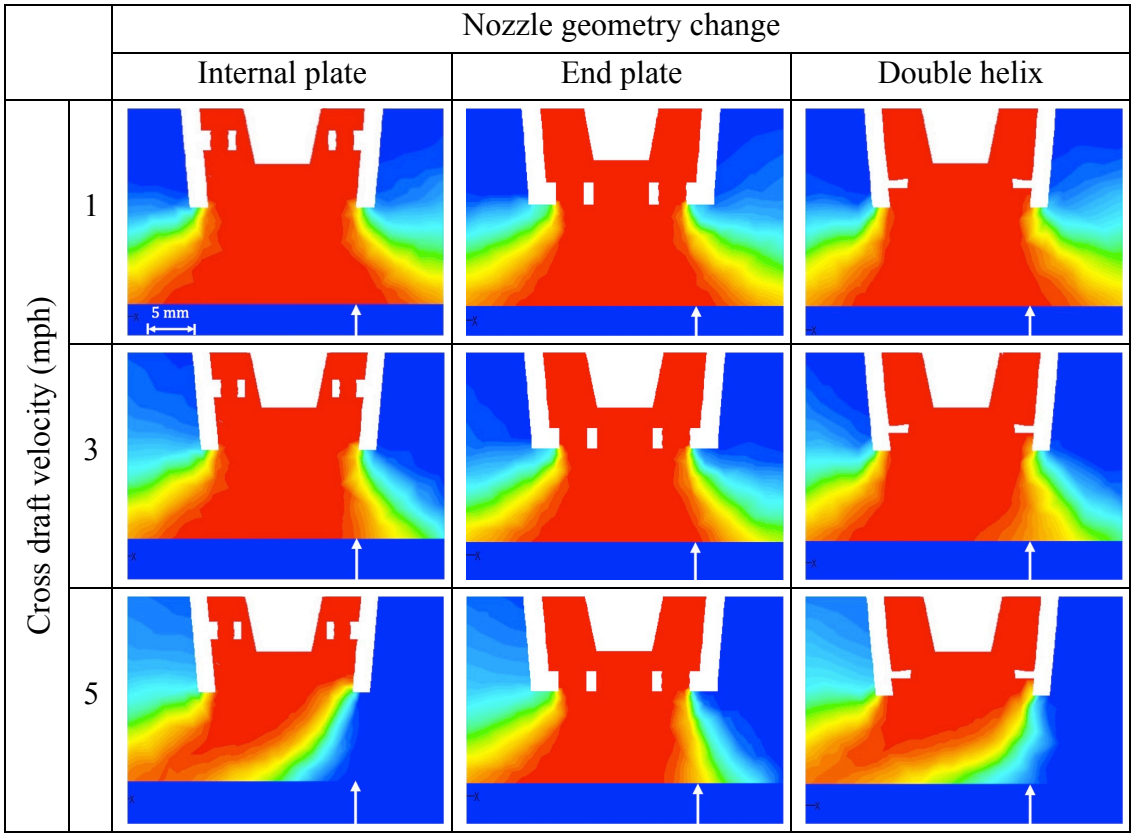

Figure 3.43: Selection of CFD results with shielding gas flow rate of 10 l/min

Figure 3.44 shows the weld classifications as obtained through the CFD approach. There are numerous publications simulating the electrical arc characteristics (detailed in Section 1.4), however the simplification of the arc to a constant temperature hemisphere is an assumption that has somewhat been overlooked. Although the model simplifications may limit accurate simulation of various arc phenomena, the good agreement between the CFD classification with the 'cold' shadowgraphy flow profile images, 'hot' shadowgraphy turbulence measurements and radiographic assessments suggests that reasonable accuracy can be obtained for modelling the effect of cross drafts on the shielding gas flow for constant weld parameters, without the need to over complicate the simulations.

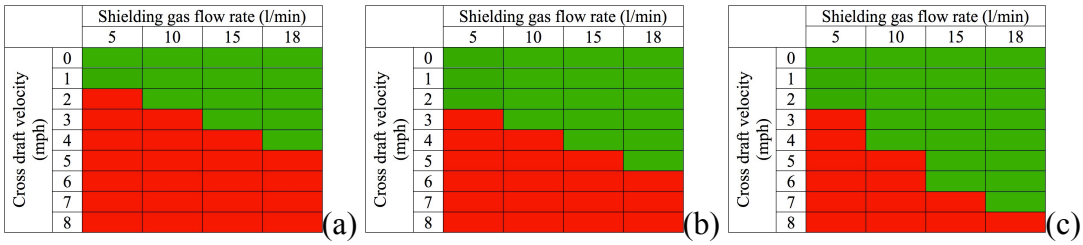

Figure 3.44: CFD classification of weld quality for (a) 16 mm nozzle, (b) 14 mm restricted nozzle, and (c) 11 mm restricted nozzle

From Figure 3.44, it can be observed that as the outlet diameter of the nozzle decreases, the shielding gas columns resistance to the adverse effects of the cross drafts increases. This can be explained due to conservation of mass, as the shielding gas is flowing through a narrower orifice, the velocity has to increase in order to maintain mass flow, as shown in Figure 3.45. The 16 mm nozzle generates shielding gas velocities of approximately 5-8 mph through its exit, while the 11 mm nozzle generates shielding gas velocities up to approximately 18 mph. In addition, as the gas flow rate was increased, the more resistance the shielding gas column had to cross drafts. Again, this is a result of an increased exit velocity.

The simulations found that for a 16 mm nozzle, with shielding gas flow rates of 15 l/min and 18 l/min, good quality welds can be achieved in the presence of drafts up to 3 and 4 mph respectively. The 14 mm nozzle followed a similar pattern and produced good quality welds for cross drafts up to 4 and 5 mph, for 15 and 18 l/min shielding gas flow rates respectively. As with the other diameters, higher shielding

gas velocities generated through the 11 mm nozzle produced greater resistance to cross drafts. 15 and 18 l/min flow rates managed to withstand cross drafts up to 6 and 7 mph respectively whilst producing good quality welds.

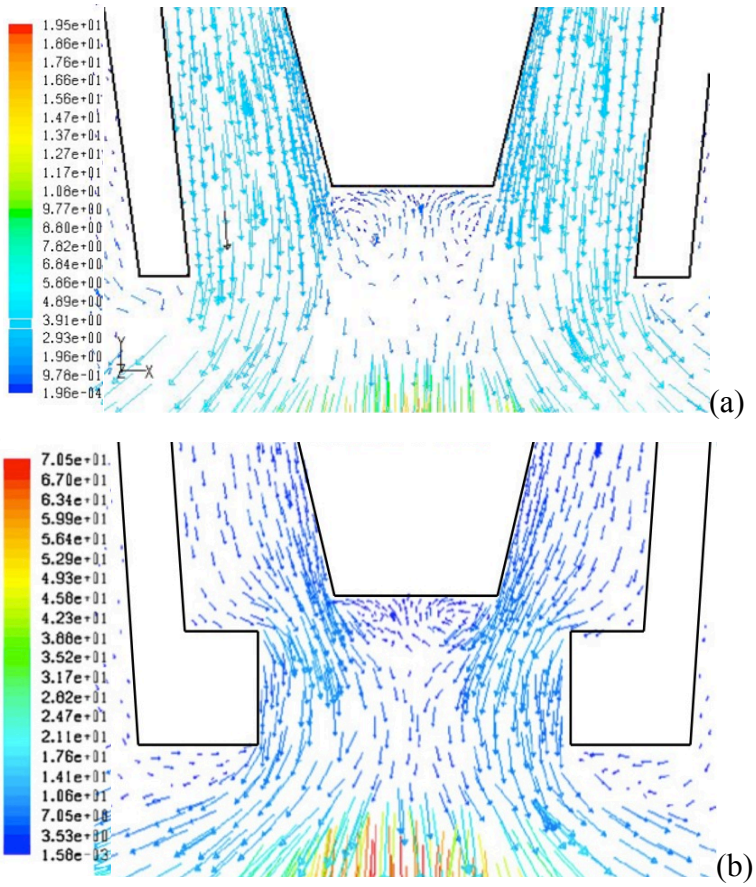

Figure 3.45: Velocity vector plot (m/s) of a 15 l/min shielding gas flow rate at nozzle exit for (a) 16 mm nozzle, and (b) 11 mm restricted nozzle.

Spatter build-up on the weld nozzle is unavoidable in practice, although it can be minimised by good control of the welding parameters. The progressive restriction of the nozzle by spatter can therefore be beneficial against the effect of cross drafts, provided the build-up is approximately uniform around the circumference of the nozzle and the overall flow is not excessively restricted.

The other geometry changes, i.e. the internal plate, end plate, and double helix modifications, did not show the same improvements to cross draft resistance as simply narrowing the nozzle exit diameter to 11 mm, Figure 3.46.

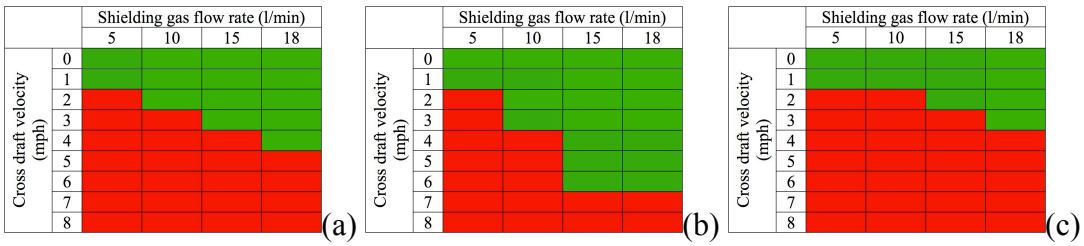

Figure 3.46: CFD classification of weld quality for (a) internal plate, (b) end plate, and (c) double helix, modifications

The end plate forces the shielding gas through a reduced cross-sectional area, thus increasing its velocity at the nozzle exit (~14 mph) as shown in Figure 3.47 (a), and as a result improved on the performance of the conventional 16 mm nozzle. However, as spatter build-up on the welding nozzle is unavoidable in practice, the 2 mm diameter holes in the end plate may be susceptible to blockage thus preventing shielding gas exiting the nozzle.

Although the internal plate increased the shielding gas velocity through the restriction (~22 mph) due to the cross-sectional area being decreased, causing the pressure to decrease and the shielding gas's velocity to increase (Figure 3.47 (b)). However, upon reaching the nozzle exit, the shielding gas had lost most of the momentum gained due to the internal restriction. The 6 mm from the inserted plate to the nozzle exit was sufficient to allow the shielding gas to expand out into the larger cross sectional area of the nozzle, reducing its exit velocity to approximately 9 mph.

The velocity vector plot for the double helix nozzle (Figure 3.47 (c)), showed that the velocities generated through the nozzle exit are approximately 13-16 mph, and considerably higher than the 5-8 mph generated by the 16 mm nozzle. However, from Figure 3.46, it can be observed that the double helix nozzle does not perform well. This has been attributed to a combination of effects: reversed flow in the central section, and a cyclone effect being generated within the nozzle as a result of the shielding gas being forced to revolve around the central welding tip. As can be seen in Figure 3.47 (c), the shielding gas flow is reversed in the central column (beneath the contact tip), with the gas flowing back towards the nozzle. The shielding gas continues to rotate as it leaves the nozzle creating a high velocity wall of rotating gas around a much lower velocity centre. This is demonstrated in Figure

3.48, which shows the velocity vectors of the shielding gas (from above) just before reaching the plate.

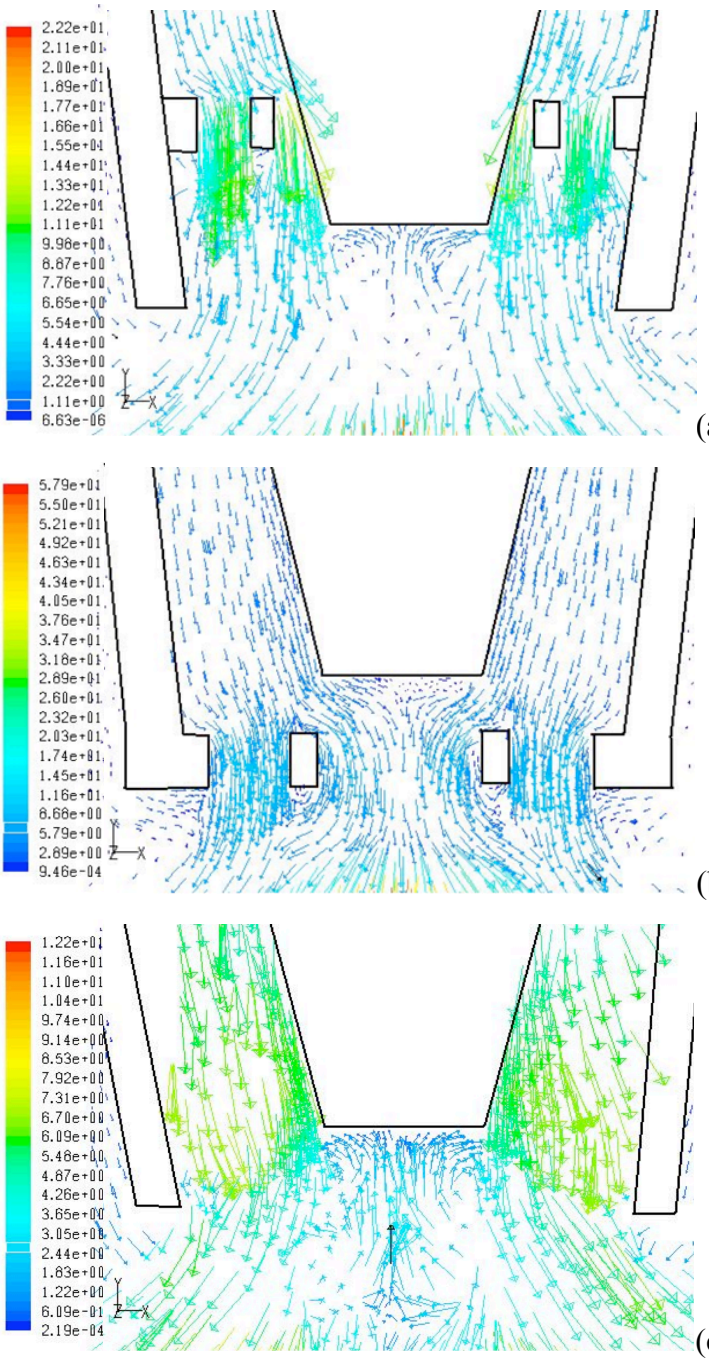

Figure 3.47: Velocity vector plot (m/s) of a 15 l/min shielding gas flow rate at nozzle exit for (a) internal plate, (b) end plate, and (c) double helix, modifications

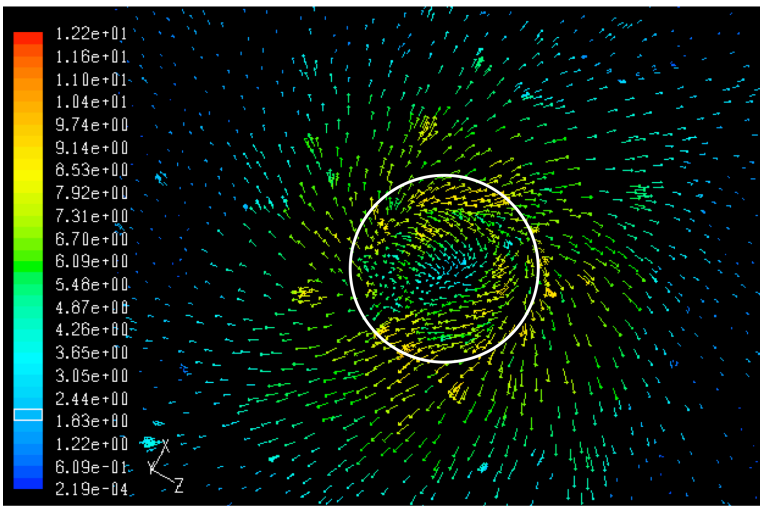

Figure 3.48: Velocity vector plot (m/s) of a 15 l/min shielding gas for a spiraled nozzle from above (showing 16 mm nozzle exit)

3.4.2.3 Computational fluid dynamics model validation

The experimental validation weld quality was evaluated using radiographic inspection, and graded according to the assessment criteria previously discussed. As stated, the double helix modification was omitted from validation trials due to manufacturing issues. However, considering the close correlation between the developed models and experimental trials that were performed, the assumption can be made that the results from the double helix nozzle model are accurate. The radiographic inspections results are shown in Figure 3.49.

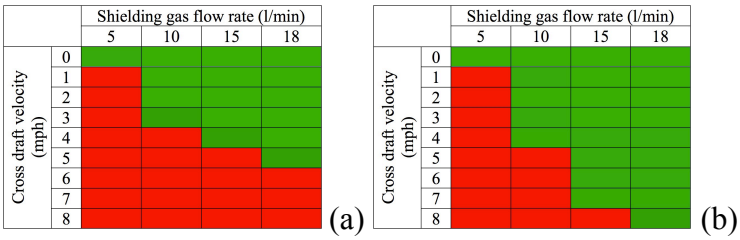

Figure 3.49: Experimental validation for (a) internal plate, and (b) end plate, modifications

The respective grading systems were found to produce an agreement in the order of 90% of the cases, which includes experimental errors, such as a fail for the 14 mm nozzle for a shielding gas flow rate of 5 l/min with no cross draft, and a pass for the

14 mm nozzle for a shielding gas flow rate of 10 l/min and a 7 mph cross draft, decreasing this percentage. Based on the surrounding results, logic would dictate that these should both be the opposite of the radiographic examination and therefore in agreement with the CFD classification.

3.5 Conclusions

Experimental trials have shown that the shielding gas flow rate can be effectively reduced, in a draft-free environment, to 6 l/min resulting in approximately 60% savings in gas cost in comparison to the 15 l/min base case, and without detriment to quality. This is in agreement with several studies that implemented gas-saving devices and reported gas savings in the region of 60% [3.4-3.7], and an optimum shielding gas flow rate of 12 times the filler wire diameter [3.2].

Furthermore, it was found that the electromagnetic gas-saving device produced additional savings when compared with a conventional flow meter; this has primarily been linked to the rapid response of the electromagnetic valve. The shielding gas consumption at weld initiation and termination due to the valve response is a constant regardless of the weld length, and consequently, the greatest percentage savings are produced over shorter weld lengths, i.e. stitch welds, where shielding gas consumption can be reduced by 20% without reducing the gas flow rate. Concurrently, as the weld length increases, the shielding gas used at weld initiation and termination has a diminishing percentage effect on the overall savings.

In addition to the savings produced by reducing the gas flow rate, a lower flow rate has been shown to increase penetration, which compounded with the increased distortion, and peak temperature indicating that there is greater convective heat transfer away from the weld for a higher shielding gas flow rate. Too high a shielding gas flow rate has previously been reported to result in poor penetration [3.2], which combined with the present results, would suggest that for lower shielding gas flow rates, the welding travel speed could be increased whilst producing equivalent levels of penetration. The use of the electromagnetic gas-saving device has shown a further increase in penetration and could therefore promote faster still travel speeds.

Although techniques have previously been used to visualise the shielding gas flow in arc welding (Chapter 1), this is the first instance of shadowgraphy images being analysed quantitatively and correlated with radiographic measurements to determine the weld quality.

In agreement with the experimental validation trials, shadowgraphy shielding gas visualisation and CFD simulations have shown that there is considerable scope to reduce the shielding gas flow rate compared to that conventionally used in industry, in the presence of cross drafts, and without detriment to the final weld quality. As the shielding gas flow rate is increased and/or the nozzle diameter decreased, the weld quality is more resilient to the adverse effects of a cross draft due to the increased exit velocity. Hence, the design of the welding process requires the selection of a minimum shielding gas flow rate for the expected maximum cross draft.

Shadowgraphy was applied successfully to GMAW to measure shielding gas flow profiles and regions of turbulence, and a quantitative analysis of the images for welding was performed. Measurements without the welding arc (cold measurements) showed that the impingement distance of the shielding gas flow, and the cross draft to shielding gas velocity ratio provide reliable indicators of the effect of cross drafts on the weld quality before welding. A pixel-wise Fourier analysis of the intensity fluctuation with time of a sequence of shadowgraphy images was proposed as a qualitative measure of turbulence in the flow, enabling prediction of weld quality from shadowgraphy during the welding process.

A simplified CFD model has been developed to determine the effects that geometry changes in the welding nozzle, and cross drafts have on the shielding gas flow coverage during GMAW. An economic benefit to industry of modifying the nozzle geometry has been identified allowing for a lower shielding gas flow rate to be implemented whilst maintaining cross draft resistance.

It was shown that the simplified computational model and experimental trials correlate closely through the use of their respective grading systems and indicated that the arc plasma simplification is sufficient in predicting the shielding gas flow profile. The results show that good shielding gas coverage, as determined in the CFD

model, translated into a good quality weld determined by radiographic inspection of the experimental trials.

In agreement with the experimental validation, a reduction in nozzle diameter (Figure 3.5) was found to increase the shielding gas columns resistance to cross drafts, primarily due to conservation of mass. Although the end plate nozzle modification produced good cross draft resistance, in practice the 2 mm diameter outlets may be susceptible to blockage by spatter, thus preventing shielding gas exiting the nozzle.

This series of work has shown the minimum shielding gas flow rate necessary for acceptable weld quality in the presence of cross drafts, which is being applied on a practical basis. In a typical shipyard, BAE Systems Naval Ships were using an average gas flow of 24–26 l/min for the 16 mm weld nozzle tested in this study, against the process norm of 18 l/min. The shadowgraphy results established that there was no loss of shielding gas coverage, and hence no degradation in the weld quality, at shielding gas flow rates of 10 l/min and above for the worst draft conditions measured in a typical shipyard fabrication hall.

Shielding gas flow controllers, preset at 12 l/min have been fitted at BAE Systems Govan shipyard (Figure 3.50), removing the welding operatives capability to increase the shielding gas flow rate. These changes were initially introduced in a workplace area where a high number of radiographs are taken, and then extended into a steel workshop and the pipe shop. To date, no defects have been found, and the next areas to be targeted are a panel line and a subassembly manufacture area. The 50% reduction in shielding gas consumption (compared to previous actual usage) will yield a predicted cost saving of approximately £300k per annum. The carbon footprint of the welding process is improved directly through reduced CO_2 useage, plus reduced energy is required for production and supply of the shielding gas. Rollout to other shipyards is planned.

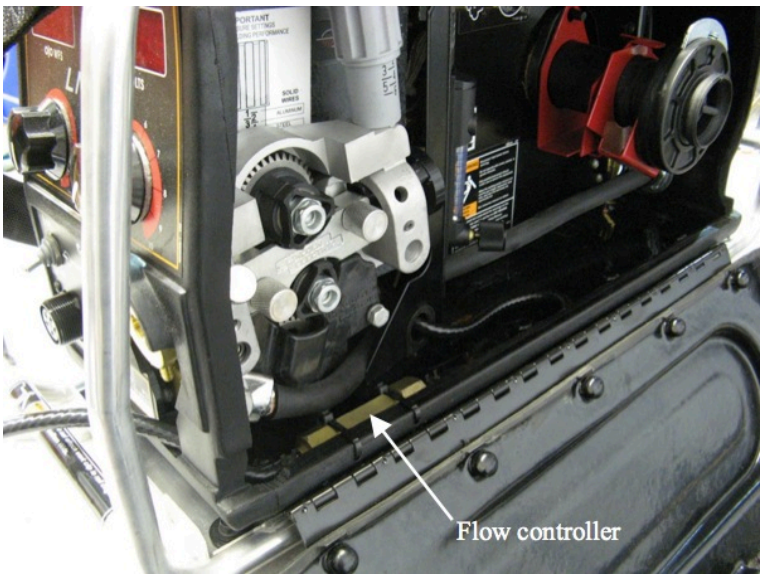

Figure 3.50: Shielding gas flow controller installed in wire feed unit

A further reduction to 10 l/min is possible, and a reduced nozzle diameter could be introduced as a result of this study. Spatter build-up on an 11 mm diameter nozzle may be a limiting factor, in which case a 14 mm diameter nozzle would seem to be reasonably practical. If a move to 14 mm diameter is judged viable, then a further reduction in flow rate to 9 l/min is also practical.

3.6 References

[3.1] McPherson, N. A., Unpublished work, BAE Systems, Glasgow, 2011.

[3.2] Loxton Industries, 'New welding gas innovation', *Australian Welding Journal*, Vol. 55, No. 1, pp. 10-11, 2010.

[3.3] Uttrachi, G. D., 'GMAW shielding gas flow control systems', *Welding Journal*, Vol. 86, No. 4, pp. 22-23, 2007.

[3.4] Stauffer, H. V., 'Apparatus and method for reducing the waste of welding gas', US Patent Number 4,341,237, 1982.

[3.5] Hanby, S. K., 'Apparatus and method for preventing gas surge in a welding gas delivery system', US Patent Number 6,390,957,B2, 2002.

[3.6] Uttrachi, G. D., 'Welding shielding gas saver device', US Patent Number 6,610,134,B1, 2003.

[3.7] Uttrachi, G. D., 'Welding shielding gas saver flow-control device', US Patent Number 7,015,412,B1, 2006.

[3.8] Lin, M. L. and Eagar, T. W., 'Pressures produced by gas tungsten arcs', *Metallurgical Transactions B*, Vol. 17, No. 3, pp. 601-607, 1986.

[3.9] Fan, H. G. and Shi, Y. W., 'Numerical simulation of the arc pressure in gas tungsten arc welding', *Journal of Materials Processing Technology*, Vol. 61, No. 3, pp. 302-308, 1996.

[3.10] Ham, H. –S., Oh, D. –S. and Cho, S, –M., 'Measurement of arc pressure and shield gas pressure effect on surface of molten pool in TIG welding', *Science and Technology of Welding and Joining*, Vol. 17, No. 7, pp. 594-600, 2012.

[3.11] Oh, D. –S., Kim, Y. –S. and Cho, S. –M., 'Derivation of current density distribution by arc pressure measurement in GTA welding', *Science and Technology of Welding and Joining*, Vol. 10, No. 4, pp. 442-446, 2005.

[3.12] Tamaki, K., Masumoto, I. and Takahashi, Y., 'Some observation on the gas shielding conditions of CO_2 arc welding by the application of a television system', *Journal of the Japan Welding Society*, Vol. 47, No. 5, pp. 37-42, 1978.

4 Derivation of arc forces based on arc pressure measurements in GTAW

4.1 Nomenclature

α - Thermal diffusivity

β - Thermal expansion coefficient

B - Self-induced azimuthal magnetic field

$\frac{\delta\gamma}{\delta T}$ - Temperature coefficient of surface tension

F_{arc} - Arc force

F_B - Buoyancy force

F_L - Lorentz force

g - Gravity

I - Current

J - Current density

L - Characteristic length

μ_0 - Permeability of free space

μ_p - Dynamic viscosity of the arc plasma

μ_w - Dynamic viscosity of the liquid weld metal

Ma - Marangoni number

P_{arc} - Arc pressure (stagnation pressure at the workpiece)

ρ_p - Density of the arc plasma

ρ_w - Density of the weld metal

r - Distance in the radial direction

τ_p - Plasma shear stress

T - Local temperature

T_{ref} - Arbitrary reference temperature (melting temperature)

V - Velocity

4.2 Introduction

As a result of their ability to produce high quality welds, arc welding processes, such as GMAW and GTAW, are indispensable joining processes for a variety of industrial applications. The arc pressure produced as a result of the plasma impinging on the weld pool surface is one of the major contributing factors influencing the depth of penetration and the size and shape of the weld bead. A high welding current is desirable for increasing productivity; however, high welding currents increase the possibility of weld defects such as humping, undercutting, split bead, parallel humping and tunnel porosity [4.1]; the relationship between welding current and arc pressure will be discussed. Ko et al. [4.2] demonstrated that the arc pressure causes oscillations in the weld pool, and a higher arc pressure resulted in weld pool depression in the centre, and a hump towards the outer portion, while Tsai and Kou [4.3] used computational modelling to individually simulate the effects of various driving forces, stating that the electromagnetic (or Lorentz) force caused a slight depression at the outer portion of the weld pool and a corresponding hump in the central portion.

A number of experimental and computational studies have been conducted, [4.4-4.10] investigating how various parameters (including welding current, shielding gas composition and pressure, tungsten electrode tip geometry, arc length and nozzle outlet diameter) influence the peak pressure and the pressure distribution in the arc column.

The alternating shielding gas process benefits achieved thus far are based upon three independent phenomena [4.11]: variation in weld pool fluidity, arc pressure variation and arc pressure peaking, which create fluid flow vectors opposite in direction for argon and helium.

Although studies have reported [4.4-4.10] on the arc pressures produced when using argon, and to a limited extent for helium and argon–helium mixtures, no data have been published for the pressure produced during the alternating shielding gas process.

Kang et al. [4.12] presented Figure 1.17, which shows the theoretical transient arc pressure when alternating between argon and helium based upon the steady state

pressure produced by argon and helium. The alternating shielding gas system implemented in the study, upon which the phenomena are based, incorporated a slider valve that meant there was a period of time when both argon and helium were present. In addition, an assumption that a pressure impulse would occur at this time, due to a build-up in line pressure, was presented (indicated by a series of 'spikes' on the graph).

Fluid flow and heat flow are key factors in determining the final weld shape [4.13], with the direction of the liquid weld metal fluid flow being estimated based upon the various body forces acting upon it. The arc pressure distribution allows for the numerical derivation of various forces acting on the liquid weld metal including arc force, plasma shear and Lorentz force. In addition, the buoyancy force can also be determined numerically, while the surface tension gradient governs the Marangoni convection mode. Kang et al. [4.12] also speculated that argon and helium produce flow vectors opposite in direction in the weld pool, Figure 1.18.

However, no experimental or computational modelling was provided to substantiate such assumptions.

4.3 Experimental setup

A schematic diagram of the arc pressure measurement setup is shown in Figure 4.1. A 200 x 150 x 6 mm thick water-cooled copper plate was used as the anode, this thickness was based upon work by Lin and Eager [4.4] who stated that a plate thicker than 6 mm produced too shallow an axial temperature gradient, whilst a thinner anode plate would not provide the same level of radial heat dissipation.

The remainder of the water-cooled assembly (Figure 4.2) was constructed using 3 mm thick copper sheet, and the cooling water was supplied through 15 mm copper pipe to the lower surface. All joints were silver soldered to ensure the assembly was impermeable.

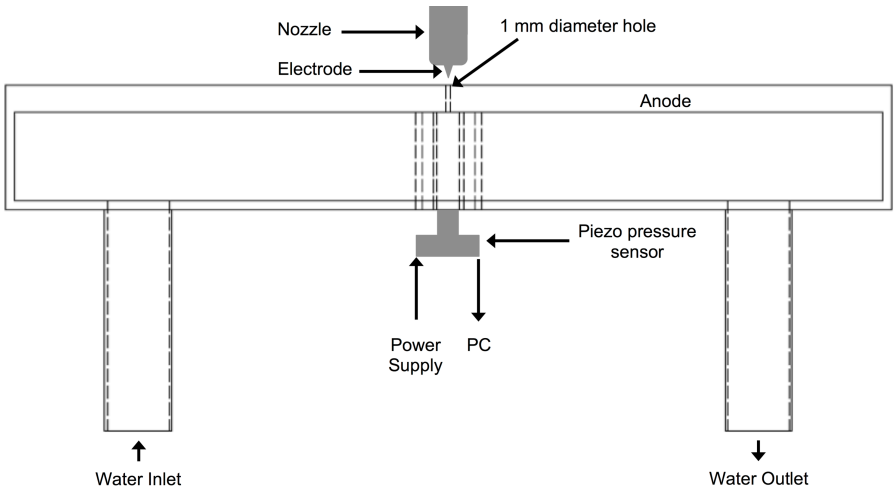

Figure 4.1: Schematic diagram of the arc pressure measurement setup

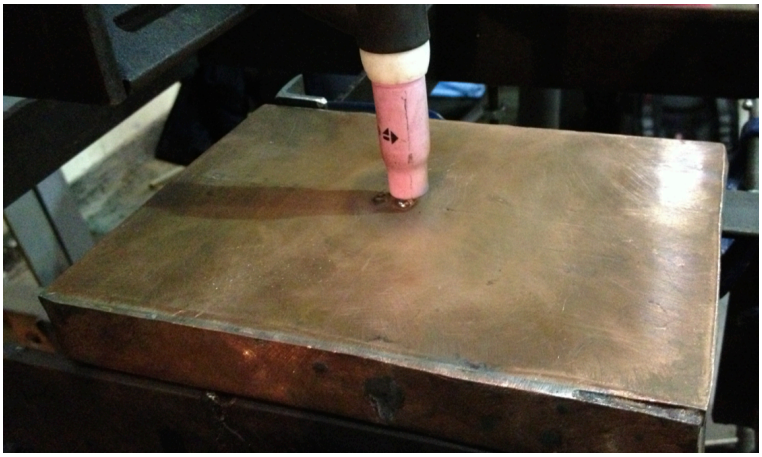

Figure 4.2: Arc pressure measurement experimental setup

A 1 mm diameter hole, as used in previous studies [4.4, 4.7, 4.10], was drilled through the centre of the copper anode plate, beneath which a piezoelectric pressure sensor was mounted to detect the arc pressure in the form of a voltage difference. The sensor was isolated from the structure using a rubber tube, and calibrated for steady state measurements using a u-tube manometer. The voltage obtained from the piezoelectric pressure sensor was then converted to a real-time pressure reading using LabVIEW.

Two shielding gas supplies were used throughout the trials, argon and helium, controlled using the dedicated electronic control unit, Figure 2.7. A shielding gas

flow rate of 10 l/min was used throughout and was set when each gas was flowing continuously. This meant that when using alternating gases, the flow rate would also be 10 l/min. Arc pressure measurements when using alternating shielding gases were conducted with an alternating frequency of 2 Hz. A 12.2 mm internal diameter alumina nozzle was used to direct the shielding gas to the weld region.

A 2.4 mm diameter, 2% thoriated tungsten electrode was used throughout, with a 45° vertex angle and 2 mm arc length. All trials were performed using DC electrode negative with a welding current of 200 A. Pulsed GTAW (GTAW-P) trials were performed with a peak and background current of 200 and 100 A respectively, set at a frequency of 2 Hz and a duty cycle of 50%, as this best represented the alternating shielding gas method.

The arc pressure was recorded every 20 ms with steady state values reported once the arc had stabilised, i.e. after the initial surge of pressure at weld initiation. Measurements were taken at the centre of the 1 mm diameter hole, and in 0.5 mm intervals until 6 mm in the radial direction by incremental step changes to the torch location, with the measurements being sequentially repeated three times allowing the maximum steady state pressure to be recorded. While the arc pressures recorded were within approximately 5% of the reported values, the maximum value has been selected rather than the average of the three measurements, as any misalignment with respect to the 1 mm hole would result in a difference in the pressure measured, thus ensuring that the error was minimised.

Subsequent trials for the measurement of weld geometry were conducted on an automated welding rig, which moved the plate beneath a stationary welding torch. Trials were performed on 250 x 100 x 6 mm thick DH36 grade steel, with the travel speed being altered to maintain a constant power input due to the varying arc voltage; a variation of <1% was achieved while assuming a constant thermal efficiency of unity. The weld parameters for this element of investigation are shown in Table 4.1.

Table 4.1: Weld parameters for weld geometry measurement

Shielding Gas Configuration	Arc Length (mm)	Voltage (V)	Current (A)	Travel Speed (mm/s)	Heat Input (J/mm)[a]
Argon	2	14.2	200	3.7	767.6
Helium	2	19.2	200	5.0	768.0
Alternating Shielding Gases	2	16.8	200	4.4	763.6
GTAW-P	2	14.2	200 (peak) 100 (background)	2.8	760.7

[a] Heat input calculated with a unity thermal efficiency factor

4.4 Results and discussion

4.4.1 Arc pressure measurements

The radial pressure distribution with respect to the arc centreline for argon and helium shielding gases is shown in Figure 4.3. The peak pressure at the arc centreline (~1900 N/m^2) and the pressure distribution for argon are, accounting for variables such as current and vertex angle, in line with previous publications [4.4, 4.7-4.10], as shown in Figure 4.4. This was also considerably higher than the peak steady state arc pressure at the arc centreline for helium (~800 N/m^2).

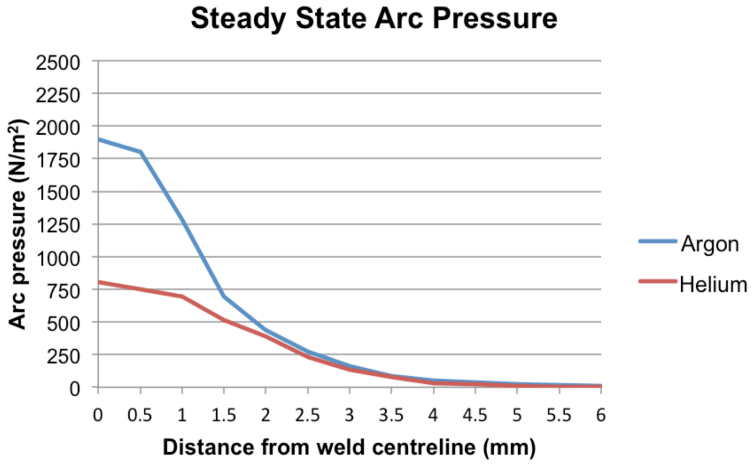

Figure 4.3: Steady state arc pressure measurements

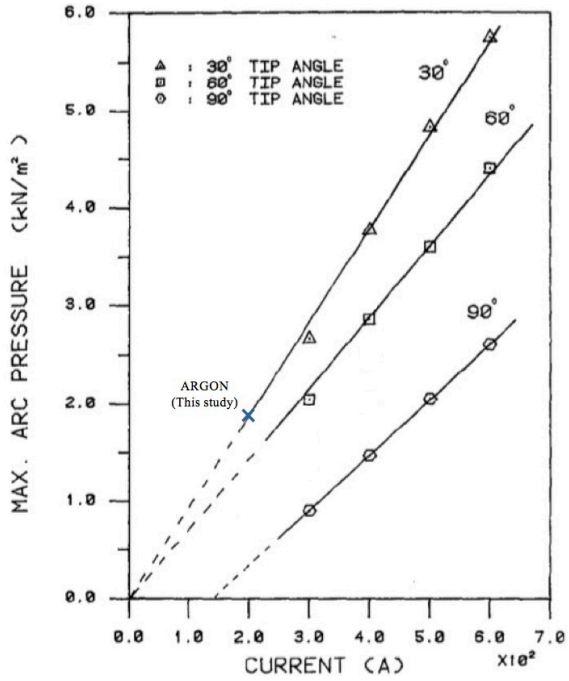

Figure 4.4: Arc pressure vs. welding current [4.4] showing argon arc pressure measured in present study

While other research groups [4.4-4.10] do not stipulate what their peak pressure is referring to, it can be assumed, based on their experimental set-up (generally a u-tube manometer) and computational methods, that the pressure recorded are steady state measurements, i.e. after the initial surge (discussed later) due to the time taken for pressure equalisation.

The transient arc pressure measurements at the arc centreline made whilst using alternating shielding operating at a frequency of 2 Hz is shown in Figure 4.5. The maximum (~2410 N/m^2) and minimum (~1010 N/m^2) arc pressures for alternating shielding gases are substantially greater than the maximum steady state pressure obtained for argon and helium respectively at the corresponding arc centreline location shown in Figure 4.3.

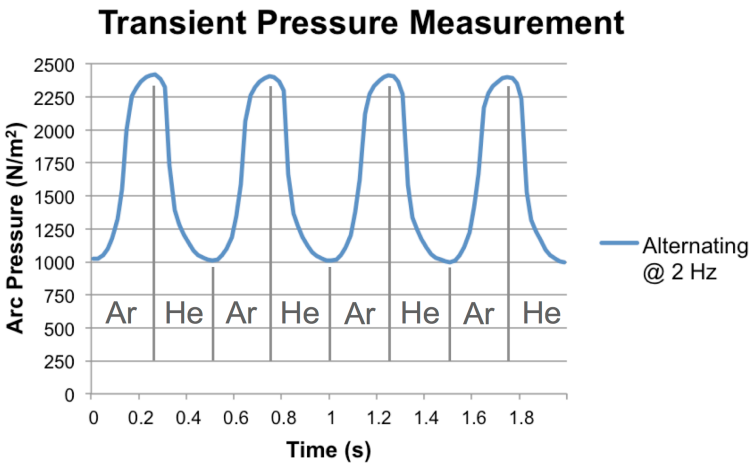

Figure 4.5: Transient arc pressure measurement of alternating shielding gases

It can be observed when comparing Figure 1.17 and 4.5 that there is a considerable difference between the previously reported theoretical arc pressure (Figure 1.17) and that generated through experimental transient pressure measurements (Figure 4.5) and can be explained due to a pressure impulse at arc initiation.

Figure 4.6 shows a transient pressure measurement at weld initiation at the arc centreline for argon and helium. As can be seen, there is a significant (~25%) pressure surge at weld initiation that corresponds to the pressures measured during alternating shielding gases, i.e. the peaks and troughs pressure measurements when using alternating shielding gases are similar to those measured at arc initiation for argon and helium respectively. It can also be observed that the time taken for the arc pressure to reach steady state is approximately 3–5 s. However, when using alternating shielding gases at 2 Hz, each gas is only supplied for 0.25 s before changing to the other gas; thus, the entire time either gas is supplied is within the arc initiation pressure impulse.

The addition of helium to an argon based mixture has been shown to considerably reduce the resulting arc pressure [4.7]; thus, the non-deliberate intermixing of argon and helium between the welding unit and welding torch resulted in a ‘smoothing’ of the peak pressures. This, coupled with the information that the shielding gas pressure has a negligible effect on the arc pressure [4.10], indicates that the theoretical peaks shown in Figure 1.17 when alternating between gases do not exist.

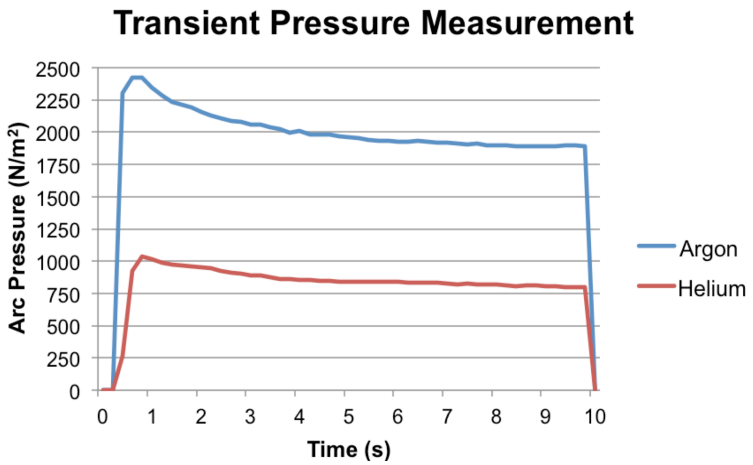

Figure 4.6: Transient arc pressure measurement at arc initiation

The comparison of arc pressure measurements at the arc centreline for alternating shielding gases and GTAW-P is shown in Figure 4.7; a background current of 100 A was selected as this produced the best correlation to the steady state helium pressure measurements.

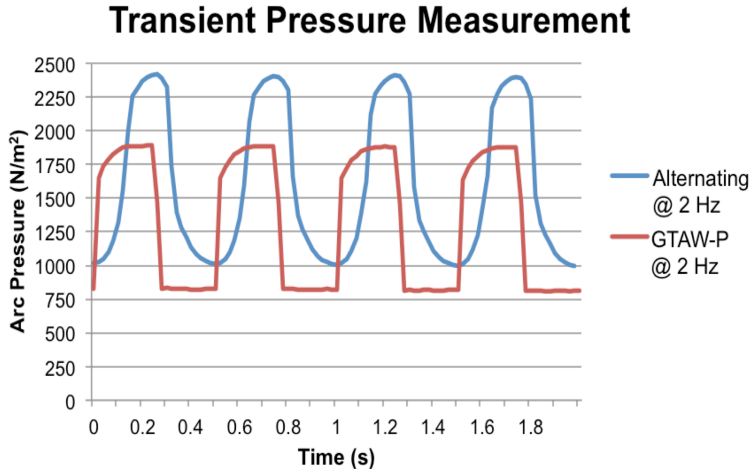

Figure 4.7: Comparison of transient arc pressure measurements during alternating shielding gases and GTAW-P

As can be observed, the argon phase in alternating shielding gases produced a higher arc pressure than the peak current phase in the GTAW-P process; this can be attributed to the surge at weld initiation discussed previously. This surge is not present within the GTAW- P process, as an arc is not being re-established; the power

source is simply changing the magnitude of the supply current. The arc pressure also has a more instantaneous decline to the background current phase than the equivalent drop in pressure in alternating shielding gases when helium is present. This is due to a degree of intermixing of shielding gases in the gas lines, whereas the change from peak to background current in GMAW-P is more sudden. While the arc pressure measurements conducted for alternating shielding gases and GTAW-P are similar in form, the main difference in these processes is the forces acting on the liquid weld metal, as will be discussed in the proceeding section.

4.4.2 Arc force derivation

The arc pressure distribution allows for the derivation of important plasma aspects including the current density distribution, plasma shear force, arc force and Lorentz force. A schematic diagram of the GTAW process and the forces acting on the liquid weld metal is shown in Figure 1.16. As can be seen, the arc force and Lorentz force are opposite in direction to the plasma shear and buoyancy force, while the direction of flow due to Marangoni convection is dependent upon the surface tension gradient.

Figure 4.8 shows the profile of the arc column, with the alternating shielding gas fluctuating between the argon and helium arc profiles, and allows the impingement diameter of the arc to be measured, i.e. the diameter of the arc in contact with the plate surface. A diameter of 7.5 and 6 mm for argon and helium respectively was measured using image analysis software.

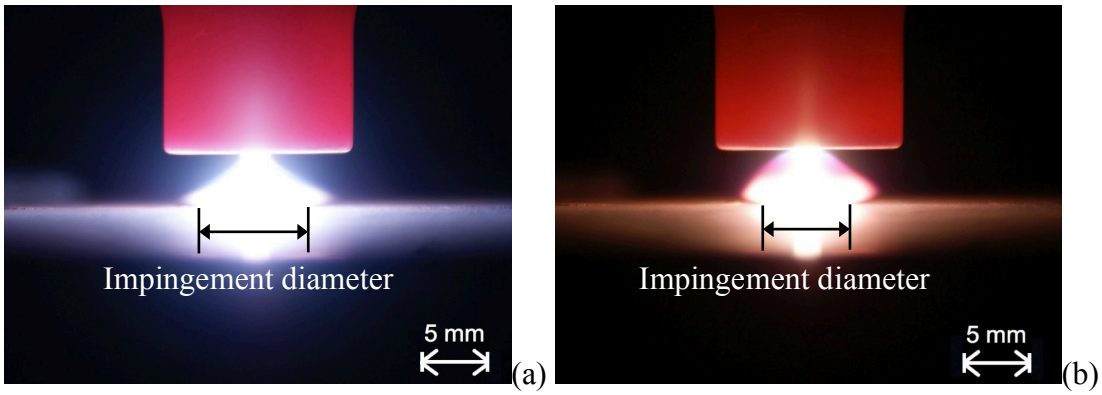

Figure 4.8: Arc profile produced using (a) argon, and (b) helium, showing location of arc width measurement

Since the arc pressure measurement is essentially the stagnation pressure of the plasma jet arrested at the anode plate surface, the velocity of the plasma jet can be determined using Bernoulli's theorem:

$$P_{arc} = \frac{1}{2}\rho_p V^2 \tag{4.1}$$

Figure 4.9 shows the axial velocity distribution of the arc plasma at the plate surface. The shielding gas densities (0.05 kg/m^3 for argon and 0.01 kg/m^3 for helium) and dynamic viscosities (both ~2.75 x 10^{-4} kg/(m.s)) at 10000 K were taken from calculated graphs presented by Traidia et al. [4.14], based on an arc plasma temperature adjacent to the workpiece surface determined by computational simulation [4.15]. The axial velocity of the helium plasma is considerably higher than that of argon, primarily due to the respective densities of the shielding gases.

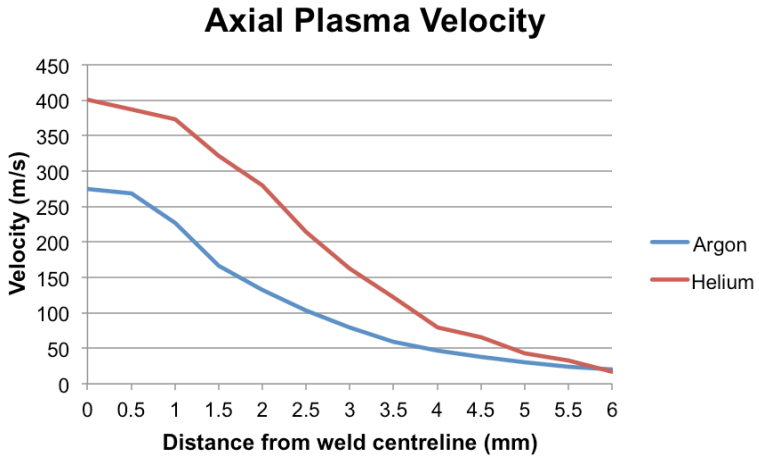

Figure 4.9: Steady state axial plasma velocity

The plasma shear stress, i.e. the surface force as a result of the arc plasma moving radially outwards, causes a drag force on the liquid metal. Consequently, the liquid weld metal flows from the centre of the pool surface towards the pool boundary and return beneath the pool surface. The plasma shear stress can be calculated using equation (4.2) and is a function of the dynamic viscosity and radial velocity of the shielding gas [4.16].

$$\tau_p = \mu_p \frac{\delta V}{\delta r}$$

(4.2)

The plasma shear stress distribution on the plate surface is shown in Figure 4.10. As can be seen, the peak shear stress occurs away from the weld centreline; this is because the plasma shear stress is a function of the gradient of the radial velocity.

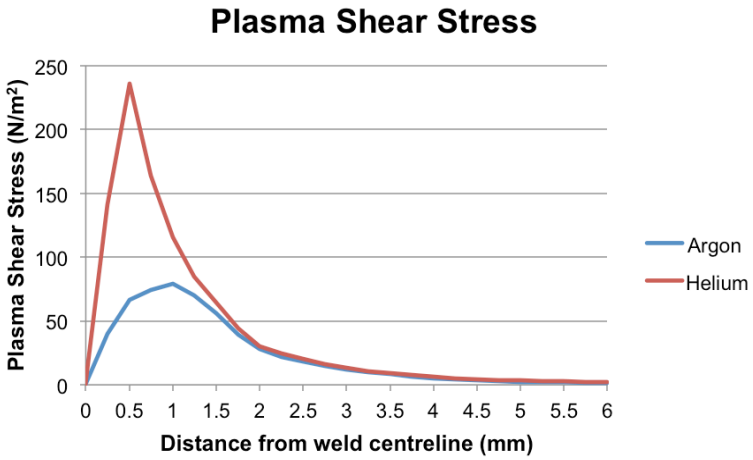

Figure 4.10: Plasma shear stress distribution

The maximum shear stress for argon (~80 N/m^2) was found to occur 1 mm from the weld centreline, which was in agreement with Lee and Na [4.6] and Hu and Tsai [4.16] who reported values of ~75 and ~90 N/m^2 using numerical modelling of the GTAW and GMAW processes respectively. Again, these values occurred at a distance ~1 mm from the weld centreline for argon.

As can be seen in Figure 4.10, the maximum shear stress generated when using helium (~240 N/m^2) was approximately three times greater than that of argon. This implies that the liquid weld metal is more likely to flow radially outwards at the pool surface when using helium than argon.

The arc force can be determined by integrating the arc pressure distribution over the impingement area of the arc [4.10]:

$$F_{arc} = \int_0^R 2\pi r P_{arc} dr$$

(4.3)

A diameter of 7.5 and 6 mm for argon and helium respectively was measured using image analysis software as previously stated. The arc force was determined by sectioning the effective area of the arc into 0.0625 mm segments and numerically integrating using equation (4.3); an arc force of ~18 mN (~1800 dynes) and ~11.4 mN (~1140 dynes) was calculated for argon and helium respectively. The arc force for argon is in good agreement with the experimental parabolic arc force relationship with current that Lin and Eagar [4.4] reported for argon (Figure 4.11). It can also be noted that the arc force generated by argon is approximately 60% greater than the corresponding value for helium.

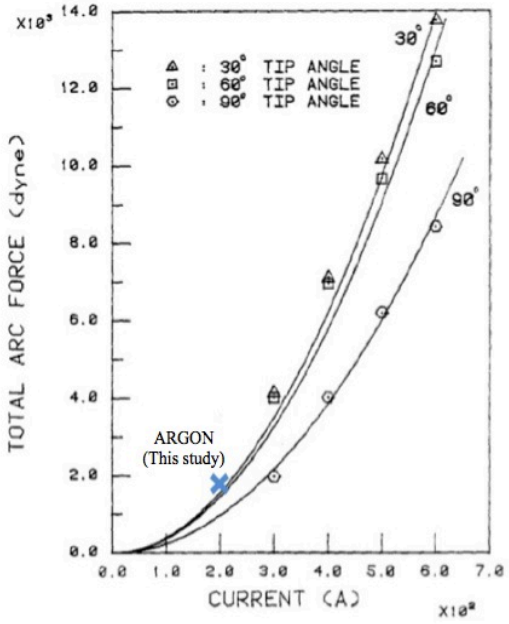

Figure 4.11: Arc force vs. welding current [4.4] showing argon arc force determined from present study

Fan et al. [4.9] stated that the welding current could be calculated by a similar method to the arc force, i.e. integrating the current density distribution over the impingement area of the arc:

$$I = \int_0^R 2\pi r J dr \tag{4.4}$$

Combining equations (4.3) and (4.4), the current density can be calculated:

$$J = \frac{P_{arc} I}{F_{arc}}$$

(4.5)

As can be noted, the current density is dependent not only on the welding current and arc pressure, but also on the arc force (which can be determined by the numerical integration of the arc pressure).

The current density distributions for argon and helium, as derived from their respective steady state arc pressure measurements, as detailed previously are shown in Figure 4.12. As can be seen, argon produces a high current density at the arc centreline (~21 A/mm^2), which quickly drops in the radial direction, while helium produces a lower peak current density at the arc centreline (~14 A/mm^2) but produces a higher current density than argon as the radial distance increases.

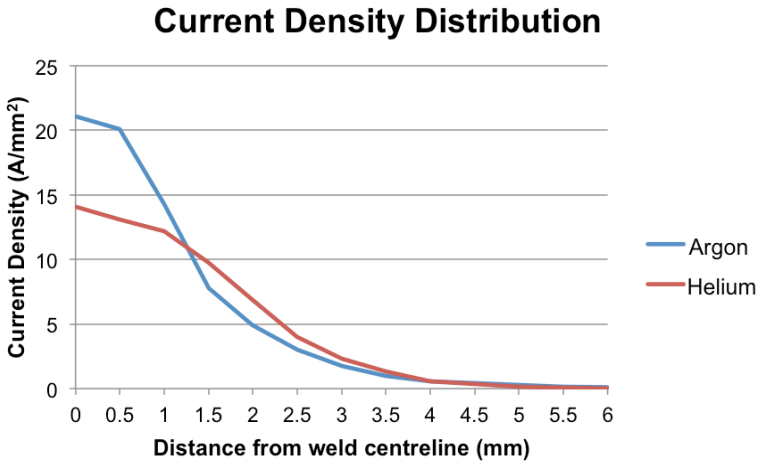

Figure 4.12: Current density distribution

The Lorentz force can be calculated using the following equation:

$$F_L = JB$$

(4.6)

Where J, the current density, and B, the self-induced azimuthal magnetic field, can be derived using equation (4.5) and Ampere's equation (equation (4.7)) respectively:

$$B = \frac{\mu_0}{r} \int_0^R Jrdr$$

(4.7)

Combining equations (4.5) and (4.7) yields:

$$B = \frac{\mu_0 I}{2\pi r} \tag{4.8}$$

The Lorentz force distribution is shown in Figure 4.13; as with the arc force, calculations have been performed over 0.0625 mm segments. As can be seen, at the arc centreline, the Lorentz force is zero; this is because the self-induced magnetic field term tends to zero, as r tends to zero. Moving radially outwards, <1.25 mm, argon produced a Lorentz force approximately double that of helium. However, helium produced a higher Lorentz force >1.25 mm to the edge of the arc. Summating the results over the arc area produced a total Lorentz force of 5.08 x 10^5 N/m^3 for argon and 3.25 x 10^5 N/m^3 for helium.

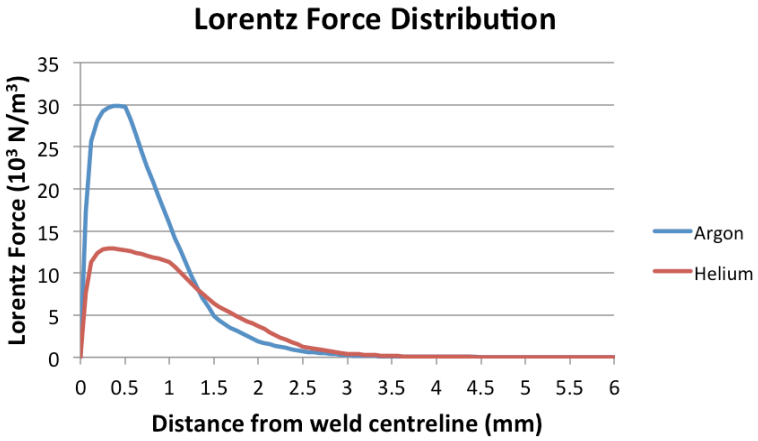

Figure 4.13: Lorentz force distribution

The buoyancy force can be calculated using the Boussinesq approximation:

$$F_B = -\rho_w g \beta (T - T_{ref}) \tag{4.9}$$

Linear thermal expansion data for the weld metal, presented in Chapter 5, produced using different shielding gas compositions, has been used in the calculation to estimate the buoyancy force. It was found that the weld metal produced using an argon / 20% carbon dioxide shielding gas mixture has a higher coefficient of thermal expansion than that produced using helium. However, the maximum difference in

thermal expansion between shielding gases, ~0.6 x 10^{-6} /K, equates to only 4.6% and can be considered negligible in comparison to the $(T - T_{ref})$ term, when considering a peak temperature in the weld pool of ~2350 and 3700 K for argon and helium respectively [4.17]. This results in helium having a $(T - T_{ref})$ term in excess of three times that of argon and, by assuming that the other terms are negligible, helium would have a buoyancy force approximately three times greater than argon.

The surface tension (or Marangoni convection mode) is generally discussed as a function of the surface active elements, such as sulphur or oxygen [4.18, 4.19]. The surface tension gradient is also a function of temperature; a negative surface tension gradient acts to pull the weld metal outwards, and, conversely, a positive surface tension gradient acts to pull the weld metal inwards.

Limmaneevichitr and Kou [4.20] simulated the fluid flow due to Marangoni convection in a transparent $NaNO_3$ solution using a laser power source for a range of power inputs and laser diameters. They found that a high beam power input produced faster, shallower convection than a low beam power input. In addition, they demonstrated that a small beam diameter produced faster, deeper convection than a larger beam diameter.

Owing to its arc characteristics, helium produces a greater voltage potential than argon: in this study, 19.2 and 14.2 V respectively and therefore a power input 35% greater than argon (assuming that the thermal efficiency is constant). The impingement diameter of the welding arc was also found to change depending on the shielding gas used; argon and helium produced an effective arc diameter of 7.5 and 6 mm respectively. Therefore, based on the findings of Limmaneevichitr and Kou [4.20], helium would produce faster convection than argon. The Marangoni number has been widely used for the measure of the extent of Marangoni convection and is given by equation (4.10):

$$Ma = \frac{-\frac{\delta\gamma}{\delta T}(T - T_{ref})L}{\mu_w \alpha} \tag{4.10}$$

Using values previously published for steel of negligible sulphur content, -($\delta\gamma/\delta T$), μ_w and α, of -0.3 dyne/(cm.K), 5 x 10^{-2} g/(cm.s) and 5 x 10^{-2} cm^2/s respectively [4.20], ($T - T_{ref}$) of 650 and 2000 K for argon and helium respectively [4.17] and a characteristic length, L, of 4.4 and 4.8 mm for argon and helium respectively as determined by this study, the Marangoni number can be determined. Therefore, since the temperature coefficient of surface tension is negative, the flow is radially outwards on the pool surface, and a Marangoni number of 3.43 x 10^4 for argon and 1.06 x 10^5 for helium was calculated; this implies that the flow becomes stronger [4.21], i.e. the flow velocity increases. The Marangoni number for argon is in line with those presented elsewhere [4.20].

Macrographs of the weld geometry produced with constant heat input using the various shielding gas and power input methods are shown in Figure 4.14. As can be seen, the weld bead produced using helium (~9.6 mm) was approximately 10% wider than that of argon (~8.8 mm), while alternating shielding gases (~9.2 mm) was in between and GTAW-P was narrower (~8.2 mm) due to the lower fluidity of the weld pool during the background current phase. The increased weld width when helium is added to the shielding gas configuration can be attributed to the greater radial flow of the weld metal due to the increased plasma shear, Marangoni convection and buoyancy forces. The maximum penetration in the centre of the weld was fairly similar (3–3.2 mm), indicating that the plasma shear stress, buoyancy force and Marangoni convection have a greater influence on the solidified weld geometry than the arc force and Lorentz force.

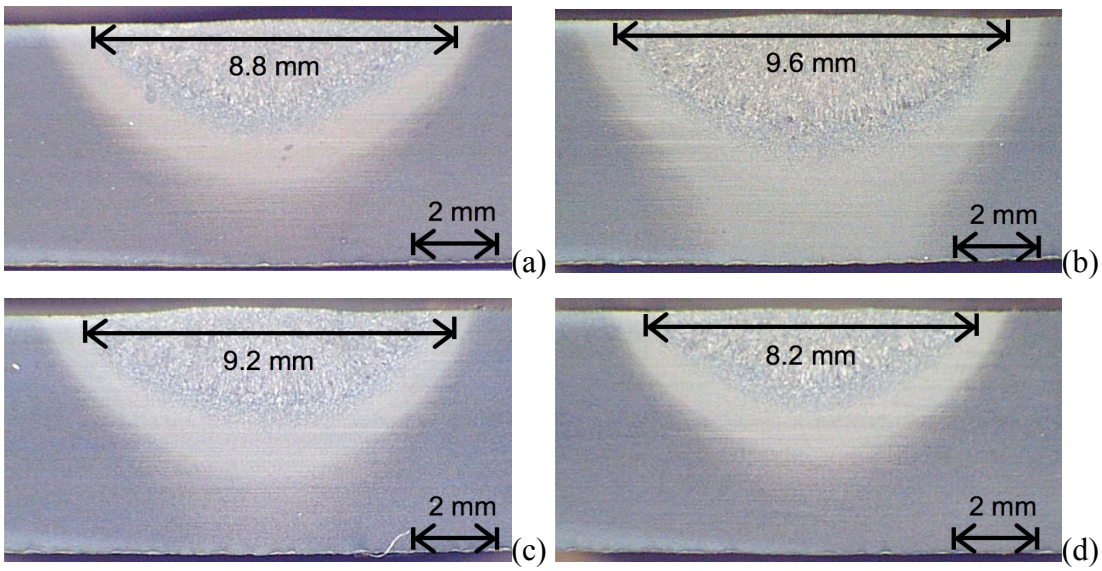

Figure 4.14: Weld macrograph for (a) argon, (b) helium, (c) alternating shielding gases and (d) GTAW-P

The practical welding current can be compared to the derived current through numerical integration [4.7]:

$$I = \sum_{i-1}^{n} \left[\pi (r_{i-1}^2 - r_i^2) \left(\frac{J_i + J_{i+1}}{2} \right) \right] \tag{4.11}$$

It was determined that the numerically derived current was within 1% of the practical welding current for both argon and helium.

4.5 Conclusions

A piezoelectric pressure sensor has been implemented for the transient arc pressure measurement whilst using argon, helium, alternating shielding gases and GTAW-P, from which various forces acting on the liquid weld metal have been calculated.

The arc pressure results can be summarised as follow:

- The arc pressure for argon is considerably higher than that of helium, with the measured pressure distribution in line with previous publications [4.4, 4.7-4.10], when accounting for variables such as current and vertex angle.

- The arc pressure for alternating shielding gases is considerably higher (~25%) than the steady state values for argon and helium due to a pressure impulse at weld initiation.
- The transient arc pressure measurement during alternating shielding gases has been shown to be considerably different from the previous theoretical assumptions:
    - Due to the length of time each gas is supplied (0.25 s), the arc pressure is always in the arc initiation phase, hence there is no steady state pressure for either gas.
    - The 'spikes' between steady state pressures do not exist.
- The transient pressure measurement of GTAW-P has been shown to be similar in form to that produced during alternating shielding gases. However, arc pressures for alternating shielding gases are comparable to those at arc initiation, whilst GTAW-P produces arc pressures comparable to the steady state values.

The arc force results can be summarised as follow:

- Helium produces a greater plasma shear stress than argon, ~240 N/m^2 and ~80 N/m^2 respectively, and occurs ~1 mm from the arc centreline. The experimentally derived values are in close agreement with published figures [4.6, 4.16], determined using computational modelling.
- Argon produces a greater arc force than helium both in the central location and over the effective area of the arc, ~18 and ~11.4 mN respectively. The arc force for argon is in good agreement with the experimental parabolic arc force relationship with current that Lin and Eagar [4.4] reported.
- Argon produces a high core current density, while helium produces a broader current density distribution than argon.
- Argon produces a greater Lorentz force than helium, 5.08×10^5 N/m^3 and 3.25×10^5 N/m^3 respectively. The Lorentz force distribution showed that

argon had a greater core (<1.25 mm) Lorentz force, while helium produced a greater outer core (>1.25 mm) Lorentz force.

- It was estimated that helium produces a buoyancy force approximately three times greater than argon due to the higher weld pool temperature.
- The Marangoni number calculated for helium is greater than argon, 1.06×10^5 and 3.43×10^4 respectively. This indicates that the Marangoni convection is stronger for helium than argon.
- The numerically derived welding current was in good agreement with the practical welding current.

Considering the forces acting on the liquid weld metal, it can be observed there is a definite magnitude change, with the potential that the flow vectors for helium and argon being in the opposite direction, creating a dynamic action within the weld pool when using alternating shielding gases. The GTAW-P process would exhibit similar effects due to the varying magnitude of the forces acting on the weld metal but all flow would be in the same direction causing a 'jerking' motion.

As shown by Traidia [4.22], the magnitude and direction of the fluid flow in the liquid weld metal is an important characteristic for the determination of the final solidified weld geometry. Hence, by controlling the shielding gas present in the arc plasma, the flow vectors can be manipulated in such a way as to provide the desired weld profile.

4.6 References

[4.1] Mendes, P. F. and Eagar, T. W., 'Penetration and defect formation in high-current arc welding', *Welding Journal*, Vol. 82, No. 10, pp. 296s-306s, 2003.

[4.2] Ko, S. H., Choi, S. K. and Yoo, C.D., 'Effects of surface depression on pool convection and geometry in stationary GTAW', *Welding Journal*, Vol. 80, No. 2, pp. 39s-45s, 2001.

[4.3] Tsai, M. C. and Kou, S., 'Electromagnetic-force-induced convection in weld pools with a free surface', *Welding Journal*, Vol. 69, No. 6, pp. 241s-246s, 1990.

[4.4] Lin, M. L. and Eagar, T. W., 'Pressures produced by gas tungsten arcs', *Metallurgical Transactions B*, Vol. 17, No. 3, pp. 601-607, 1986.

[4.5] Choo, R. T. C., Szekely, J. and Westhoff, R. C., ' On the calculation of the free surface temperature of gas-tungsten-arc weld pools from first principles. Part 1: modeling the welding arc', *Metallurgical Transactions B*, Vol. 23, No. 3, pp. 357-369, 1992.

[4.6] Lee, S. Y. and Na, S. J., 'Analysis of TIG welding using boundary fitted coordinates', *Proceedings of the Institution of Mechanical Engineers, Part B: Journal of Engineering Manufacture*, Vol. 209, No. 2, pp. 153-164, 1995.

[4.7] Oh, D. –S., Kim, Y. –S. and Cho, S. –M., 'Derivation of current density distribution by arc pressure measurement in GTA welding', *Science and Technology of Welding and Joining*, Vol. 10, No. 4, pp. 442-446, 2005.

[4.8] Fan, H. G. and Shi, Y. W., 'Numerical simulation of the arc pressure in gas tungsten arc welding', *Journal of Materials Processing Technology*, Vol. 61, No. 3, pp. 302-308, 1996.

[4.9] Fan, D., Ushio, M. and Matsuda, F., 'Numerical computation of arc pressure distribution', *Transactions of the Joining and Welding Research Institute*, Vol. 15, No. 1, pp. 1-5, 1986.

[4.10] Ham, H. –S., Oh, D. –S. and Cho, S, –M., 'Measurement of arc pressure and shield gas pressure effect on surface of molten pool in TIG welding', *Science and Technology of Welding and Joining*, Vol. 17, No. 7, pp. 594-600, 2012.

[4.11] Chang, Y. H., 'Improve GMAW and GTAW with alternating shielding gases', *Welding Journal*, Vol. 85, No. 2, pp. 41-43, 2006.

[4.12] Kang, B. Y., Prasad, Y. K. D. V., Kang, M. J., Kim, K. J. and Kim, I.S., 'Characteristics of alternate supply of shielding gases in aluminium GMA welding', *Journal of Materials Processing Technology*, Vol. 209, No. 10, pp. 4716-4721, 2009.

[4.13] Cho, M. H., Lim, Y. C. and Farson, D. F., 'Simulation of weld pool dynamics in the stationary pulsed gas metal arc welding process and final weld shape', *Welding Journal*, Vol. 85, No. 12, pp. 271s-283s, 2006.

[4.14] Traidia, A., Roger, F., Chidley, A., Shroeder, J. and Marlaud, T., 'Effect of helium-argon mixtures on the heat and fluid flow in gas tungsten arc welding', *World Academy of Science, Engineering and Technology*, Vol. 49, pp. 1053-1058, 2011.

[4.15] Lago, F., Gonzalez, J. J., Freton, P. and Gleizes, A., 'A numerical modelling of an electric arc and its interaction with the anode. Part 1: the two-dimensional model', *Journal of Physics D: Applied Physics*, Vol. 37, No. 6, pp. 883-897, 2004.

[4.16] Hu, J. and Tsai, H. L., 'Heat and mass transfer in gas metal arc welding. Part 1: the arc', *International Journal of Heat and Mass Transfer*, Vol. 50, No. 5-6, pp. 883-846, 2007.

[4.17] Traidia, A. and Roger, F., 'A computational investigation of different helium supplying methods for the improvement of GTA welding', *Journal of Materials Processing Technology*, Vol. 211, No. 9, pp. 1553-1562, 2011.

[4.18] Mills, K. C., Keene, B. J., Brookes, R. F. and Shirali, A., 'Marangoni effects in welding', *Philosophical Transactions of The Royal Society A: Mathematical, Physical and Engineering Sciences*, Vol. 356, pp. 911-925, 1998.

[4.19] Aidun, D. K. and Martin, S. A., 'Effect of sulphur and oxygen on weld penetration of high-purity austenitic stainless steel', *Journal of Materials Engineering and Performance*, Vol. 6, No. 4, pp. 496-502, 1997.

[4.20] Limmaneevichitr, C. and Kou, S., 'Visualization of Marangoni convection in simulated weld pools', *Welding Journal*, Vol. 79, No. 5, pp. 126s-135s, 2000.

[4.21] Kou, S., Limmaneevichitr, C. and Wei, P. S., 'Oscillatory Marangoni flow: a fundamental study by conduction-mode laser spot welding', *Welding Journal*, Vol. 90, No. 12, pp. 229s-240s, 2011.

[4.22] Traidia, A., 'Multiphysics modelling and numerical simulation of GTA weld pools', Ph.D Thesis, Ecole Polytechnique, 2011.

5 Mechanical and thermal property assessment of GMAW with alternating shielding gases

5.1 Nomenclature

α - Thermal diffusivity

β - Thermal expansion coefficient

C_p - Specific heat capacity

$\varepsilon_{thermal}$ - Thermal strain

H_{net} - Net heat input

k - Thermal conductivity

L_f - Latent heat of fusion

L_{final} - Final length

$L_{initial}$ - Initial length

ρ - Density

R - Cooling rate

S_t - Solidification time

T_c - Temperature of interest

T_{final} - Final temperature

$T_{initial}$ - Initial temperature

T_m - Melting temperature

5.2 Introduction

In recent times, there have been very few advances regarding shielding gas technology in GMAW. However, relatively recently there has been positive research [5.1-5.3] into the effects of alternating shielding gases in both GMAW and, to a lesser extent, in GTAW [5.1]. These studies have shown beneficial results such as increased travel speed, reduced porosity, and increased strength. Chang [5.1] reported that the use of alternating shielding gases created beneficial effects on the weld pool and, different flow vectors being created in the weld pool for different shielding gases [5.2]. However, when alternating between shielding gases, complex

flow patterns are created which cause a dynamic action in the weld pool. This dynamic action was previously attributed to three independent theoretical phenomena occurring simultaneously in the weld area:

- Arc pressure variation
- Arc pressure peaking
- Variation in weld pool fluidity

However, as determined in Chapter 4, although there is an initial peak in arc pressure when initiating an electrical arc (~25% higher than steady state), as a result of the short time that each shielding gas is present in the alternating gas process (0.25 s for 2 Hz), the arc pressure is always within the arc initiation phase and no steady state region exists.

Porosity is formed when atmospheric gases contaminate the welding arc. Due to the intense heat in the arc column, these gases are dissociated, absorbed into, and spread throughout the weld pool. During solidification, gas bubbles form, creating voids within the weld (porosity), some of which escape due to buoyancy effects. The dynamic action created through the use of alternating gases has previously been reported to assist the buoyancy effect with the removal of the gas bubbles, thus reducing porosity [5.1].

Several industries [5.4, 5.6] are moving towards thinner, lighter and stronger materials (such as AA6082T6) to reduce the overall mass of the structure, and with the aim of improving efficiency. For example, the transportation industries are continually striving to increase fuel efficiency as a consequence of legislation governing exhaust emissions. It has been reported [5.6] that a 10% reduction in a vehicle's weight corresponds to a 5.5% reduction in fuel consumption, with each kilogram saving said to equate to a 20 kg reduction in CO2 emissions over a 170,000 km lifetime, and since the density of aluminium is approximately one-third that of steel, there is considerable scope for improvement. Aluminium alloys also have a use in the shipping industry where its use allows for a smaller portion of the ship to be beneath water level allowing for a greater number of passenger decks. Aluminium alloys are also used higher up the naval structure in order to enhance structure stability. Al–Cu–Mg (2xxx series) alloys are used extensively in the aerospace

sector, however, movements are being made towards 6xxx series alloys owing to benefits associated with improved weldability and cost, with the added benefit of weight saving as a consequence of not requiring cladding to prevent corrosion.

However, it is widely acknowledged that these thinner materials are more susceptible to distortion induced by the welding process, which is an expected consequence, closely linked to the induced heat input. The effort required to rectify the distortion from the plate is highly resource intensive, and it is therefore beneficial to eliminate as much distortion at source as possible. This is largely achievable through good practices mainly related to reducing the heat going into the plates and the concentration of heat in specific areas. For this reason, a reduction in heat input is a primary manufacturing goal.

Computational modelling has become increasingly popular over the past few decades for the prediction of various aspects of the welding process. Extensive studies have been conducted in areas fundamental to the final structure, namely residual stresses in the weld region [5.7-5.9], weld induced distortion [5.8-5.10] and the solidified weld geometry [5.9].

However, due to a lack of experimental data, the difference in thermal properties between the parent plate and weld metal are often neglected, and many computational modelling simulations generally make the assumption that the thermal properties of the weld metal [5.8], i.e. specific heat capacity, coefficient of thermal expansion, thermal conductivity and thermal diffusivity, are the same as those for the parent plate. However, particularly in GMAW, the filler material generally has a different chemical composition and mechanical property data to that of the parent material. In addition, Camilleri et al. [5.9] and Mollicone et al. [5.10] presented dilatometer data, which indicated that the parent plate and filler material possess different coefficient of thermal expansions and, from this, it can therefore be inferred that the other thermal properties will also differ. Thus the accuracy of the simulation is only as accurate as the material property data supplied.

Zhu and Chao [5.11] used a computational model to investigate the effect that temperature dependant thermal properties have on the temperature field produced during the GMAW process. Temperature fields were modelled using room

temperature, averaged linear, and temperature variant values for specific heat capacity and thermal conductivity, and concluded that temperature variant thermal properties produced the most accurate results.

Zhu and Chao [5.11] also describe, in detail, previous authors that have conducted studies into temperature dependant material properties and concluded that the unavailable material property data at higher temperatures has negligible effect on the residual stresses and distortion. However, these studies did not perform computational simulations to compare their assumptions with accurate thermal property data, nor did they differentiate between the thermal properties of the parent plate and the weld metal, thus the conclusions that they reached are unfounded.

This chapter will assess the techno-economic effects that an alternating shielding gases supply has on the welded joint. In addition, the effect that alternating shielding gases have on various thermal property data including the linear thermal expansion coefficient, specific heat capacity, thermal conductivity and thermal diffusivity, within the weld material itself and for the parent plate will be investigated.

5.3 Experimental setup

In order to assess the effects that alternating shielding gases have on the mechanical properties of the welded joint, experimental trials were conducted on both steel and aluminium workpieces. In addition, the effects that the shielding gas composition has on the thermal properties of the weld were assessed on a steel workpiece.

This section details the experimental setup used to conduct each series of experimental trials conducted, with reference to Experimental apparatus and procedures, Chapter 2, used in each stage.

5.3.1 Mechanical property trials – DH36 grade steel

Experimental welding trials were conducted upon an automatic welding rig using 8 mm thick DH36 grade steel in the form of 500 x 250 mm plates, with a 30° edge preparation, in a butt weld configuration. To follow industrial practice, the base case

for comparison was conducted with a 3 mm root gap. The root gap was reduced to 2 mm for the trials conducted using alternating shielding gases as the addition of helium was predicted to increase weld penetration, as shown in Figure 5.1. In each case, the weld root was supported using a ceramic backing strip, which was positioned on the underside of the workpiece, as shown in Figure 5.2.

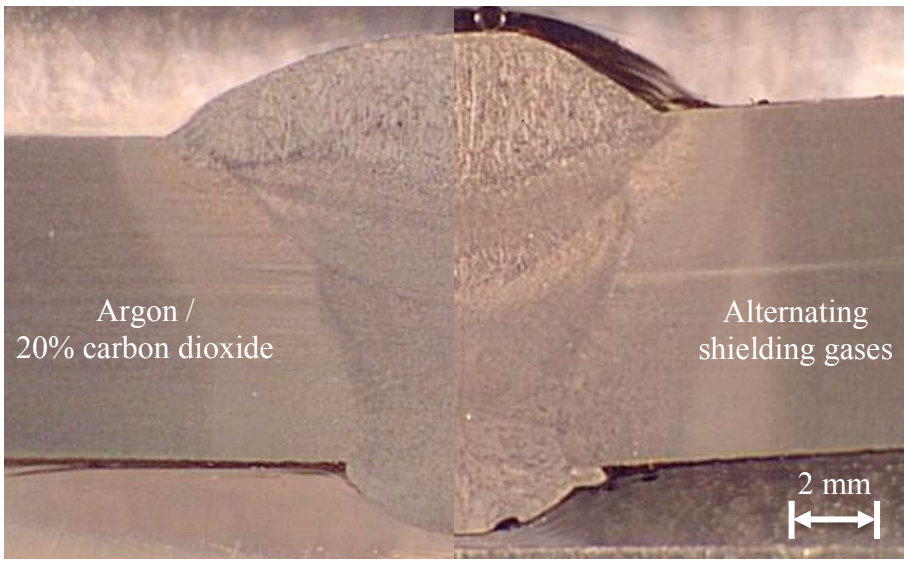

Figure 5.1: Macrograph showing adequate penetration achieved using reduced root gap with alternating shielding gases

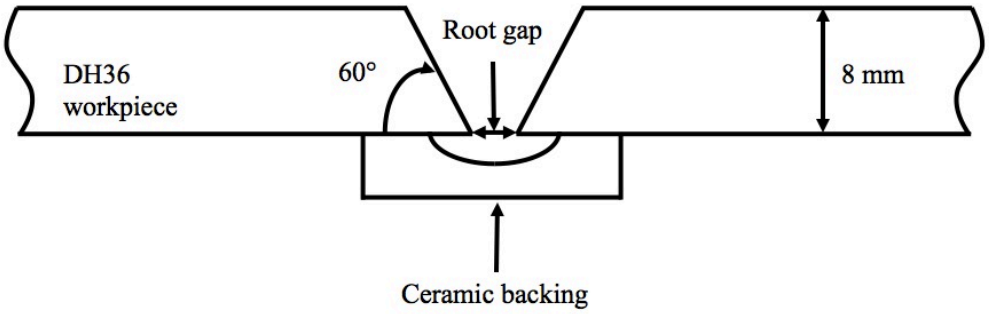

Figure 5.2: Schematic diagram of DH36 experimental setup

In modern shipbuilding, a range of weld filler materials are used including solid wire, metal-cored wire, and flux-cored wire. These wires are used for specific applications and their ability to be used in various weld positions. The experimental base case followed the parameters that are typically employed in industry to weld 8

mm DH36, which uses 1 mm diameter MC-1 metal-cored wire for the first pass and 1.2 mm diameter SF-1A flux-cored wire for the second and third passes; the chemical compositions of each wire are shown in Table 2.4. The wire feed rate was kept constant at 111 mm/s for both wires.

Two separate shielding gases were used throughout the experimentation; premixed argon / 20% carbon dioxide, and helium. The base case was the premixed argon / carbon dioxide mixture, and was compared against alternating between helium and argon / carbon dioxide at four alternating frequencies; 2, 4, 6, and 8 Hz. The shielding gases were delivered at a constant flow rate of 15 l/min.

Thermal data was captured during and after welding by locating K-type thermocouples located at the mid-length of the plate, 10 and 60 mm from the weld centreline. Hence, it was assumed that the temperature distribution was symmetrical about the centreline of the weld.

The deformation of the workpiece was measured using an optical distance sensor prior to welding (after the plates had been tacked in the butt configuration), and after a cooling period of 45 minutes from completion of the final weld pass, the difference between the two data sets being the weld-induced distortion.

The welding parameters were recorded using an AMV3500 P.A.M.S. unit, and the shielding gas flow rate set using a Regula® welding monitor; the average parameters for each weld pass are shown in Table 5.1.

Table 5.1: DH36 trials typical welding parameters

		Shielding gas configuration				
		Ar / CO_2	Alternating @ 2 Hz	Alternating @ 4 Hz	Alternating @ 6 Hz	Alternating @ 8 Hz
Pass 1	Voltage (V)	21.85	22.05	21.90	21.90	21.80
	Current (A)	154.0	145.0	159.0	163.5	168.0
	Travel speed (mm/s)	2.6	2.6	2.6	2.6	2.6
	Filler wire	MC-1	MC-1	MC-1	MC-1	MC-1
Pass 2	Voltage (V)	23.95	24.10	24.10	24.10	24.05
	Current (A)	205.5	151.5	155.5	167.5	169.5
	Travel speed (mm/s)	3.4	4.0	4.0	4.0	4.0
	Filler wire	SF-1A	MC-1	MC-1	MC-1	MC-1
Pass 3	Voltage (V)	24.15	24.25	24.35	24.15	24.15
	Current (A)	195.5	149.5	154.0	165.5	164.0
	Travel speed (mm/s)	3.4	6.2	6.2	6.2	6.2
	Filler wire	SF-1A	MC-1	MC-1	MC-1	MC-1

5.3.2 Mechanical property trials – 6082T6 aluminium

Experimental welding trials were conducted upon an automatic welding rig using 6 mm thick 6082T6 grade aluminium in the form of 250 x 125 mm plates, with a 30° edge preparation while leaving a 1.5 mm root face. Butt welds were conducted with a ceramic backing strip applied to the underside of the workpiece to support the weld root, as shown in Figure 5.3.

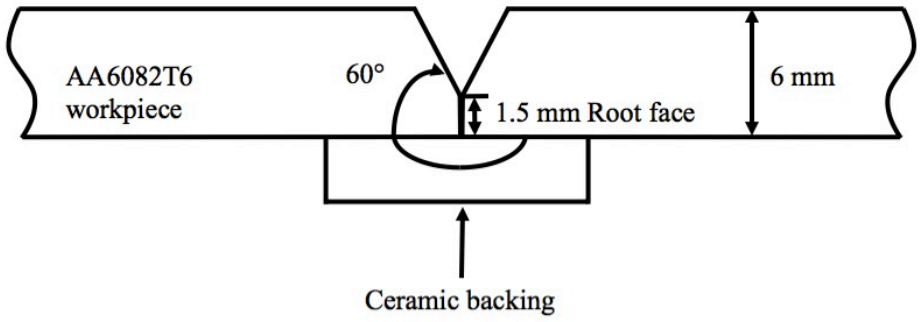

Figure 5.3: Schematic diagram of AA6082T6 experimental setup

The filler wire used throughout was 1.2 mm diameter Alumig Si5 4043 aluminium wire with the typical chemical composition shown in Table 2.4.

Three separate shielding gas supplies were used throughout this experimental programme: argon, helium and premixed argon / 10% helium. This allowed a number of comparisons to be made between the effects of (a) alternating gases, (b) premixed argon + 10% helium, and (c) pure argon (used as the base case for comparison). In each case, a flow rate of 15 l/min was adopted when flowing continuously.

Thermal data for each weld was captured using both a thermal imaging camera and K-type thermocouples at the mid-point of the plates, between 10 and 80 mm from the weld centreline in 10 mm increments. It was assumed that the temperature distribution within the plates was symmetrical; hence, readings were captured from one side of the weld. The symmetry assumption was confirmed through the thermal imaging camera, which was positioned directly above the workpiece and analysed using ThermaCAM Researcher. Prior to welding, the workpieces were coated with high emissivity paint (≅1) to ensure accurate data collection by the thermal imaging camera.

The deformation of the workpiece was measured using an optical distance sensor prior to welding (after the plates had been tacked in the butt configuration), and after a cooling period of 45 minutes from completion of the final weld pass, the difference between the two data sets being the weld-induced distortion.

The welding parameters were recorded using an AMV3500 P.A.M.S. unit, and the shielding gas flow rate set using a Regula® welding monitor; the average parameters for each weld pass are shown in Table 5.2.

Table 5.2: 6082T6 trials typical welding parameters

	Shielding gas configuration				
	Argon	Ar / He	Alternating @ 2.5 Hz	Alternating @ 5 Hz	Alternating @ 7.5 Hz
Mass flow ratio (argon : helium)	1 : 0	9 : 1	10 : 1	10 : 1	10 : 1
Voltage (V)	20.7	20.7	20.7	20.7	20.7
Current (A)	129	126	121	121	125
Travel speed (mm/s)	6.2	6.4	6.7	6.9	7.1

Preliminary experiments were conducted in the form of bead-on-plate trials to determine the travel speed required to produce equivalent levels of penetration. This determined that for each 2.5 Hz increase in alternating frequency; a 0.2 mm/s increase in travel speed could be permitted. This theory was then extended to the butt weld set-up, in which a number of trials were conducted at 2.5 Hz to determine what travel speed would result in full penetration of the joint.

5.3.3 Thermal property analysis

A series of bead-on-plate welds were performed using an automatic welding rig at a constant travel speed of 3.2 mm/s. Trials were performed on 150 x 500 x 8 mm DH36 steel plate using 1.2 mm diameter SF-1A filler wire and a constant stand-off distance of 10 mm. Nominal weld parameters of 210 A and 24.7 V were used throughout.

Two shielding gas supplies were used throughout, premixed argon / 20% carbon dioxide and pure helium. The shielding gas configurations analysed are presented in Table 5.3.

Table 5.3: Shielding gas configurations

Shielding gas	Delivery method	Flow rate (l/min)
Argon / 20% carbon dioxide	Constant	5, 10, 15
Helium	Constant	5, 10, 15
Argon / 20% carbon dioxide Helium	Alternating @ 2, 4, 6, 8 Hz	5, 10, 15

All thermal analysis specimens were machined from the weld metal and, for comparison purposes; a set was also prepared from the parent material. Specimens were prepared as follows; 4 mm diameter cylindrical rods, 25.5 mm length samples were taken in the longitudinal weld direction for dilatometry, 4 mm diameter discs, 2 mm in height, for simultaneous thermal analysis, and 12.5 mm discs, 3 mm height for laser flash analysis.

5.4 Results and discussion

5.4.1 Mechanical property trials – DH36 grade steel

The average heat input, Table 5.4, for each shielding gas configuration was calculated using equation (2.1). Ignoring the effects of a thermal efficiency factor (i.e. assuming unity thermal efficiency), the average current and voltage for each shielding gas configuration were obtained from the P.A.M.S. unit.

The heat transmitted to the workpiece is important due to a correlation with temperature distributions, and consequently the level of weld-induced distortion produced. In addition, the heat input also affects the recrystalisation rate of the HAZ [5.12]. As expected, the increased travel speed permitted when using alternating shielding gas configurations for the second and third passes showed a considerable

reduction in heat input. In contrast, the argon / 20% carbon dioxide base case had an increased heat input caused by the higher current and slower travel speed used. There is also a trend between the frequency of alternation and the induced heat input with the lower frequency producing the lowest heat input and higher frequencies resulting in higher heat inputs.

Table 5.4: Heat input data

	Shielding gas configuration				
	Ar / CO_2	Alternating @ 2 Hz	Alternating @ 4 Hz	Alternating @ 6 Hz	Alternating @ 8 Hz
Pass 1 (J/mm)	1294.19	1229.71	1339.27	1377.17	1408.62
Pass 2 (J/mm)	1447.57	912.79	936.89	1009.19	1019.12
Pass 3 (J/mm)	1388.63	584.74	604.82	644.65	638.81
Total (J/mm)	4130.39	2727.24	2877.98	3031.01	3066.55

The thermal transient data for each shielding gas configuration is shown in Figure 5.4. It can be observed that the argon / 20% carbon dioxide produces a higher peak temperature in each of the three passes than any of the alternating cases. This can be partially attributed to the width of the root gap for the argon / 20% carbon dioxide case, which was 1 mm wider than used for the alternating cases. In addition, the travel speed used in the second and third passes was considerably slower for the argon / 20% carbon dioxide case, thus increasing the heat transfer to the workpiece.

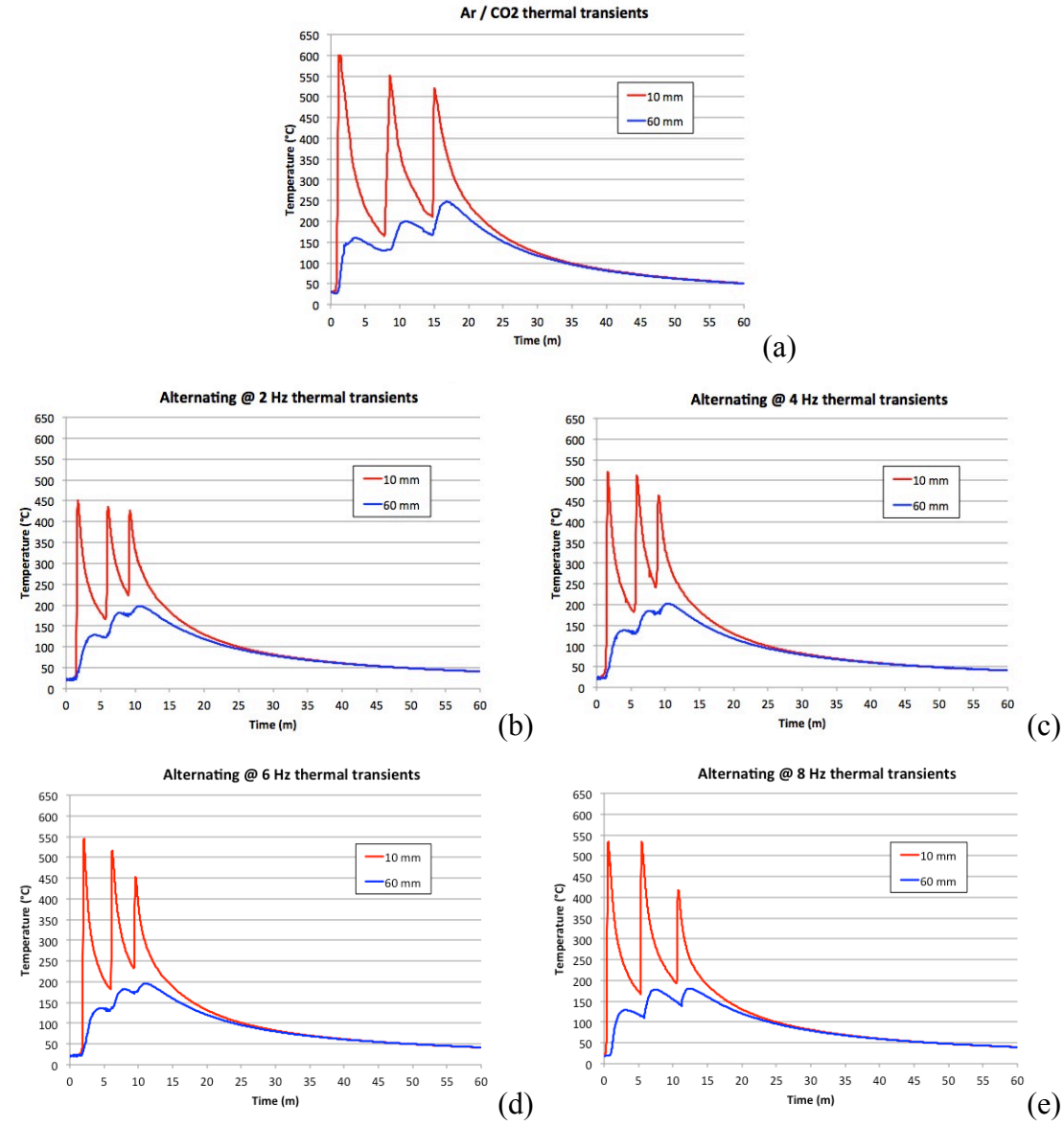

Figure 5.4: Thermal transients for (a) Argon / 20 % carbon dioxide, (b) alternating at 2 Hz, (c) alternating at 4 Hz, (d) alternating at 6 Hz, and (e) alternating at 8 Hz

When considering the thermal transients for the alternating gas cases, it can be noted that the peak temperature draws a parallel to the heat input, i.e. the faster the alternating frequency, the higher the heat input and consequently peak temperature.

Many structures are constructed using an assembly process, and consequently distortion can be detrimental when the welded sub-structures have to be aligned and joined together. Distortion rectification is a major expenditure for manufacturing

companies and therefore, a reduction in distortion at source will reduce the amount of rework required and will consequently lead to productivity savings.

All welded plates distorted according to a classic saddle-like shape as previously illustrated in Figure 3.14. The maximum levels of distortion present in each plate are shown in Table 5.5. Longitudinal distortion is an averaged value of the distortion experienced at the start and end of the weld, whereas the transverse distortion is an averaged value of the left and right edges of the plate. As can be seen, the distortion experienced by the alternating shielding gas compositions is considerably lower than the premixed base case. Overall, the use of alternating shielding gases has resulted in the distortion at the centre of the plate being reduced by 18 – 38%, longitudinal distortion by 16 – 30%, and transverse distortion by 11 – 15%. This is mainly due to the reduced heat input as a consequence of the increased travel speeds and the lower volume of weld metal in the joint.

Table 5.5: Average distortion measurements

Shielding gas configuration	Distortion at centre of plate (mm)	Longitudinal distortion (mm)	Transverse distortion (mm)
Argon / CO_2	-4.405	-8.054	3.488
Alternating @ 2 Hz	-3.346	-6.211	3.030
Alternating @ 4 Hz	-3.482	-6.473	3.070
Alternating @ 6 Hz	-3.180	-6.187	3.144
Alternating @ 8 Hz	-3.733	-6.959	3.065

The distortion was also broken down into its transverse (angular) and longitudinal components. Transverse distortion data is presented at the mid-length of the workpiece, perpendicular to the weld bead, while longitudinal distortion data is parallel to the weld bead.

The transverse distortion for each shielding gas configuration is shown in Figure 5.5, with the mid-point of the workpiece taken as the zero reference in order to provide a direct comparison

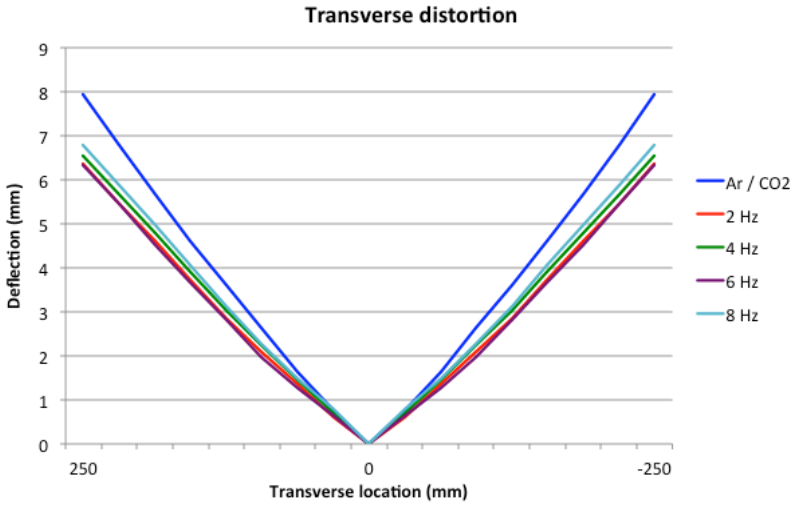

Figure 5.5: Transverse distortion

It can be observed that the transverse distortion experienced by the four alternating configurations (6.32 – 6.80 mm) is considerably lower than that experienced by the argon / 20% carbon dioxide base case (7.94 mm). The deflection angle can therefore be determined to be 1.45 – 1.56° and 1.82°, for the alternating and base cases respectively.

Similarly, the longitudinal distortion component of distortion, Figure 5.6, showed that the argon / 20% carbon dioxide case resulted in approximately 1 – 2 mm more distortion than the alternating gas cases. This corresponds to the alternating shielding gas process producing a reduction in longitudinal distortion of 16 – 33%, when averaged along the length of the workpiece.

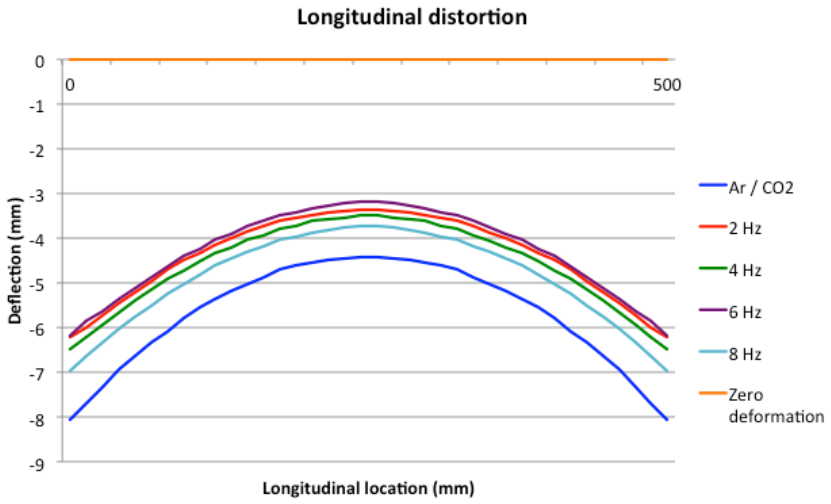

Figure 5.6: Longitudinal distortion

It can be noted in the distortion plots that the alternating cases produce considerably less deformation that the argon / 20% carbon dioxide base case, which is in line with the heat input calculated previously. In addition, when considering only the alternating cases, it can be observed that, in general, a higher alternating frequency results in higher levels of deformation.

Longitudinal all-weld and transverse tensile tests were conducted in accordance with BS EN ISO 10002-1:2001. The all-weld tensile results are important to determine the tensile properties of weld metal to ensure the mechanical properties conform to the filler metal specifications, and to determine the effect that shielding gas composition has on such mechanical properties. The results for the all-weld tests are shown in Table 5.6. When compared to the argon / 20% carbon dioxide base case, the 0.2 per cent proof stress (0.2% PS) and ultimate tensile strength (UTS) of the alternating shielding gas welds were found to increase by 4.6 – 6.9% and 5.6 – 9.6%, respectively. More specifically, the 2 Hz alternating frequency showed the greatest increase in strength with the 0.2% PS and UTS increasing by 9.6 and 6.9%, respectively.

Table 5.6: Longitudinal all-weld tensile results

Shielding gas configuration	0.2 % PS (MPa)	UTS (MPa)	% Elongation	% Reduction in area
Argon / CO_2	446	554	32.0	73.0
Alternating @ 2 Hz	489	592	28.0	68.0
Alternating @ 4 Hz	472	580	26.5	68.0
Alternating @ 6 Hz	471	586	30.0	67.5
Alternating @ 8 Hz	471	585	29.0	73.0

The percentage elongation and percentage reduction in area was reduced for the alternating gas compositions, indicating that the ductility of the weld is reduced. Hence, alternating shielding gases produces a higher strength, lower ductility weld than the argon / 20% carbon dioxide base case.

Transverse tensile testing is normally conducted to ensure that the joint produced by the welding procedure meets or exceeds the design strength requirements. As a result of its orientation, the test incorporates a full cross section of the weld metal, heat affected zone, and parent material.

Transverse tensile tests were also conducted, Table 5.7, and these showed results favourable to the use of alternating shielding gases, with a percentage increase of between 4 – 7.5% UTS, again with the alternating at 2 Hz configuration showing the greatest benefits. All transverse tensile tests failed within the weld metal.

Table 5.7: Transverse tensile results

Shielding gas configuration	UTS (MPa)
Argon / CO_2	580
Alternating @ 2 Hz	624
Alternating @ 4 Hz	621
Alternating @ 6 Hz	617
Alternating @ 8 Hz	606

The impact toughness of the weld metal and the HAZ was assessed by means of Charpy impact toughness tests, conducted in accordance with EN 10045-1:1990. Due to the thickness of the workpiece, sub-sized specimens of 10 x 5 x 55 mm were used. A conversion factor of 3/2 was subsequently used to normalise the sub-size specimen to that of a standard specimen, with the results presented in Table 5.8. The average energy absorbed in the weld metal and HAZ of each alternating gas configuration is greater than that of the argon / 20% carbon dioxide base case, increases of 4.2 – 18.9% and 4.6 – 53.1% respectively.

Table 5.8: Charpy impact results (conducted at -20°C)

Shielding gas configuration	Absorbed energy (J) - weld	Absorbed energy (J) - HAZ
Argon / CO_2	78.00	76.75
Alternating @ 2 Hz	87.00	80.25
Alternating @ 4 Hz	92.75	116.75
Alternating @ 6 Hz	81.25	87.50
Alternating @ 8 Hz	82.75	95.00

The increase in impact toughness is, accounting for anomalies such as the absorbed energy in the HAZ for the alternating at 4 Hz cases, consistent and proportional to the decrease in ductility values presented previously for the tensile tests.

The Charpy V-notch impact test is often regarded as the accepted method of toughness assessment for welded joints due to complications in conventional fracture toughness methods as a result of the fusion zone and HAZ exhibiting a heterogeneous microstructure that can have widely varying strength and toughness values.

Face and root bend tests were carried out on the samples according to EN 910:1996, these tests showed that there were no detrimental effects associated with the use of alternating gases.

Microhardness tests were carried out on each specimen using a 200 g weight and 10 s dwell time. The microhardness tests were performed on two axes, vertically from the weld cap to the root in order to obtain the hardness of weld metal only, i.e. the weld centreline, and horizontally from the weld centreline out to the parent plate. This allowed the effect of the shielding gas configuration to be considered with respect to hardness position. The average hardness of the weld metal using alternating gases was 213 Hv, an increase of 8.7% when compared to the argon / 20% carbon dioxide base case, for which an average microhardness of 196 Hv was measured. The average hardness obtained from the horizontal testing is shown in Figure 5.7. This shows that supplying alternating shielding gases increases the hardness of both the weld metal (8.3%) and the HAZ (4.0%), and correlates with the findings of Juan et al. [5.13] that increasing the heat input can reduce microhardness. The increased microhardness of the alternating cases can be attributed to the reduced grain size and had a positive influence on the mechanical properties as discussed previously.

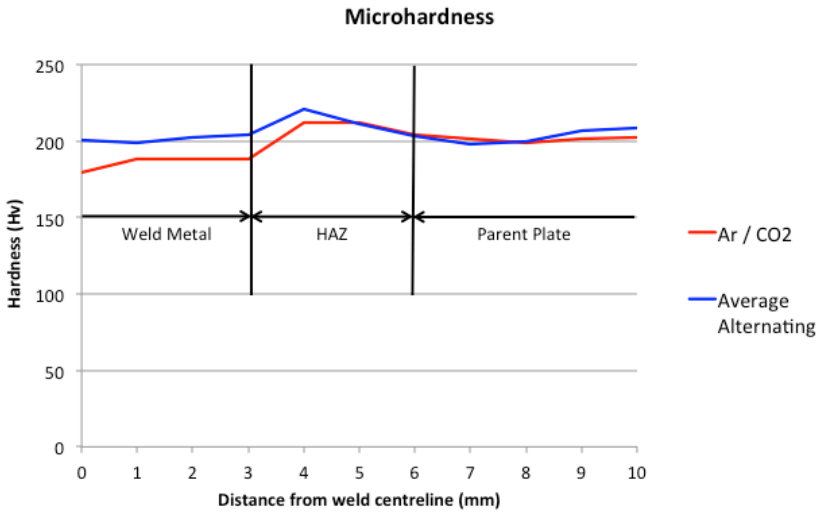

Figure 5.7: Microhardness results

The microstructure of the weld metal and HAZ, shown in Figure 5.8 and 5.9, shows that the grain orientation and grain refinement are enhanced through the application of alternating shielding gases due to the increased cooling rates experienced. The typical microstructure of the weld metal and HAZ for the argon / 20% carbon dioxide specimen is shown in Figure 5.8(a) and Figure 5.9(a). The higher heat input argon / 20% carbon dioxide base case specimens resulted in a coarser microstructure in the HAZ (average grain size of ~8.2 μm), which is a consequence of an increased driving force for grain boundary migration and coarsening. In contrast, the microstructure of the alternating shielding gas case, Figure 5.8(b) and Figure 5.9(b), consist of more acicular ferrite, which are more interlocking and less distinctive in character. The grain boundary ferrite present within the weld metal is also reduced and more diffuse in the alternating shielding gas case. The fine grain structure in the HAZ (average grain size of ~5.1 μm) is a result of accelerated cooling from a higher temperature, thus allowing pearlite to be more evenly distributed resulting in more uniform properties throughout than the spheroidal pearlite found in the argon / 20% carbon dioxide base case. Non-metallic inclusions are also present within the argon / 20% carbon dioxide base case weld metal; these are silicate inclusions as a result of the flux-cored filer wire used. In contrast, the alternating cases exhibit inclusion-free (clean steel) welds, which is primarily due to a combination of the metal-cored wire used and the dynamic action of alternating shielding gases. Banded ferrite pearlite microstructure is also present within the HAZ of the base case, which, theoretically,

could result in different properties for each layer. The observed improvements in mechanical properties discussed previously are most likely to be a consequence of the refined microstructure of the HAZ. The results are comparable to those obtained by Min et al. [5.12] relating grain size to the heat input. The grain structure of the weld cap in all cases was of a classical columnar microstructure, which is indicative of rapid cooling. This feature is typical of mild steel alloy welding where directional solidification due to the heat distribution from the electric arc source occurs.

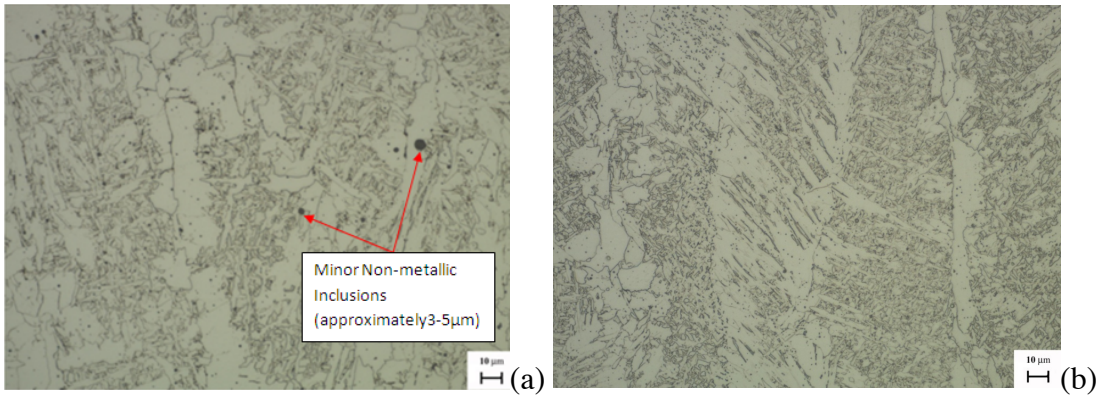

Figure 5.8: Weld metal microstructure (x500 magnification) for (a) argon / 20% carbon dioxide base case showing non-metallic inclusions, and (b) alternating shielding gases at 2 Hz

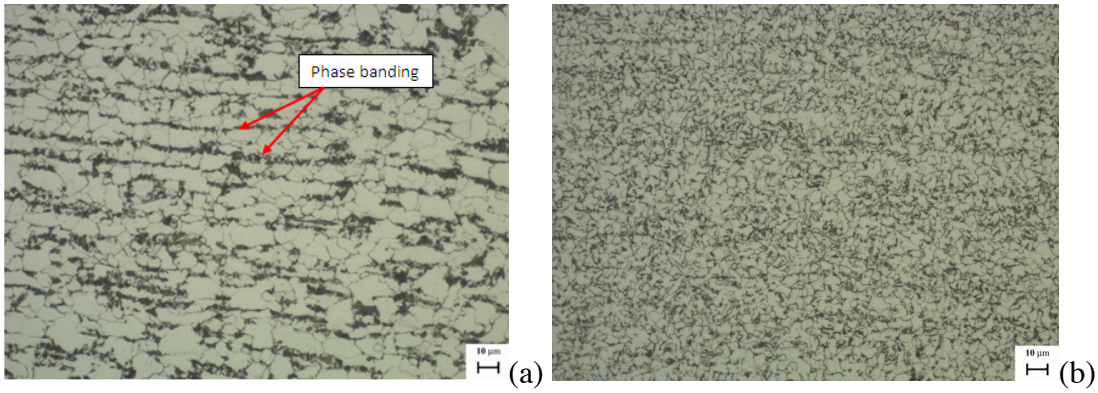

Figure 5.9: HAZ microstructure (x500 magnification) for (a) argon / 20% carbon dioxide showing phase banding, and (b) alternating shielding gases at 2 Hz

The overall cost involved with the use of various shielding gases is also important. Shielding gas compositions involving helium are often neglected due the high gas

unit costs. However, as shown in Table 5.9, the gas cost makes up such a small contribution to the total cost of the weld in comparison to the labour costs and filler wire costs that it is in fact the travel speed that has a major bearing on the weld cost. Therefore, the increase in travel speed permitted through the use of helium outweighs the unit cost of the gas.

For calculation purposes, welding labour costs were estimated at £15/h with 1/3 arc time, while gas and filler wire costs were calculated using proprietary bulk prices. It can be seen in Figure 5.10, that the high unit cost of helium increases the gas cost of alternating shielding gases to about five times the price of premixed argon / 20% carbon dioxide. However, the gas cost in relation to the total weld cost is minimal when compared to the labour costs, which accounts for approximately 80% of the overall cost. Therefore, welding travel speed is the controlling factor in the overall cost of a weld, and if it can be significantly increased, as in the alternating gas cases, not only will the weld productivity increase and a cost reduction be experienced, but there will also be a reduction in filler wire costs. The increased speeds associated with alternating shielding gases has contributed to an approximately 17% saving when comparing the total costs of each gas configuration. In addition to the 17% saving in overall weld costs, there would also be considerable productivity savings associated with the reduced weld-induced distortion discussed previously.

Table 5.9: Cost analysis of alternating shielding gases

		Alternating shielding gases	Argon / 20% carbon dioxide
Time / pass (s)	Pass 1	192.31	192.31
	Pass 2	125.00	147.06
	Pass 3	80.65	147.06
	Total	397.96	486.43
Labour cost (£/m)	Total	9.95	12.17
Gas cost / plate (£)	Pass 1	0.20	0.03
	Pass 2	0.13	0.02
	Pass 3	0.09	0.02
	Total	0.42	0.08
Gas cost (£/m)	Total	0.85	0.16
Wire cost / plate (£)	Pass 1	0.55	0.55
	Pass 2	0.36	0.45
	Pass 3	0.23	0.45
	Total	1.13	1.46
Wire cost (£/m)	Total	2.27	2.91
Electricity usage (kWh)	Pass 1	0.56	0.44
	Pass 2	0.41	0.50
	Pass 3	0.26	0.50
	Total	1.23	1.44
Electricity cost (£/m)	Total	0.12	0.17
Total (£/m)	Total	13.18	15.41
Percentage saving	Total	16.85	

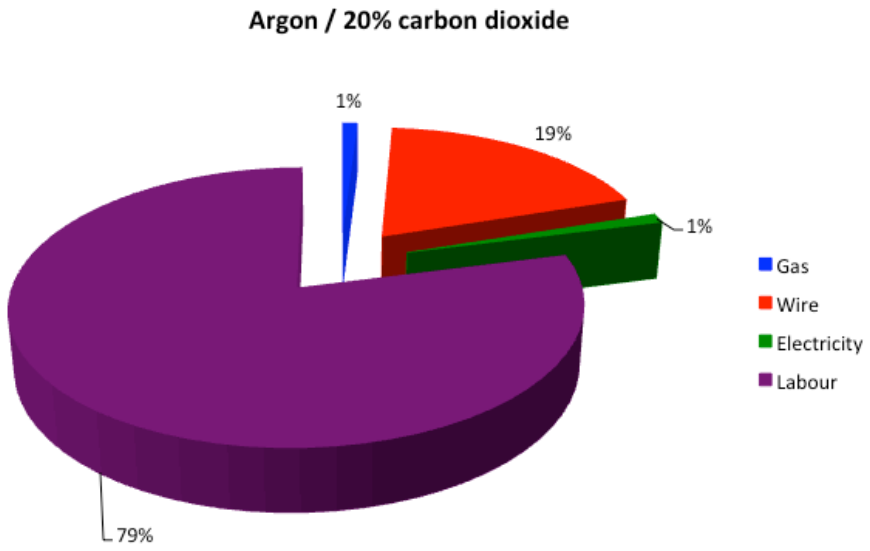

(a)

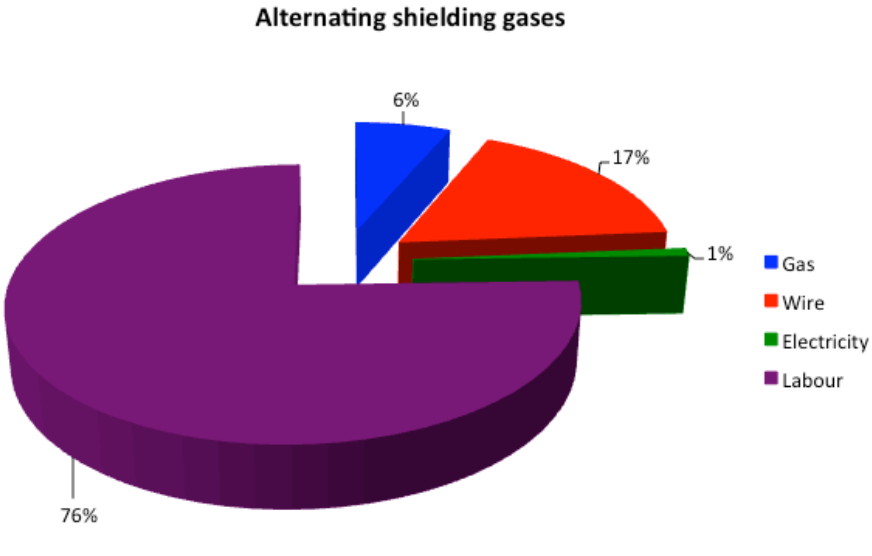

(b)

Figure 5.10: Cost analysis breakdown for (a) argon / 20% carbon dioxide, and (b) alternating shielding gases

5.4.2 Mechanical property trials – 6082T6 aluminium

As was the case for the trials conducted on steel, the average heat input for each shielding gas configuration was calculated using equation (2.1), Table 5.10. The heat input for the alternating cases is greatly reduced as an outcome of the increased travel speed.

Table 5.10: Heat input data

	Shielding gas configuration				
	Argon	Ar / He	Alternating @ 2.5 Hz	Alternating @ 5 Hz	Alternating @ 7.5 Hz
Heat input (J/mm)	430.7	407.5	373.8	363.0	364.4

Thermal imaging data was collected in order to validate the data obtained through the use of thermocouples. Figures 5.11 and 5.12 show the data produced through thermocouples and thermal imaging, respectively, for argon and alternating gases at 7.5 Hz. The points indicated on the thermal imaging correspond to the approximate location of each thermocouple, and their values show good correlation to that recorded by each thermocouple.

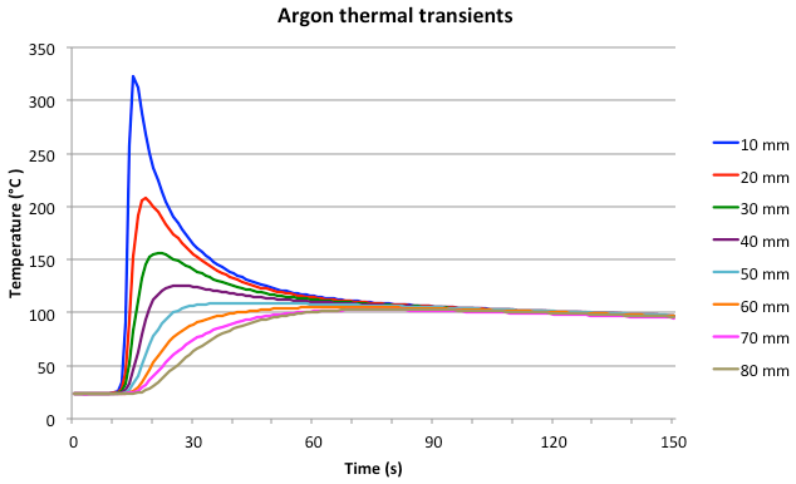

(a)

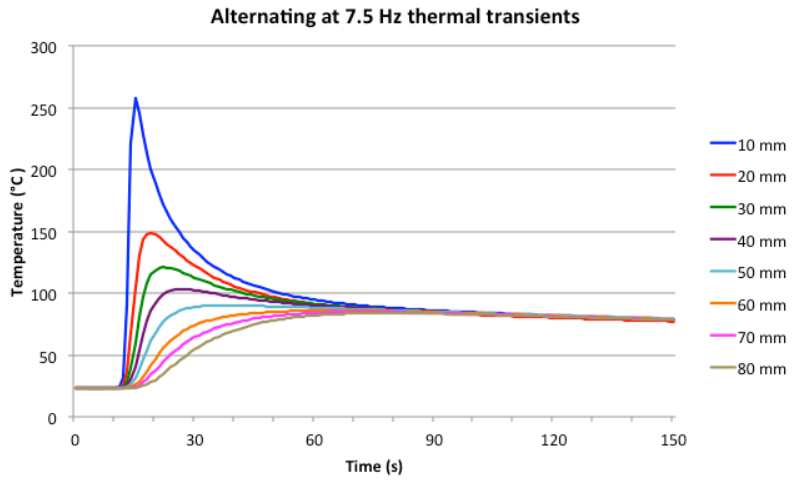

(b)

Figure 5.11: Thermal transients for (a) argon, and (b) alternating at 7.5 Hz

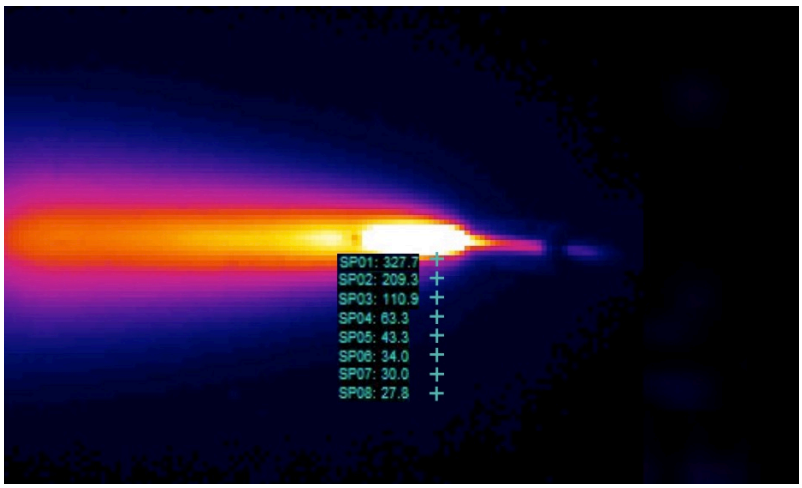

(a)

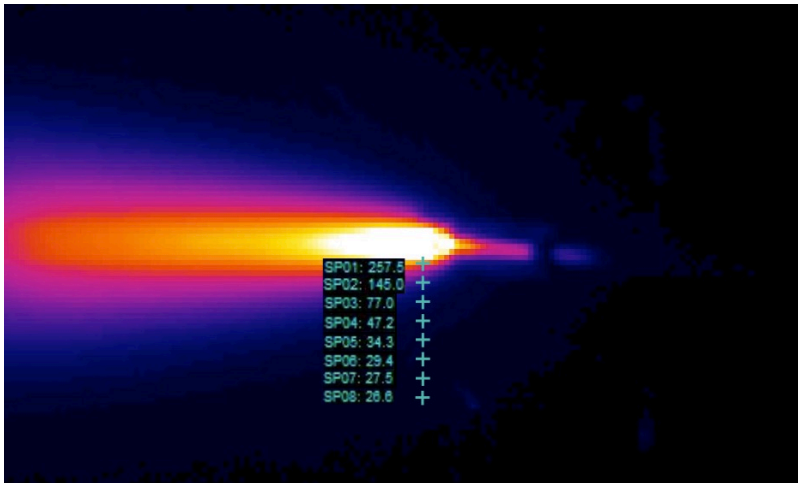

(b)

Figure 5.12: Thermal imaging data for (a) argon, and (b) alternating at 7.5 Hz

The peak temperature (Table 5.11), i.e. 10 mm from the weld centreline, and the temperature distribution of the alternating gas cases are shown to be considerably reduced compared with the premixed argon + 10% helium gas and the argon base case. The peak temperature of the alternating cases (255 – 280 °C) were found to be approximately 45 – 70 °C lower than that of the constant argon case (~325 °C), while the premixed argon / 10% helium case was approximately half way between (~295°C). This is a result of both the reduced heat input and the narrower arc column produced by helium [5.15]. The thermal data also corresponds to those obtained in the DH36 trials, which found that the peak temperature when implementing alternating shielding gases was reduced.

Table 5.11: Peak temperature data (recorded by thermocouple)

	Shielding gas configuration				
	Argon	Ar / He	Alternating @ 2.5 Hz	Alternating @ 5 Hz	Alternating @ 7.5 Hz
Temperature (°C)	324.3	296.5	278.2	262.1	255.7

As a result of longitudinal and transverse shrinkage, the workpiece deformed according to a classical saddle-like shape. Table 5.12 shows the percentage reduction in the maximum distortion experienced by the structure as a function of the shielding gas configuration when compared with the argon base case. The lower heat input, as a result of the increased travel speed, permitted through the addition of helium to the shielding gas configuration has resulted in an overall reduction in distortion; the premixed argon / 10% helium gas has reduced the maximum distortion present by 12%, whilst the use of alternating shielding gases resulted in a considerable reduction of 25–36%.

Table 5.12: Distortion reduction compared to argon base case

	Shielding gas configuration			
	Ar / He	Alternating @ 2.5 Hz	Alternating @ 5 Hz	Alternating @ 7.5 Hz
Distortion reduction (%)	12	25	36	34

The level of distortion in each plate has been shown to be proportional to the amount of welding heat input. The reduced heat input for the alternating cases, as a result of the increased travel speed, therefore correlates with the reduction in distortion achieved by supplying a premixed shielding gas and by the alternating method. This is a result of the alternating method taking advantage of the supply of pure helium, which produces greater penetration than argon as a result of its higher first ionisation energy, therefore producing a smaller cathode spot.

Transverse tensile tests were conducted in accordance with BS EN ISO 10002-1:2001, the results of which can be seen in Figure 5.13, with all tests failing within the weld metal.

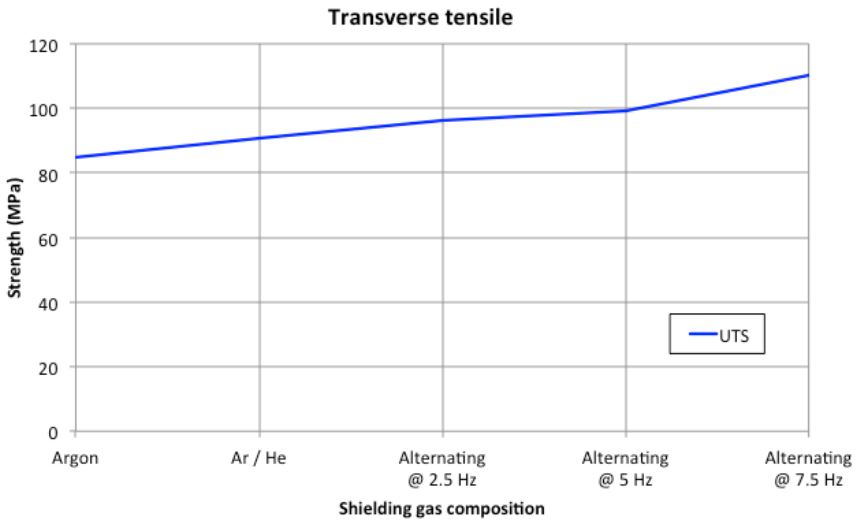

Figure 5.13: Transverse tensile results

As can be seen, the argon base case produced a weld strength of approximately 85 MPa, while premixed argon / 10% helium produced a strength of approximately 91 MPa, and alternating shielding gases produced welds with strength in the region 95 – 110 MPa. It has been shown that the frequency of alternation also has an influence on the tensile strength of the weld, with an increased frequency resulting in an increased strength. This is contrary to the results obtained for steel, which showed a lower alternating shielding gas frequency produced higher strength welds.

Root bend tests were carried out on the samples according to EN 910:1996, these tests showed that there were no detrimental effects associated with the use of alternating gases.

In order to assess any effects that the various shielding gas supply methods have on the microstructure and HAZ of the weld, metallographic analyses were performed on a sample from each shielding gas configuration. Macro sections were extracted and prepared according to Section 2.8.1.

Helium is generally used on thicker sections of material, and in applications where the workpiece has a high thermal conductivity, such as aluminium, due to its higher

heat flux [5.16]. Jönsson et al. [5.15] reported that helium is added to gas combinations due to its ability to increase the weld depth to width ratio in comparison with constant argon. This has also been shown to be the case when implementing alternating shielding gases, even with a faster travel speed, as presented in Table 5.13 and depicted in Figure 5.14. The weld area indicates that the shielding gas configuration has a pronounced effect on the melting efficiency; the addition of helium to the shielding gas (both in the premixed and alternating cases) producing a larger weld area than the constant argon base case. When comparing the helium containing shielding gas configurations, alternating shielding gases was found to generate a larger weld area than the premixed argon / 10% helium shielding gas. While the frequency of alternation does not appear to have a huge influence on the weld area, the small difference generated between each frequency is a result of the different travel speeds implemented.

Table 5.13: Weld geometry

	Shielding gas configuration				
	Argon	Ar / He	Alternating @ 2.5 Hz	Alternating @ 5 Hz	Alternating @ 7.5 Hz
Weld width (mm)	10.5	10.0	10.0	9.5	8.0
Weld depth (mm)	5.0	Full	Full	5.5	Full
Weld area (mm^2)	29.6	35.0	40.8	39.7	38.3

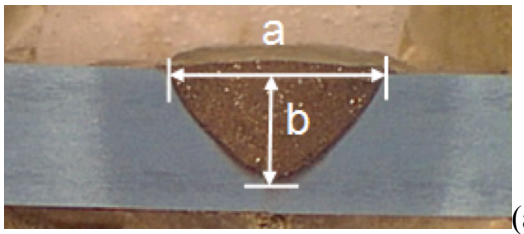

(a)
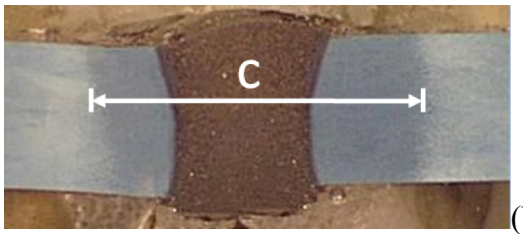

(b)

Figure 5.14: Weld macrograph for (a) argon (showing measurements for weld width and depth), and (b) alternating at 7.5 Hz (showing measurement for the HAZ width)

The addition of helium, both in premixed and alternating shielding gas configurations, was found to constrict the width of the HAZ, Table 5.13. This is, in part, due to the reduced heat input, as a result of the increased travel speeds permitted, but also a consequence of the temperature distribution in the arc column. Moreover, it has been shown that increasing the frequency of alternation further reduces the HAZ width, primarily linked to the increased travel speed.

The percentage inclusions was determined using ImageJ, which determined the percentage of each image that exhibited a shade contrast to that of the bulk material. Images were taken systematically from around the weld pool in order to categorise the cleanliness of the weld, examples of the images analysed are shown in Figure 5.15, and the inclusion percentage for each gas configuration are documented in Table 5.14.

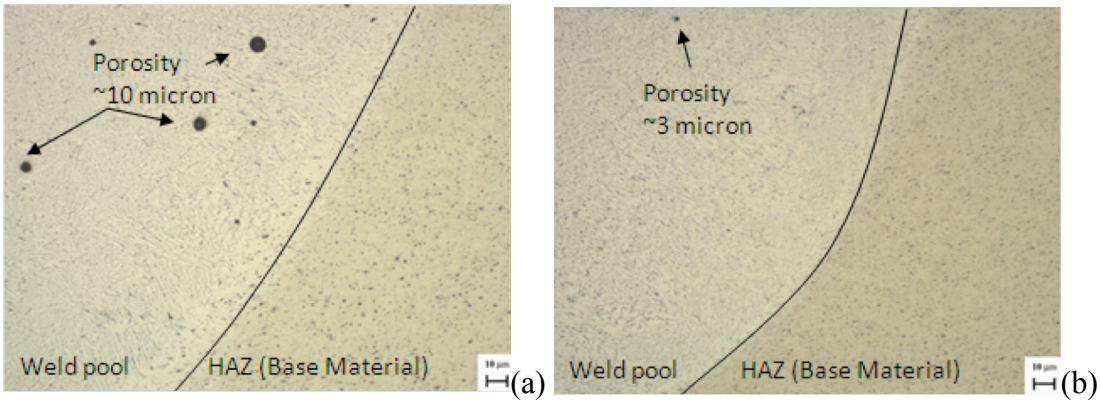

Figure 5.15: Weld micrograph (x100 magnification) for (a) argon, and (b) alternating at 5 Hz

Table 5.14: Inclusion percentage

	Shielding gas configuration				
	Argon	Ar / He	Alternating @ 2.5 Hz	Alternating @ 5 Hz	Alternating @ 7.5 Hz
Inclusion percentage (%)	0.5252	0.3973	0.2484	0.1234	0.0926

The premixed argon / 10% helium mixture produced a reduction in percentage inclusions compared with the argon base case, which has been attributed to an

increase in weld pool fluidity. It can also be noted that the inclusion percentage is further reduced through the application of alternating shielding gases, this is in agreement with the findings of Kang et al. [5.2] who demonstrated that alternating shielding gases reduced the porosity present in the welding of 1420 and 1460 aluminium.

It can therefore be inferred that the stirring action generated as a result of the oscillating arc forces, calculated in Chapter 4, when using alternating shielding gases, aids the gas bubbles escape the molten weld pool. It has also been shown that increasing the frequency of alternation can further reduce the levels of porosity present within the weld. The percentage inclusions therefore follows the same trend as the tensile strength of the weld, in that an increasing frequency of alternation resulted in less inclusions in the solidified weld, and consequently increased the tensile strength of the weld.

5.4.3 Thermal property analysis

The coefficient of linear thermal expansion for each specimen was evaluated through the use of a push-rod dilatometer in accordance with ASTM E228-11.

Figure 5.16 shows the fractional change in specimen length, and thermal expansion coefficient vs. temperature, for alternating shielding gases at a frequency of 8 Hz over the shielding gas flow rates investigated, and shows the characteristic phase change at approximately 700 °C. As expected, there is a degree of variation in the thermal property data around the phase change temperature. The important aspect that is being emphasised is that there is a definite difference in the thermal properties as a function of the shielding gas parameters. The technical alpha curve gives the average expansion coefficient over the temperature range, and is given by:

$$\beta = \frac{1}{L_{initial}} \frac{(L_{final} - L_{initial})}{(T_{final} - T_{initial})} \tag{5.1}$$

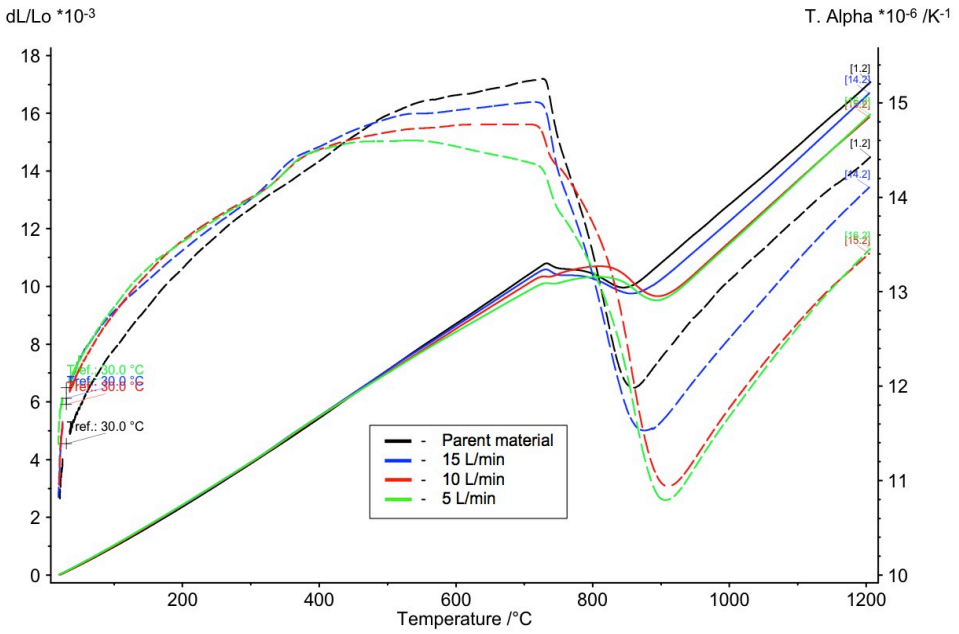

Figure 5.16: Thermal expansion data for alternating shielding gases at 8 Hz

The parent material consistently exhibited the highest linear thermal expansion coefficient above approximately 400 °C, which was in line with other studies [5.9, 5.10], and was consistently higher than all weld metal specimens. As can be noted when comparing the weld metal specimens, the 15 l/min shielding gas flow rate specimen exhibited the greatest linear thermal expansion coefficient over the temperature range of the experiment. A similar trend was found for each shielding gas configuration, i.e. the lower the shielding gas flow rate, the lower the linear thermal expansion coefficient of the weld metal.

When comparing the linear thermal expansion coefficient for the weld metal for the same shielding gas flow rate, Figure 5.17, it can be noted that the argon / 20% carbon dioxide specimen maintained a higher thermal expansion coefficient than the helium configuration, this was the case each of the three shielding gas flow rates evaluated. However, no trend could be found within the alternating shielding gas configurations used, although they were generally within the upper bound of the argon / 20% carbon dioxide, and the lower bound of the helium specimen.

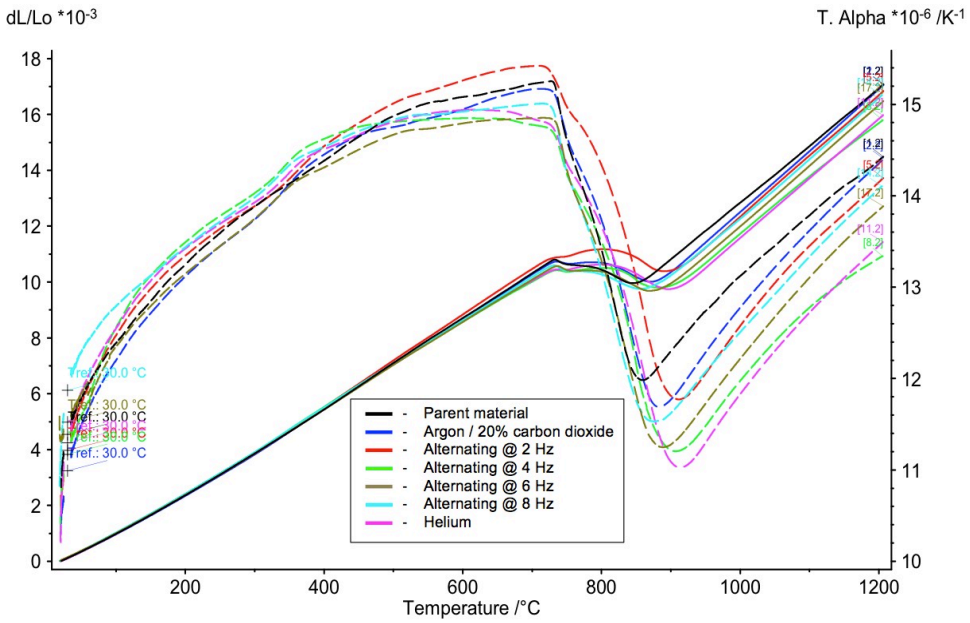

Figure 5.17: Thermal expansion data for constant shielding gas flow rate (15 l/min)

As the thermal expansion coefficient changes in a material, its expansion-contraction due to various temperatures is understandably affected. Due to the rapid, non-equilibrium heating/melting of the weld metal, coupled with the constraint imposed by the surrounding plate, the filler material does not have sufficient time to expand. Upon cooling of the weld metal, heat is conducted to the adjacent plate, resulting in contraction of the weld metal and expansion of the surrounding material. Once thermal equilibrium between the weld metal and the adjacent plate occurs, further cooling will take place by convection and approximately uniform contraction will occur. Thus, the majority of weld-induced distortion is introduced to the structure during the cooling phase. This is evident within the welding process where this expansion-contraction effect is highly significant as it has a direct impact upon the residual stresses present within the structure following cooling. The thermal strain introduced to the structure is given by:

$$\varepsilon_{thermal} = \frac{(L_{final} - L_{initial})}{L_{initial}} \tag{5.2}$$

Hence, the thermal strain is proportional to the change in temperature, and can be estimated using:

$$\varepsilon_{thermal} = \beta(T_{final} - T_{initial}) \tag{5.3}$$

As previously stated, higher shielding gas flow rates were found to produce specimens with a higher thermal expansion coefficients over the experimental temperature range. This will therefore lead to a greater volumetric contraction within the weld metal, which will in turn lead to greater residual stress within the structure.

Therefore, when considering the thermal expansion of the weld metal, theoretically the use of a lower flow rate proves beneficial for reducing the distortion present within the final structure. However, this statement is based solely on the experimental temperature range, and therefore neglects temperatures above 1200 °C and the fact that the shielding gas parameters influence the peak temperature within the weld pool. Nevertheless, the solidification temperature for the parent/filler material should be constant across the specimen range, and therefore the temperature at which residual stresses are introduced is constant.

The specific heat capacity for each specimen was evaluated using STA in accordance with ASTM E1269-11.

Figure 5.18 shows specific heat capacity vs. temperature for alternating shielding gases at 2 Hz, and comparing the various flow rates. It was found that the specific heat capacity of the parent material was considerably higher than any of the weld metal configurations, whilst the 5 l/min shielding gas flow rate weld metal exhibits the greatest specific heat capacity, followed by 10 l/min and 15 l/min respectively. A similar trend was found for each shielding gas configuration, i.e. the lower the shielding gas flow rate, the greater the heat capacity of the weld metal.

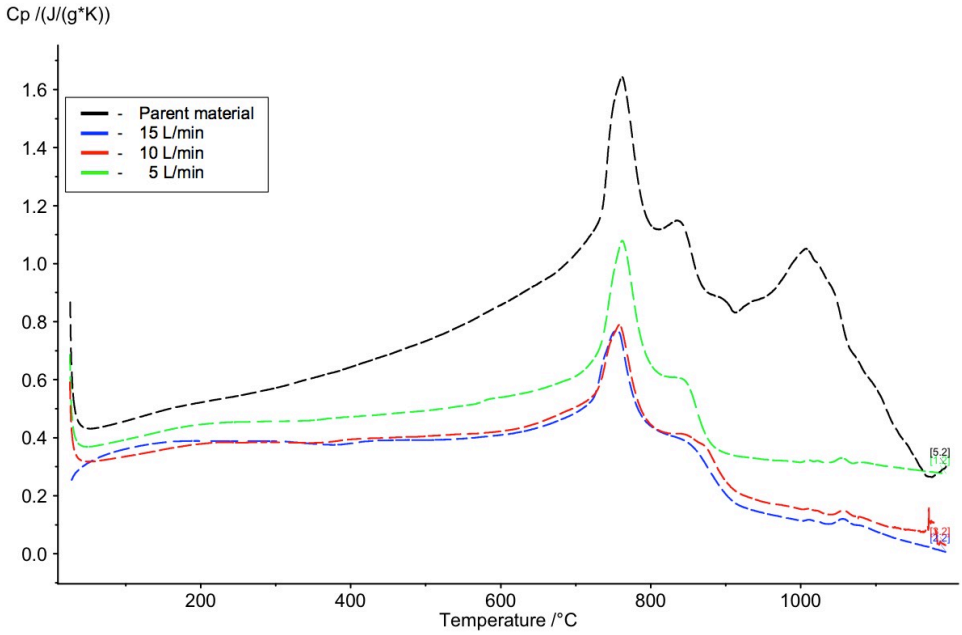

Figure 5.18: Specific heat capacity data for alternating shielding gases at 2 Hz

The specific heat capacity influences various aspects of the welding process, the cooling rate along the centreline of thin plate and the solidification time of the weld metal are given by equation (5.4) and (5.5) respectively [5.17]. These parameters are known to have a significant affect on the metallurgical structure, properties, response to heat treatment, and soundness of the material [5.17].

$$R = 2\pi k\rho C_p \left(\frac{t}{H_{net}}\right)^2 + (T_c - T_0)^2 \tag{5.4}$$

$$S_t = \frac{L_f H_{net}}{2\pi k\rho C_p (T_m - T_{initial})^2} \tag{5.5}$$

As can be noted, a larger weld metal specific heat capacity will result in a faster cooling rate and quicker solidification time than that of a lower heat capacity. A slower cooling rate increases the driving force for grain boundary migration and coarsening. Concurrently, a finer microstructure can be achieved by increasing cooling rate, up to a limit at which point bainitic and subsequently, martensitic transformations occur.

The specific heat capacity for a constant shielding gas flow rate of 10 l/min is shown in Figure 5.19. This allowed for the effect that the shielding gas composition had on the heat capacity and it was found that the helium configuration specimen exhibited a consistently higher heat capacity than the argon / 20% carbon dioxide specimen. Although there was no trend for the alternating frequencies, they generally come within the upper and lower limits imposed by the constant flow shielding gases.

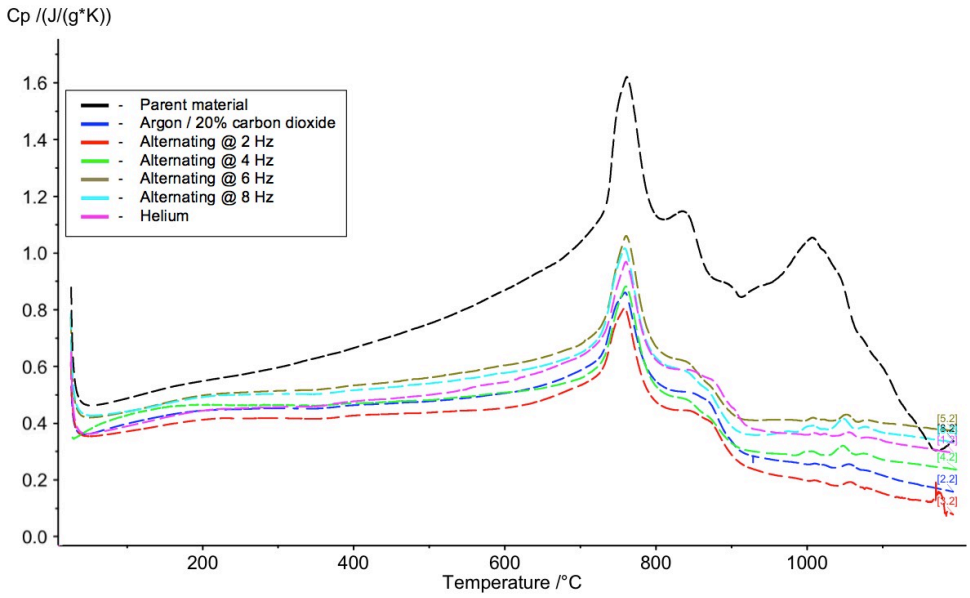

Figure 5.19: Specific heat capacity data for constant shielding gas flow rate (10 l/min)

The thermal diffusivity and thermal conductivity for each specimen was determined using LFA, with the specific heat data obtained from the STA being imported to the LFA to increase the accuracy of the analysis, in accordance with ASTM E1461-11.

As can be seen in Figure 5.20, the 5 l/min shielding gas flow rate produced a higher thermal conductivity than 10 and 15 l/min cases, as the temperature is increased. As with the other analysis conducted, a similar trend was found for each shielding gas configuration, i.e. the lower the shielding gas flow rate, the greater the thermal conductivity of the weld metal.

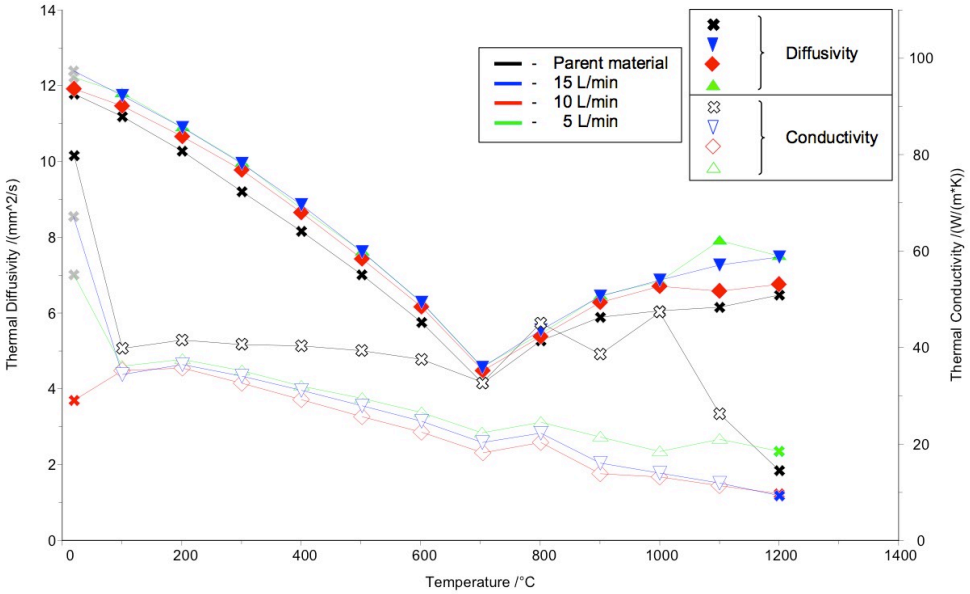

Figure 5.20: Thermal diffusivity and conductivity data for alternating shielding gases at 4 Hz

It can also be noted that the thermal diffusivity across the three welds was almost the same with no configuration being significantly higher or lower. The final pulse however shows some variation, at this temperature it is believed that this effect is a result of the materials physical properties changing. Again, this trend was apparent across all the sets of welds where input flow rate was compared within the same gas configurations.

The thermal conductivity for a constant shielding gas flow rate of 10 l/min is shown in Figure 5.21. It can be seen that the specimen for the argon / 20% carbon dioxide configuration exhibited a marginally higher thermal conductivity than the helium specimen. Although there was no trend for the alternating frequencies, they generally follow the data obtained for the constant flow configurations.

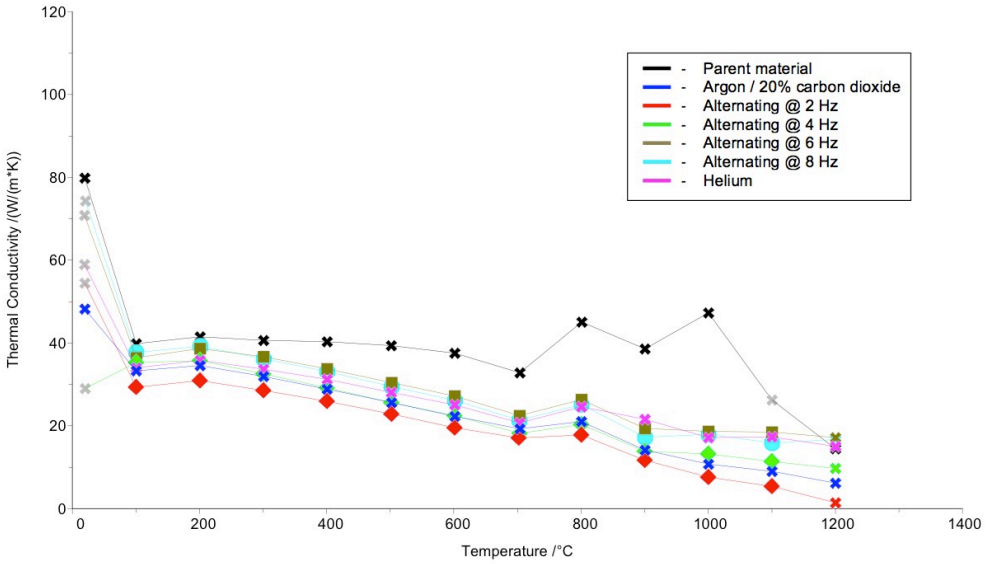

Figure 5.21: Thermal conductivity data for constant shielding gas flow rate (10 l/min)

As thermal conductivity increases, the elevated temperature in the liquid weld metal will change more quickly as the heat can be transferred faster to the surrounding material, resulting in an increased temperature away from the weld [5.18]. This was found to be the case in Chapter 3, when a lower shielding gas flow rate resulted in an increase in temperature 10 mm from the weld centreline. This increase in heat flow will result in the heat flux during the weld being diffused in a shorter space of time. It is suggested that as a result of the temperature flux caused by the welding process being dissipated faster to the surrounding plate, the weld metal and surrounding plate will reach thermal equilibrium quicker and as a result the residual stresses will be lower as the thermal conductivity is increased. Lower residual stresses are expected to occur as the plate will cool more evenly, and there will be a smaller temperature gradient across the structure.

As can be seen in Figure 5.20, the thermal diffusivity is similar for each shielding gas configuration, even though the thermal conductivity varies. This can be explained through equation (5.6) for thermal diffusivity:

$$\alpha = \frac{k}{\rho C_p} \tag{5.6}$$

As discussed previously, the specific heat capacity, was found to follow the same trend as that of the thermal conductivity, i.e. as the flow rate is increased both the heat capacity and thermal conductivity decrease. Although this was not at the same rate, it explains why the thermal diffusivity across all data sets is almost identical when varying the input parameters.

5.5 Conclusions

The mechanical property assessment of alternating shielding gases has identified numerous benefits of implementing this shielding gas supply method in GMAW. The addition of helium permitted a reduced root gap, thus the main benefit determined was an increase in welding travel speed. It is this primary benefit that many of the other benefits are attributed to.

The increase in travel speed has resulted in higher productivity, generating savings of approximately 17%. Although helium containing shielding gases are often disregarded due to their high unit cost, the gas contribution to the total cost of the weld is relatively low in comparison to the labour costs and filler wire costs, that it is in fact the travel speed that has a major bearing on the weld cost. Therefore, by increasing the travel speed, the weld cost can be reduced in spite of the higher gas costs.

In addition to the productivity benefits, the reduced weld metal volume and faster travel speed used when implementing alternating shielding gases has also been shown to have a positive benefit in reducing the distortion induced in the workpiece, and consequently the rework required to rectify it. Overall, these two findings have a positive benefit on the overall productivity associated with this joining process. Similarly, Kang et al. [5.3] observed a reduction in angular distortion when implementing the alternating shielding gas technique on austenitic stainless steel.

It has also been shown that the application of alternating shielding gases has no detrimental effect on the mechanical properties of the weld and HAZ. In fact, marginal improvements in yield and tensile strength, Charpy impact toughness, and hardness are achieved as a consequence of the refined microstructure associated with

the use of the alternating gases. Again, this can be related back to the increased travel speed, reducing the heat input and subsequently the degree of grain migration and coarsening.

The addition of helium to the shielding gas has shown a reduction in the percentage inclusion present within the solidified weld. Kang et al. [5.2] determined that the alternating shielding gas method produced a lower degree of porosity in 5083 Al–Mg aluminium alloy. The reduction in porosity can be attributed to the increased weld pool fluidity as a result of the addition of helium, thus encouraging the gas bubbles to escape from the molten metal. It has also been shown that the application of alternating shielding gases can further reduce the level of inclusions present within the weld. This is mainly attributed to a combination of the variation in weld pool fluidity and the dynamic action that the weld pool experiences owing to the fluctuation between different shielding gas environments.

In summary, the use of alternating shielding gases during GMAW offers clear manufacturing cost reduction benefits which arise from measurable increases in productivity, improved distortion control and re-work reduction, and overall improvements to the mechanical properties of the weld.

The thermal property assessment has highlighted the influence that the shielding gas parameters have on the weld metal properties, and therefore each set of welding parameters will exhibit unique aspects. Therefore, the accuracy of computational simulations to predict the temperature field, and consequently residual stresses and deformation can be improved through the use of temperature dependent thermal properties for the parent plate and weld metal.

It has been determined that the shielding gas flow rate has a significant effect on the thermal properties of the solidified weld. The dilatometry results are in agreement with Camilleri et al. [5.9] and Mollicone et al. [5.10] who determined that the weld metal exhibits a lower coefficient of thermal expansion than the parent material. A lower shielding gas flow rate was found to reduce the linear thermal expansion coefficient, whilst increasing the specific heat capacity and thermal conductivity, with the thermal diffusivity being independent of the shielding gas flow rate. It can therefore be inferred that a lower shielding gas flow rate will result in less weld-

induced distortion as a result of lower degree of weld metal contraction, and quicker dissipation of the heat to the surrounding plate, resulting in quicker thermal equilibrium with the surrounding material. In addition, the higher specific heat capacity associated with the lower shielding gas flow rate results in a faster weld metal cooling rate, which produces a finer microstructure.

There were no real trends in the data produced when varying the frequency of alternating shielding gases, although the results were generally found to be within the upper and lower limits imposed by the argon / 20% carbon dioxide and helium cases.

5.6 References

[5.1] Chang, Y. H., 'Improve GMAW and GTAW with alternating shield gases', *Welding Journal*, Vol. 85, No. 2, pp. 41-43, 2006.

[5.2] Kang, B. Y., Prasad, Y. K. D. V., Kang, M. J., Kim, H. J., and Kim, I. S., 'Characteristics of alternate supply of shielding gas in aluminium GMA welding', *Journal of Materials Processing Technology*, Vol. 209, No. 10, pp. 4716-4121, 2009.

[5.3] Kang, B. Y., Prasad, Y. K. D. V., Kang, M. J., Kim, H. J., and Kim, I. S., 'The effect of alternate supply of shielding gases in austenite stainless steel GTA welding', *Journal of Materials Processing Technology*, Vol. 209, No. 10, pp. 4722–4127, 2009.

[5.4] McPherson, N., 'Correcting thin-plate distortion in shipbuilding', Welding Journal, Vol. 89, No. 1, pp. 30-34, 2010.

[5.5] Deng, D. and Murakawa, H., 'Prediction of welding distortion and residual stress in a thin plate butt-welded joint', Computational Materials Science, Vol. 43, No. 2, pp. 353-365, 2008.

[5.6] Polmear, I., 'Light alloys: from traditional alloys to nanocrystals', Oxford: Elsevier Ltd, 4th edition, pp. 170–184, 2006.

[5.7] Armentani, E., Esposito, R. and Sepe, R., 'The effect of thermal properties and weld efficiency on residual stresses in welding', *Journal of Achievements in Materials and Manufacturing Engineering*, Vol. 20, No. 1-2, pp. 319-322, 2007.

[5.8] Michaleris, P., Feng, Z. and Campbell, G., 'Evaluation of 2D and 3D FEA models for predicting residual stresses and distortion', *Approximate Methods in the Design and Analysis of Pressure Vessels and Piping Components*, American Society of Mechanical Engineers, Pressure Vessels and Piping Division, Vol. 347, pp. 91-102, 1997.

[5.9] Camilleri, D., Mollicone, P. and Gray T. G. F., 'Alternative simulation techniques for distortion of thin plate due to fillet-welded stiffeners', *Modelling and Simulation in Materials Science and Engineering*, Vol. 14, No. 8, pp. 1307-1327, 2006.

[5.10] Mollicone, P., Camilleri, D., Gray, T. G. F. and Comlekci, T., 'Simple thermo-elastic-plastic models for welding distortion simulation', *Journal of Materials Processing Technology*, Vol. 176, No. 1-3, pp. 77-86, 2006.

[5.11] Zhu, X. K. and Chao, Y. J., 'Effects of temperature-dependant material properties on welding simulation', *Computers and Structures*, Vol. 80, No. 11, pp. 967-976, 2002.

[5.12] Min, D., Shen, J., Lai, S. and Chen, J., 'Effect of heat input on the microstructure and mechanical properties of tungsten inert gas arc butt-welded AZ61 magnesium alloy plates', *Materials Characterization*, Vol. 60, No. 12, pp. 1583-1590, 2009.

[5.13] Juan, W., Yajiang, L. and Peng, L., 'Effect of weld heat input on toughness and structure of HAZ of a new super-high strength steel', Bulletin of Materials Science, Vol. 23, No. 3, pp. 301-305, 2003.

[5.14] Cullison, A. ed., 'Fact sheet: shielding gases for tungsten arc welding', *Welding Journal (American Welder supplement),* pp. 20, 2000.

[5.15] Jönsson, P. G., Eagar, T. W. and Szekely, J., 'Heat and metal transfer in gas metal arc welding using argon and helium', *Metallurgical and Materials Transactions B*, Vol. 26, No. 2, pp. 383-395, 1995.

[5.16] Tanaka, M., Tashiro, S., Satoh, T., Murphy, A. B. and Lowke, J. J., 'Influence of shielding gas composition on arc properties in TIG welding', *Science and Technology of Welding and Joining*, Vol. 13, No. 3, pp. 225-231, 2008.

[5.17] ‘ASM metals handbook, Vol. 6: Welding, Brazing and Soldering’, Ohio: ASM, 8th edition, pp. 37-38, 1993.

[5.18] Armentani, E., Esposito, R. and Sepe, R., ‘The effect of thermal properties and weld efficiency on residual stresses in welding’, Journal of Achievements in Materials and Manufacturing Engineering, Vol. 20, No. 1-2, pp. 319-322, 2007.

6 Artificial neural networking

6.1 Nomenclature

α - The momentum constant

δ_i - Computed error at the i^{th} PE

f - Function

η - The step size

J - The output from the PE

n - The iteration number

o - Number of network outputs

p - Number of patterns

σ_k^2 - Variance of the input perturbation

S_k - Sensitivity for input k

w_{ij} - The weight that connects the i^{th} PE to the j^{th} PE

y - Model output

$\bar{y}$ - Model output with fixed weights

6.2 Introduction

The GMAW process is extremely complex and involves the interaction of several nonlinear welding variables. ANNs have the ability to develop patterns and detect subtle link/trends that are too complex to be observed via other techniques, therefore allowing for the strong indicators of new situations of interest. In addition, other computational modelling environments are unidirectional, i.e., calculate an output for a given set of input variables, and often require extensive computational power to process complex models whereas ANNs are bidirectional and have the ability to predict the input variables required to produce a given output. ANNs can, therefore, be employed to accurately predict mechanical properties and other important weld characteristics without the need for destructive testing, while precise models will provide confidence in the welds produced.

This type of computational model can be effectively applied to the welding process where the input layer consists of the welding parameters and the output layer is the desired property, i.e. weld geometry, distortion, mechanical properties, and other factors as a consequence of the input parameters.

ANNs were first applied to the welding process around the early 1980s [6.1, 6.2]. Since then they have been used extensively in the prediction of weld characteristics such as mechanical properties [6.3-6.7] and have been shown to be fairly accurate in determining tensile strength, hardness, elongation, and impact energy. They have been used to determine the weld quality [6.8] based upon differing input settings including current, voltage, and gas compositions. ANNs have also been implemented for the prediction of weld-induced deformation [6.9, 6.10] and weld geometry [6.11-6.13].

The basic architecture of an ANN applied to the prediction of weld geometry is shown in Figure 6.1, and consists of interconnected processing elements in the different layers of the system:

- An input layer - represents the raw data that are fed into the system (welding parameters)
- One or more hidden layers - the output from which is determined by the activities of the inputs and the weights of the connections
- An output layer - conveys the signals to the environment and is dependent upon the processes and weights of the hidden units (weld geometry)

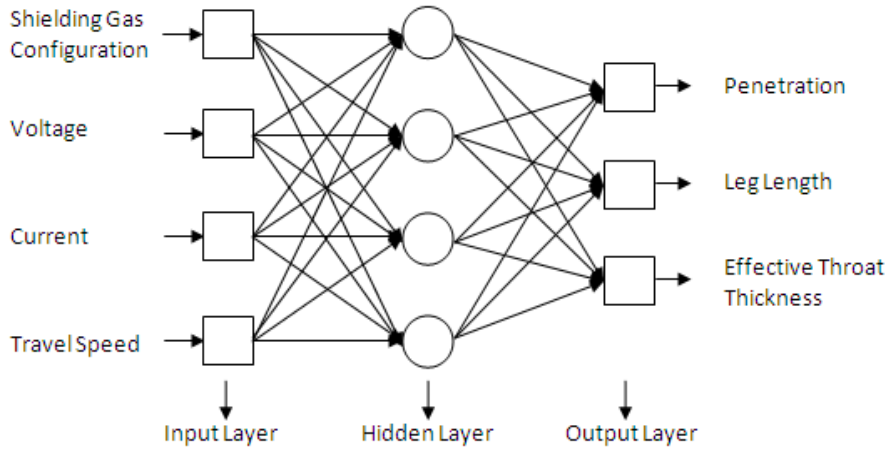

Figure 6.1: Multilayer perceptron architecture with one hidden layer

This chapter focuses on the application of ANN models to predict various weld aspects including geometry when implementing alternating shielding gases, weld quality when alternating shielding gases are subjected to cross drafts, with the additional aim of generating a safe criteria for reducing the shielding gas consumption, and distortion as a function of the welding parameters, with the subsequent transient induction heating parameters required to rectify it.

6.3 Experimental setup

A basic requirement when designing any ANN model is that sufficient data is input to accurately train and validate a model. Hence, extensive experimental trials have been conducted in three phases in order to produce enough data, this involved producing fillet welds for geometry measurement, bead-on-plate for cross draft assessment, and fillet welds for distortion / distortion rectification.

This section details the experimental setup used to conduct each series of experimental trials, with reference to Experimental apparatus and procedures, Chapter 2.

6.3.1 Weld geometry

All experimental welds were deposited on an automatic welding rig where the plate, held rigid, moved at a preset speed under a fixed welding nozzle. Fillet welds were performed using 1000 x 60 x 6 mm DH36 grade steel bar tacked together in the form of an inverted ‘T’, i.e. horizontal vertical position, as shown in Figure 6.2. In each case the welds were produced using a torch preset at a 45° angle and fixed in position.

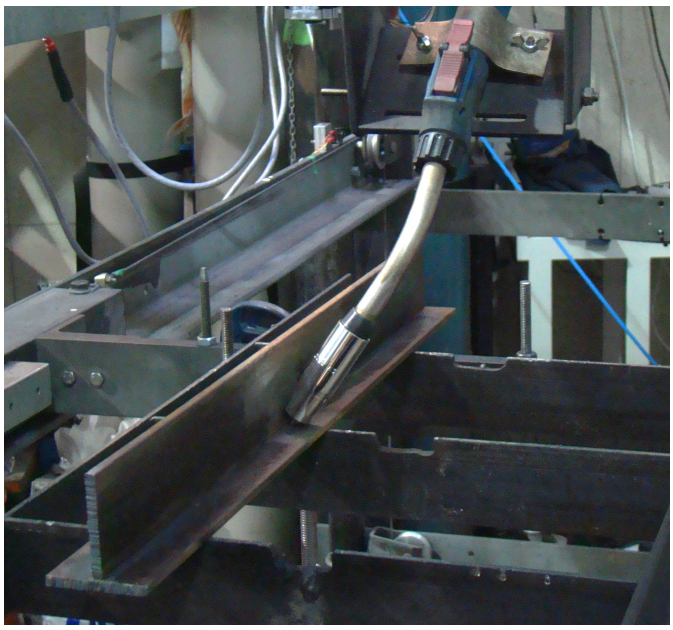

Figure 6.2: Weld setup for geometry measurement trials

1.0 mm diameter MC-1 filler wire, with a typical chemical composition as shown in Table 2.4, was used throughout experimentation at a constant feed speed of 90 mm/s.

Two independent shielding gas supplies were used throughout; argon / 20% carbon dioxide, and helium, with the gas flow controlled using an electronic control unit (Section 2.4), which allowed the alternating frequency to be accurately set prior to welding while implementing an oscilloscope for validation. The shielding gas flow rate was preset at 15 l/min when flowing continuously, with a duty cycle of 50% for alternating shielding gases. The typical, specified welding parameters are shown in Table 6.1.

Table 6.1: Typical weld parameters

Shielding gas	Delivery method	Flow rate (l/min)	Voltage (V)	Current (A)	Travel speed (mm/s)
Ar / 20% CO_2	Constant	15	22, 24, 26	155	2.0, 2.5, 3.0
Ar / 20% CO_2 Helium	Alternating @ 2, 4, 6, 8 Hz	15	22, 24, 26	155	2.0, 2.5, 3.0

6.3.2 Shielding gas optimisation

Bead-on-plate trials were performed upon an automatic welding rig, which held the plate rigid while moving at a preset velocity of 3.2 mm/s beneath the stationary welding torch. The nozzle was positioned with a 10 mm stand-off distance, centrally located above a 500 x 150 x 8 mm DH36 steel plate. The susceptibilities of two different internal nozzle diameters, 12 and 16 mm, were evaluated.

1.2 mm diameter SF-1A filler wire was used throughout the experimentation, using nominal welding parameters of 210 A and 24.7 V, with accurate weld parameters obtained using the P.A.M.S. unit being used for the development of the ANN model.

Two independent shielding gases were used throughout experimentation; argon / 20% carbon dioxide, and helium. This allowed for comparative data to be generated for the conventional argon / 20% carbon dioxide gas mixture and alternating shielding gases, with the ANN model encompassing both methods. The typical, specified welding parameters are shown in Table 6.2.

Table 6.2: Typical weld parameters

Shielding gas	Delivery method	Flow rate (l/min)	Nozzle diameter (mm)	Cross draft velocity (m/s)
Ar / 20% CO_2	Constant	5, 10, 15	12, 16	0 – 5.5 (0.5 increments)
Ar / 20% CO_2 Helium	Alternating @ 2, 4, 6, 8 Hz	5, 10, 15	12, 16	0 – 5.5 (0.5 increments)

A flow device (containing a diffuser and a flow straightener) was used to produce a steady, uniformly distributed, laminar cross draft at its output. The flow device was positioned such that the nozzle centre was located 300 mm from the outlet and at an angle of 90° to the welding direction, as shown in Figure 6.3.

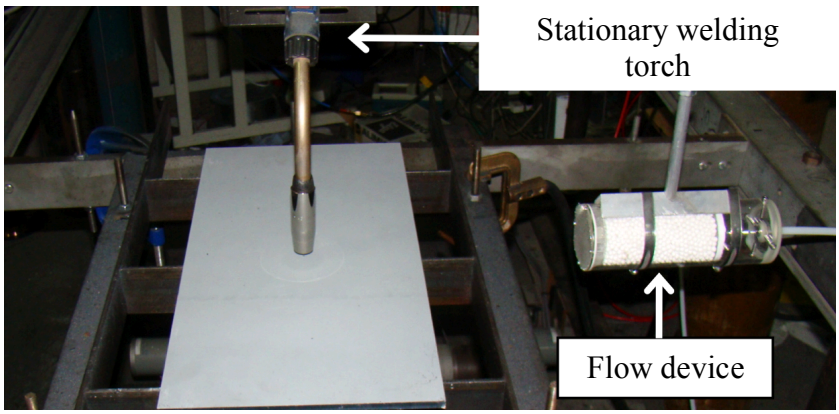

Figure 6.3: Experimental setup showing flow device used to induce cross draft

The velocity of the cross draft was measured using a hot wire anemometer in the throat between the nozzle and plate at a height of 5 mm above the plate surface. The cross-draft flow profile was calibrated at numerous velocities by measuring the velocity at 121 locations across the plate at a height of 5 mm above the plate surface. Examples of the flow profiles generated are shown in Figure 6.4 with the cross draft flow originating from the lower edge. As can be observed, the flow in the test region, that is, the area where the welding nozzle would be located (circle indicating the location of the welding nozzle), the flow is uniform with the flow velocity dropping rapidly ±20 mm from the nozzle centreline.

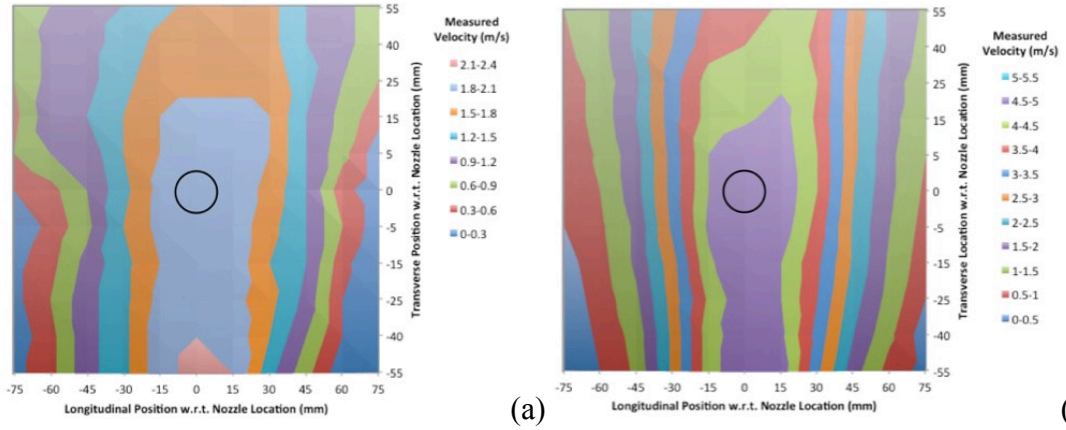

Figure 6.4: Calibration plot for (a) 2 m/s cross draft, and (b) 5 m/s cross draft

Weld quality was evaluated using a combination of visual and radiographic examination. However, due to its ability to detect defects through the thickness of the weld, the results displayed, and consequently those used in the ANN model

development, are from the radiographic examination. Due to the binary classification method employed in the ANN model, the results had to be entered in the form of pass / fail; therefore, a grading system was developed such that clean welds, or welds free from harmful defects, would pass, and those containing harmful defects would fail.

6.3.3 Distortion prediction

Experimental trials were conducted on 1000 x 200 mm DH36 steel plates of various thicknesses (detailed in Table 6.3) with a 1000 x 100 x 8 mm stiffener welded along one side of the centreline to form an inverted 'T' fillet weld, Figure 6.5. Prior to conducting the experimental weld, the stiffener was tack welded to the base plate with a series of 25 mm welds, located 160, 330, 500, 670 and 840 mm along the opposite side of the stiffener.

Table 6.3: Typical weld and induction coil parameters

Shielding gas	Flow rate (l/min)	Plate thickness (mm)	Weld travel speed (mm/s)	Induction coil travel speed (mm/s)
Ar / 20% CO_2	15	6, 8, 10	2.0, 2.5, 3.0	10, 15, 20, 25, 30

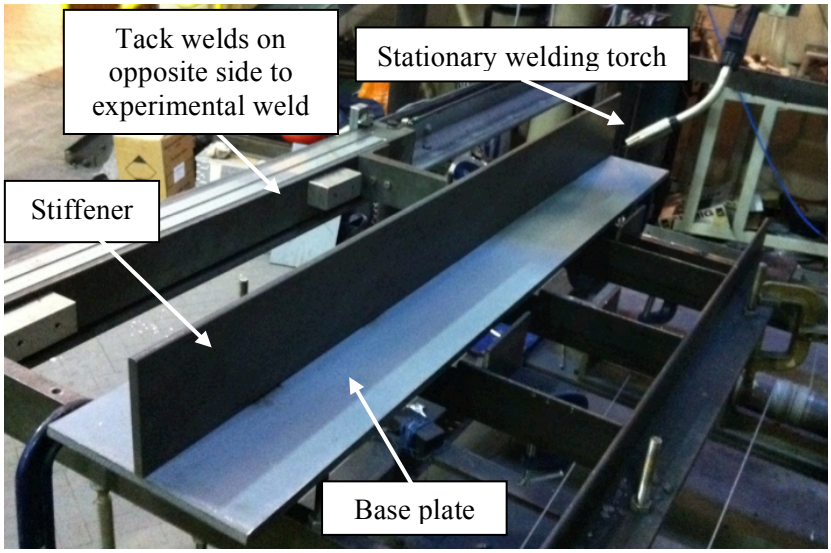

Figure 6.5: Experimental setup for welding

All experimental welds were performed upon an automatic welding rig, which held the plate rigid upon four locating points, and moved the plates at a preset speed beneath a fixed welding torch.

Nominal welding parameters were used throughout the experimental trials, and the average values were recorded using the P.A.M.S. unit. The level of heat input was varied in order to generate different levels of distortion to train the ANN model, by implementing different welding travel speeds. Five plates of each thickness were welded at each travel speed.

An EFD Induction MINAC 18/25 system with a standard 100 mm long induction coil designed for stationary steel plate bending was used during the induction heating phase of the experimental trials. To automate the movement of the induction coil, the hand-held transformer was mounted to a GULLCO KAT welding tractor allowing for a consistent travel speed to be preset. The coil was positioned at a height of 5 mm above the workpiece surface, and 9 mm from the stiffener plate centreline to travel along the opposite side of the plate from the weld, following the centre of the weld heat affected zone as shown in Figure 6.6. The system was set to produce a constant power output of 19 kW, with five different travel speeds being used to produce different levels of bending. The plate and travel speed combinations are given in Table 6.3.

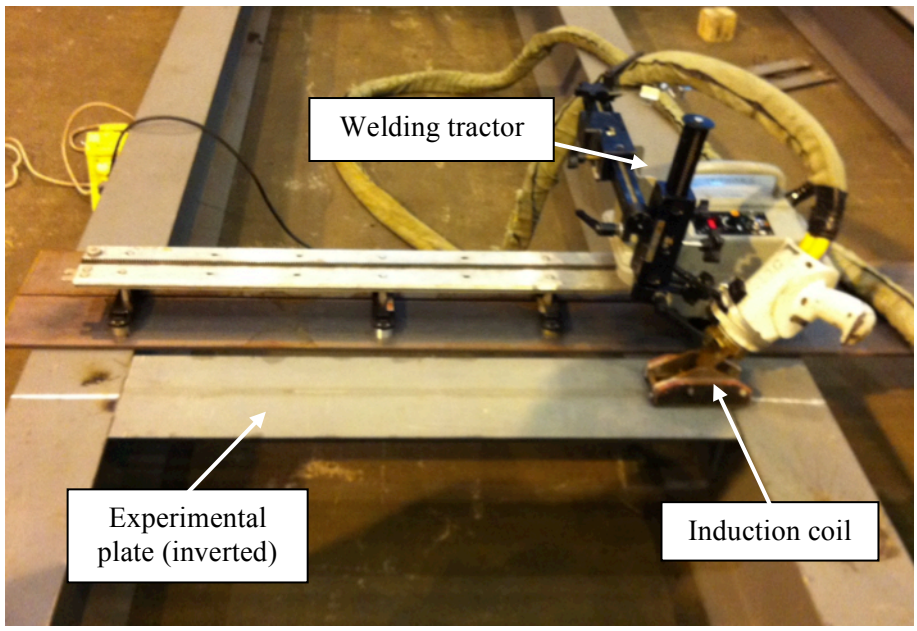

Figure 6.6: Experimental setup for induction heating

Distortion data was captured using an optical distance sensor, Chapter 2, with measurements taken every 25 mm in the longitudinal direction and every 10 mm in the transverse direction. The workpiece was scanned three times throughout the process: prior to welding (but after the stiffener had been tacked), after welding and after induction heating. In each case, the plates had been allowed to cool to room temperature to ensure no further distortion would occur as no further thermal contraction due to cooling will take place.

6.4 Experimental results

6.4.1 Weld geometry

The average welding parameters, as recorded by the P.A.M.S. unit, are shown in Table 6.4. Macro sections were extracted and prepared according to Section 2.8.1, and the weld geometry, as detailed in Figure 2.12 (c), measured using ImageJ image analysis software. The reported (Table 6.4) dimension for penetration and leg length is the average value of the respective horizontal and vertical components, and are the average measurements from 3 specimens.

Table 6.4: Training / testing weld data

Weld Parameters				**Weld Outputs**		
Shielding gas configuration	Voltage (V)	Current (A)	Travel speed (mm/s)	Penetration (mm)	Leg length (mm)	Effective throat (mm)
Ar / 20% CO_2	21.7	158	2.0	1.168	6.739	4.626
Ar / 20% CO_2	23.6	157	2.0	1.471	6.541	4.710
Ar / 20% CO_2	26.0	157	2.0	0.992	7.628	4.943
Ar / 20% CO_2	22.0	151	2.5	1.483	6.249	4.626
Ar / 20% CO_2	23.9	154	2.5	1.044	6.687	4.182
Ar / 20% CO_2	26.1	157	2.5	1.070	6.894	4.357
Ar / 20% CO_2	21.9	152	3.0	1.078	5.300	3.298
Ar / 20% CO_2	23.8	158	3.0	1.391	6.371	3.916
Ar / 20% CO_2	26.1	158	3.0	1.136	6.506	4.228
Alternating @ 2 Hz	21.8	153	2.0	1.229	6.803	5.637
Alternating @ 2 Hz	23.4	156	2.0	1.421	6.977	4.646
Alternating @ 2 Hz	26.4	159	2.0	1.365	7.171	4.616
Alternating @ 2 Hz	22.0	157	2.5	1.020	6.559	4.964

Alternating @ 2 Hz	23.7	156	2.5	1.269	5.789	3.807
Alternating @ 2 Hz	25.8	159	2.5	1.116	7.634	5.236
Alternating @ 2 Hz	21.9	152	3.0	1.107	5.365	4.748
Alternating @ 2 Hz	23.4	155	3.0	1.426	5.319	4.556
Alternating @ 2 Hz	26.2	154	3.0	1.342	5.498	4.200
Alternating @ 4 Hz	21.6	150	2.0	1.148	6.913	5.752
Alternating @ 4 Hz	23.9	155	2.0	1.494	6.680	5.091
Alternating @ 4 Hz	25.8	156	2.0	1.499	6.582	4.879
Alternating @ 4 Hz	21.7	157	2.5	1.277	6.196	4.818
Alternating @ 4 Hz	23.7	155	2.5	1.315	6.467	4.869
Alternating @ 4 Hz	25.6	157	2.5	1.371	6.207	4.032
Alternating @ 4 Hz	21.9	154	3.0	1.235	5.727	4.798
Alternating @ 4 Hz	23.8	159	3.0	1.581	5.969	3.333
Alternating @ 4 Hz	26.1	156	3.0	1.290	5.699	4.407
Alternating @ 6 Hz	21.7	154	2.0	1.338	6.416	5.680
Alternating @ 6 Hz	23.5	159	2.0	1.690	6.352	4.855
Alternating @ 6 Hz	25.6	159	2.0	1.347	7.069	4.563
Alternating @ 6 Hz	22.0	152	2.5	1.172	6.239	4.975
Alternating @ 6 Hz	24.3	153	2.5	1.477	5.926	4.044
Alternating @ 6 Hz	25.5	156	2.5	1.198	6.303	3.928
Alternating @ 6 Hz	21.8	156	3.0	1.069	5.133	3.812
Alternating @ 6 Hz	24.0	151	3.0	1.216	5.703	3.679
Alternating @ 6 Hz	25.6	156	3.0	1.702	5.856	3.609
Alternating @ 8 Hz	21.7	155	2.0	0.915	7.326	5.589
Alternating @ 8 Hz	24.0	158	2.0	1.039	7.279	4.475
Alternating @ 8 Hz	25.9	158	2.0	1.522	7.368	4.617
Alternating @ 8 Hz	21.9	154	2.5	1.141	6.459	4.664
Alternating @ 8 Hz	23.9	153	2.5	1.244	6.490	4.093
Alternating @ 8 Hz	26.0	155	2.5	1.415	6.901	4.265
Alternating @ 8 Hz	22.2	153	3.0	1.503	5.365	4.449
Alternating @ 8 Hz	24.0	157	3.0	1.263	5.370	4.014
Alternating @ 8 Hz	26.0	155	3.0	1.711	5.886	3.940

6.4.2 Shielding gas optimisation

Weld quality was assessed through the use of radiographic examination, the results of which are displayed in Figure 6.7 (a) – (e) and 6.8 (a) – (e). For each weld nozzle and gas configuration, there is an obvious increase in cross draft resistance as the shielding gas flow rate is increased. As would be expected, the lower, 5 l/min, flow rate is more susceptible to the adverse effects of cross drafts, ultimately resulting in poor weld quality at low cross draft velocities.

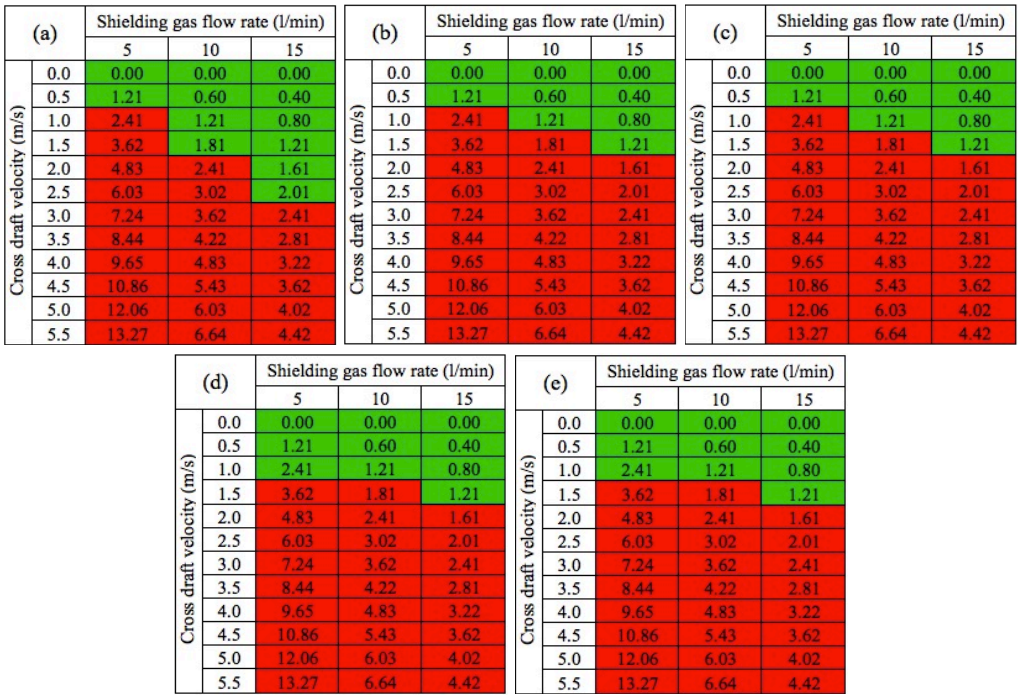

(a)	Shielding gas flow rate (l/min)		
Cross draft velocity (m/s)	5	10	15
0.0	0.00	0.00	0.00
0.5	1.21	0.60	0.40
1.0	2.41	1.21	0.80
1.5	3.62	1.81	1.21
2.0	4.83	2.41	1.61
2.5	6.03	3.02	2.01
3.0	7.24	3.62	2.41
3.5	8.44	4.22	2.81
4.0	9.65	4.83	3.22
4.5	10.86	5.43	3.62
5.0	12.06	6.03	4.02
5.5	13.27	6.64	4.42

(b)	Shielding gas flow rate (l/min)		
Cross draft velocity (m/s)	5	10	15
0.0	0.00	0.00	0.00
0.5	1.21	0.60	0.40
1.0	2.41	1.21	0.80
1.5	3.62	1.81	1.21
2.0	4.83	2.41	1.61
2.5	6.03	3.02	2.01
3.0	7.24	3.62	2.41
3.5	8.44	4.22	2.81
4.0	9.65	4.83	3.22
4.5	10.86	5.43	3.62
5.0	12.06	6.03	4.02
5.5	13.27	6.64	4.42

(c)	Shielding gas flow rate (l/min)		
Cross draft velocity (m/s)	5	10	15
0.0	0.00	0.00	0.00
0.5	1.21	0.60	0.40
1.0	2.41	1.21	0.80
1.5	3.62	1.81	1.21
2.0	4.83	2.41	1.61
2.5	6.03	3.02	2.01
3.0	7.24	3.62	2.41
3.5	8.44	4.22	2.81
4.0	9.65	4.83	3.22
4.5	10.86	5.43	3.62
5.0	12.06	6.03	4.02
5.5	13.27	6.64	4.42

(d)	Shielding gas flow rate (l/min)		
Cross draft velocity (m/s)	5	10	15
0.0	0.00	0.00	0.00
0.5	1.21	0.60	0.40
1.0	2.41	1.21	0.80
1.5	3.62	1.81	1.21
2.0	4.83	2.41	1.61
2.5	6.03	3.02	2.01
3.0	7.24	3.62	2.41
3.5	8.44	4.22	2.81
4.0	9.65	4.83	3.22
4.5	10.86	5.43	3.62
5.0	12.06	6.03	4.02
5.5	13.27	6.64	4.42

(e)	Shielding gas flow rate (l/min)		
Cross draft velocity (m/s)	5	10	15
0.0	0.00	0.00	0.00
0.5	1.21	0.60	0.40
1.0	2.41	1.21	0.80
1.5	3.62	1.81	1.21
2.0	4.83	2.41	1.61
2.5	6.03	3.02	2.01
3.0	7.24	3.62	2.41
3.5	8.44	4.22	2.81
4.0	9.65	4.83	3.22
4.5	10.86	5.43	3.62
5.0	12.06	6.03	4.02
5.5	13.27	6.64	4.42

Figure 6.7: Radiographic examination results for a 16 mm nozzle using (a) Argon, (b) Alternating @ 2 Hz, (c) Alternating @ 4 Hz, (d) Alternating @ 6 Hz and (e) Alternating @ 8 Hz

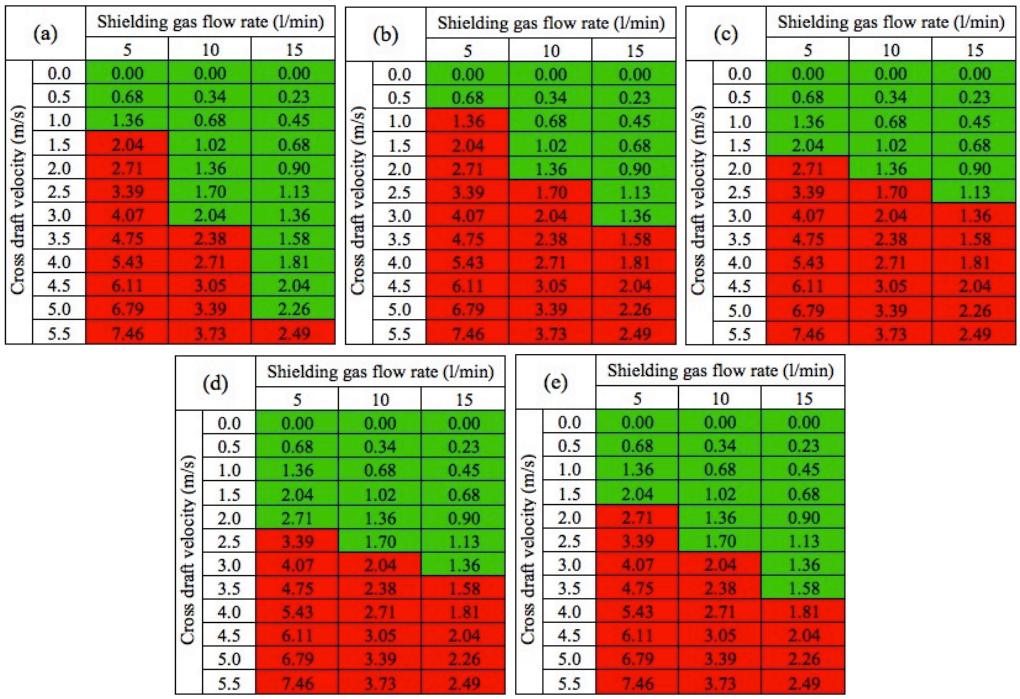

(a)	Shielding gas flow rate (l/min)		
Cross draft velocity (m/s)	5	10	15
0.0	0.00	0.00	0.00
0.5	0.68	0.34	0.23
1.0	1.36	0.68	0.45
1.5	2.04	1.02	0.68
2.0	2.71	1.36	0.90
2.5	3.39	1.70	1.13
3.0	4.07	2.04	1.36
3.5	4.75	2.38	1.58
4.0	5.43	2.71	1.81
4.5	6.11	3.05	2.04
5.0	6.79	3.39	2.26
5.5	7.46	3.73	2.49

(b)	Shielding gas flow rate (l/min)		
Cross draft velocity (m/s)	5	10	15
0.0	0.00	0.00	0.00
0.5	0.68	0.34	0.23
1.0	1.36	0.68	0.45
1.5	2.04	1.02	0.68
2.0	2.71	1.36	0.90
2.5	3.39	1.70	1.13
3.0	4.07	2.04	1.36
3.5	4.75	2.38	1.58
4.0	5.43	2.71	1.81
4.5	6.11	3.05	2.04
5.0	6.79	3.39	2.26
5.5	7.46	3.73	2.49

(c)	Shielding gas flow rate (l/min)		
Cross draft velocity (m/s)	5	10	15
0.0	0.00	0.00	0.00
0.5	0.68	0.34	0.23
1.0	1.36	0.68	0.45
1.5	2.04	1.02	0.68
2.0	2.71	1.36	0.90
2.5	3.39	1.70	1.13
3.0	4.07	2.04	1.36
3.5	4.75	2.38	1.58
4.0	5.43	2.71	1.81
4.5	6.11	3.05	2.04
5.0	6.79	3.39	2.26
5.5	7.46	3.73	2.49

(d)	Shielding gas flow rate (l/min)		
Cross draft velocity (m/s)	5	10	15
0.0	0.00	0.00	0.00
0.5	0.68	0.34	0.23
1.0	1.36	0.68	0.45
1.5	2.04	1.02	0.68
2.0	2.71	1.36	0.90
2.5	3.39	1.70	1.13
3.0	4.07	2.04	1.36
3.5	4.75	2.38	1.58
4.0	5.43	2.71	1.81
4.5	6.11	3.05	2.04
5.0	6.79	3.39	2.26
5.5	7.46	3.73	2.49

(e)	Shielding gas flow rate (l/min)		
Cross draft velocity (m/s)	5	10	15
0.0	0.00	0.00	0.00
0.5	0.68	0.34	0.23
1.0	1.36	0.68	0.45
1.5	2.04	1.02	0.68
2.0	2.71	1.36	0.90
2.5	3.39	1.70	1.13
3.0	4.07	2.04	1.36
3.5	4.75	2.38	1.58
4.0	5.43	2.71	1.81
4.5	6.11	3.05	2.04
5.0	6.79	3.39	2.26
5.5	7.46	3.73	2.49

Figure 6.8: Radiographic examination results for a 12 mm nozzle using (a) Argon, (b) Alternating @ 2 Hz, (c) Alternating @ 4 Hz, (d) Alternating @ 6 Hz and (e) Alternating @ 8 Hz

As was the case in Chapter 3, the narrower, 12 mm diameter, nozzle has consistently provided better protection to the weld region when subjected to cross drafts. This is due to the conservation of mass, and therefore, the shielding gas will accelerate through the nozzle and exit at a far higher velocity than it would when using the 16 mm diameter nozzle.

As can be noted from the experimental results, the conventional argon / 20% carbon dioxide base case faired considerably better than all of the alternating shielding gas frequencies. In this series of trials, the argon / 20% carbon dioxide base case produced a critical cross draft velocity to shielding gas exit velocity ratio of approximately 2.4 and 2, for the 16 and 12 mm nozzle, respectively. However, when implementing alternating shielding gases, this ratio reduces, on average, to approximately 1.6 and 1.4 for the 16 and 12 mm nozzles, respectively. The decrease in the critical ratio can be attributed to a combination of effects: (a) alternating between two gases produces turbulence in the shielding gas column, which in a draft free environment has no effect but when subjected to a draft encourages intermixing of the atmospheric gases to the shielding gas column, and (b) helium has a considerably lower density than air meaning it drifts rather than creating a blanket effect that the argon / 20% carbon dioxide shielding gas does.

At 5 l/min, alternating shielding gases have been shown to produce better protection to the weld pool. This can be attributed to a shielding gas pressure impulse, which occurs due to a build-up in line pressure and is released when the valve is opened, causing an increase in the shielding gas exit velocity. Concurrently, when using conventional argon / 20% carbon dioxide, there is no pressure impulse, the exit velocity is low and is therefore blown from the weld area before it is able to reach weld level, thus preventing the blanket effect from occurring.

When solely comparing alternating shielding gas frequencies, there is very little difference in the resultant weld quality when using the 16 mm nozzle. However, for the 12 mm diameter nozzle, as the frequency increases, the resistance to cross drafts also increases. This is mainly due to a trade-off between an impulse in pressure (lower frequencies having a longer time for pressure to accumulate) and turbulence due to the alternating process (lower frequencies creating greater turbulence).

6.4.3 Distortion prediction

The angular distortion was determined by applying a best-fit straight line to the distortion data, thus the gradient of the line is representative of the relative angle on each side of the plate, as shown in Figure 6.9.

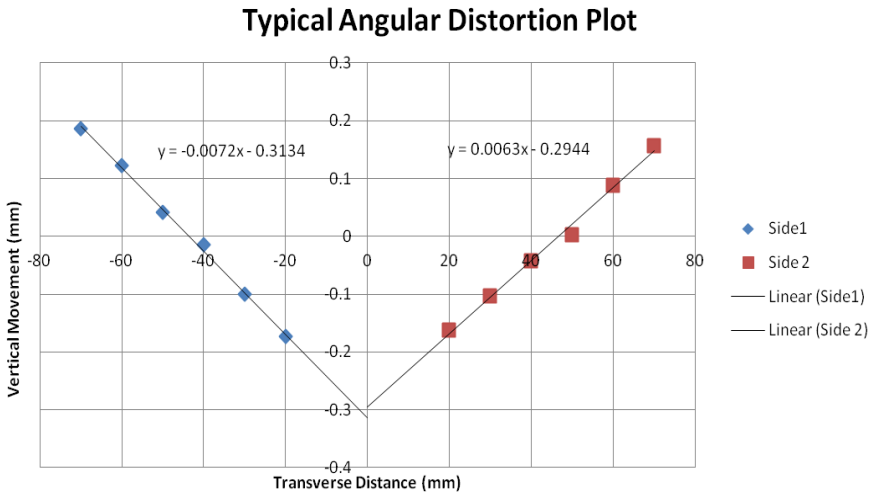

Figure 6.9: Angular distortion plot (axes not to scale)

The average welding parameters, as recorded by the P.A.M.S. unit, and the induction heating parameters used to train the ANN models are shown in Table 6.5.

Table 6.5: Training / testing experimental data

	Weld parameters			**Weld Output**	**Induction heating parameters**	**Induction heating output**
Plate thickness (mm)	Voltage (V)	Current (A)	Travel speed (mm/s)	Angular distortion (°)	Travel speed (mm/s)	Angular distortion (°)
6	20.5	219	2.0	0.619	10	-0.229
6	20.5	209	2.0	0.688	15	-0.171
6	20.5	213	2.0	0.693	20	-0.166
6	20.5	214	2.0	0.680	25	0.292
6	20.6	217	2.0	0.630	30	0.115
6	20.6	210	2.5	1.031	10	0.447
6	20.6	216	2.5	0.882	15	-0.074
6	20.5	214	2.5	0.985	20	0.367
6	20.5	217	2.5	0.773	25	0.366
6	20.6	212	2.5	0.905	30	0.469
6	20.5	206	3.0	1.050	10	0.962

6	20.5	210	3.0	1.100	15	0.292
6	20.5	211	3.0	1.150	20	0.447
6	20.6	209	3.0	1.088	25	0.487
6	20.6	208	3.0	1.048	30	0.642
8	20.5	209	2.0	1.420	10	0.745
8	20.7	211	2.0	1.432	15	0.951
8	20.7	219	2.0	1.455	20	1.077
8	20.7	208	2.0	1.352	25	1.071
8	20.6	212	2.0	1.541	30	1.306
8	20.4	213	2.5	1.535	10	0.854
8	20.6	216	2.5	1.409	15	0.985
8	20.5	213	2.5	1.644	20	1.283
8	20.5	209	2.5	1.443	25	1.123
8	20.4	213	2.5	1.334	30	1.066
8	20.5	209	3.0	1.575	10	1.111
8	20.6	210	3.0	1.506	15	1.145
8	20.5	209	3.0	1.209	20	0.962
8	20.5	216	3.0	1.409	25	1.346
8	20.5	208	3.0	1.455	30	1.272
10	20.6	220	2.0	1.329	10	0.871
10	20.6	216	2.0	1.197	15	0.979
10	20.6	211	2.0	1.312	20	1.157
10	20.7	212	2.0	1.243	25	1.140
10	20.5	214	2.0	1.226	30	1.134
10	20.7	206	2.5	1.094	10	0.659
10	20.7	207	2.5	1.066	15	0.819
10	20.7	210	2.5	1.060	20	0.945
10	20.8	214	2.5	1.071	25	0.945
10	20.7	214	2.5	1.146	30	1.054
10	20.7	207	3.0	0.831	10	0.516
10	20.6	208	3.0	0.934	15	0.682
10	20.6	209	3.0	1.077	20	0.928
10	20.8	215	3.0	1.054	25	0.939
10	20.6	205	3.0	1.071	30	1.026

6.4.3.1 Welding distortion

The results for angular distortion due to welding for the 6 mm thick plate samples (Figure 6.10) display an unusual pattern; the lowest level of distortion is observed on the plates welded at 2 mm/s with the greatest observed on the plates welded at 3 mm/s. This is in contrast to the expected pattern of distortion, which has been shown to decrease with a reduction in heat input [6.10]. However, it is believed that the low welding speeds used, which were intended to generate high heat input levels and consequently large levels of distortion, caused this unexpected pattern. While

welding the 6 mm samples, the heated zone was clearly visible on the underside of the plate. Hence, the intentionally high heat input level resulted in a significant rise in temperature through the thickness of the plate. This subsequently reduced the temperature difference between the weld and base material, and subsequently, the difference in thermal contraction resulted in lower levels of angular distortion.

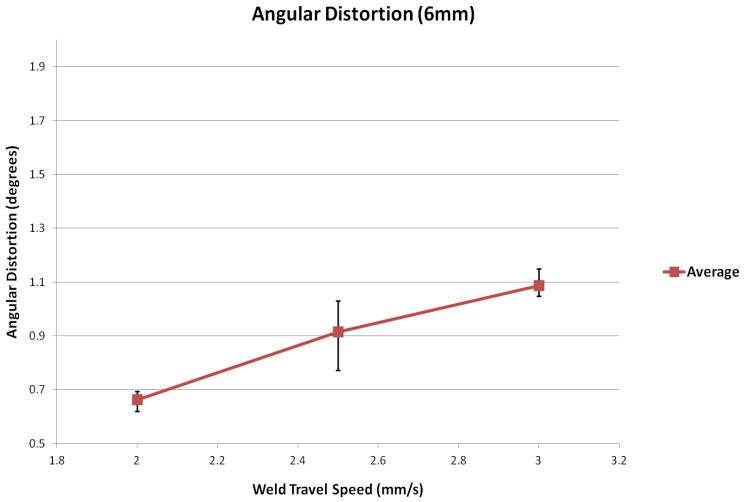

Figure 6.10: Welding distortion (6 mm thick plate)

A different trend is seen in the distortion results for the 8 mm thick plate, as illustrated in Figure 6.11. The level of angular distortion appears to be almost constant with welding speed, and the overall distortion is greater than the distortion seen in the 6 mm thick samples, with the distortion in the range of 1.209 – 1.644° for 8 mm and 0.630 – 1.150° for 6 mm.

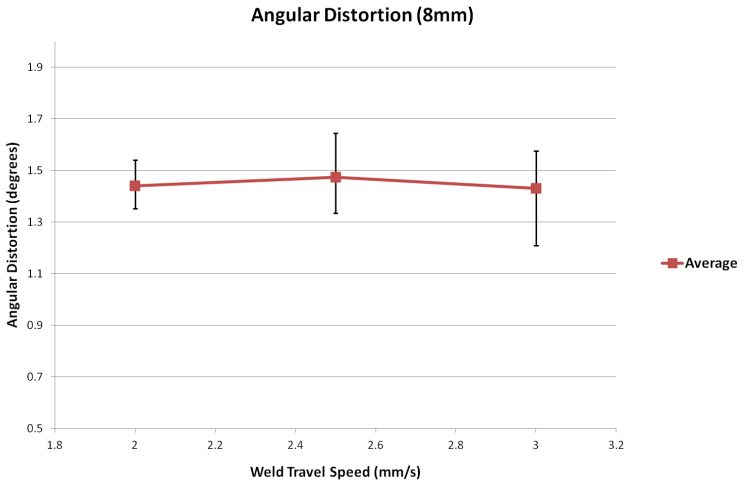

Figure 6.11: Welding distortion (8 mm thick plate)

The angular distortion results for the 10 mm thick samples exhibit the expected trend of distortion (Figure 6.12), i.e. distortion increasing as weld travel speed decreases. Overall, the level of distortion is lower than that found for 8 mm thick samples, with the 10 mm thick plate showing distortion in the range 0.831 – 1.329°. This follows the expected pattern of decreasing distortion with increasing plate thickness. This trend is most likely to be a result of the temperature gradient through the thickness of the plate. As a result of the thinner plates being heated too far through its thickness, in-plane tensile stresses would be produced on the underside of the plate, thus counteracting those on the welded side.

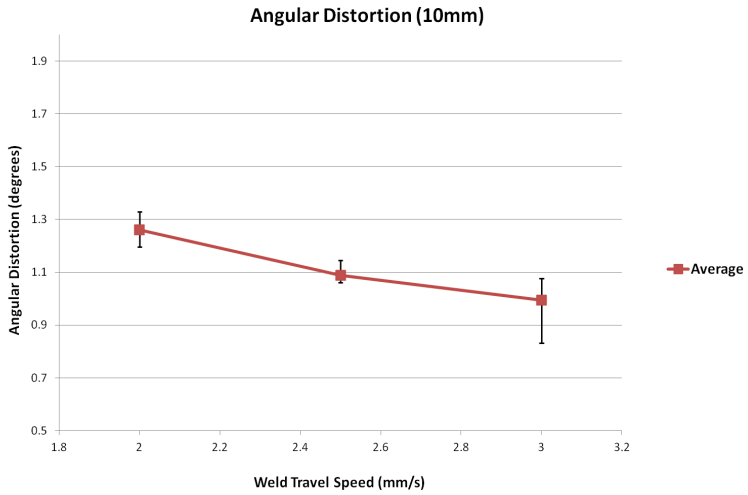

Figure 6.12: Welding distortion (10 mm thick plate)

6.4.3.2 Induction heating distortion

The angular distortion due to induction heating process was calculated by subtracting the final value of angular distortion from the post-weld value. Figure 6.13 shows the distortion rectification achieved on the 6 mm thick plate, and highlights an evident increase in the level of rectification achieved as travel speed is decreased from 30 to 15 mm/s, however there was a significant decrease observed when the travel speed is decreased further to 10 mm/s. This trend is similar to the trend seen in welding distortion with an increase in heat input, due to reduced travel speed, resulting in a reduction in the rectification bend.

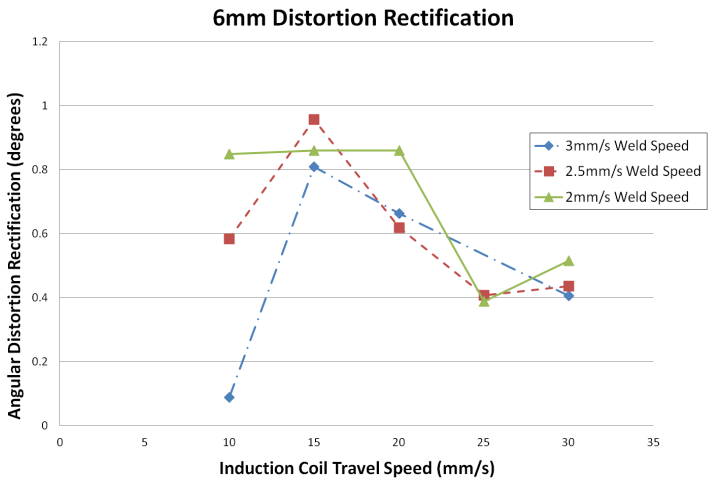

Figure 6.13: Distortion rectification (6 mm thick plate)

This leads to the hypothesis that a critical coil travel speed exists, where bending increases with a reduction in travel speed until this critical speed, and thereafter, a further reduction in travel speed causes the rectification achieved to reduce. For the 6 mm thick plate, the induction heating process was capable of almost eliminating the post-weld distortion as the maximum rectification observed was 0.956° while the maximum welding distortion at this thickness was 1.150°. This indicates that by optimising the induction heating parameters, it may be possible to eliminate welding distortion in the 6 mm thick plate for the welding parameters used in this study.

Figure 6.14 shows the distortion rectification achieved on the 8 mm thick plate, the critical speed for peak rectification that occurred around 15 mm/s as seen in the 6 mm thick plate is not evident. Instead, there is an overall trend of increasing rectification with a reduction in travel speed, although there is an anomalous value at 25 mm/s within the 3 mm/s weld travel speed data set. The overall maximum rectification value of 0.681° is lower than that of the 6 mm results (0.956°), and can be attributed to the increase in plate thickness, and consequently greater stiffness. Thus, the critical speed for the 8 mm thick plate may be in the region of 10 mm/s, or lower. The parameters used for the induction heating process dictated that a coil travel speed of 10 mm/s was the minimum speed used; trials conducted at 5 mm/s resulted in the surface of the heated zone beginning to liquefy due to the extreme level of heat input. At this thickness of plate, the induction heating process is capable

of reducing the welding distortion but not eliminating it completely as the maximum measured welding distortion was 1.644° while the maximum distortion observed post-rectification was only 0.681°.

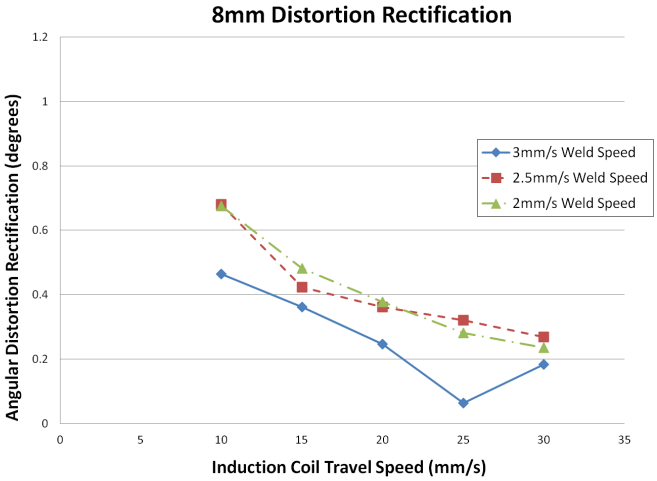

Figure 6.14: Distortion rectification (8 mm thick plate)

The results obtained for the 10 mm thick plate (Figure 6.15) exhibit similar trends to the 8 mm thick plate, i.e. increasing rectification with a reduction in travel speed. The results also reinforce the trend of the maximum rectification reducing as plate thickness increases, with a maximum rectification of 0.458°, the lowest of the rectification results for the three plate thicknesses. Again, the induction heating process parameters have not been capable of eliminating welding distortion; the maximum rectification observed was 0.458° while the maximum post-weld distortion was 1.329°.

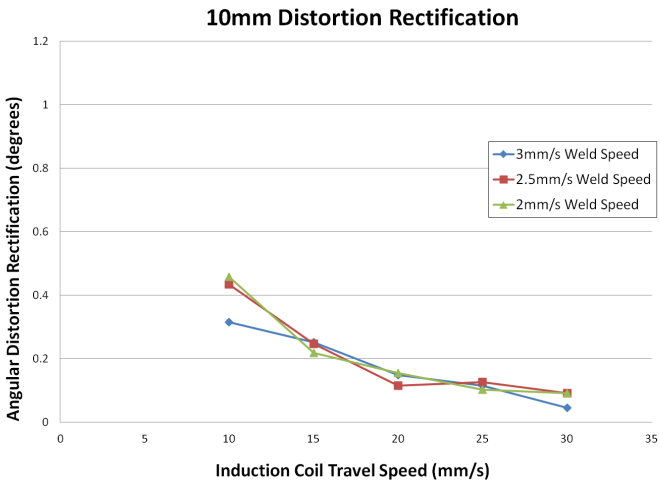

Figure 6.15: Distortion rectification (10 mm thick plate)

From the results, there is a clear relationship between the travel speed of the induction coil and the rectification that can be achieved using this process. As the coil speed is reduced below the critical value, the coil begins to heat the plate through the entire thickness limiting the non-uniform thermal contraction and hence reducing the bending caused by the process. The increasing plate thickness limits the maximum bending that will occur through a combination of increased plate stiffness and an increase in the conductive heat transfer.

6.5 ANN model development

The software implemented for this study was NeuroSolutions®, which had previously been used successfully for the prediction of weld geometries [6.13] and distortion [6.9].

The model selection process involved a systematic approach to determine the model topology, number of iterations, number of hidden layers, momentum coefficient, and processing method that produced the lowest prediction error. The accuracy of the ANN model was quantified by comparing the actual weld parameter with that predicted by the model.

MLF neural networks operate in two modes: training and prediction mode. Thus, we require two data sets, the training set and the set that we want to predict (testing and prediction).

A hold-out method was used throughout the model generation process, in which, approximately 15% of the samples were used for testing and prediction with the remainder used for training the model. The same samples were used for each category, with a spread across different welding parameters, in order to produce a direct comparison on the accuracy of the model using each of the configurations. Throughout the model generation, each model was run a minimum of three times, and the average error taken. This was done since the same topology with the same training data set can produce many different sets of final weights. There are three main reasons behind this:

- There are many symmetries in the input-output mapping created by the MLP.
- There is no guarantee that the problem has a single solution.
- The final weights are obtained in an iterative fashion from random initial values.

6.5.1 Model topology

There are many different ANN architectures, and there is no way to determine a good network topology based on the number of inputs and outputs [6.14]. MLF neural networks are the most popular networks, and the following network topologies were considered:

- Multilayer perceptron (MLP)
- Generalised feed-forward (GFF)
- Modular feed-forward (MFF)

The systematic model selection process implemented is detailed below for the case of the weld geometry prediction model, which involved comparing the values for the leg length, penetration and effective throat. Tables 6.6 – 6.8 shows the effect of model topology on the predicted weld geometry.

Table 6.6: MLP topology

Topology: MLP, Hidden layers: 1, Iterations: 10,000, Momentum: none, Processing: batch								
Leg length (mm)			**Penetration (mm)**			**Effective throat (mm)**		
Actual	Predicted	Error	Actual	Predicted	Error	Actual	Predicted	Error
6.7390	6.7324	0.0974	1.1680	1.4494	24.0934	4.6260	4.8529	4.9046
6.8030	6.6652	2.0262	1.2285	1.4704	19.6910	5.6370	4.8520	13.9258
6.9130	7.0380	1.8085	1.1475	1.2307	7.2515	5.7520	5.1656	10.1943
6.4155	6.9521	8.3641	1.3375	1.2776	4.4776	5.680	5.1356	9.5847
7.3260	6.7307	8.1254	1.0385	1.3921	34.0491	5.5890	4.7949	14.2080
	Average	**4.0843**		**Average**	**17.9125**		**Average**	**10.5635**
							MSE	**0.03238**

Table 6.7: GFF topology

Topology: GFF, Hidden layers: 1, Iterations: 10,000, Momentum: none, Processing: batch								
Leg length (mm)			**Penetration (mm)**			**Effective throat (mm)**		
Actual	Predicted	Error	Actual	Predicted	Error	Actual	Predicted	Error
6.7390	6.9176	2.6506	1.1680	1.5138	29.6044	4.6260	4.4358	4.1116
6.8030	7.1074	4.4740	1.2285	1.1703	4.7404	5.6370	4.8658	13.6818
6.9130	7.0186	1.5279	1.1475	1.2127	5.6782	5.7520	5.0893	11.5219
6.4155	7.2186	12.5176	1.3375	1.2464	6.8095	5.680	5.0373	11.3148
7.3260	6.7885	7.3366	1.0385	1.5930	53.3963	5.5890	4.6270	17.2115
	Average	**5.7013**		**Average**	**20.0458**		**Average**	**11.5683**
							MSE	**0.02266**

Table 6.8: MFF topology

Topology: MFF, Hidden layers: 1, Iterations: 10,000, Momentum: none, Processing: batch								
Leg length (mm)			**Penetration (mm)**			**Effective throat (mm)**		
Actual	Predicted	Error	Actual	Predicted	Error	Actual	Predicted	Error
6.7390	6.6179	1.7973	1.1680	1.4674	25.6362	4.6260	4.8367	4.5548
6.8030	6.8285	0.3744	1.2285	1.3892	13.0849	5.6370	4.9653	11.9158
6.9130	6.9032	0.1416	1.1475	1.2755	11.1542	5.7520	4.8249	16.1180
6.4155	6.6882	4.2501	1.3375	1.6504	23.3965	5.680	5.2380	7.7811
7.3260	5.9478	18.8120	1.0385	1.5004	44.4807	5.5890	4.4101	21.0939
	Average	**5.0751**		**Average**	**23.5505**		**Average**	**12.2927**
							MSE	**0.00838**

It can therefore be seen in Tables 6.6 - 6.8, that the MLP topology produced a higher mean square error (MSE) than the GFF and MFF topologies. The MSE is often used as a stopping criterion for ANN training. However, choosing the correct MSE threshold can be difficult; the MSE may never decrease to the threshold and the training never end, or the MSE threshold could stop training early, before optimum accuracy is achieved. When comparing the percentage errors of the test data sets, it was found that the MLP topology produced the lowest error. As a result, the MLP topology was selected and used throughout of the model selection process.

6.5.2 Number of iterations

There are two main methods to decide how many training iterations are used to train the model; setting a MSE threshold or specifying the number of training iterations. Contrary to what would be logically expected, an ANN network can become

overtrained and the percentage error actually increases with additional iterations. Specifying a MSE threshold does not address the problem of generalisation, i.e. how well the model performs with data that does not belong to the training data set. This is indicated in Figure 6.16, where the MSE of a MLP trained with backpropagation will continue to decrease, while the accuracy of the validation set deteriorates. This is an indication that the network is overtraining, i.e. it is memorising the patterns of the training data set rather than to general properties. Thus, training should be terminated when the MSE of the validation set reaches a minimum.

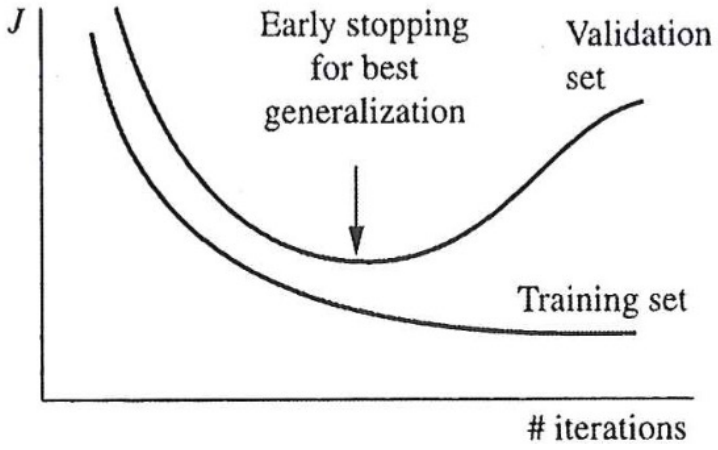

Figure 6.16: Overtraining [6.15]

This can be done using a cross validation method, which utilises the MSE in the validation set and stops training when the MSE begins to rise. However, as the optimum MSE for the network was unknown, a systematic approach was taken to determine the number of iterations that produced the lowest error when compared to the actual measurements. Tables 6.9 – 6.13 show the ANN predictions, and corresponding error, for 4,000 to 20,000 iterations.

Table 6.9: 4,000 iterations

Topology: MLP, Hidden layers: 1, Iterations: 4,000, Momentum: none, Processing: batch								
Leg length (mm)			**Penetration (mm)**			**Effective throat (mm)**		
Actual	Predicted	Error	Actual	Predicted	Error	Actual	Predicted	Error
6.7390	6.6973	0.6192	1.1680	1.5502	32.7236	4.6260	4.8734	5.3471
6.8030	6.5215	4.1384	1.2285	1.3511	9.9781	5.6370	4.8718	13.5753
6.9130	6.4992	5.9854	1.1475	1.2579	9.6210	5.7520	4.8854	15.0658
6.4155	6.5105	1.4808	1.3375	1.4304	6.9428	5.680	4.8531	14.5574
7.3260	6.5680	10.3465	1.0385	1.6204	56.0299	5.5890	4.8145	13.8577
	Average	**4.5141**		**Average**	**23.0591**		**Average**	**12.4807**
							MSE	**0.02741**

Table 6.10: 8,000 iterations

Topology: MLP, Hidden layers: 1, Iterations: 8,000, Momentum: none, Processing: batch								
Leg length (mm)			**Penetration (mm)**			**Effective throat (mm)**		
Actual	Predicted	Error	Actual	Predicted	Error	Actual	Predicted	Error
6.7390	6.5904	2.2057	1.1680	1.4398	23.2709	4.6260	4.6408	0.3194
6.8030	6.7885	0.2137	1.2285	1.3372	8.8518	5.6370	5.2057	7.6517
6.9130	6.8230	1.3012	1.1475	1.0732	6.4742	5.7520	5.2591	8.5685
6.4155	6.6592	3.7984	1.3375	1.0830	19.0271	5.680	5.2575	7.4384
7.3260	6.3124	13.8355	1.0385	1.3923	34.0674	5.5890	4.7655	14.7340
	Average	**4.2709**		**Average**	**18.3383**		**Average**	**7.7424**
							MSE	**0.02982**

Table 6.11: 12,000 iterations

Topology: MLP, Hidden layers: 1, Iterations: 12,000, Momentum: none, Processing: batch								
Leg length (mm)			**Penetration (mm)**			**Effective throat (mm)**		
Actual	Predicted	Error	Actual	Predicted	Error	Actual	Predicted	Error
6.7390	6.8190	1.1866	1.1680	1.4104	20.7502	4.6260	4.8072	3.9179
6.8030	6.7914	0.1712	1.2285	1.3648	11.0984	5.6370	4.8739	13.5365
6.9130	6.8920	0.3042	1.1475	1.3327	16.1404	5.7520	4.9278	14.3297
6.4155	6.9486	8.3096	1.3375	1.4117	5.5469	5.680	4.9614	12.6516
7.3260	6.8393	6.6434	1.0385	1.4593	40.5158	5.5890	4.7712	14.6332
	Average	**3.3230**		**Average**	**18.8104**		**Average**	**11.8138**
							MSE	**0.03090**

Table 6.12: 16,000 iterations

Topology: MLP, Hidden layers: 1, Iterations: 16,000, Momentum: none, Processing: batch								
Leg length (mm)			**Penetration (mm)**			**Effective throat (mm)**		
Actual	Predicted	Error	Actual	Predicted	Error	Actual	Predicted	Error
6.7390	6.6719	0.9955	1.1680	1.5652	34.0027	4.6260	4.8483	4.8063
6.8030	6.4991	4.4666	1.2285	1.2585	2.4457	5.6370	4.8732	13.5501
6.9130	6.4814	6.2438	1.1475	1.1244	2.0126	5.7520	4.8973	14.8593
6.4155	6.4850	1.0835	1.3375	1.3667	2.1834	5.680	4.8479	14.6502
7.3260	6.5402	10.7269	1.0385	1.6444	58.3441	5.5890	4.7821	14.4376
	Average	**4.7032**		**Average**	**19.7977**		**Average**	**12.4607**
							MSE	**0.02647**

Table 6.13: 20,000 iterations

Topology: MLP, Hidden layers: 1, Iterations: 20,000, Momentum: none, Processing: batch								
Leg length (mm)			**Penetration (mm)**			**Effective throat (mm)**		
Actual	Predicted	Error	Actual	Predicted	Error	Actual	Predicted	Error
6.7390	6.5400	2.9530	1.1680	1.3997	19.8332	4.6260	4.7657	3.0200
6.8030	7.3976	8.7408	1.2285	1.2860	4.6817	5.6370	4.9202	12.7163
6.9130	7.6560	10.7486	1.1475	1.2949	12.8411	5.7520	4.9363	14.1803
6.4155	7.0184	9.3968	1.3375	1.4101	5.4303	5.680	4.8442	14.7148
7.3260	6.9070	5.7191	1.0385	1.5225	46.6058	5.5890	4.7243	15.4706
	Average	**7.5116**		**Average**	**17.8784**		**Average**	**12.0204**
							MSE	**0.03258**

From Tables 6.9 – 6.13 it can be seen that the most accurate predictions were obtained using 8,000 iterations, as the average percentage error was the lowest. The overtraining of the network can be seen in Figure 6.17, which shows a trendline for the average of the three errors reported, and shows that the accuracy decreases above an optimum number of iterations, in this case 8000 iterations.

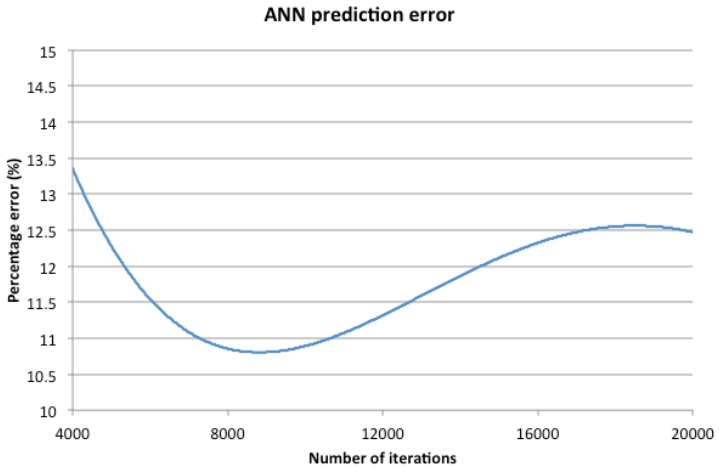

Figure 6.17: Prediction error trendline

6.5.3 Number of hidden layers

MLP networks extend the perceptron with hidden layers, i.e. layers of PEs that are not connected to the outside world. The MLP constructs input-output mappings that are of the form:

$$y = f\left(\sum f\left(\sum(*)\right)\right) \tag{6.1}$$

Where the number of function compositions is given by the number of network layers, i.e. a one hidden layer MLP has two levels of function composition, a two hidden layer MLP has three levels of function composition, and so on.

The addition of a hidden layer introduces important mapping capabilities to the MLP as it allows it to construct a 'bump' in the input space, i.e. a single, large value surrounded by a region of low values, and even disjoint regions. A second hidden layer can essentially combine bumps in disjoint regions. This is important as several theorems state that a linear combination of localised bumps can approximate a reasonable function [6.15].

One of the key disadvantages of increasing the number of hidden layers is that it increases the time taken to conduct the training iterations [6.16]. The theorems do not state the number of hidden layers required to solve a given problem, thus the complexity of the model was increased through the addition of hidden layers to try and improve its accuracy. This involved maintaining the MLP network topology and number of iterations constant and varying the number of hidden layers between 1 and 5, with the effect displayed in Tables 6.14 – 6.18.

Table 6.14: 1 hidden layer

Topology: MLP, Hidden layers: 1, Iterations: 8,000, Momentum: none, Processing: batch								
Leg length (mm)			**Penetration (mm)**			**Effective throat (mm)**		
Actual	Predicted	Error	Actual	Predicted	Error	Actual	Predicted	Error
6.7390	6.5904	2.2057	1.1680	1.4398	23.2709	4.6260	4.6408	0.3194
6.8030	6.7885	0.2137	1.2285	1.3372	8.8518	5.6370	5.2057	7.6517
6.9130	6.8230	1.3012	1.1475	1.0732	6.4742	5.7520	5.2591	8.5685
6.4155	6.6592	3.7984	1.3375	1.0830	19.0271	5.680	5.2575	7.4384
7.3260	6.3124	13.8355	1.0385	1.3923	34.0674	5.5890	4.7655	14.7340
	Average	**4.2709**		**Average**	**18.3383**		**Average**	**7.7424**
							MSE	**0.02982**

Table 6.15: 2 hidden layers

Topology: MLP, Hidden layers: 2, Iterations: 8,000, Momentum: none, Processing: batch								
Leg length (mm)			**Penetration (mm)**			**Effective throat (mm)**		
Actual	Predicted	Error	Actual	Predicted	Error	Actual	Predicted	Error
6.7390	6.3628	5.5818	1.1680	1.5917	36.2763	4.6260	4.6908	1.4011
6.8030	6.8752	1.0613	1.2285	1.2785	4.0732	5.6370	4.9512	12.1660
6.9130	6.1516	11.0138	1.1475	1.4240	24.0915	5.7520	4.7403	17.5880
6.4155	6.0180	6.1957	1.3375	1.5351	14.7732	5.680	4.8033	15.4343
7.3260	6.2420	14.7968	1.0385	1.5784	51.9876	5.5890	4.7877	14.3372
	Average	**7.7299**		**Average**	**26.2404**		**Average**	**12.1853**
							MSE	**0.01684**

Table 6.16: 3 hidden layers

Topology: MLP, Hidden layers: 3, Iterations: 8,000, Momentum: none, Processing: batch								
Leg length (mm)			**Penetration (mm)**			**Effective throat (mm)**		
Actual	Predicted	Error	Actual	Predicted	Error	Actual	Predicted	Error
6.7390	6.4249	4.6609	1.1680	1.2894	10.3906	4.6260	4.7882	3.5067
6.8030	6.6402	2.3927	1.2285	1.3546	10.2672	5.6370	4.8837	13.3634
6.9130	6.6170	4.2816	1.1475	1.5413	34.3164	5.7520	4.9078	14.6765
6.4155	6.6972	4.3909	1.3375	1.5407	15.1908	5.680	4.9041	13.6606
7.3260	6.6493	9.2373	1.0385	1.4739	41.9264	5.5890	4.8490	13.2406
	Average	**4.9927**		**Average**	**22.4183**		**Average**	**11.6896**
							MSE	**0.00595**

Table 6.17: 4 hidden layers

Topology: MLP, Hidden layers: 4, Iterations: 8,000, Momentum: none, Processing: batch								
Leg length (mm)			**Penetration (mm)**			**Effective throat (mm)**		
Actual	Predicted	Error	Actual	Predicted	Error	Actual	Predicted	Error
6.7390	7.0438	4.5229	1.1680	0.8700	25.5137	4.6260	5.0436	10.5263
6.8030	6.8869	1.2336	1.2285	1.2091	1.5779	5.6370	4.3271	24.7723
6.9130	6.3135	8.6721	1.1475	1.7349	51.1907	5.7520	3.9345	30.7303
6.4155	7.5038	16.9632	1.3375	1.0916	18.3838	5.680	4.4916	19.6353
7.3260	6.5870	10.0867	1.0385	1.4403	38.6918	5.5890	4.8404	4.8385
	Average	**8.2957**		**Average**	**27.0716**		**Average**	**18.1005**
							MSE	**0.00185**

Table 6.18: 5 hidden layers

Topology: MLP, Hidden layers: 5, Iterations: 8,000, Momentum: none, Processing: batch								
Leg length (mm)			**Penetration (mm)**			**Effective throat (mm)**		
Actual	Predicted	Error	Actual	Predicted	Error	Actual	Predicted	Error
6.7390	6.2769	6.8570	1.1680	1.3532	15.8550	4.6260	3.9152	15.3647
6.8030	6.9594	2.2986	1.2285	1.4672	19.4331	5.6370	4.7809	15.1870
6.9130	6.7594	2.2218	1.1475	0.9620	16.1680	5.7520	4.0623	29.3758
6.4155	6.0030	6.4298	1.3375	1.1856	11.3587	5.680	5.0518	11.0598
7.3260	5.7753	21.1677	1.0385	1.6492	58.8012	5.5890	4.6030	17.6421
	Average	**7.7950**		**Average**	**24.3232**		**Average**	**17.7259**
							MSE	**0.00179**

As can be seen in Tables 6.14 – 6.18, with an increased in the number of hidden layers, the MSE decreases from 0.03238 for a 1 hidden layer network to 0.00179 for a 5 hidden layer network. However, this reduction in MSE did not correspond to an improvement in model accuracy, with the average error of 10.1172% and 16.6147% for the 1 and 5 hidden layer networks respectively. The one hidden layer model was found to produce the most accurate predictions and was subsequently taken forward to the next stage of model development.

6.5.4 Momentum learning

The addition of a momentum coefficient is an improvement to the straight gradient-decent method and is used to speed up and stabilise convergence.

The gradient-decent method is a simple first order algorithm. It involves determining the error values associated with each unit and transferring the information to a weight change between units i and j:

$$\Delta w_{ij}(n) = -\eta \nabla J(w_{ij}) \tag{6.2}$$

Since the gradient-decent method is based only upon local gradient information, it is clear that it will 'get stuck' in a local minimum of the training error, and stop training.

The momentum learning method essentially adds a memory term to the weight updating and helps bypass a local minimum by making the movement more pronounced in the current iteration:

$$\Delta w_{ij}(n+1) = w_{ij}(n) + \eta \delta_i(n) x_j(n) + \alpha \left(w_{ij}(n) - w_{ij}(n-1) \right) \tag{6.3}$$

For example, in a narrow local minimum, the standard gradient-decent method algorithm dictates that $\Delta w_{ij}(n)$ will change direction and the solution will stop. Therefore, if narrow enough, the additional contribution from the previous iteration may be enough for the solution to carry on past this local minimum, as depicted in Figure 6.18.

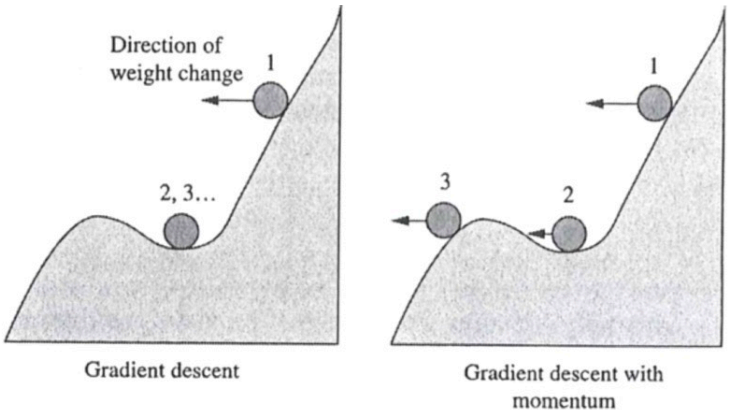

Figure 6.18: Effect of momentum coefficient [6.15]

The momentum constant can have a value of between 0 and 1. In addition to the cases discussed previously, which discussed a network with no momentum

coefficient, the model was trained with values of 0.3, 0.5, 0.7 and 0.9, whilst maintaining the previously discussed parameters constant, the results for which shown in Tables 6.19 – 6.23.

Table 6.19: No momentum

Topology: MLP, Hidden layers: 1, Iterations: 8,000, Momentum: none, Processing: batch								
Leg length (mm)			**Penetration (mm)**			**Effective throat (mm)**		
Actual	Predicted	Error	Actual	Predicted	Error	Actual	Predicted	Error
6.7390	6.5904	2.2057	1.1680	1.4398	23.2709	4.6260	4.6408	0.3194
6.8030	6.7885	0.2137	1.2285	1.3372	8.8518	5.6370	5.2057	7.6517
6.9130	6.8230	1.3012	1.1475	1.0732	6.4742	5.7520	5.2591	8.5685
6.4155	6.6592	3.7984	1.3375	1.0830	19.0271	5.680	5.2575	7.4384
7.3260	6.3124	13.8355	1.0385	1.3923	34.0674	5.5890	4.7655	14.7340
	Average	**4.2709**		**Average**	**18.3383**		**Average**	**7.7424**
							MSE	**0.02982**

Table 6.20: 0.3 momentum

Topology: MLP, Hidden layers: 1, Iterations: 8,000, Momentum: 0.3, Processing: batch								
Leg length (mm)			**Penetration (mm)**			**Effective throat (mm)**		
Actual	Predicted	Error	Actual	Predicted	Error	Actual	Predicted	Error
6.7390	6.7306	0.1249	1.1680	1.4832	26.9852	4.6260	4.7655	3.0153
6.8030	6.7168	1.2678	1.2285	1.5106	22.9604	5.6370	4.7994	14.8584
6.9130	6.7612	2.1956	1.1475	1.4139	23.2119	5.7520	4.9523	13.9033
6.4155	6.7592	5.3568	1.3375	1.4513	8.5106	5.680	4.9107	13.5438
7.3260	6.7310	8.1212	1.0385	1.4564	40.2397	5.5890	4.8741	12.7904
	Average	**3.4133**		**Average**	**24.3815**		**Average**	**11.6222**
							MSE	**0.03015**

Table 6.21: 0.5 momentum

Topology: MLP, Hidden layers: 1, Iterations: 8,000, Momentum: 0.5, Processing: batch								
Leg length (mm)			**Penetration (mm)**			**Effective throat (mm)**		
Actual	Predicted	Error	Actual	Predicted	Error	Actual	Predicted	Error
6.7390	6.8599	1.7943	1.1680	1.3684	17.1564	4.6260	4.7574	2.8394
6.8030	6.7042	1.4518	1.2285	1.3357	8.7285	5.6370	4.7653	15.4638
6.9130	6.6973	3.1199	1.1475	1.2391	7.9813	5.7520	4.8399	15.8572
6.4155	6.7601	5.3706	1.3375	1.2779	4.4545	5.680	4.8207	15.1293
7.3260	6.5912	10.0304	1.0385	1.3864	33.5021	5.5890	4.7405	15.1821
	Average	**4.3534**		**Average**	**14.3646**		**Average**	**12.8944**
							MSE	**0.03270**

Table 6.22: 0.7 momentum

Topology: MLP, Hidden layers: 1, Iterations: 8,000, Momentum: 0.7, Processing: batch								
Leg length (mm)			**Penetration (mm)**			**Effective throat (mm)**		
Actual	Predicted	Error	Actual	Predicted	Error	Actual	Predicted	Error
6.7390	6.6406	1.4602	1.1680	1.3042	11.6567	4.6260	4.7981	3.7205
6.8030	6.6320	2.5138	1.2285	1.2135	1.2189	5.6370	4.8655	13.6864
6.9130	6.6318	4.0675	1.1475	1.2197	6.2926	5.7520	5.0267	12.6095
6.4155	6.6314	3.3649	1.3375	1.2784	4.4155	5.680	5.0047	11.8891
7.3260	6.6705	8.9469	1.0385	1.5109	45.4901	5.5890	4.6851	16.1721
	Average	**4.0707**		**Average**	**13.8148**		**Average**	**11.6155**
							MSE	**0.03038**

Table 6.23: 0.9 momentum

Topology: MLP, Hidden layers: 1, Iterations: 8,000, Momentum: 0.9, Processing: batch								
Leg length (mm)			**Penetration (mm)**			**Effective throat (mm)**		
Actual	Predicted	Error	Actual	Predicted	Error	Actual	Predicted	Error
6.7390	6.8027	0.9459	1.1680	1.4492	24.0754	4.6260	4.7422	2.5114
6.8030	6.6650	2.0286	1.2285	1.3575	10.4978	5.6370	4.8792	13.4430
6.9130	6.4727	6.3688	1.1475	1.1532	0.4978	5.7520	4.8613	15.4850
6.4155	6.4961	1.2556	1.3375	1.1703	12.5041	5.680	4.8181	15.1743
7.3260	6.5150	11.0697	1.0385	1.2745	22.7290	5.5890	4.9076	12.1912
	Average	**4.3337**		**Average**	**14.0608**		**Average**	**11.7610**
							MSE	**0.03317**

From Tables 6.19 – 6.23 above, it can be seen that the addition of a momentum coefficient is effective in reducing the prediction percentage error, with a coefficient of 0.7 producing the most accurate predictions.

6.5.5 Processing method

The final stage in the model development involved specifying when the weights are updated, i.e. batch or online processing. Batch learning updates the weights after the presentation of the entire training set. In contrast, online learning updates the weights after the presentation of each data set. The effect of each processing method is shown in Tables 6.24 and 6.25.

Table 6.24: Batch processing

Topology: MLP, Hidden layers: 1, Iterations: 8,000, Momentum: 0.7, Processing: batch								
Leg length (mm)			**Penetration (mm)**			**Effective throat (mm)**		
Actual	Predicted	Error	Actual	Predicted	Error	Actual	Predicted	Error
6.7390	6.6406	1.4602	1.1680	1.3042	11.6567	4.6260	4.7981	3.7205
6.8030	6.6320	2.5138	1.2285	1.2135	1.2189	5.6370	4.8655	13.6864
6.9130	6.6318	4.0675	1.1475	1.2197	6.2926	5.7520	5.0267	12.6095
6.4155	6.6314	3.3649	1.3375	1.2784	4.4155	5.680	5.0047	11.8891
7.3260	6.6705	8.9469	1.0385	1.5109	45.4901	5.5890	4.6851	16.1721
	Average	**4.0707**		**Average**	**13.8148**		**Average**	**11.6155**
							MSE	**0.03038**

Table 6.25: Online processing

Topology: MLP, Hidden layers: 1, Iterations: 8,000, Momentum: none, Processing: online								
Leg length (mm)			**Penetration (mm)**			**Effective throat (mm)**		
Actual	Predicted	Error	Actual	Predicted	Error	Actual	Predicted	Error
6.7390	6.7054	0.4993	1.1680	1.3255	13.4864	4.6260	4.6669	0.8846
6.8030	6.4555	5.1080	1.2285	1.2832	4.4515	5.6370	4.9452	12.2719
6.9130	6.4555	6.6179	1.1475	1.2832	11.8245	5.7520	4.9452	14.0259
6.4155	6.4941	1.2249	1.3375	1.6067	20.1271	5.680	4.8560	14.5077
7.3260	6.8186	6.9259	1.0385	1.3195	27.0585	5.5890	4.3721	21.7731
	Average	**3.8755**		**Average**	**15.3896**		**Average**	**12.6926**
							MSE	**0.03238**

As can be seen in Tables 6.24 and 6.25, the application of online processing decreased the accuracy of prediction, and marginally increased the MSE, thus batch processing was selected.

6.5.6 ANN architecture

The refinement process detailed previously was implemented in the generation of each ANN model.

The architecture used for the prediction of weld geometry is as follows:

- Topology - Multilayer perceptron
- Iterations - 8,000
- Hidden layers - 1
- Momentum coefficient - 0.7
- Processing method - Batch

The architecture used for shielding gas optimisation is as follows:

- Topology - Multilayer perceptron
- Iterations - 8,000
- Hidden layers - 1
- Momentum coefficient - 0.7
- Processing method - Batch

Three ANN models were generated in the distortion prediction stage; one to predict the distortion due to welding, and the other two the final distortion of steel plate after both welding and induction heating with and without weld distortion as an input.

The architecture used for the prediction of weld distortion is as follows:

- Topology - Multilayer perceptron
- Iterations - 10,000
- Hidden layers - 2
- Momentum coefficient - 0.7
- Processing method - Batch

The architecture used for the prediction of weld and induction heating distortion is as follows:

- Topology - Multilayer perceptron
- Iterations - 14,000
- Hidden layers - 2
- Momentum coefficient - 0.7
- Processing method - Batch

The architecture used for the prediction of induction heating parameters is as follows:

- Topology - Multilayer perceptron
- Iterations - 10,000
- Hidden layers - 2
- Momentum coefficient - 0.7
- Processing method - Batch

6.6 Results and discussion

6.6.1 Weld geometry

The ANN model, constructed according to the network architecture specified previously, was subsequently validated against experimental data (Table 6.26) not contained within the training or testing data. This was used solely to ensure the model was learning the trends among the training data, with the testing data being used for comparison in the later discussions.

Table 6.26: Validation weld data

Weld Parameters				**Weld Outputs**		
Shielding gas configuration	Voltage (V)	Current (A)	Travel speed (mm/s)	Penetration (mm)	Leg length (mm)	Effective throat (mm)
Alternating @ 5 Hz	21.7	153	2.0	1.288	6.835	5.675
Alternating @ 5 Hz	23.8	156	2.0	1.534	6.922	4.923
Alternating @ 5 Hz	25.8	157	2.0	1.421	7.052	4.652
Alternating @ 5 Hz	21.9	157	2.5	1.201	6.177	4.955
Alternating @ 5 Hz	24.0	154	2.5	1.363	6.431	4.366
Alternating @ 5 Hz	26.1	155	2.5	1.315	6.661	4.211
Alternating @ 5 Hz	22.1	154	3.0	1.218	5.295	4.352
Alternating @ 5 Hz	23.9	157	3.0	1.341	5.480	3.934
Alternating @ 5 Hz	25.8	156	3.0	1.523	5.794	3.892

6.6.1.1 Prediction of weld geometry

The trained model was then applied to a given set of input parameters with the only variable being the shielding gas composition. The model was shown to accurately represent the weld penetration, leg length, and effective throat thickness by comparing the actual values with those predicted by the NeuroSolutions® package, as shown in Figure 6.19. The software was found to, on average, overestimate weld penetration by 0.06 mm and underestimate leg length and effective throat thickness by 0.23 and 0.52 mm, respectively. When compared with the experimental data, this equates to percentage errors of 4.9, 3.4, and 9.6%, respectively, which is deemed as highly accurate in any ANN study.

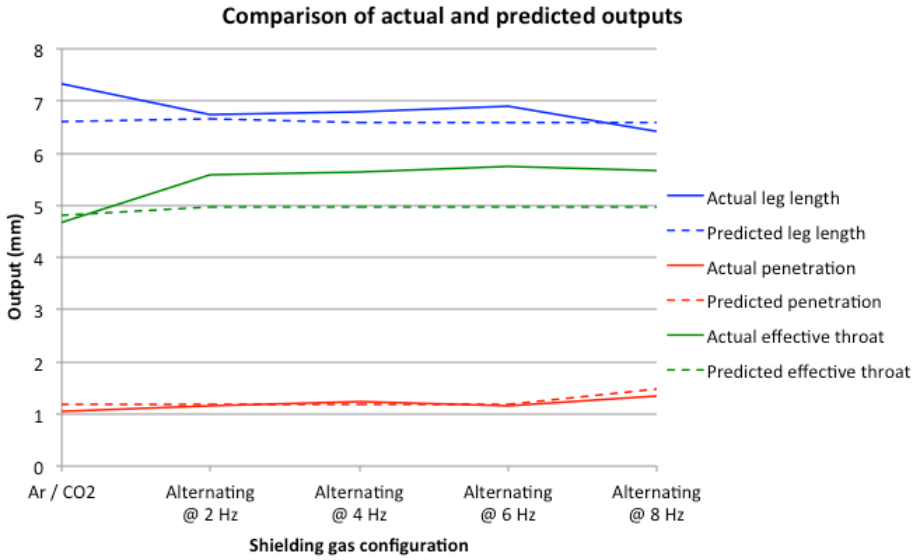

Figure 6.19: Comparison of experimental and ANN predicted weld geometries

Looking specifically at penetration prediction, Figure 6.20, the addition of helium has resulted in an increase in penetration, due to the narrower, more concentrated arc column that helium produces [6.17]. In addition, the prediction has shown that increasing the frequency of shielding gas alternation from 2 to 8 Hz resulted in an increase in penetration, and is in agreement with findings previously reported in Section 5.2.2.

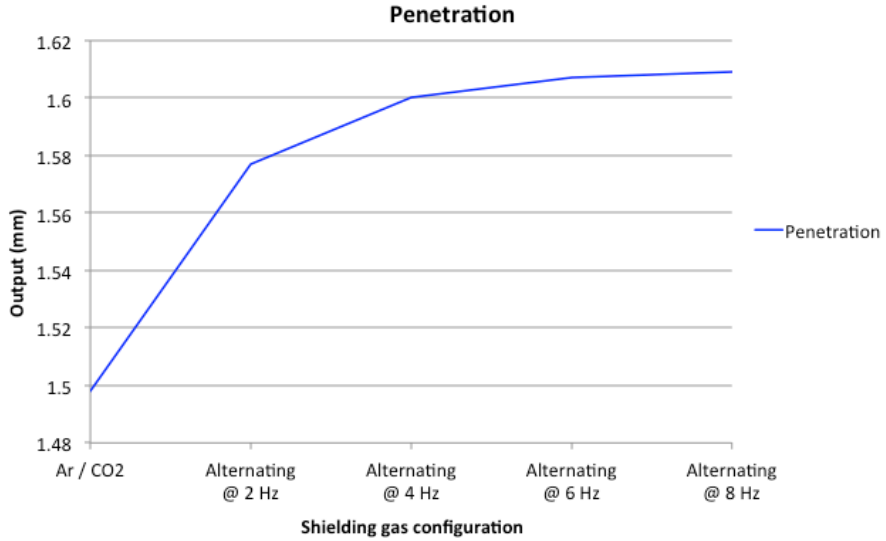

Figure 6.20: ANN prediction showing the effect of shielding gas configuration on penetration

As a result of the increase in penetration when using alternating shielding gases, for a given level of penetration, the travel speed can be increased, thus reducing the cost of the weld. The ANN model was therefore trained in reverse, i.e. specifying the weld outputs as model inputs, and weld travel speed as the prediction output. It was predicted that for an equivalent level of penetration, the travel speed for alternating shielding gases could be increased by, on average, 28% when compared to the argon / 20% carbon dioxide base case, and therefore has the potential to greatly increase the productivity of the welding process, whilst reducing weld induced distortion. This is in agreement with the findings of Section 5.2.1, which demonstrated that the travel speed can be increased by 18% on the second pass and 82% on the third pass, thus resulting in an overall time reduction of 22%.

The ANN model has also predicted that the application of alternating shielding gases results in a shorter leg length (Figure 6.21), while the effective throat thickness is shown to increase, Figure 6.22. This is primarily linked to the added convexity of the weld metal with the addition of helium.

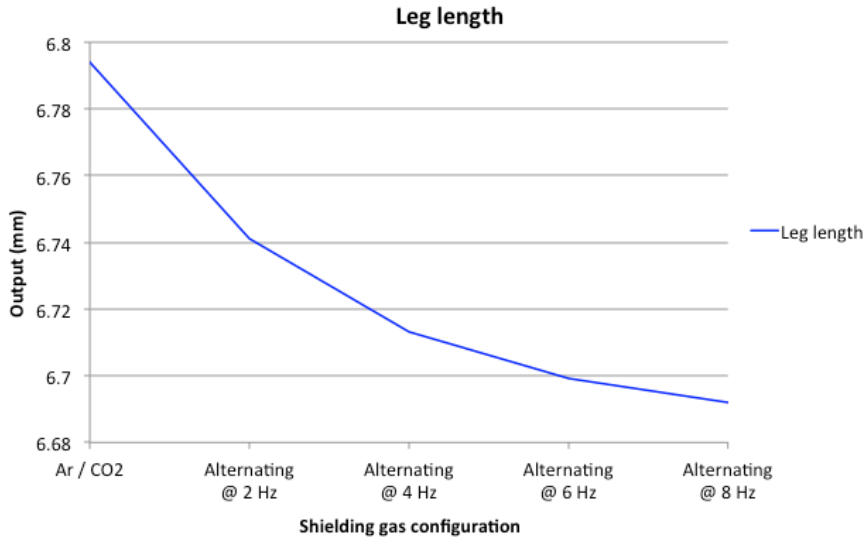

Figure 6.21: ANN prediction showing the effect of shielding gas configuration on leg length

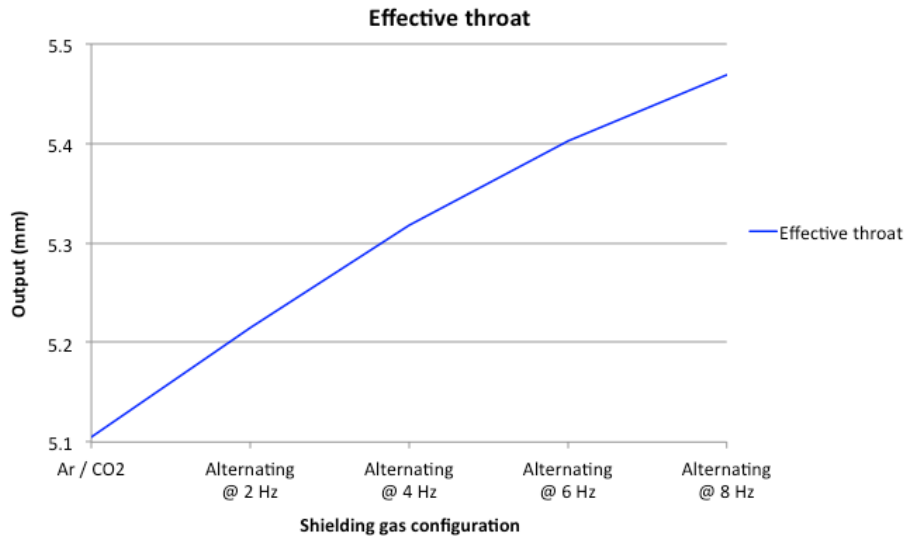

Figure 6.22: ANN prediction showing the effect of shielding gas configuration on effective throat

The macro images, Figures 6.23, show that a typical alternating shielding gas weld produces a narrower weld with increased convexity than the argon / 20% carbon dioxide base case. This along with the results generated by the ANN model (Figures 6.20 – 6.22) show that there is a trend between the shielding gas and the weld geometry. Although the concavity of the argon / 20% carbon dioxide weld can be the result of too low a filler wire feed speed or too fast a travel speed, the fact that the alternating gas case produces a convex weld with the same parameters can be attributed to surface tension effects and potentially different flow vectors in the liquid weld metal. Kang et al. [6.18] stated that alternating shielding gases creates complex flow vectors within the molten weld pool, whereas constant gas flows produce a steady flow vector. It was speculated that helium produces a flow vector that flows radially outwards at the pool surface, and upwards in the central location, which will result in a more convex, weld profile. Although no supporting data accompanied the previous statement, the arc forces derived in Chapter 4 indicate that the variation in fluid flow vectors is possible.

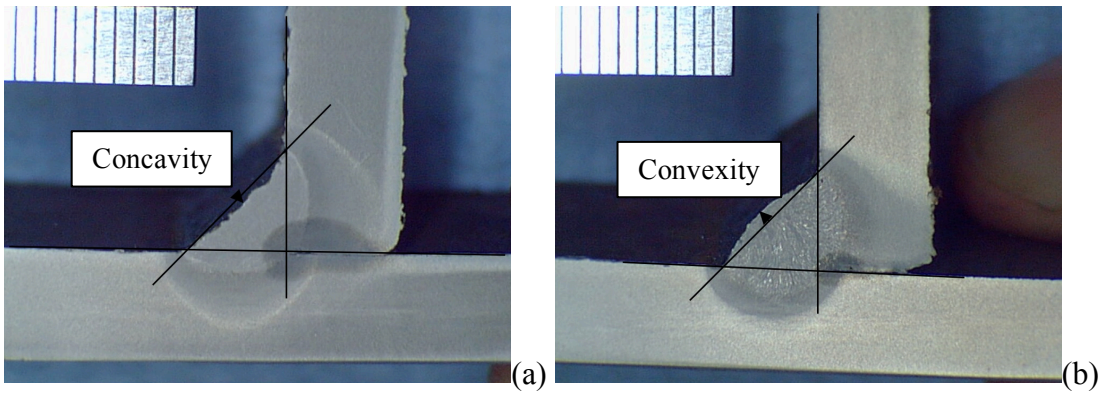

(a) (b)

Figure 6.23: Weld macro for (a) argon / 20% carbon dioxide showing the concavity of a typical weld, and (b) alternating shielding gases showing the convexity of a typical weld

6.6.1.2 Sensitivity study

A sensitivity study is an extremely powerful tool in the NeuroSolutions package, which can be used to determine the influence of each of the input variables on the output of the model.

In order to perform the sensitivity analysis, the neural network must first be trained as normal. The analysis then perturbs each of the inputs, one at a time, by a known variance from the mean whilst keeping all other variables at their respective means and measuring the change in the output.

The sensitivity for the input k can be expressed as shown:

$$S_k = \frac{\sum_{p=1}^{p} \sum_{i=1}^{o} (y_{ip} - \bar{y}_{ip})^2}{\sigma_k^2} \tag{6.4}$$

This, when applied across the training data, can compute how much a change in the input affects the output. The sensitivity of a model is not only important in the context of this model, i.e. determining the key factors for weld penetration etc., but also aids the training of the model with inputs of high sensitivities having more importance in the mapping.

The results of the sensitivity study, Figure 6.24, show that the travel speed is the most influential input variable in affecting the output variables. This is to be

somewhat expected since the heat input is directly related to the travel speed through equation (2.1).

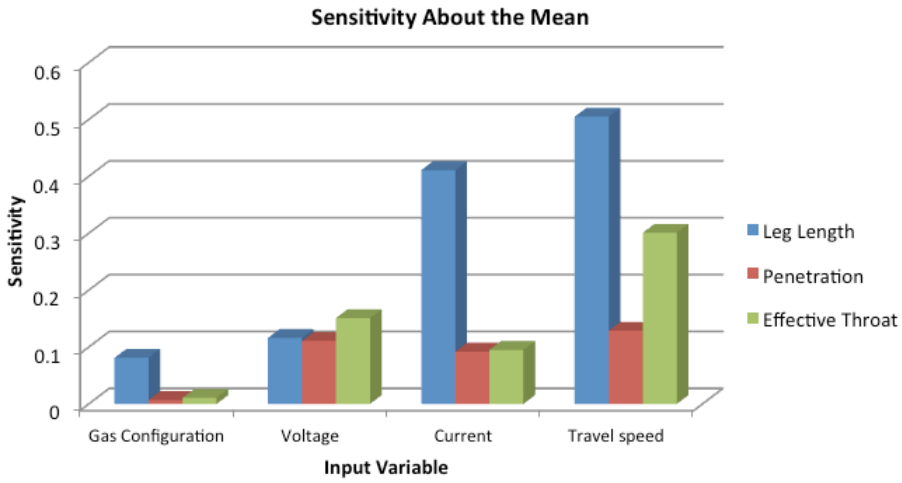

Figure 6.24: Sensitivity analysis results

The sensitivity study results show that the shielding gas configurations have the lowest contribution of the inputs on the weld geometries. However, this is a result of the sensitivity study perturbing the alternating frequency e.g. comparing an alternating frequency of 5.9 Hz with 6 Hz. As can be seen in Figures 6.20 – 6.22, although there is a slight change in the geometries using different alternation frequencies, the greatest step change is observed between the use of argon / 20% carbon dioxide and alternating at 8 Hz, although, in fact, any frequency of alternation provides a similar step change. Figures 6.20 – 6.22 also show that alternating shielding gases have a positive effect on the level of weld penetration while also reducing leg length and increasing the effective throat thickness.

6.6.2 Prediction of weld quality

When set in pattern recognition (or classification) mode, NeuroSolutions not only indicates whether an output is a binary 0 or 1, but also indicates how accurate the prediction is, i.e. a prediction of 0.95 is far more likely to be a 1 than a 0, thus allowing a comparison of two different network structures with the same binary

predictions. The ANN model, constructed according to the network architecture specified previously.

In order to ensure the validity of the model and ensure that the model had not simply remembered the data that were used to train the model, validation welds were used to test the generated models robustness and accuracy. A number of weld input parameters were selected that were within the training data range and had not previously been used in the model generation. Shielding gas flow rates of 7.5 and 12.5 l/min were used to prevent the model potentially providing a previously 'learned' answer. The weld input variables were then entered into the ANN model, and the results compared to the radiographic inspection of the experimental weld. Table 6.27 presents the input parameters used, along with the ANN prediction and radiographic inspection results of these trials.

The validation welds were selected to give a spread of datasets across the shielding gas and cross draft ranges, with particular attention being paid to the transitional region for each shielding gas configuration. This meant that the result for each dataset could not simply be read from the experimental trials and presented a far more challenging prediction for the model, while validation trials away from the transitional region have been omitted from the discussion in order to highlight the benefit of using such an ANN model to optimise welding parameters in this region.

As can be seen in Table 6.27, the ANN model predicted 17 out of the 20 validation welds successfully. However, this prediction accuracy can be easily misinterpreted due to the location of incorrect predictions. The three welds that the model incorrectly predicted are along the pass / fail transition boundary.

The trend between cross draft velocity and the predicted output is shown in Figure 6.25. Remembering that an output of '1' is defined a pass and an output of '0' defined a fail, all validation welds were carried out at predicted cross draft velocities that would produce borderline results, i.e. in the central portion of this graph as indicated by dashed lines.

Table 6.27: Validation weld data

Weld Parameters				Weld Output	ANN Output
Shielding gas configuration	Nozzle diameter (mm)	Gas flow rate (l/min)	Cross draft velocity (m/s)	Radiographic examination	ANN prediction
Ar / 20% CO_2	12	7.5	1.0	Pass	Pass
Ar / 20% CO_2	12	7.5	3.0	Fail	Fail
Ar / 20% CO_2	16	7.5	1.5	Pass	Pass
Ar / 20% CO_2	16	12.5	1.5	Fail	Fail
Alternating @ 2 Hz	12	12.5	2.0	Pass	Pass
Alternating @ 2 Hz	12	12.5	3.0	Pass	Fail
Alternating @ 2 Hz	16	7.5	1.5	Fail	Fail
Alternating @ 2 Hz	16	12.5	1.5	Pass	Fail
Alternating @ 4 Hz	12	7.5	2.0	Fail	Fail
Alternating @ 4 Hz	12	7.5	2.5	Pass	Fail
Alternating @ 4 Hz	16	7.5	1.5	Fail	Fail
Alternating @ 4 Hz	16	12.5	1.5	Pass	Pass
Alternating @ 6 Hz	12	12.5	2.5	Pass	Pass
Alternating @ 6 Hz	12	12.5	3.0	Fail	Fail
Alternating @ 6 Hz	16	7.5	1.5	Pass	Pass
Alternating @ 6 Hz	16	12.5	1.5	Pass	Pass
Alternating @ 8 Hz	12	7.5	2.5	Fail	Fail
Alternating @ 8 Hz	12	7.5	2.0	Pass	Pass
Alternating @ 8 Hz	12	12.5	2.0	Pass	Pass
Alternating @ 8 Hz	16	12.5	2.0	Fail	Fail

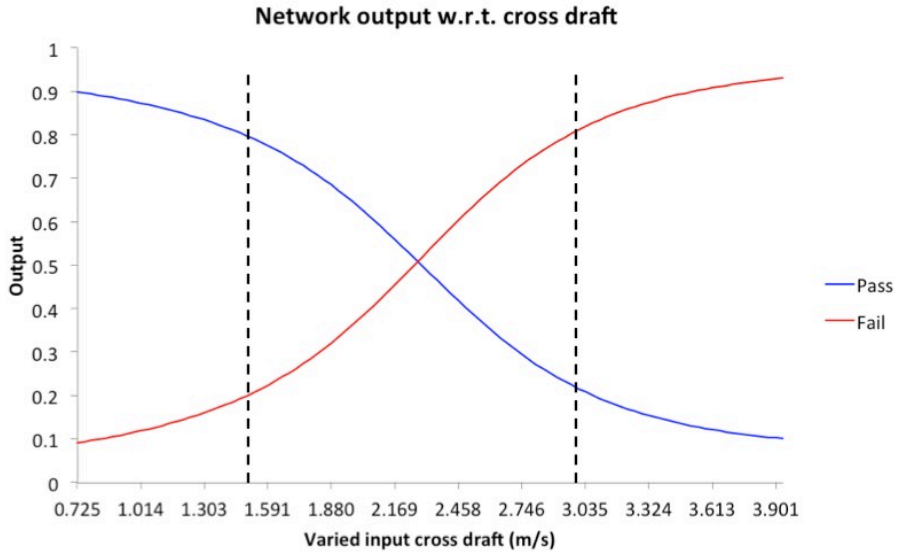

Figure 6.25: ANN output with respect to cross draft velocity

The accuracy of prediction could be enhanced by providing a greater density of datasets for the transitional region, that is, varying the cross draft velocity by 0.1 m/s rather than 0.5 m/s, and/or varying the shielding gas flow rate in 1 l/min increments rather than 5 l/min. This would provide the model with a better understanding of where the weld transitioned from good to poor quality, and would ultimately increase the accuracy of prediction. However, as an industrial tool, it is not expected that this level of risk would be employed and some safety factor would be used; therefore these additional data were not required.

6.6.2.1 Sensitivity study

A sensitivity study was conducted to determine the influence of each of the input variables on the models prediction. The results of the sensitivity study, Figure 6.26, show that the cross draft velocity is the most influential input variable affecting the weld quality. This was somewhat expected, given the cross draft is the primary reason the weld will fail. The other major parameters, again as predicted, were nozzle diameter and the shielding gas flow rates.

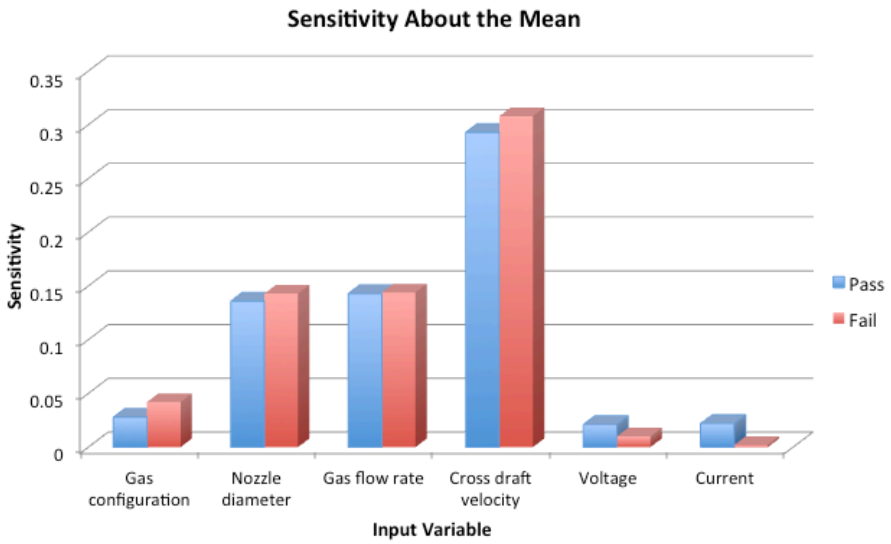

Figure 6.26: Sensitivity analysis results

As was the case previously, the shielding gas configuration had the lowest contribution of the inputs on the weld quality. Again, this is a result of the sensitivity study analysing the effect of a small variation in alternating frequency rather than comparing alternating shielding gases to a conventional flow.

6.6.3 Prediction of distortion

Three ANN models were developed for distortion prediction, with their network architecture specified previously.

6.6.3.1 Weld induced distortion prediction (Model 1)

Firstly, a model was constructed to predict the resulting angular distortion using the welding parameters, i.e. voltage, current, travel speed, and the plate thickness as inputs.

The range of the prediction error for this model during testing was 0.0469 – 0.0859° with a mean error of 0.0651°, when compared to the testing data sets as shown in Figure 6.27.

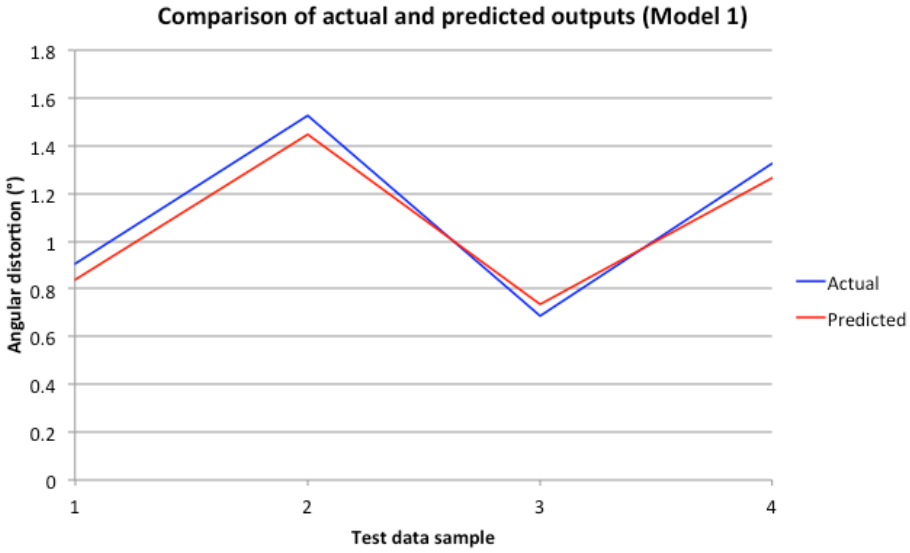

Figure 6.27: Model 1 comparison of measured and predicted weld distortion

Sensitivity study

A sensitivity study was conducted to determine the influence of each of the input variables on the models prediction. The results of the sensitivity study, Figure 6.28, show that, for the experimental welds carried out in this study, plate thickness is the most dominant parameter affecting distortion while weld travel speed also has a small but visible influence.

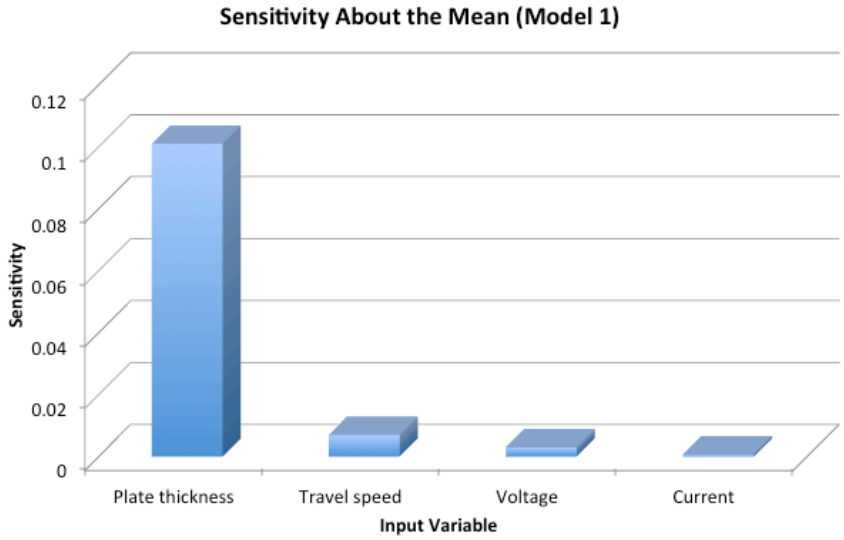

Figure 6.28: Model 1 sensitivity analysis results

6.6.3.2 Final distortion prediction (Model 2)

The next stage involved the generation of an ANN model to predict the final distortion following both welding and induction heating processes. The inputs in this case were the welding parameters, plate thickness, induction coil travel speed and post-weld angular distortion. The measured post-weld distortion has been selected as an input for this model to allow the model to predict only the effect of the induction heating process on the resulting distortion of the plate. As the power output of the induction coil was constant for all experiments it has not been included as an input.

Overall, this model appears to have predicted the rectification distortion for the testing data successfully. As can be seen in Figure 6.29, there is a relatively large error of 0.257° present in the prediction of the first test sample. However, the prediction error for the remaining test samples range between 0.022° and 0.082°, with a mean overall error of 0.107°. Although the mean absolute error is larger than that for Model 1, this is due to the large percentage error for the first test sample, which is likely due to the more complex relationships between the inputs and output.

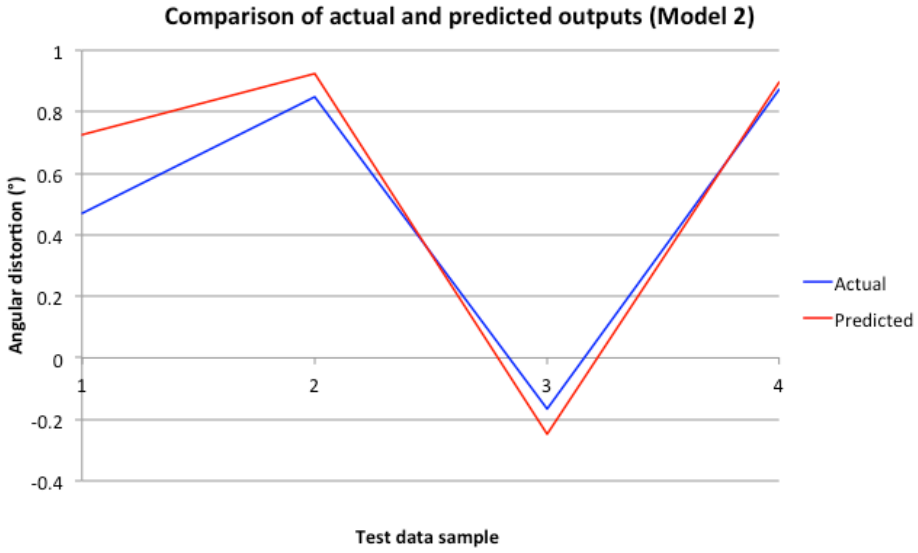

Figure 6.29: Model 2 comparison of measured and predicted distortion rectification

Sensitivity study

The sensitivity study results for model 2, Figure 6.30, show that the welding distortion is the dominant factor affecting the final distortion. This is to be expected, as the induction heating process will produce a given level of rectification, which, combined with the post-weld distortion, results in the residual distortion. The next most dominant factor is the travel speed of the induction coil as this directly controls the heat input to the plate from the coil. The plate thickness and welding parameters have a much lower influence than the previous two but still affect the output as they influence the geometry of the weld which will have an impact if the stiffness and conductive heat transfer of the plate in the region of the weld.

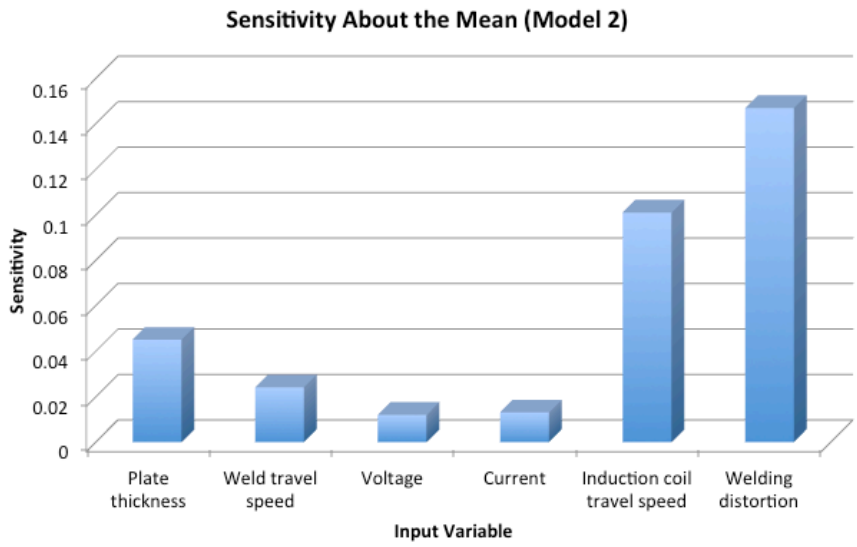

Figure 6.30: Model 2 sensitivity analysis results

6.6.3.3 Final distortion prediction (Model 3)

The final model was again developed to predict the final distortion of the plate after both welding and induction heating, but with different training inputs. The inputs in this case were the welding parameters, plate thickness and induction coil travel speed. In doing so, creating a model capable of predicting the final distortion of the plate without the need to measure the angular distortion after welding. This model was then used to predict the induction coil travel speed required to minimise or eliminate angular distortion.

The prediction error for the testing data, Figure 6.31, ranges from 0.061° to 0.142°, with a mean error of 0.087°. The absolute errors for this model are not significantly higher than those of the first model even with the added complexity of the model having to capture both the effects of welding and induction heating without having access to the post-weld distortion value.

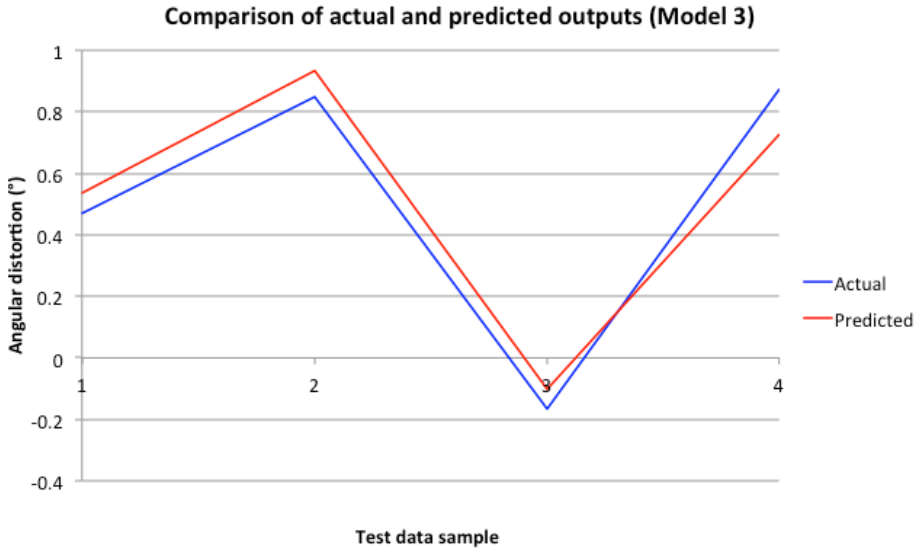

Figure 6.31: Model 3 comparison of measured and predicted distortion rectification

Sensitivity study

Similar to model 1, the sensitivity study conducted for model 3 (Figure 6.32) found the plate thickness to have the greatest influence on the final distortion. This is somewhat expected given this model is predicting the welding distortion within the prediction, and plate thickness was previously found to be the dominant factor affecting weld induced distortion. The induction coil travel speed had the second largest effect on distortion; following the results from model 2, this is a logical result. In agreement with the previous two models, the welding parameters have a much lower influence on the resulting distortion. This suggests that, for this experimental setup, the welding parameters have only a small impact on the results when compared to the influence of the plate thickness and induction coil travel speed.

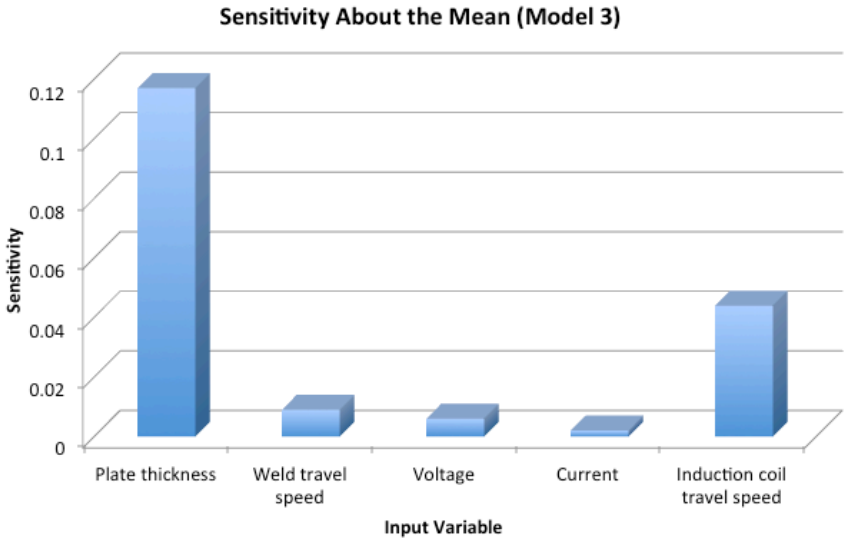

Figure 6.32: Model 3 sensitivity analysis results

6.6.3.4 Comparison of rectification models (Model 2 and 3)

The distortion rectification models, i.e. models 2 and 3, were evaluated by comparing their prediction accuracy when presented with validation data not contained within the training or testing data, Table 6.28.

Table 6.28: Validation weld data

		Weld parameters			Weld Output
Validation plate number	Plate thickness (mm)	Voltage (V)	Current (A)	Travel speed (mm/s)	Angular distortion (°)
1	6	20.7	214	2.75	0.900
2	8	20.7	221	2.75	1.535
3	8	20.6	222	2.25	1.266
4	10	20.6	218	2.25	1.409

The appropriate parameters from Table 6.28 were used as inputs for models 2 and 3, while the induction coil travel speed input was varied between 10 and 20 mm/s in increments of 1 mm/s.

The final distortion prediction for validation plate 1, Figure 6.33, shows a critical coil travel speed at which the minimum final distortion occurs. There is a slight difference between the two models as to where critical speed occurs; model 2

predicts that an induction coil travel speed of 13 mm/s will effectively eliminate the distortion, while model 3 predicts at a critical speed of 12 mm/s the final distortion will be 0.23°. For the final experimental induction heating process, 13 mm/s has been chosen as the coil travel speed.

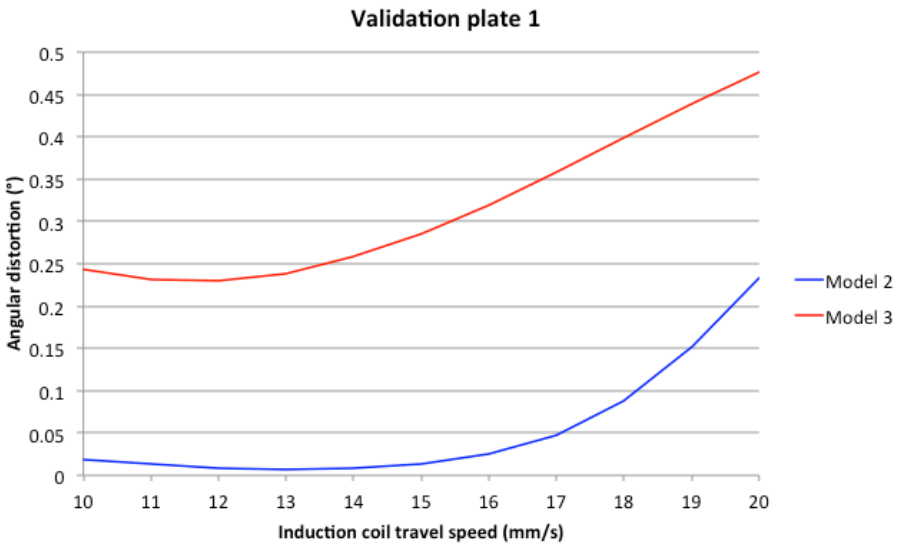

Figure 6.33: Validation plate 1 final distortion prediction

The predicted final distortion for validation plates 2, 3 and 4 (Figures 6.34) show that both models are in agreement, and the minimum final distortion will be achieved when an induction coil travel speed of 10 mm/s is used. There are some discrepancies in the predicted distortion for validation plates 2 and 3, model 2 predicting 0.12° lower distortion for plate 2 and 0.17° lower for plate 3, while the predicted results for plate 4 are very similar. A coil travel speed of 10 mm/s was chosen for the induction heating process for validation plate 2–4.

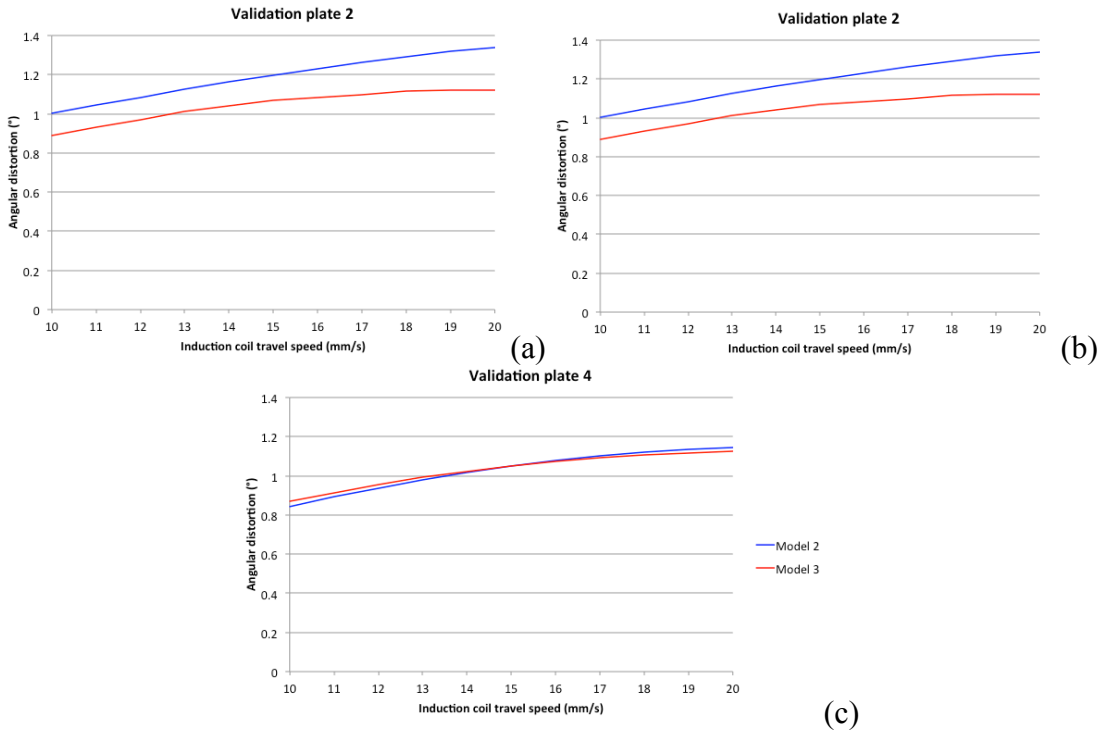

Figure 6.34: Final distortion prediction for validation plate (a) 2, (b) 3, and (c) 4

The validation study results, Figure 6.35, show that model 2 underestimated the final distortion of validation plate 1 by 0.331°, while the error of the other results ranges from 0.006° to 0.158°. The average error for the results is 0.136° indicating that the overall accuracy of the predictions is relatively good even when taking into account the larger error in the prediction of validation plate 1. The results also show that model 3 predicted the distortion of the validation plates reasonably well. In each case, the predictions by model 3 underestimated the actual values, although not to a significant degree. The maximum and average errors for the validation results were 0.18° and 0.12° respectively, which are lower than those for model 2.

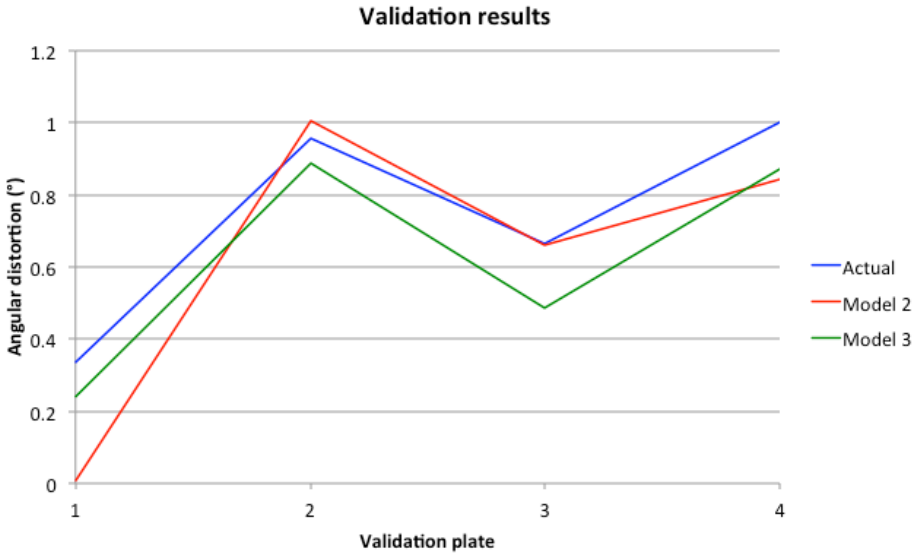

Figure 6.35: Comparison of measured and predicted distortion for validation plates

As with the models for weld geometry and quality, the accuracy of prediction is likely to be improved by a larger set of training data, with an increased resolution of induction coil travel speeds. Reducing the induction coil travel speed increments should allow the model to more accurately highlight the critical coil travel speed for each plate thickness.

The results indicate that the final distortion prediction accuracy is not detrimentally affected by discarding post-weld distortion as a model input. Similarly to the second model, the accuracy of this model is likely to be improved further with a larger set of training data with an increased resolution of induction coil travel speeds.

6.7 Conclusions

ANNs have been developed and applied to various weld aspects; due to their bi-directionality, they are able to calculate an output for a given set of input variables and vice versa. ANNs are a computational modelling technique that has the ability to develop patterns and detect subtle link/trends in data making them ideal for the implementation to a welding process, which exhibits extremely complex interactions between several nonlinear welding variables.

A comparison of experimental and predicted results show that ANN modelling can be successfully employed to predict weld geometries. The ANN model was able to accurately identify subtle trends in the input-output relationships, and has consequently highlighted the influence of the alternating frequency on the weld penetration. In doing so, this has shown that there is an inherent relationship between the frequency of alternation and the travel speed.

Training the ANN model in reverse, i.e. specifying the weld outputs as model inputs, and weld travel speed as the prediction output, determined that for an equivalent level of penetration, the travel speed for alternating shielding gases could be increased by, on average, 28% when compared to the argon / 20% carbon dioxide base case, producing a noticeable economic benefit.

The results of the sensitivity analysis, i.e. travel speed having the greatest influence on weld geometry, was in agreement with both the experimental investigation and findings in other literature.

The experimental study conducted found that the alternating shielding gas process does not provide the same level of resistance to the adverse effects of cross drafts when compared to a conventional argon / 20% carbon dioxide mixture. This is primarily due to the density of the helium being considerably lighter that air; thus, the gas is far more susceptible to drifting from the weld pool.

This study has highlighted the potential of ANN software to improve the efficiency of the GMAW process, through its ability to predict the quality of a weld using a specified set of inputs, thus enabling the operator to predict the weld quality prior to performing the weld itself. For example, should a higher cross draft be detected, the software can predict the weld inputs (nozzle diameter, shielding gas flow rate, etc.) required to produce a high quality weld.

The ability to predict the weld quality for lower shielding gas flow rates leads to obvious benefits on an industrial scale. Investment in an ANN model, which has been thoroughly developed and validated for the specific process it is to predict, would lead not only to time and material saving, but also help reduce wastage of gas in the process itself.

It has been shown that a travelling induction coil can be used to rectify weld induced distortion. The results have shown that there is a critical coil travel speed at which maximum rectification bending occurs for a 6 mm thick plate, and that welding distortion can essentially be eliminated using this method.

The experimental setup used in this trial was able to rectify up to 0.95° of angular distortion for the 6 mm thick plate, signifying that this technique may be particularly useful when dealing with thin steel plate. This critical speed was not evident in the 8 and 10 mm thick plate, but it is believed that by optimising the induction coil length and power input, a similar pattern of results would be achieved.

ANNs have been used to predict both distortion due to welding and the final distortion of steel plate after both welding and induction heating. A practical model for determining the optimum induction heating parameters required to rectify welding distortion, using easily obtainable information, has been created. This model would have a genuine industrial application where distortion reduction and rectification is of interest. With increased training data, this model shows the potential of being a robust and useful tool to systematically correct angular distortion.

As a consequence of computational models becoming ever more advanced, their ability to accurately predict key weld aspects for a given set of parameters will help increase confidence that the resultant weld will be of this desired quality.

6.8 References

[6.1] Dornfeld, D. A., Tomizuka, M. and Langari, G., 'Modeling and adaptive control of arc welding processes', *ASME Special Publication: Measurement and Control for Batch Manufacturing*, 1982.

[6.2] McGlone, J. C., 'Weld bead geometry prediction – a review', *Metal Construction*, Vol. 14, No. 7, pp. 378-384, 1982.

[6.3] Sterjovski, Z., Nolan, D., Carpenter, K. R., Dunne, D. P. and Norrish, J., 'Artificial neural networks for modelling the mechanical properties of steels in

various applications', *Journal of Materials Processing Technology*, Vol. 170, No. 3, pp. 536-544, 2005.

[6.4] Pal, S., Pal, S. K. and Samantaray, A. K., 'Artificial neural network modeling of weld joint strength prediction of pulsed metal inert gas welding process using arc signals', *Journal of Materials Processing Technology*, Vol. 202, No. 1-3, pp. 464-474, 2008.

[6.5] Lakshminarayanan, A. K. and Balasubramanian, V., 'Comparison of RSM with ANN in predicting tensile strength of friction stir welded AA7039 aluminium alloy joints', *Transactions of Nonferrous Metals Society of China*, Vol. 19, No. 1, pp. 9-18, 2009.

[6.6] Reddya, N. S., Krishnaiahb, J., Hong, S. and Lee, J. S., 'Modeling medium carbon steels by using artificial neural networks', *Materials Science and Engineering A*, Vol. 508, No. 1-2, pp. 93-105, 2009.

[6.7] Ates, H., 'Prediction of gas metal arc welding parameters based on artificial neural networks', *Materials and Design*, Vol. 28, No. 7, pp. 2015-2023, 2007.

[6.8] Pal, S., Pal, S. K. and Samantaray, A. K., 'Prediction of the quality of pulsed metal inert gas welding using statistical parameters of arc signals in artificial neural network', *International Journal of Computer Integrated Manufacturing* Vol. 23, No. 5, pp. 453–465, 2010.

[6.9] Lightfoot, M. P., Bruce, G. J., McPherson, N. A. and Woods, K., 'The application of artificial neural networks to weld-induced deformation in ship plate', *Welding Journal*, Vol. 84, No. 2, pp. 23-26s, 2005.

[6.10] Lightfoot, M. P., McPherson, N. A., Woods, K., and Bruce, G. J., 'Artificial neural networks as an aid to steel plate distortion reduction', *Journal of Materials Processing Technology*, Vol. 172, No. 2, pp. 238–242, 2006.

[6.11] Nagesh, D. S. and Datta, G. L., 'Modeling of fillet welded joint of GMAW process: integrated approach using DOE, ANN, and GA', *International Journal on Interactive Design and Manufacturing*, Vol. 2, No. 3, pp. 127–136, 2008.

[6.12] Nagesh, D. S. and Datta, G. L., 'Genetic algorithm for optimization of welding variables for height to width ratio and application of ANN for prediction of

bead geometry for TIG welding process', *Applied Soft Computing*, Vol. 10, No. 3, pp. 897–907, 2010.

[6.13] Beckett, S., MacPherson, M. J. and McPherson, N. A., 'Improved welding control of automated fillet welding for ship structures using artificial neural networks (ANN)', Presented at 16th International Conference on the Joining of Materials Conference (JOM-16), May 2011, Tisvildeleje, Denmark.

[6.14] Svozil, D., Kvasnička, V. and Pospíchal, J., 'Introduction to multi-layer feed-forward neural networks', *Chemometrics and Intelligent Laboratory Systems*, Vol. 39, No. 1, pp. 43-62, 1997.

[6.15] Principe, J. C., Euliano, N. R. and Lefebvre, W.C., 'Neural and adaptive systems: fundamentals through simulations', New York: John Wiley & Sons, Inc., 2000.

[6.16] Lightfoot, M., 'Prediction of weld distortion using artificial neural networks', Ph.D. Thesis, Newcastle University, 2008.

[6.17] Jönsson, P. G., Eagar, T. W. and Szekely, J., 'Heat and metal transfer in gas metal arc welding using argon and helium', *Metallurgical and Materials Transactions B*, Vol. 26, No. 2, pp. 383-395, 1995.

[6.18] Kang, B. Y., Prasad, Y. K. D. V., Kang, M. J., Kim, K. J. and Kim, I.S., 'Characteristics of alternate supply of shielding gases in aluminium GMA welding', *Journal of Materials Processing Technology*, Vol. 209, No. 10, pp. 4716-4721, 2009.

7 Magnetohydrodynamics modelling of shielding gas effects in GTAW

7.1 Nomenclature

A - Cross-sectional area of the arc plasma

B - Self-induced azimuthal magnetic field

$C_{\varepsilon 1}, C_{\varepsilon 2}$ - Constants

C_p - Specific heat capacity

ε - Turbulence dissipation rate

ε_a - Emissivity of the anode

$e.c.$ - Electrical conductivity

E - Electric field

φ_{wa} - Work function of the anode material

F_{emag} - Electromagnetic force

g - Gravity

h - Enthalpy

h_a - Average plasma enthalpy

h_{tot} - Total enthalpy

I - Current

J - Current density

j_e - Electron current density

k - Turbulent kinetic energy

KE_{ave} - Average kinetic energy

k_t - Thermal conductivity

μ - Dynamic viscosity

μ_t - Turbulent viscosity

m - Mass

P - Pressure

P_k - Turbulent kinetic energy due to viscous forces

$P_{\varepsilon b}$ - Buoyancy force contribution to the rate of dissipation

P_{kb} - Turbulent kinetic energy due to buoyancy forces

ρ - Density

ρ_a - Average plasma density

ρ_e - Electric charge density

σ - Stefan-Boltzmann constant

σ_ε - Turbulent Prandtl number for rate of dissipation

σ_k - Turbulent Prandtl number for turbulent kinetic energy

S_a - Heat flux to anode

S_E - Resistive heating

S_M - Momentum source

τ - Viscous stress

t - Time

T - Temperature

ΔT - Temperature differential

v - Bulk fluid velocity

v_a - Average plasma velocity

V - Voltage

7.2 Introduction

The electrical arc in any arc welding process is not only a heat source but also a force source [7.1], a combination of the heat transfer from the arc plasma to the workpiece, and the fluid flow forces that the arc imparts on the liquid weld metal, determine the solidified weld geometry.

During GTAW, an inert shielding gas is delivered through the nozzle to protect the weld region from contamination by atmospheric gases. The properties of a GTAW arc, and the corresponding weld, are strongly dependent upon the shielding gas used. Argon is the most widely used shielding gas for GTAW due to its relatively low cost and inert nature. However, when using argon, the heat flux to the anode is low, and in applications where the workpiece has a high thermal conductivity, such as aluminium, the shielding gas is replaced with helium, or mixtures of argon and helium, hydrogen or nitrogen [7.2].

In addition to preventing contamination, the shielding gas is a critical variable for GTAW as a result of the extreme temperatures of the electrical arc. Due to temperatures in excess of 12,000 K, the gas becomes (partially) ionised; the plasma flow facilitates the transfer of electric current towards the workpiece through the rapid change of its thermophysical properties.

Modelling of heat transfer in GTAW has been well documented, and simulations generally make the assumption that the arc plasma is 2D axisymmetric. GTAW is a highly complex process and involves a solid, liquid, gas and plasma in close proximity. Simulations are based on the governing equations of CFD, i.e. Navier-Stokes equations, with modifications to account for electromagnetism, i.e. Maxwell's equations, Figure 7.1.

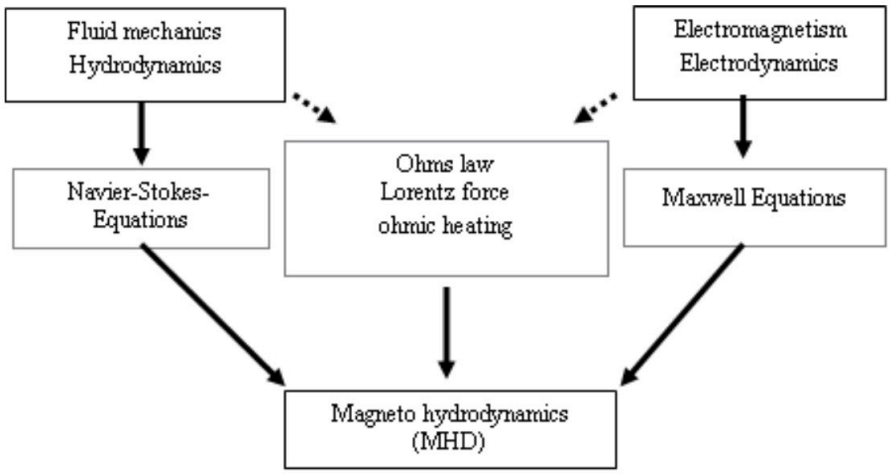

Figure 7.1: Magnetohydrodynamics model [7.3]

Simulations of different shielding gas compositions, and the knowledge of the effects of different themophysical properties, could lead to shielding gases being tailored for a specific requirement, i.e. penetration, based on the arc characteristics.

This chapter focuses on the development of a CFD model to simulate the effects of an argon and helium shielding environment, and examines the effects of individual thermophysical shielding gas properties. The model generated will form the initial development stage of a transient CFD model to simulate the effects of alternating between shielding gases.

7.3 Model generation

Two geometrically different, 3D models were developed to analyse the effect that the shielding gas composition has on various arc characteristics; a 6° axisymmetric model was implemented to be computationally efficient in the generation of boundary conditions, while a 180° symmetrical model was used for the final result comparison. Numerous studies [7.4-7.6] have previously implemented a 6° and 90° model simulation setup, stating that while the 6° model provided a computationally efficient simulation but was deficient in simulating the shielding gas flow in the welding nozzle.

Ansys CFX 14.0 CFD software was used to conduct the numerical simulations through the implementation of the magnetohydrodynamics (MHD) module, and several assumptions were made:

- The arc plasma is axisymmetric and its properties, i.e. density, viscosity, specific heat capacity, thermal conductivity and electrical conductivity, are a function of temperature alone.
- The arc plasma is in local thermodynamic equilibrium (LTE), i.e. collisions between the particles dominate over other physical processes such as applied forces [7.7].
- The arc plasma is defined as a fluid at atmospheric pressure, and the simulation is steady state, i.e. characteristic of a fully developed flow, independent of time.
- The effect of metal vapour has been neglected. Although metal vapour is known to influence the arc characteristics, the fraction of metal vapour in the arc plasma is unknown, and has a greater influence in GMAW due to emissions from the molten electrode.
- The effect of demixing has been neglected. Demixing is a phenomenon driven by diffusion, leading to the partial separation of different gases [7.8]. However, for argon-helium mixtures, there is no significant change in heat flux density [7.9].

- Plasma radiation is accounted for through a net emission coefficient, and does not account for self absorption effects in the outer regions of the arc due to radiation emitted from the arc centre.

MHD is the study of the interactions between magnetic fields and electrically conducting fluids. The MHD module solves the Navier-Stokes equations for fluid mechanics and Maxwell equations for electromagnetism simultaneously, thus there are four governing conservation equations for the model, which were solved using the finite volume method of Patankar [7.10].

- The conservation of mass:

$$\frac{\partial \rho}{\partial t} + \nabla \cdot (\rho \boldsymbol{v}) = 0 \tag{7.1}$$

- The conservation of momentum:

$$\frac{\partial (\rho \boldsymbol{v})}{\partial t} + \nabla \cdot (\rho \boldsymbol{v}\boldsymbol{v}) = -\nabla P - \nabla \cdot \tau + \boldsymbol{S_M} + \boldsymbol{F}_{emag} + \rho \boldsymbol{g} \tag{7.2}$$

The terms of the right hand side represent the forces due to pressure gradients, viscous stress, momentum source, electromagnetic force, and gravity. $\boldsymbol{F}_{emag}$ denotes the source of momentum arising from the electromagnetic forces and, for a continuous fluid, is given by:

$$\boldsymbol{F}_{emag} = \boldsymbol{J} \cdot \boldsymbol{B} \tag{7.3}$$

- The conservation of energy:

$$\frac{\partial (\rho h_{tot})}{\partial t} - \frac{\partial P}{\partial t} + \nabla \cdot (\rho \boldsymbol{v} h_{tot}) = \nabla \cdot (k_t \nabla T) + \nabla \cdot (\boldsymbol{v} \cdot \tau) + \boldsymbol{v} \cdot \boldsymbol{S_M} + \boldsymbol{S_E} \tag{7.4}$$

The terms on the right hand side represent the forces due to thermal conduction, viscous stress, external momentum sources, and resistive heating. Where h_{tot} is the total enthalpy, and is given by:

$$h_{tot} = h + \frac{1}{2}\boldsymbol{v}^2$$

(7.5)

The resistive heating source term, S_E, is given by:

$$\boldsymbol{S_E} = \boldsymbol{J} \cdot \boldsymbol{E}$$

(7.6)

- The conservation of electric charge (continuity equation):

$$\nabla \cdot \boldsymbol{J} = \frac{\partial \rho_e}{\partial t}$$

(7.7)

A two-equation, k-epsilon turbulence model was used to simulate the flow regimes present. Two-equation models offer a good compromise between computational effort and numerical accuracy, and solve both the velocity and length scale using separate transport equations. CFX determines the value of k and ε directly from the transport equations for the turbulence kinetic energy and turbulence dissipation rate:

$$\frac{\partial(\rho k)}{\partial t} + \frac{\partial(\rho v_j k)}{\partial x_j} = \frac{\partial}{\partial x_j}\left[\left(\mu + \frac{\mu_t}{\sigma_k}\right)\frac{\partial k}{\partial x_j}\right] + P_k - \rho\varepsilon + P_{kb}$$

(7.8)

$$\frac{\partial(\rho \varepsilon)}{\partial t} + \frac{\partial(\rho v_j \varepsilon)}{\partial x_j} = \frac{\partial}{\partial x_j}\left[\left(\mu + \frac{\mu_t}{\sigma_\varepsilon}\right)\frac{\partial \varepsilon}{\partial x_j}\right] + \frac{\varepsilon}{k}(C_{\varepsilon 1}P_k - C_{\varepsilon 2}\rho\varepsilon + C_{\varepsilon 1}P_{\varepsilon b})$$

(7.9)

The models generated consists of a 2.4 mm diameter tungsten electrode, with a 45° vertex angle and 2 mm arc length, 12.2 mm diameter alumina nozzle, and 6 mm thick DH36 steel plate. The geometry used for the 6° model is shown in Figure 7.2. The fluid region was simulated as the shielding gas, with the material properties detailed in Figures 1.1 and 7.3.

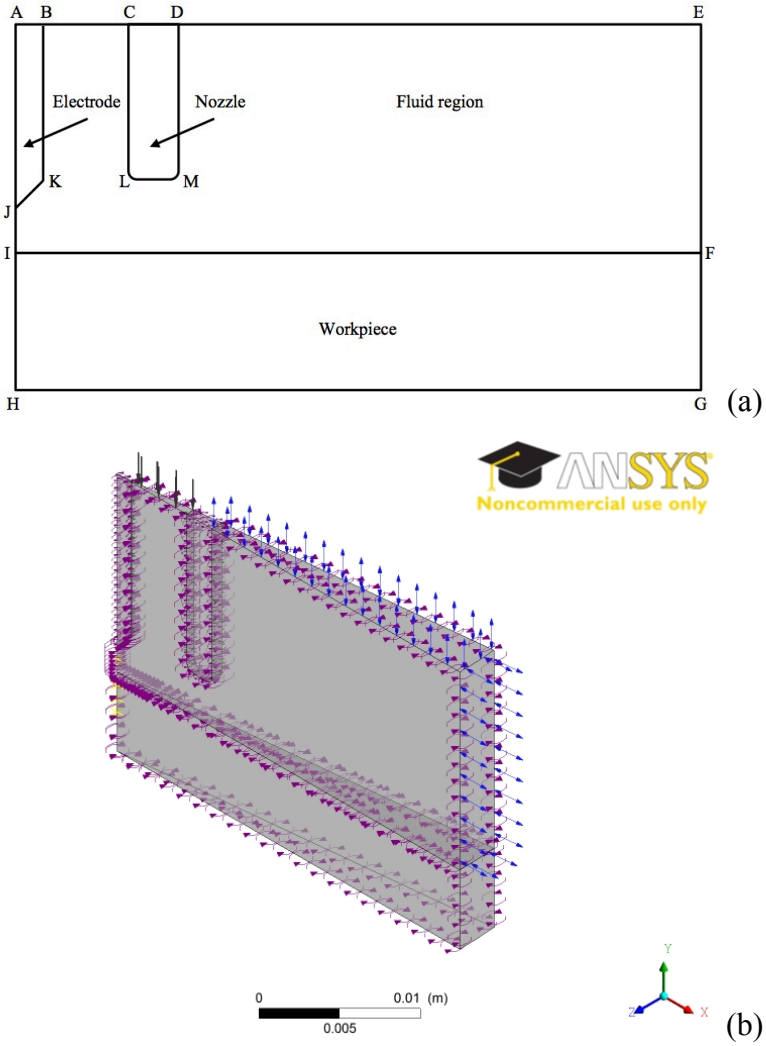

Figure 7.2: 6° model (a) schematic, and (b) 3D geometry with boundary conditions applied

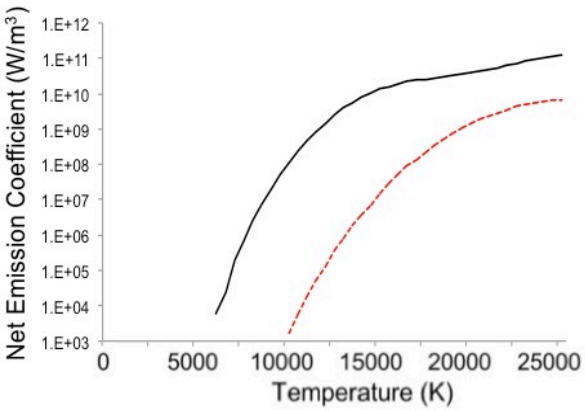

Figure 7.3: Net emission coefficient of argon and helium at 1 atm (adapted from [7.12] and [7.13])

In order to numerically solve the governing equations, realistic initial values and boundary conditions must be specified. A domain interface was generated where two domains share a common boundary, e.g. a general connection fluid-solid domain interface is defined between the shielding gas and electrode domains. The domain interfaces are defined as no slip walls with conservative interface flux boundary conditions; thus allowing for electric and magnetic fields, and heat transfer to be calculated. Similarly, a rotational periodicity domain interface was specified for each component in the model. The electrical current was applied through the application of a uniform current density to the upper surface of the electrode (cathode). The voltage is an output quantity, with the exception of the earth potential (0 V), which was applied to the lower surface of the plate (anode). The shielding gas inflow was specified as a volume flow rate at the fluid surface between the electrode and the nozzle, which could be changed to investigate the effect of shielding gas flow rate. The outer surfaces of the fluid, i.e. surfaces D-E and E-F, were specified as outlets with atmospheric pressure and temperature, in addition these regions were defined as electrical insulators, i.e. zero magnetic and electric potentials. A summary of the boundary conditions applied to the 6° model are shown in Table 7.1.

Table 7.1: 6° model boundary conditions

Region	Type	Temperature (K)	Magnetic potential	Electric potential	Flow rate / pressure	Slip
A-B	Wall	300	0	200 A	-	-
B-C	Inlet	300	0	0	10 l/min	-
C-D	Wall	300	0	0	-	-
D-E-F	Opening	300	0	0	0 Pa	-
F-G	Wall	300	0	0	-	-
G-H	Wall	300	0	0	-	-
H-I-J-A	Rotational axis	-	-	-	-	-
B-K-J	Interface	Flux	Flux	Flux	-	No slip
C-L-M	Interface	Flux	Flux	Flux	-	No slip
F-I	Interface	Flux	Flux	Flux	-	No slip

In reality, the arc ignition phase is far from the LTE simulation assumption, and was modelled through the application of a local heat source. This is because the electrical conductivity of each gas is essentially zero at atmospheric temperature, thus in order

to allow the electrical arc to initiate, the temperature of the arc region was artificially raised to 15,000 K. This artificial heat source was applied through a combination of user-defined expressions within CFX and switched off after 50 iterations so that it does not influence the converged solution.

Radiation emission was included within the model through the use of the net emission coefficient data for argon and helium, presented by Menart and Malik [7.12], and Moscicki et al. [7.13] respectively. The net emission coefficients used were those for a 1 mm absorption length, as previously used by Tanaka et al. [7.14], with no account for self absorption effects in the outer regions of the arc due to radiation emitted from the arc centre.

A variable mesh size was used, in which the density was greatly increased in the volume between the electrode and plate surface by applying an element size of 0.02 mm within a sphere of influence, due to the high gradients experienced in this location.

The model geometry constructed for the 180° mirror symmetric model followed that of the 6° model and consisted of the same geometric features. The 180° model had a simulation volume of 30 x 60 x 16 mm, to ensure that all arc properties of interest could be captured, as shown in Figure 7.4. The initial and boundary conditions developed for the 6° model were extended to the 180° model.

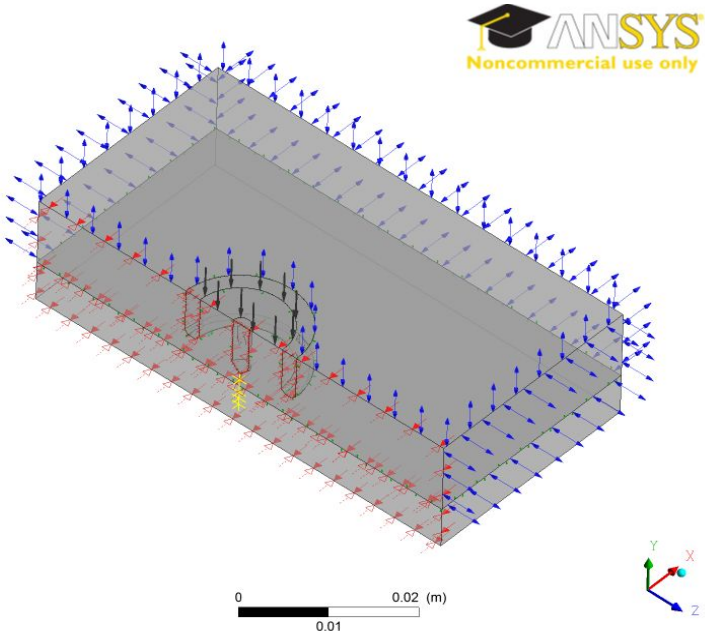

Figure 7.4: 180° model geometry

7.4 Results and discussion

7.4.1 Argon and helium arc plasmas

The shielding gas used in GTAW has a pronounced effect on the properties of the electrical arc; this is clearly apparent in Figure 7.5, which shows the effect that the shielding gas, i.e. argon or helium, has on the temperature distribution of the simulation. It can be seen that helium produces a considerably higher peak temperature (~19,800 K) than argon (~13,800 K). The profile of the arc plasma simulation is very similar to those generated by Tanaka et al. [7.14] and the experimental profiles shown in Figure 4.8, produced using the setup in Chapter 4. The fact that the experimental argon arc is considerably brighter than that of helium can be attributed to the higher net emissions of argon, indicating that the helium arc is more efficient at transmitting the electrical energy to heat (rather than light).

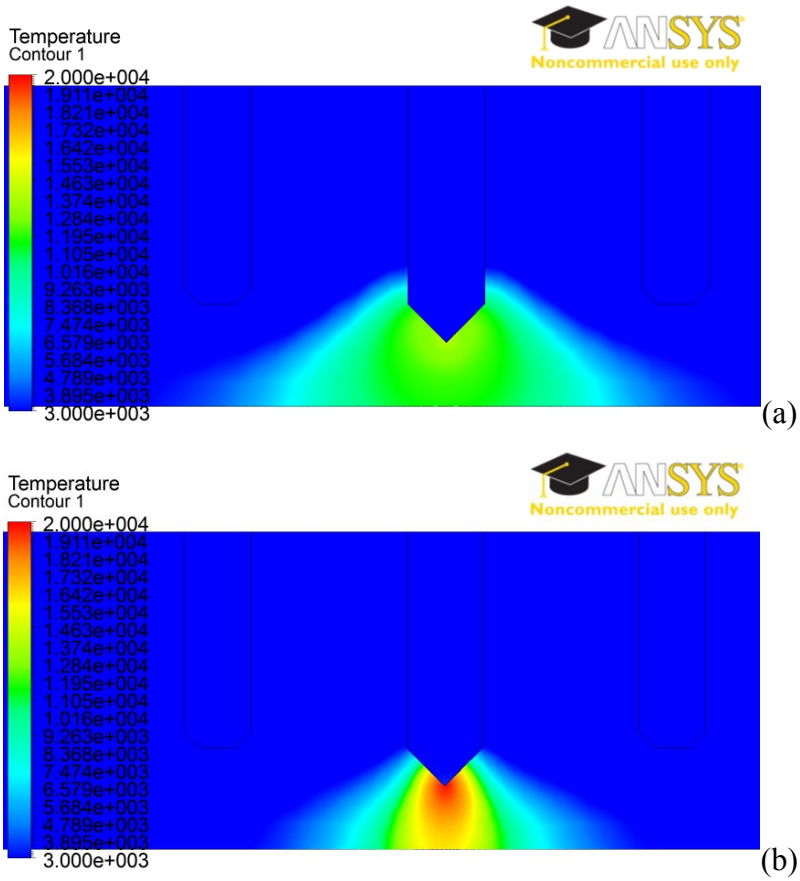

Figure 7.5: Comparison of temperature contours (K) for (a) argon and (b) helium, at an arc current of 200 A and arc length of 2 mm

The heat flux transferred by the arc plasma to the anode is given by equation (7.10), where the three terms describe the heating by electron capture, thermal conduction and blackbody radiation [7.8]. The results of the simulation are shown in Figure 7.6, and are in agreement with previous publications [7.7-7.8, 7.11, 7.15].

$$S_a = j_e \varphi_{wa} - k_t \frac{\partial T}{\partial z} - \varepsilon_a \sigma T^4 \tag{7.10}$$

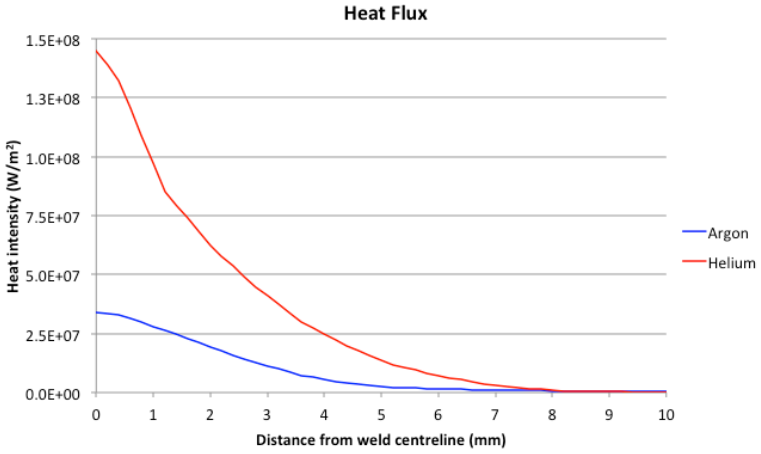

Figure 7.6: Radial distribution of heat flux at the workpiece surface

The total heat flux for the helium arc is larger than that for the argon arc by a factor of approximately 3.5, and is primarily a result of an increased arc voltage. The heat intensity at the axis of the arc plasma is approximately 4 times greater for helium than it is for argon, indicating that a higher proportion of the arc energy is concentrated at the core of the plasma. According to equation (7.10), this will occur either due to an increase in current density in the core region, or due to a decrease in thermal conductivity in the central region. As can be seen in Figure 7.7, the current density at the arc axis is approximately five times greater for helium than it is for argon at the mid-length of the arc. It can also be seen that the thermal conductivity of helium is approximately double that of argon at the arc axis at the anode surface for their respective temperatures shown in Figure 1.1.

The increased current density in the central portion of the arc plasma can be attributed to the electrical conductivity of the plasma medium. As can be seen in

Figure 1.1, the electrical conductivity of helium is almost zero for temperatures up to 10,000 K and a factor of approximately three lower at the arc plasma temperature of argon (~13,800 K). It is not until approximately 22,000 K that the electrical conductivity of helium is greater than that of argon. Therefore, current only flows in the high temperature core region of the plasma, consequently resulting in higher current densities in this region.

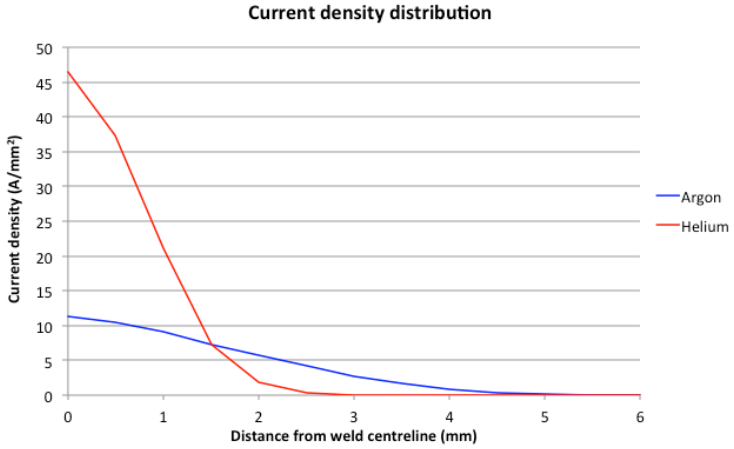

Figure 7.7: Radial distribution of current density 1 mm above the workpiece surface

The increased temperature in the arc is a result of the increased current density in the core region, which results in a greater resistive heating ($\boldsymbol{J} \cdot \boldsymbol{E}$) component in the conservation of energy (equation (7.4)).

The calculated velocity in the plasma region (Figure 7.8), was found to be a factor of approximately three greater for helium than argon, with a peak velocity of about 60 m/s and 175 m/s for argon and helium respectively. However, away from the core plasma region, there is not a considerable difference in velocity magnitude. The increase in the core plasma region can be attributed to a greater electromagnetic force ($\boldsymbol{J} \cdot \boldsymbol{B}$) component in the conservation of momentum (equation (7.2)).

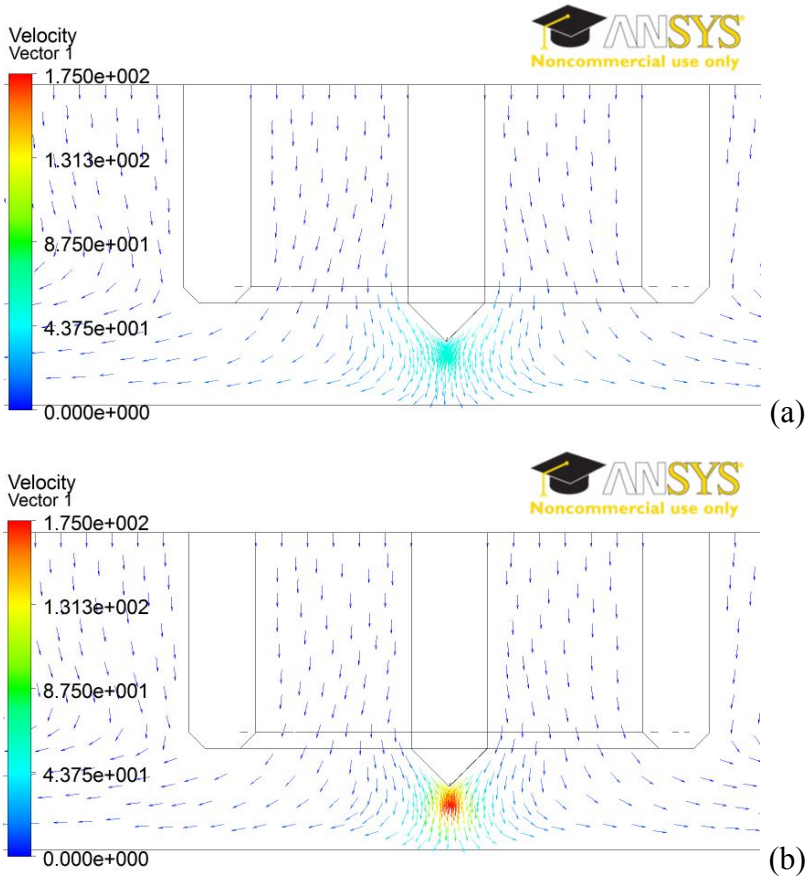

Figure 7.8: Comparison of velocity vectors (m/s) for (a) argon and (b) helium, at an arc current of 200 A and arc length of 2 mm

The pressure distribution within the arc plasma for argon and helium is shown in Figure 7.9. The peak pressure at the anode surface when using argon is approximately 1400 N/m^2, and occurs at the arc centreline. In line with the experimental measurements, this was considerably higher than the maximum pressure at the corresponding location for helium, which was approximately 600 N/m^2. As can be seen in Figure 7.9, the maximum arc pressure occurs adjacent to the electrode tip, and a minimum on the arc centreline, which occurs approximately 1/3 of the arc length above the anode surface, as previously found by Fan et al. [7.16].

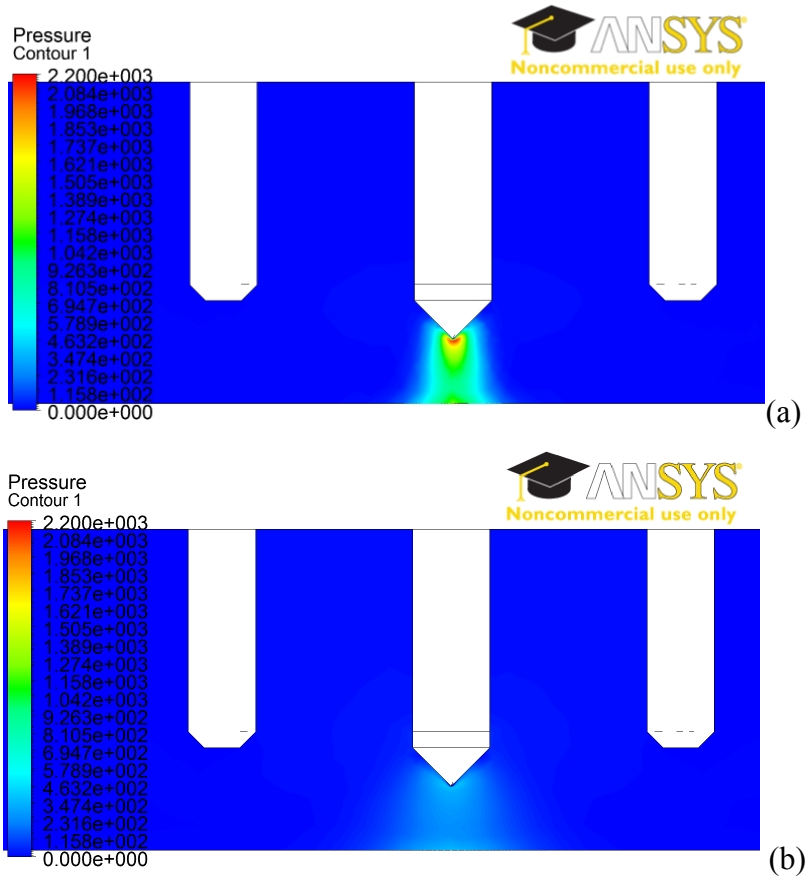

Figure 7.9: Comparison of pressure contours (N/m^2) for (a) argon and (b) helium, at an arc current of 200 A and arc length of 2 mm

7.4.2 Imaginary gas arc plasma

As has previously been shown, the results from the simulation are strongly dependent upon the properties of the shielding gas. However, due to the fact that the thermodynamic and transport properties vary depending on the shielding gas composition, it is unclear which properties are responsible for the effects observed.

In order to isolate the effect of the individual thermophysical properties, a process of 'imaginary gases' was implemented, as previously used by Murphy et al. [7.11]. This involves substituting one property of a gas into a model that contains all other properties of a second gas, e.g. substituting the specific heat capacity of helium into a model that contains all other properties belonging to argon. Thus ascertaining the influence of each property with respect to that property of the 'host' gas. In each

case, the temperature contours and velocity vectors are presented, as well as the current density at the mid-height of the arc, i.e. 1 mm above the anode surface.

Tanaka and Lowke [7.7] presented equation (7.11), which highlights the effect that various parameters and themophysical properties have on the arc plasma. This makes the assumption that the total electrical energy is transmitted to the workpiece and neglects radiation losses.

$$IV \sim \rho_A h_A v_A A \tag{7.11}$$

The simulations have shown that decreasing the shielding gas density to that of helium (Figure 7.10) leads to bulbous profile and an increase in cross-sectional area of the arc plasma. The peak temperature in the plasma was found to decrease to approximately 12,600 K adjacent to the electrode tip, and the low temperature (~3,000 - 5,000 K) isotherms are present at a greater radial distance from the arc centreline, as previously found by Murphy et al. [7.11] (Figure 1.2). As can be derived from equation (7.11), this effect was somewhat expected; in addition to the reduced fluid density, the voltage was also marginally reduced, culminating in an increase in area.

The velocity in the arc plasma was also found to decrease in the core region; a maximum flow velocity of approximately 37 m/s was calculated. This can be explained through the average kinetic energy, equation (7.12); as the temperature decreases, the velocity will also decrease. It can also be seen that the velocity increases in the outer arc areas, i.e. where there is a higher temperature than the argon base case.

$$KE_{ave} = \overline{\left(\frac{1}{2} m v^2\right)} = \frac{3}{2} \sigma T \tag{7.12}$$

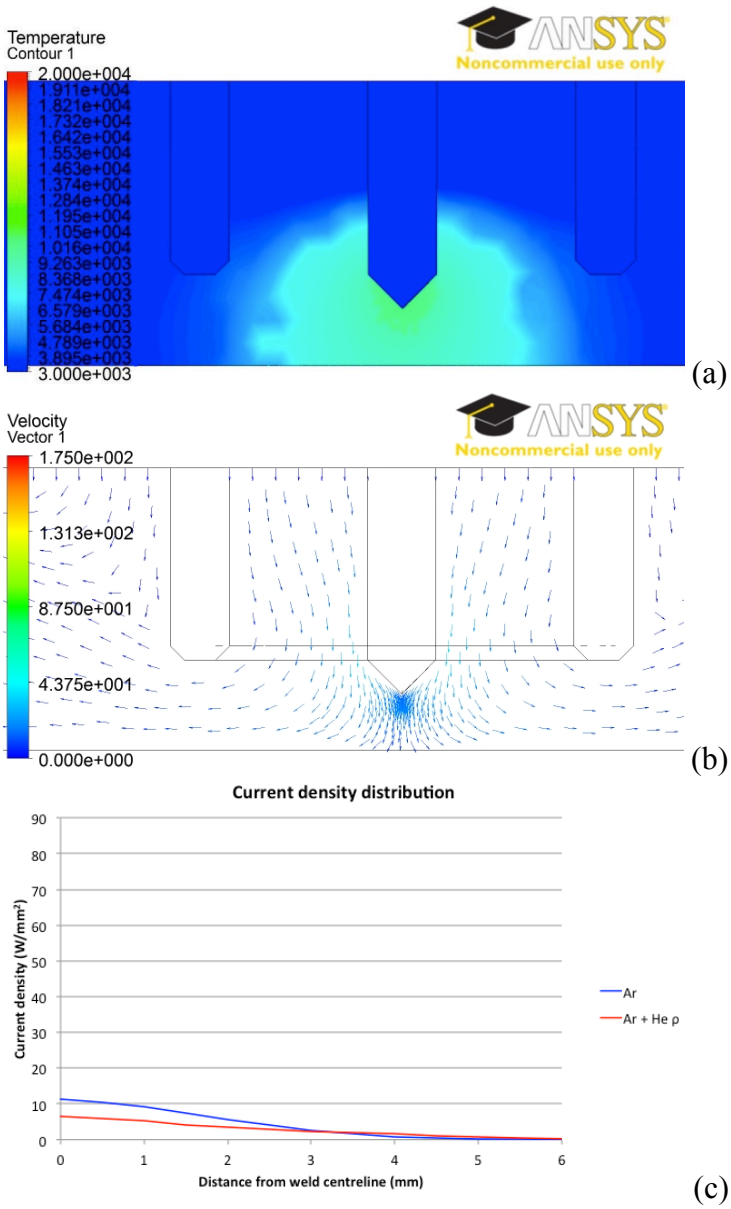

Figure 7.10: Imaginary gas of argon with helium density (a) temperature contours, (b) velocity vectors, and (c) current density distribution

In Figure 7.11, the effect of increasing the specific heat capacity to that of helium is depicted, which clearly shows a constriction of the arc plasma. Tanaka and Lowke [7.7] proposed that the arc constriction was due to a thermal pinch mechanism and is given through equation (7.11).

In addition, an increase in peak temperature (peak temperature of approximately 22,500 K) and axial velocity (maximum velocity of approximately 507 m/s) can be

observed. This is a result of the increased current density in the core region, leading to greater resistive heating and electromagnetic force in the core arc region.

Although the increased peak temperature and maximum velocity are in agreement with the simulations of Tanaka et al. [7.11] (approximately 25,000 K and 721 m/s, respectively), the plasma profile differs. The simulation by Tanaka et al. [7.11] had a very wide 3,000 K isotherm adjacent to the workpiece, which was not observed in the current study. However, according to equation (7.11), increasing the specific heat capacity results in a constriction of the arc, as displayed in Figure 7.11 (a).

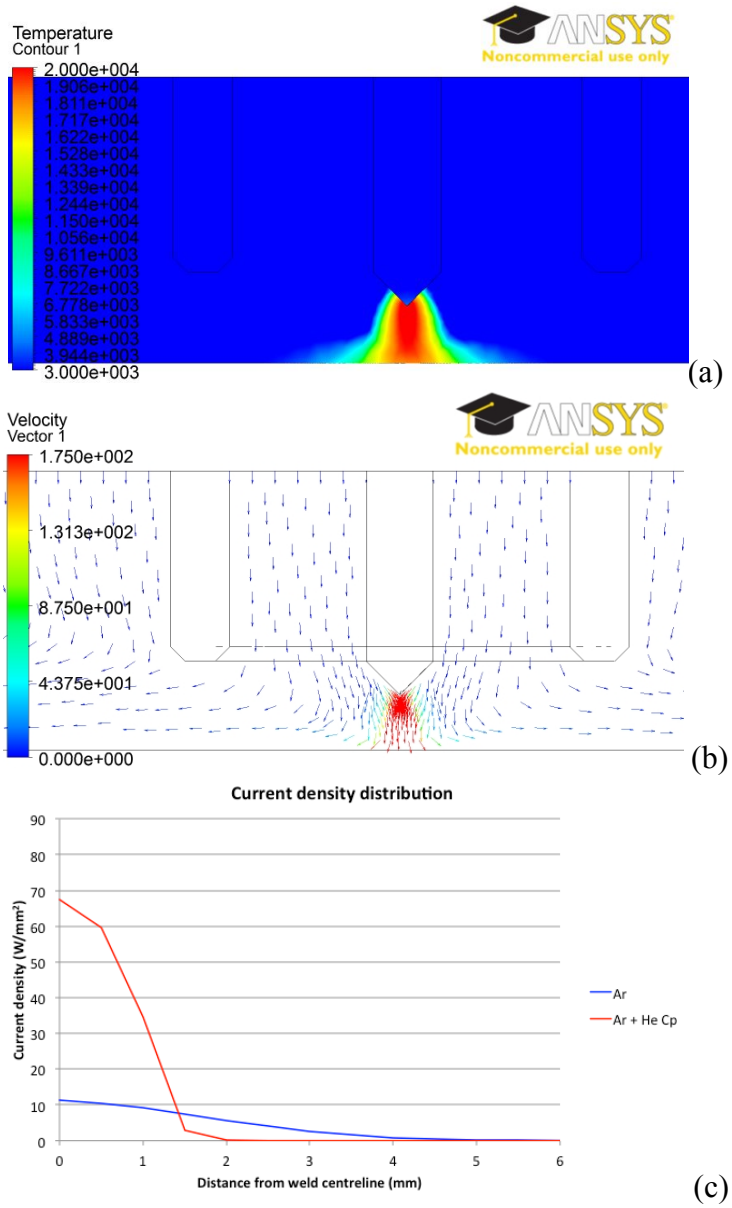

Figure 7.11: Imaginary gas of argon with helium specific heat capacity (a) temperature contours, (b) velocity vectors, and (c) current density distribution

The effect of increasing the viscosity to that of helium is shown in Figure 7.12. As can be seen, the arc profile and current density is similar to that of argon, with only a very small increase in arc width and decrease in peak temperature (~13,200 K). The main effect associated with the higher viscosity was on the axial flow velocity, which is reduced near the arc axis (~38 m/s), producing a flatter velocity profile, correlating with the findings of Tanaka et al. [7.11].

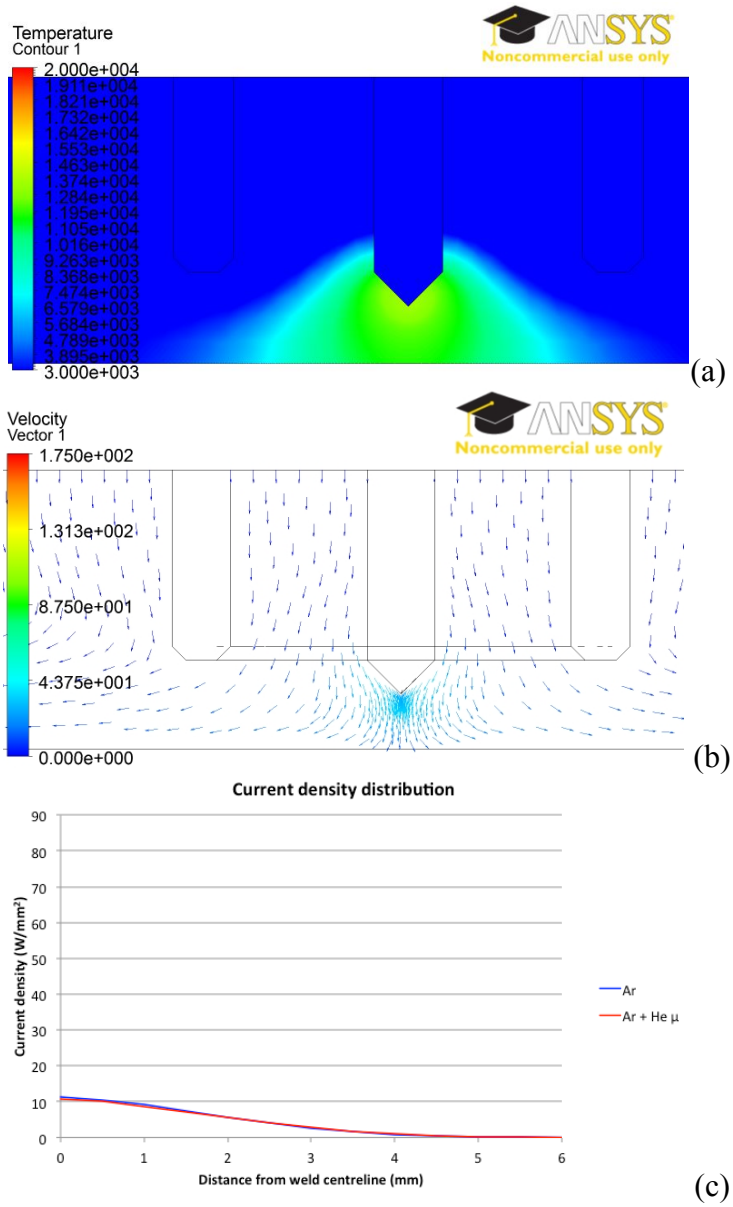

Figure 7.12: Imaginary gas of argon with helium viscosity (a) temperature contours, (b) velocity vectors, and (c) current density distribution

It has previously been suggested that a higher thermal conductivity would lead to a more constricted arc due to an increase in current density [7.9], and increased energy density [7.17], in the core arc region. Conversely, Murphy et al. [7.11] stated that a higher thermal conductivity leads to a less constricted arc, with a lower temperature on the arc axis than argon.

The effect of substituting the higher thermal conductivity of helium into the imaginary gas is shown in Figure 7.13. The profile of the arc core has again taken on a bulbous form, with a high temperature gradient occurring around 8,000 K. It can be noted that both previous claims relating to the effect of thermal conductivity are correct in certain aspects; the higher temperature (>8,000 K) isotherms are more constricted at the anode surface, whereas lower temperature (<8,000 K) isotherms in the upper region of the arc are less constricted.

The peak temperature was found to be approximately 14,000 K, marginally higher than that of pure argon. The axial flow velocity was also marginally higher in the arc region for the imaginary gas, with a maximum velocity of 62 m/s.

As can be seen in Figure 7.13 (c), the current density at the mid-height of the arc is higher for the imaginary gas than argon until 2.5 mm in the radial direction, thus confirming the previous assumptions of higher current density in the core region. The greater temperature and velocity experienced in the arc plasma can therefore be attributed to a higher degree of resistive heating and electromagnetic force, respectively.

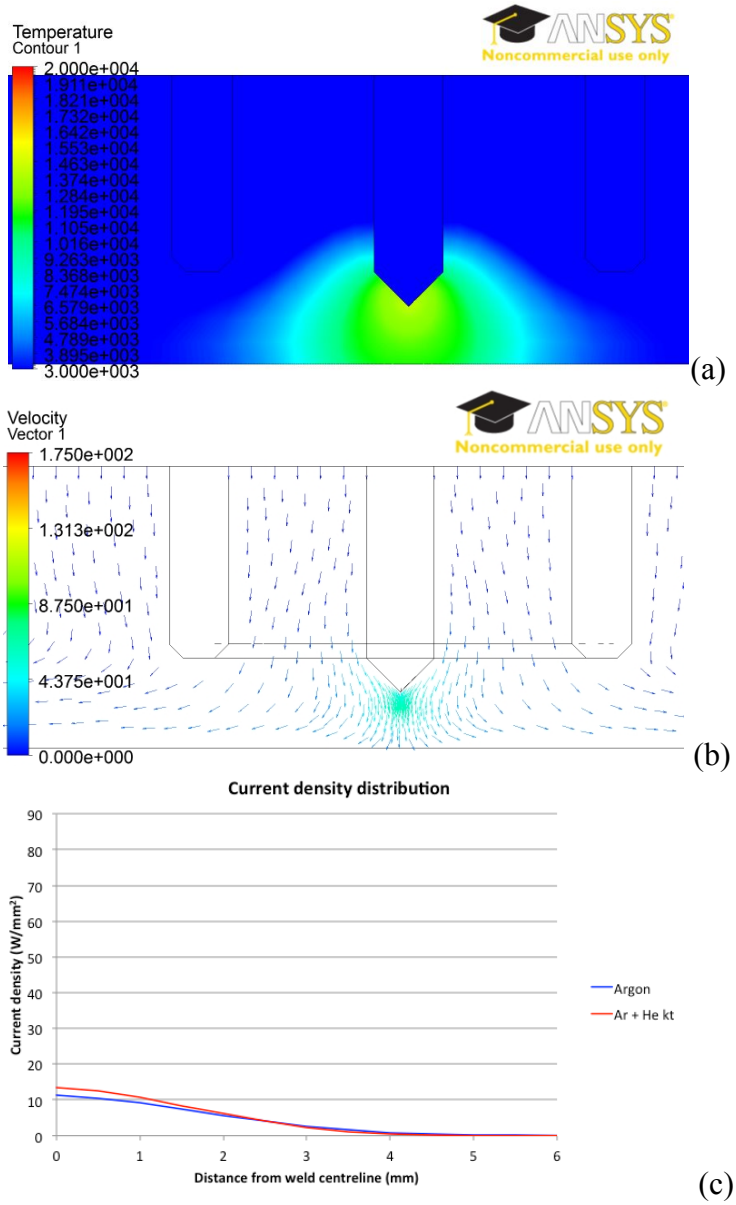

Figure 7.13: Imaginary gas of argon with helium thermal conductivity (a) temperature contours, (b) velocity vectors, and (c) current density distribution

Finally, the effect of substituting helium's electrical conductivity was investigated, Figure 7.14. From the earlier discussion, the electrical conductivity of helium is almost zero for temperatures up to 10,000 K, and lower than argon up to approximately 22,000 K. Therefore, current only flows in the high temperature core region of the plasma, consequently resulting in higher current densities in this region.

The peak temperature and velocity in the arc plasma is considerably higher in the arc plasma, with values of approximately 28,900 K and 665 m/s calculated, respectively.

This is similar to the results generated by Tanaka et al. [7.11] who found a peak temperature of approximately 27,000 K and maximum velocity of 1219 m/s; the reduced velocity can be attributed to the longer arc length in the current simulation, reducing the momentum transfer. As with the specific heat capacity, this is a result of the increased current density in the core region, leading to greater resistive heating and electromagnetic forces.

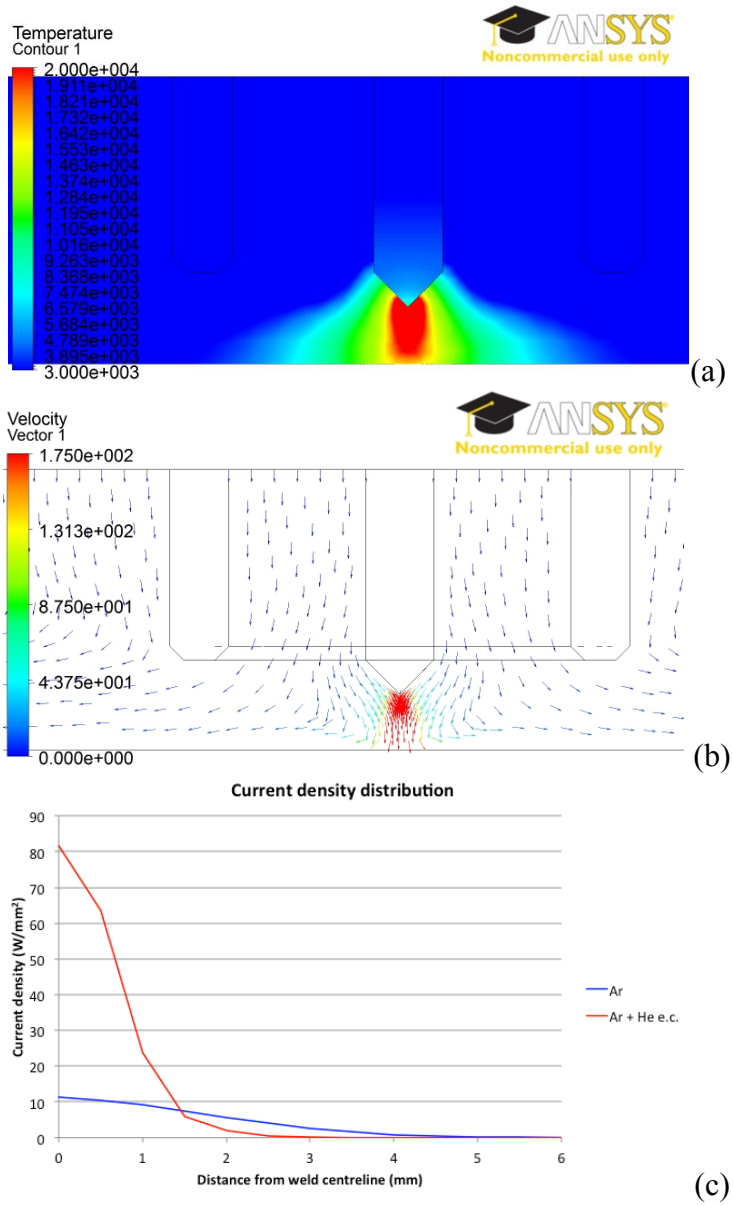

Figure 7.14: Imaginary gas of argon with helium electrical conductivity (a) temperature contours, (b) velocity vectors, and (c) current density distribution

The electrical conductivity is the primary reason for helium arc plasma constriction and, consequently, concentrated heat flux. Although the arc diameter is greater for the imaginary gas with electrical conductivity than that produced for specific heat capacity substituted, the fact that the specific heat capacity is approximately ten times greater for helium than argon and the density being approximately ten times greater for argon than helium, the product of these two properties essentially cancel one another for much of the temperature range.

From the simulations, it can be inferred that the cross-sectional area of the arc plasma is proportional to the viscosity, and electrical conductivity, and inversely proportional to the density and specific heat capacity:

$$A \propto \frac{\mu \cdot ec}{\rho \cdot C_P} \tag{7.13}$$

It can also be observed that the peak arc temperature and velocity are a function of the thermophysical properties:

$$T, v \propto \frac{\rho \cdot C_P \cdot k_t}{\mu \cdot ec} \tag{7.14}$$

7.5 Conclusions

CFD models have been developed to simulate MHD effects, i.e. electromagnetism and fluid flow, in the electrical arc produced in GTAW for different shielding gas compositions.

The simulations have shown that helium produces a considerably higher peak temperature (~19,800 K) than argon (~13,800 K), with a velocity in the arc region approximately 3 times greater.

The total heat flux to the workpiece was approximately 3.5 times greater for the helium arc than the argon arc, primarily due to an increased arc voltage. The heat intensity at the axis of the arc plasma is approximately 4 times greater for helium than it is for argon, indicating that a higher proportion of the arc energy is

concentrated at the core of the plasma, and is in line with previous publications [7.7-7.8, 7.11, 7.15]. Hence, the helium arc plasma is more constricted than argon as a result of an increased current density in the central portion of the arc plasma due to the electrical conductivity of the plasma medium.

The application of imaginary gases has illustrated the contribution that the individual thermophysical properties have on the arc plasma, and the simulations are in agreement with the results presented by Tanaka et al. [7.11]. It has been shown that the density, specific heat capacity and electrical conductivity have the greatest influence on the plasma; however, the product of the specific heat capacity and density essentially cancel one another for much of the temperature range.

Hence, simulations of different shielding gas compositions could lead to shielding gases being tailored to produce a weld of a specific requirement, i.e. penetration, based on the arc characteristics. By examining the effect that each of the thermophysical properties has on the temperature contours and velocity vectors, as well as the current density, it can be concluded that a shielding gas with a high ionisation potential, i.e. high electrical conductivity at high temperatures (>20,000 K), and high specific heat capacity will result in an increased weld pool depth.

7.6 References

[7.1] Fan, H. G. and Shi, Y. W., 'Numerical simulation of the arc pressure in gas tungsten arc welding', *Journal of Materials Processing Technology*, Vol. 61, No. 3, pp. 302-308, 1996.

[7.2] Tanaka, M., Tashiro, S., Satoh, T., Murphy, A. B. and Lowke, J. J., 'Influence of shielding gas composition on arc properties in TIG welding', *Science and Technology of Welding and Joining*, Vol. 13, No. 3, pp. 225-231, 2008.

[7.3] Schnick, M., Füssel, U. and Zschetzsche, J., 'Simulation of plasma and shielding gas flows in welding and cutting arcs with Ansys CFX', Presented at the International Scientific Colloquium on Modelling of Material Processing, June 2006, Riga, Latvia.

[7.4] Dreher, M., Füssel, U. and Schnick, M., 'Numerical optimization of gas metal arc welding torches using ANSYS CFX', Presented at 63rd Annual Assembly & International Conference of the International Institute of Welding, July 2010, Istanbul, Turkey.

[7.5] Schnick, M., Dreher, M., Zschetzsche, J., Fuessel, U. and Spille-Kohoff, A., 'Visualization and optimization of shielding gas flows in arc welding', *Welding in the World,* Vol. 56, No. 1-2, pp. 54-61, 2012.

[7.6] Dreher, M., Füssel, U. and Schnick, M., 'Simulation of shielding gas flow inside the torch and in the process region of GMA welding', Presented at Mathematical Modelling of Weld Phenomena 9, September 2009, Graz, Austria.

[7.7] Tanaka, M. and Jowke, J. J., 'Predictions of weld pool profiles using plasma physics', *Journal of Physics D: Applied Physics*, Vol. 40, No. 1, R1-R23, 2007.

[7.8] Murphy, A. B., Tanaka, M., Tashiro, S., Sato, T. and Lowke, J. J., 'A computational investigation of the effectiveness of different shielding gas mixtures for arc welding', *Journal of Applied Physics D: Applied Physics*, Vol. 42, No. 11, Article No. 115205 (14pp), 2009.

[7.9] Murphy, A. B., 'Demixing in free-burning arcs' *Physical Review E*, Vol. 55, No. 6, pp. 7473-7494, 1997.

[7.10] Patanker, S. V., 'Numerical heat transfer and fluid flow', New York: McGraw-Hill, 1980.

[7.11] Murphy, A. B., Tanaka, M., Yamamoto, K., Tashiro, S., Sato, T. and Lowke, J. J., 'Modelling of thermal plasmas for arc welding: the role of the shielding gas properties and of metal vapour', *Journal of Physics D: Applied Physics*, Vol. 42, No. 19, Article No. 194006 (20pp), 2009.

[7.12] Menart, J. and Malik, S., 'Net emission coefficients for argon-iron thermal plasmas', *Journal of Physics D: Applied Physics*, Vol. 35, No. 9, pp. 867-874, 2002.

[7.13] Moscicki, T., Hoffman, J. and Szymanski, Z., 'Net emission coefficients of low temperature thermal iron-helium plasma ', *Optica Applicata*, Vol. 38, No. 2, pp. 365-373, 2008.

[7.14] Tanaka, M., Tashiro, S., Satoh, T., Murphy, A. B. and Lowke, J. J., 'Influence of shielding gas composition on arc properties in TIG welding', *Science and Technology of Welding and Joining*, Vol. 13, No. 3, pp. 225-231, 2008.

[7.15] Gonzalez, J. J., Freton, P. and Masquère, M., 'Experimental quantification in thermal plasma medium of the heat flux transferred to an anode material', *Journal of Physics D: Applied Physics*, Vol. 40, No. 18, pp. 5602-5611, 2007.

[7.16] Fan, D., Ushio, M. and Matsuda, F., 'Numerical computation of arc pressure distribution', *Transactions of the Joining and Welding Research Institute*, Vol. 15, No. 1, pp. 1-5, 1986.

[7.17] Tušek, J., 'Experimental investigation of gas tungsten arc welding and comparison with theoretical predictions', *IEEE Transactions on Plasma Science*, Vol. 28, No. 5, pp. 1688-1693, 2000.

8 Schlieren optical visualisation of the shielding gas flow

8.1 Nomenclature

a - Unobstructed height of the source image

c - Gas concentration

C - Contrast (or sensitivity) of the schlieren system

D - Coefficient of diffusion

ε_x - Angle of the refracted light ray

erf - Error function

E - Coefficient of dispersion

f_2 - Focal length of mirror 2

L - Mixing length

t - Time

z - Distance in z direction

8.2 Introduction

Schlieren optical visualisation is a technique that allows variations in the refractive index gradient of a transparent fluid at a particular reference plane to be imaged.

During gas shielded arc welding process, a shielding gas is delivered through the nozzle to the welding region. The main functions of the shielding gas is to provide a medium for the electrical arc to flow, and to protect the metal transfer and the molten weld pool from contamination by atmospheric gases, which can cause defects in the solidified weld, for example porosity.

Due to their transparent nature, shielding gases are essentially invisible to the naked eye. During the MHD flow present in arc welding, large temperature and pressure gradients form. Additionally, density gradients arise where the shielding gas meets, and mixes with, the environment. All of these result in density gradients developing in the flow region. The local variations in density translate to refractive index gradients, making the shadowgraphy and schlieren methods useful for imaging the gas flow.

In Chapter 3, shadowgraphy was implemented to project the steady state shielding gas shadow onto a high speed camera to assess the effect that shielding gas flow rate, cross draft velocity and weld nozzle design have on the quality of the solidified weld for a conventional shielding gas supply.

The schlieren technique also operates on the principle that fluids of different densities possess different refractive indexes, and hence distort the path of a light source but differs from the shadowgraphy method in that the schlieren technique projects the image at a specific plane, rather than a shadow, onto a high speed camera according to the 4-f Fourier correlator, Figure 8.1.

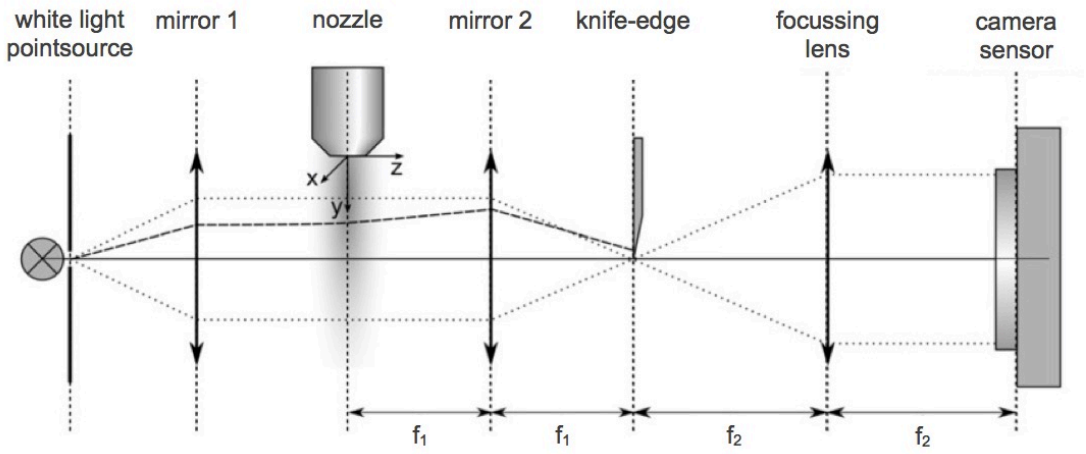

Figure 8.1: 4-f Fourier correlator in Schlieren system (adapted from [8.1])

The main advantages of the Z-type schlieren technique (Figure 8.2) are that both chromatic and spherical aberrations are eliminated, and Fourier filtering is accomplished through the geometric optics and knife-edge orientation, which allows either the vertical or horizontal component of the density gradient to be imaged. The knife-edge is used to improve the contrast of the schlieren image; a light ray refracted in one direction is blocked fully or partially by the knife-edge, while light rays refracted in the other direction increase the brightness of the spot it lands on. In addition, assuming the mirrors are the same angle, the Z-type geometric setup eliminates coma and spherical aberrations in the Fourier plane [8.2]. Although astigmatism is unavoidable without corrective optics, it can be minimised by

reducing the angle of the mirrors with respect to the parallel light beam, generally an angle of 3° is generally deemed acceptable [8.3].

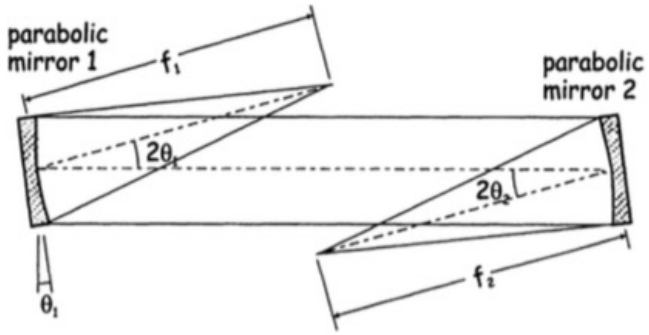

Figure 8.2: Diagram of Z-type schlieren setup [8.3]

The application of the schlieren technique to gas shielded arc welding processes is somewhat limited (especially so with the electrical arc present), with the technique primarily used in aeroplane aerodynamics, ballistics and ventilation technology [8.3]. Schnick et al. [8.4] and Dreher et al. [8.5] used the schlieren technique as a shielding gas flow validation tool for CFD models and assessed the effect of shielding gas flow rates. Siewert et al. [8.6] also investigated the effect of the shielding gas flow rate, however, their study focussed on the development of schlieren apparatus parameters (light source, and source aperture geometry and orientation) to enhance the schlieren image.

The shielding gas flow vectors present when implementing the alternating shielding gas process are transient in nature. This chapter therefore focuses on the application of the schlieren method to the GTAW process in order to visualise the flow regimes present when implementing this novel process, due to its ability to focus on a plane within the flow region.

8.3 Experimental setup

Experimental trials were conducted on an automated welding rig, Figure 2.2, in two phases; due to the setup and sensitivity of the schlieren system, stationary ‘cold’ flow measurements without the electrical arc and ‘hot’ spot welds were used to visualise

the shielding gas flow, whilst bead-on-plate welds using the same configurations were conducted to analyse the shielding gas effect on various weld aspects.

Two shielding gas supplies were used throughout the trials, argon and helium, controlled using a dedicated electronic control unit, Figure 2.7. Two shielding gas flow rates were investigated; 5 and 10 l/min, and were set when each gas was flowing continuously. This meant that when using alternating gases the flow rate would also be either 5 or 10 l/min.

8.3.1 Schlieren setup

The schlieren setup used the water-cooled copper plate, discussed in Chapter 4, to prevent melting of the anode surface. A 2.4 mm diameter, 2% thoriated tungsten electrode was used throughout, with a 45° vertex angle. A 12.2 mm internal diameter nozzle with a 5 mm stand-off distance was used to direct the shielding gas flow. All trials were performed using DC electrode negative with a welding current of 100 A.

The schlieren apparatus was set up using Toepler's double parabolic mirror system [8.7], in order to minimise optical aberrations in the Fourier plane [8.2], and followed the theory as detailed in Chapter 2.

In order to facilitate the accurate setup of the portable system, the components were mounted on parallel guide rails, shown in Figure 8.3.

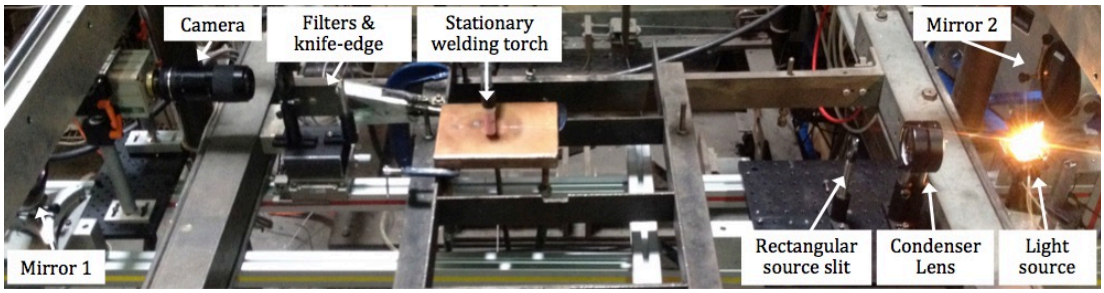

Figure 8.3: Portable schlieren setup

Two, 100 mm diameter, parabolic field mirrors, with a focal length of 1.27 m, were located approximately two focal lengths apart. Aligned in a Z-type arrangement, the first field element collimates the light while the second mirror focuses it to a small

spot. The stationary welding torch setup allowed for the shielding gas flow to be located between the collimating mirrors.

Due to the construction of the welding rig, compromises had to be made with the positioning of the system, this resulted in the 'Z' angles of the mirrors being approximately 8° (higher than the generally accepted 3° [8.3]), increasing the separation of the tangential and sagittal focus planes.

The light source was a 10,000 lm flux warm white Bridgelux® LED, with an intensity spectrum peaking around 630 nm, as shown Figure 8.4. The light was collected using a combination of two plano-convex lenses, placed together to form a condenser lens with an effective focal length of 60 mm.

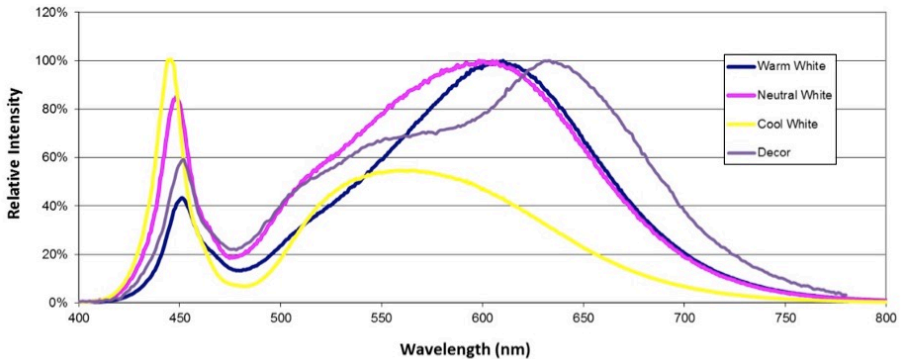

Figure 8.4: LED intensity spectrum

The correct geometry of the source slit was critical, since the sensitivity and measuring range of the schlieren system is dependent on its shape and dimensions [8.3]. As recommended by Siewert et al. [8.6], a vertical rectangular (2 x 6 mm) source aperture was positioned one focal length away from the condenser lens. The source slit was placed at the focus of the first mirror, allowing the source image to be analysed to its frequency components at the focus of the second mirror, where the Fourier plane lies.

In order to match the cutoff to the source slit, a vertical knife-edge was positioned at the Fourier plane, using a micrometer precision XY stage. The vertical knife-edge allowed filtering of the refracted light so that that the formed image represented the change in intensity proportional to the gradient of the refractive index $\partial n/\partial x$. Since density is proportional to the refractive index, this corresponds to the density

gradient $\partial\rho/\partial x$. In order to achieve an even measuring range, the knife-edge was positioned so that 50% of the light was blocked.

The contrast of the system is:

$$C = \frac{f_2 \varepsilon_x}{a} \tag{8.1}$$

The greatest challenge presented when imaging arc welding processes is the bright light emitted from the electric arc. Spectroscopic analyses of the GTAW arc revealed that at a wavelength of 633 nm, as there are no spikes in emissions at this wavelength [8.8]. Thus, a combination of a ±10 nm full width at half maximum (FWHM) band pass filter centred on a wavelength of 633 nm, and a neutral density filter were used to eliminate as much arc light as possible. As a result, maximising the ratio of source light to arc light. A polariser was also used to remove glare from the workpiece. As the arc's self-luminance was brighter than the source, the features of the flow near the argon arc could not be imaged due to excess light. For the case of helium, the net emission coefficient is 1-2 orders of magnitude smaller (Figure 7.3); therefore more features were visible using the same setup. The use of a narrower band pass filters (±1 nm and ±3nm) blocked the entirety of the source light, thus the ±10 nm FWHM filter was selected as the best compromise.

Camera images were recorded at a resolution of 256(H) × 256(V) pixels using a Kodak Ektapro high speed camera, with a variable focus and macro lens. Exposure times were varied based on the level of radiation from the object. Due to light spillage inherent to the Z-type imaging layout and heavy filtering, image formation was difficult at lower frame rates. However, removing the radiation from the welding arc meant that light filtering was not necessary, thus 'cold' nozzle flows were imaged at 4500 frames per second (FPS), while for GTAW welding 1125 FPS was found to be optimal. Reference images of the 'cold' flows were also taken at 1125 FPS and varying levels of schlieren sensitivity through adjustment of the source slit.

8.3.2 Bead-on-plate setup

Bead-on-plate trials were performed on a DH36 grade steel workpiece, of dimensions 250 x 100 x 6 mm, which moved under a stationary welding torch. This section of investigation was conducted using a welding speed of 3.2 mm/s, with a constant current power source of 100 A, and the voltage recorded using the P.A.M.S. unit (~13 V for argon, ~14.5 for alternating shielding gases and ~19 V for helium). A 2.4 mm diameter, 2% thoriated tungsten electrode was used throughout, with a 45° vertex angle. A 12.2 mm internal diameter nozzle with a 5 mm stand-off distance was used to direct the shielding gas flow.

8.4 Results and discussion

In order to analyse the motion, and identify the flow features of the gases used during the GTAW process, both 'cold' measurements (shielding gas but no welding arc) and 'hot' measurements (shielding gas and welding arc) were carried out. To provide a comprehensive reference, flow rates of 5 and 10 l/min for argon, helium, and alternating gases at frequencies of 2 and 8 Hz were imaged.

The difference in refractive index between the environmental medium and the gas to be visualised dictates the degree of refraction, and inevitably, the visibility of flow features [8.9]. By approximating the gas flow as a cylindrical column extruding from the nozzle, an analysis of the observable intensity changes due to the respective refraction angles of the source light may be made [8.9], as shown in Figure 8.5.

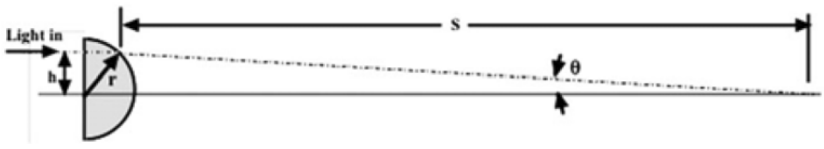

Figure 8.5: Refraction of light by a column of dense gas [8.9]

Using this analysis for argon and helium, and the dimensions of a typical nozzle, Figure 8.6 was generated. Hence, it is apparent that light passing through an idealised helium column refracts an order of magnitude more than that of argon, resulting in much weaker visualisations of the latter under ambient conditions. Despite the weak

observable gradients, fluid motion and mixing of argon with air was observable in the reconstructed high speed videos by using a 3.2 mm diameter iris slit.

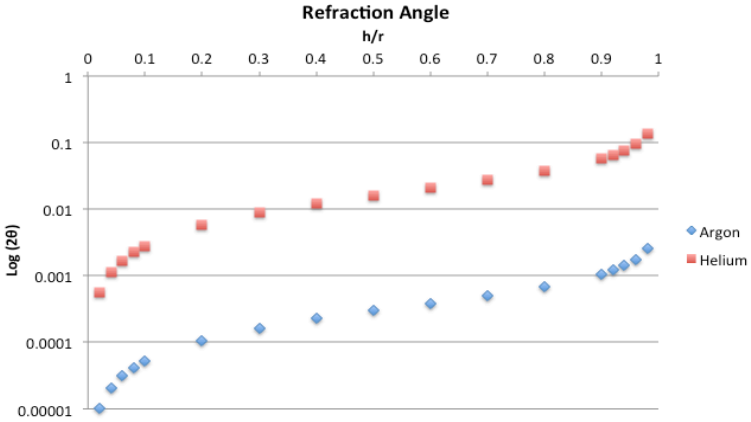

Figure 8.6: Total refraction angle for a gas column

Through comparison of the 'hot' and 'cold' flows, different flow features are observable, especially near the arc. Resistive, thermoelectric and thermionic heating effects create strong temperature gradients [8.10], which cause the dissociation of gas particles, thus dramatically changing their bulk thermophysical properties. The complex behaviour of the resulting thermal plasma is due to its interaction with the electromagnetic fields as well as the high pressure and temperature regimes within its flow.

In the electrical arc region, ionised particles are accelerated due to Lorentz forces, comprising the primary plasma jet [8.11]. The axial component of this 'pinched' flow generally results in fluid being accelerated towards the workpiece, one of the reasons for the observed primary density gradients. The horizontal component of the electromagnetic forces generates a localised inward flow, entraining gas from the secondary jet and atmosphere. The degree to which the secondary jet mixes with the surrounding air determines the extent of oxygen or nitrogen contamination in the weld.

In addition, the effect of these parameters has been investigated through a parallel study to analyse various weld aspects to ensure weld quality is maintained.

8.4.1 Initial flow

The shielding gas flow purging the welding region prior to arc initiation is shown in Figure 8.7. The 'cold' flow visualisation of argon is very weak and appears mildly turbulent with relatively large eddies, characteristic of gas expansion after nozzle exit. The outer extremity of the argon flow is difficult to visualise and is highlighted on the images using a dashed line. The helium visualisations show a smoother flow; as the gas leaves the nozzle, it impinges on the workpiece surface and slips to create large eddies while the gas initially mixes with air.

It has been shown from gas chromatography that the regions that appear brighter or darker correspond principally to concentration gradients [8.12]. Comparing the steady state flows between 5 and 10 l/min showed that the coverage diameter is increased when using the higher flow rate. However, in either case, the diameter of the weld was not exposed to contaminants.

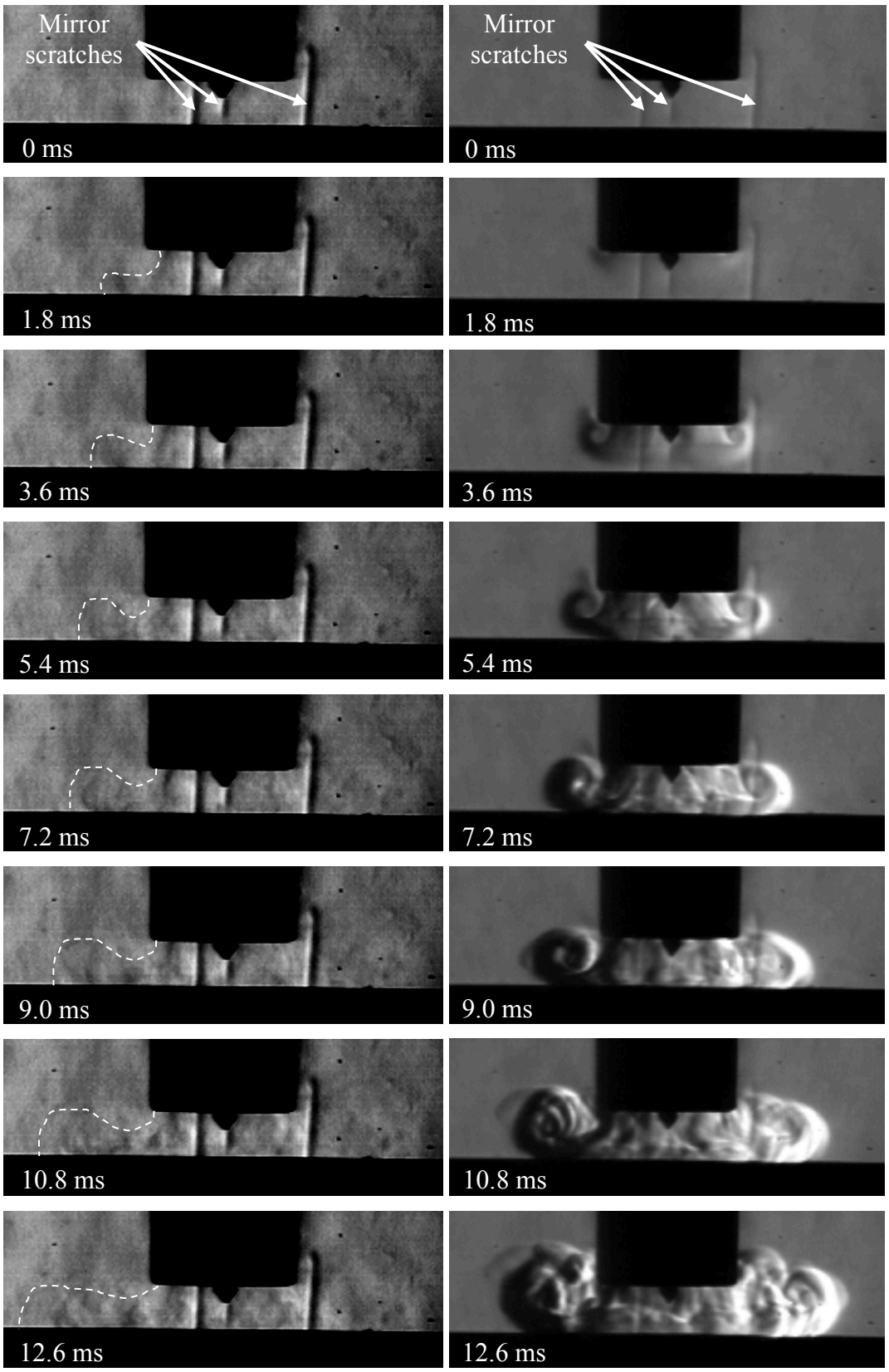

Figure 8.7: 'Cold' flow schlieren images for argon (left) and helium (right) with a 10 l/min shielding gas supply showing the purging of the weld region

8.4.1 Steady state argon flow

The flow visualisations of argon are shown in Figure 8.8. The 'cold' flow of Argon appeared mildly turbulent with relatively large eddies, characteristic of gas expansion after nozzle exit. Due to its relative density in comparison to air, a horizontal flow develops after the fluid stagnates at the workpiece surface, creating a blanket effect. At higher flow rates, convection increased proportionally.

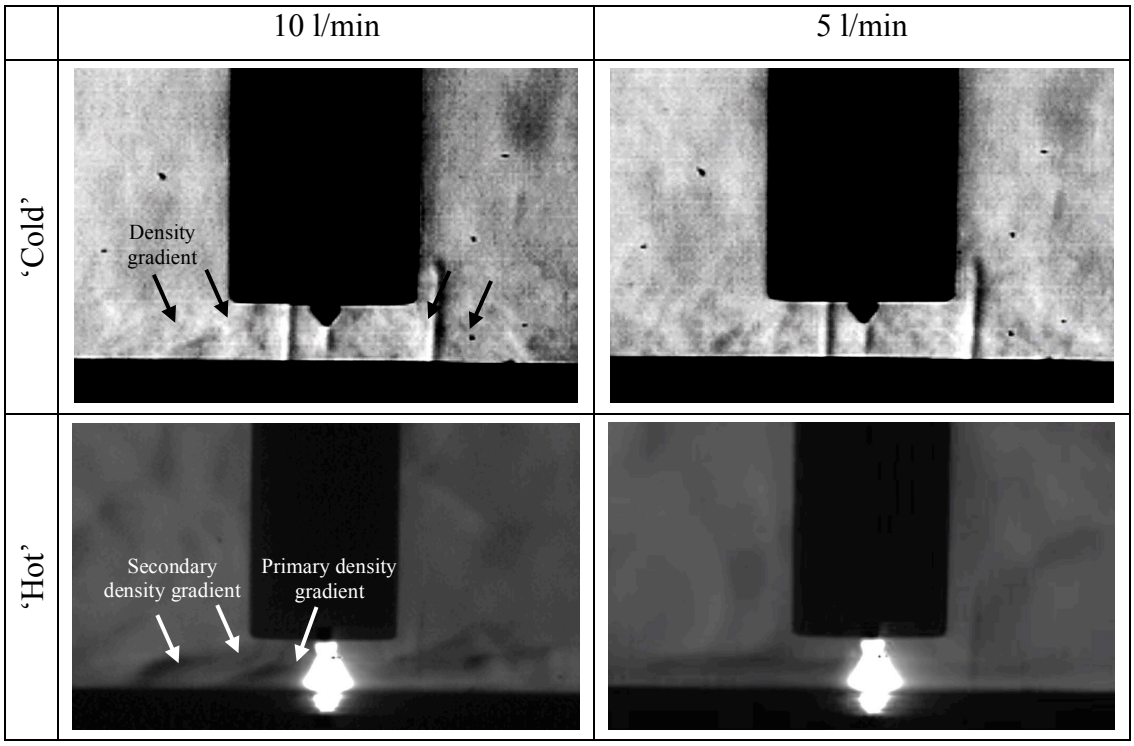

Figure 8.8: Steady state schlieren images of argon gas flows showing density gradients observed during 'cold' and 'hot' flows

For the case of the 'hot' argon visualisations, a horizontal density gradient (stream of gas) is formed, originating from the arc and moving downwards. However, due to intense radiation, axial features generated as a consequence of this were not visible. Nevertheless, as the stream stagnates, the pressure on the weld pool surface increases, causing the flow to be directed outwards, parallel to the workpiece. It can be noted that, after exiting the nozzle area, heated argon rises up due to its reduced density and mixes with air. At 5 l/min there is a strong parallel density gradient, suggesting a local gradient in concentrations at the argon-air interphase. At 10 l/min,

the mixing becomes more turbulent and no steady state schliere were observed within the relative timescales.

Overall, a laminar stream exits the weld nozzle, preventing environmental contamination. Further in the radial direction, the flow is mildly turbulent for the 10 l/min case with eddies forming away from the weld region, where the gas mixes with the surrounding air.

It can be observed that not all of the gas is interacting heavily with the arc and closer to the nozzle edges a bulk flow is also present. This forms a secondary jet, with a mean velocity that is orders of magnitude lower than that of the 'pinched' flow, but still enough to be create subtle light refractions. Within the secondary jet, momentum and gravity are the main driving forces: the flow is similar to that of the respective gas under 'cold' flow conditions.

The observations are not as clear as those presented in Figure 1.11 and 1.12 due in part to the shielding gas visualised (argon / 50% helium), which has a higher refractive index (Figure 8.6) and lower arc plasma emissions (Figure 7.3) than argon. In addition, the camera also had a lower resolution (256 x 256 pixels) than used in the literature (1024 x 1024 pixels). However, the general features, i.e. the horizontal primary density gradient originating from the arc plasma and the secondary density gradient indicating the extent of the flow, are both visible.

8.4.2 Steady state helium flow

The 'cold' flow visualisations for helium show a smoother flow; as the gas impinges on the workpiece surface, large eddies are formed while the gas initially mixes with air. Buoyancy forces carry the gas upwards creating a 'bulb' shaped plume, as internal viscous forces eventually eliminate the vortices and a steady state flow is reached after 500 ms, Figure 8.9. Comparing the steady state flows of 5 and 10 l/min showed that coverage diameter is increased when using the higher flow rate. However, in either case, the diameter of the weld was not exposed to contaminants.

The thermal conductivity of helium is greater than that of argon across the temperature range encountered in the arc plasma, although the electrical conductivity

is lower. This implies than more heat is transmitted to the workpiece when using helium, although it is more difficult to reach the critical energy levels required to ionise the gas to the same extent. As a result, numerical models [8.13-8.15] predict an overall contraction of the arc, with higher temperatures and increased electrical potentials near the anode surface. The strong contraction of the arc causes the axial electromagnetic force to change magnitude and direction [8.13], thus decelerating the plasma jet.

This effect is illustrated through the lack of a long highlighted area underneath the tungsten electrode, but rather a short, cylindrical feature. No inter-electrode vortices were observed, however the visualisation of gradients in the y-direction may reveal more flow features. Furthermore, the reduction in stagnation pressure measured in Chapter 4 by helium may be validated by the lack of a strong horizontal jet parallel to the workpiece.

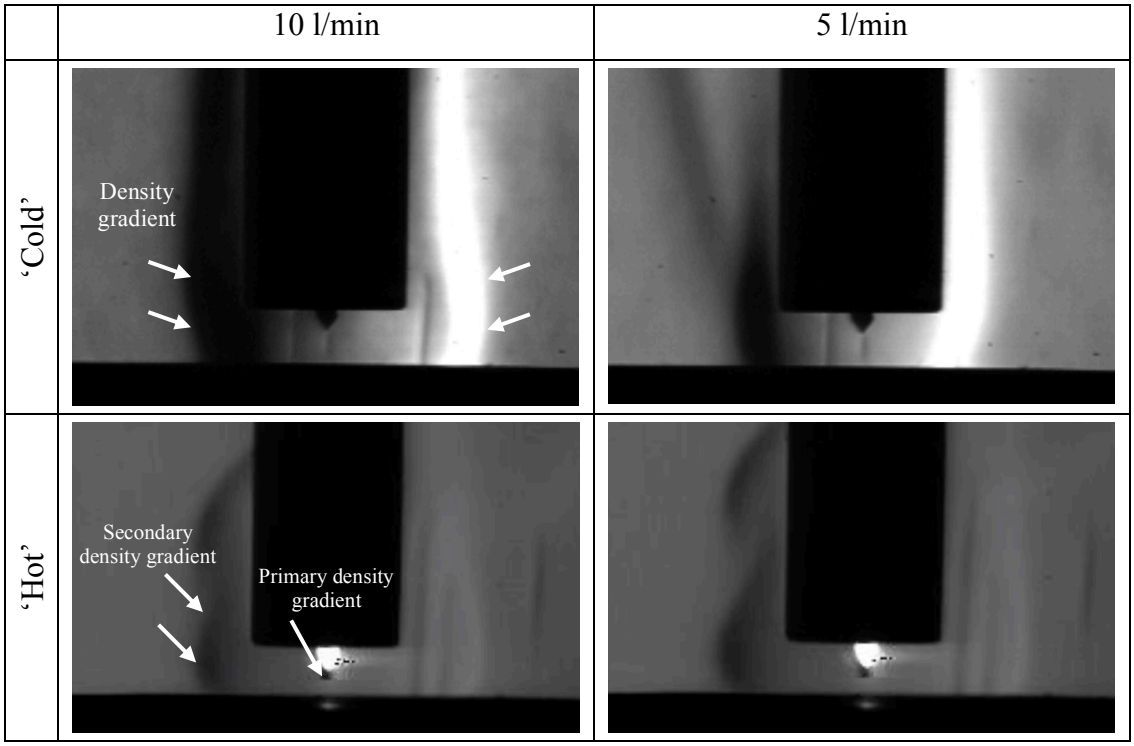

Figure 8.9: Steady state schlieren images of helium gas flows showing density gradients observed during 'cold' and 'hot' flows

8.4.3 Alternating shielding gases

When using the alternating shielding gas technique, the flow transitions from one with the characteristics of argon, to one with the characteristics of helium. A short transition period exists where a mixture of both gases are present, as shown in Figure 8.10. Although helium rising upwards is observed, no clear axial, steady state concentration gradients are visible. This is attributed to two factors: the degree of intermixing both within the delivery tube (premixing) and the weld region making the final product heavier, as well as the argon-air mixture restricting the helium buoyancy effects.

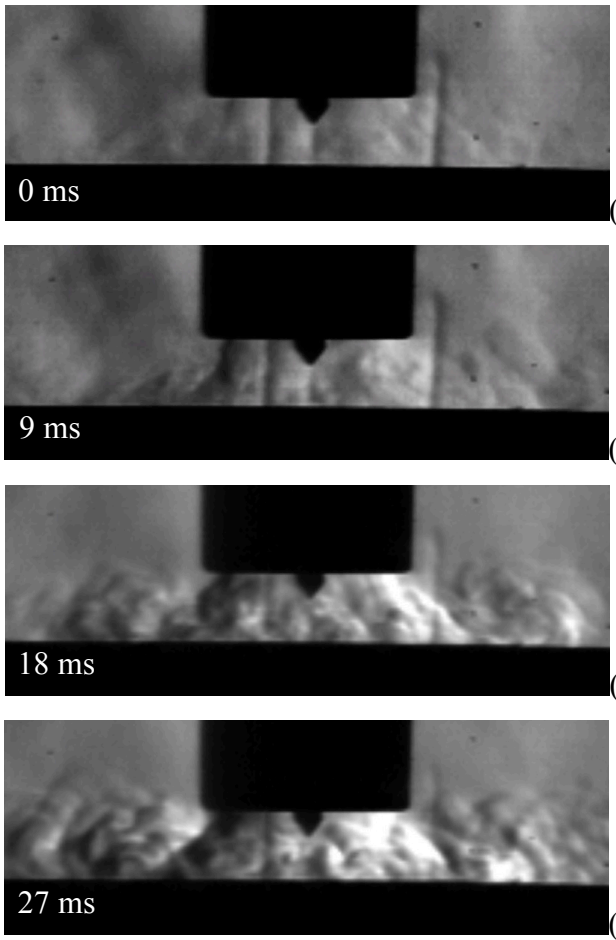

Figure 8.10: Schlieren images showing the different 'cold' flow regimes present during the transition gas period of alternating shielding gases; (a) argon, (b) predominantly argon, (c) predominantly helium, and (d) helium

The degree of premixing is important because the alternating gas technique is proposed instead of a premixed gas, and the effects of mixing at nozzle exit play an important role to the technique's effectiveness as will be discussed.

In order to quantify the degree of premixing, a theoretical analysis of axial dispersion in the gas line was carried out. It was assumed that one full pulse of argon was followed by a pulse of helium, with the degree of dispersion of helium being determined in terms of a distance from the moving interface between these pulses. Taking a control volume, and conserving mass at that initial reference, the diffusion equation may be derived:

$$\frac{\partial c}{\partial t} = D\frac{\partial^2 c}{\partial z^2} \tag{8.2}$$

A coefficient, E, characteristic of dispersion was used, which into account both convection and diffusion. Since the flow's Reynold's number within the gas line is estimated to be a maximum of 200. Boltzmann's analytic solution [8.16] yields the concentration of helium as a function of time and distance from the reference point.

$$c(z,t) = erf\frac{z}{\sqrt{4Et}} \tag{8.3}$$

Considering the error function plot, Figure 8.11, it can be seen that 99.5% concentration is achieved when the function equals 2. This implies that the mixing length after which this concentration is achieved is given by:

$$L = 4\sqrt{Et} \tag{8.4}$$

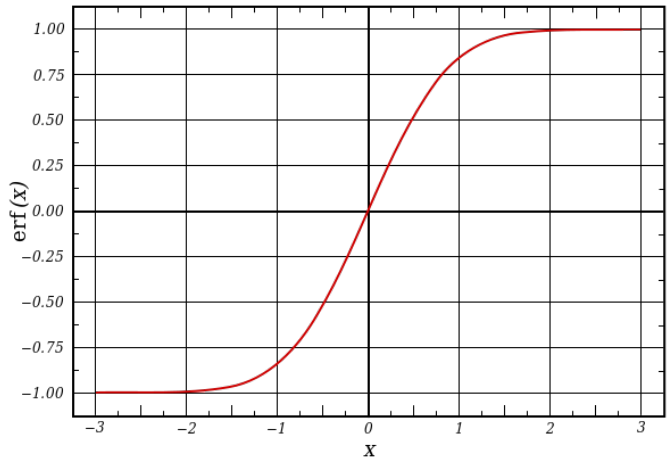

Figure 8.11: Error function plot

Considering the alternating at 2 Hz, 10 l/min case, a mixing length of 0.2 m was calculated, equating to 14.5% of the pulse length. As the alternating frequency increases to 8 Hz, the relative dispersion is increased to 57.9%, since the length of each gas pulse is four times smaller. For the 5 l/min shielding gas flow rate, the premixing is stronger and was estimated to be 28% and 110% for the 2 Hz and 8 Hz frequencies, respectively. The fact that dispersion was calculated to be greater than 100% of the pulse length indicates that the gas pulses will mix almost completely within the hose, but regions of higher concentrations are encountered when mixing occurs between two pulses of the same gas.

Analysis of the image sequence indicates that the transition period was approximately 27 ms. When considering an alternating frequency of 2 Hz, the transition period accounts for 10.8% of the total pulse time of the gas, which increases to 43% for alternating at 8 Hz. Consequently, the transition period accounts for a larger percentage of the total pulse time for higher alternating frequencies.

It would be expected that the ‘hot’ flow characteristics alternate between those described for argon to that of helium. However, subtle differences can be observed as the mass fraction of each constituent varied over time, with different features present at the transition from one gas to the other. In addition to the flow visualisations, the concentration of the shielding gas can be identified at any given time due to the relative brightness and size of the arc, as well the theoretical mixing calculation

presented above. The main features of the alternating cycle can be observed in Figure 8.12.

For the 2 Hz alternating frequency, assuming that the alternating cycle starts with a pulse of argon present in the weld region, and a concentration equal to 1, the flow is in steady state argon flow for approximately 220 ms. As helium enters to the weld region, less turbulence is observed and mixing starts to occur more uniformly, suggested by the formation of a large horizontal gradient. This horizontal feature persists throughout the helium pulse, replacing the 'bulb' shaped buoyant plume observe in the steady state images. This suggests that helium is restricted from flowing upwards, due to the heavier argon-air mixture, which acts to supress it. As the mass fraction of argon increases, so does the degree of mixing until the cycle restarts.

Considering the 8 Hz alternating frequency, the separation of gas pulses was less clear, since their length relative to the mixing time is much shorter, and premixing in the gas line has a greater effect. As such, a mixture of varying argon-helium concentration is always present with brief periods of argon and helium dominated flow, indicated by the fact that arc brightness did not reach the clear peaks observed in the lower alternating frequency. Overall more turbulence was present; the steady horizontal gradient during the helium pulse begins to establish but does not have sufficient time to form completely, and is disrupted by the argon flow.

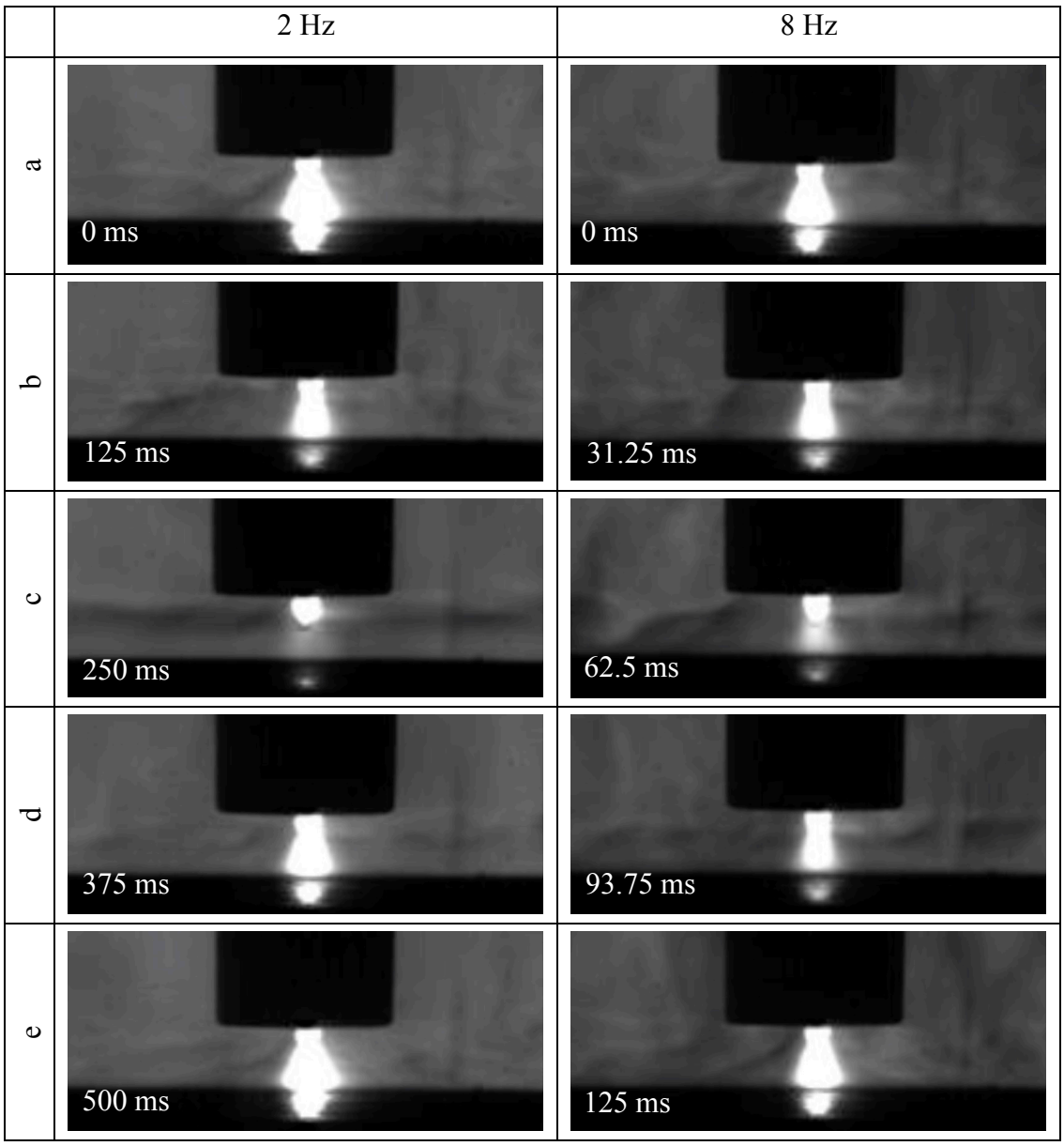

Figure 8.12: Schlieren images during alternating shielding gases at (a) argon dominated, (b) argon-helium transition, (c) helium dominated, (d) helium-argon transition, (e) argon dominated, showing the variation in arc geometry as a function of shielding gas

8.4.4 Bead-on-plate

The effect of the shielding gas parameters investigated using the schlieren technique were assessed through a parallel study; bead-on-plate welds were performed to ensure weld quality was maintained.

The 'cleanliness' of the weld was assessed through a combination of radiographic and metallographic examination.

Radiographic examination was performed on each experimental weld due to its' ability to detect discontinuities through the thickness of the weld. All shielding gas configurations produced clean welds, free from harmful imperfections, which would pass industrial testing.

A metallographic analysis was performed on transverse cross-sections from each set of weld parameters. The defect level was assessed through the analysis of numerous images from around the weld metal.

The defect level, i.e. the percentage of the image that exhibited a shade contrast to that of the bulk material, which is a combination of micro-porosity, metallic and non-metallic inclusions, and its distribution was consistent throughout the range of shielding gas parameters (composition and flow rate) investigated, and therefore all configurations produced 'clean' welds, in which the imperfection level present would not be detrimental to the overall weld integrity.

The macrographs of the weld geometry produced in the bead-on-plate investigation using the various shielding gas configurations are shown in Figure 8.13. As can be seen, the weld produced using helium resulted in a considerably larger weld bead compared to the other shielding gas configurations due to a considerably higher arc voltage (~19 V for helium and ~13 V for argon). This results in a greater heat flux at the anode surface for helium as was shown in Chapter 7.

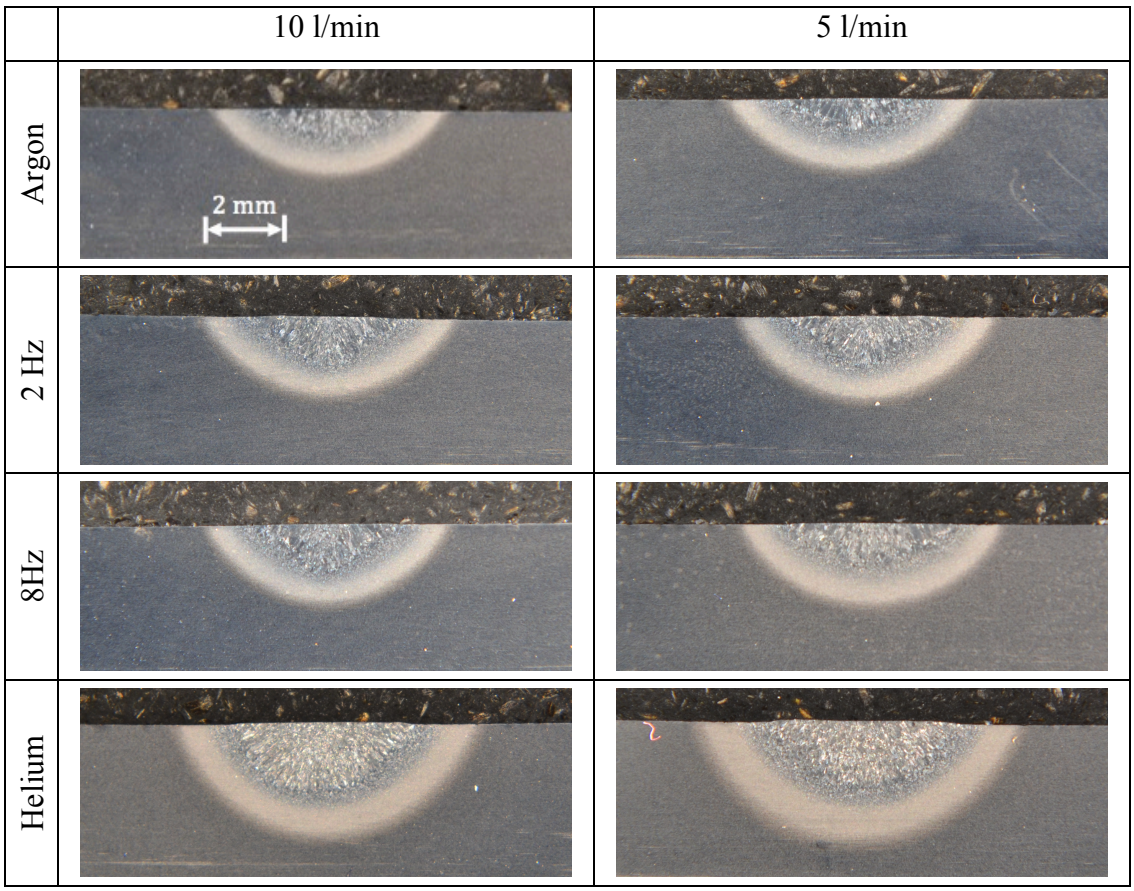

Figure 8.13: Weld macrographs showing effect of shielding gas configuration showing increased weld penetration through the addition of helium

When considering the alternating shielding gas configurations, the weld width was found to increase, on average, by 5% when compared to the argon base case. While, the depth of penetration was found to increase, on average, by 25%. This increase can be attributed to an increase in arc voltage (~14.5 V), but also due to the variation in arc forces established in Chapter 4. Within the alternating conditions, the 2 Hz frequency was found to increase the weld width by 4% and penetration by 8%.

The main aspect of the bead-on-plate investigation was to ensure that weld quality was not detrimentally affected by the shielding gas configuration or flow rates studied. The combination of radiographic and metallographic assessments therefore confirms the schlieren visualisations that that sufficient shielding is provided for all shielding gas configurations including 5 l/min cases.

8.5 Conclusions

When examining the steady state flow during spot GTAW, the argon flow was mildly turbulent with large eddies, whereas that of helium was smoother, with buoyancy forces carrying the gas upwards, creating a bulb shaped feature. The primary density gradients differed in shape and behaviour, as the differences in ionisation potentials and gas properties resulted in different arc characteristics.

Through comparison of the visualisations under 5 and 10 l/min flow rates, it was found that the former was sufficient for good quality welds, regardless of the shielding gas composition or supply method, provided no cross drafts were present in the welding region. Similar weld quality results were achieved for low shielding gas flow rates in a draft free environment in Chapter 3. These results are specific to the welding setup used, and the stand-off distance or indeed nozzle diameter would influence the degree of porosity in the weld. Despite this, a general trend in gas behaviour was observed, which can be expected of most GTAW setups, provided a reasonable combination of welding parameters are implemented.

The degree of turbulence for pure argon in the visualisations generally contradicts common treatments of the MHD flow as purely laminar, while the flow of helium showed no vortices, apart from the brief period where the flow develops. The vortices of the argon shield are highly transient and average to form a horizontal gradient when considering a steady state flow. The flow transient characteristics identified should be predicted through a time dependent model and using appropriate turbulence modelling, since they heavily influence the mixing process and consequently, the degree of air entrainment.

It has been shown throughout this thesis that the alternating gas technique generates technical and economic advantages to the GTAW process. The segment of investigation has shown that there is a greater degree of helium entrainment in the primary jet due to a constriction of its flow in the secondary jet. Through this mechanism, it would be expected that a greater proportion of helium is present in the arc plasma, influencing the arc's behaviour and inferring more of the associated benefits.

The theoretical analyses of the degree of premixing conducted, and experimental observations indicated that a lower degree of premixing was present for a lower alternating frequency. It was found that maximising the length of the pulses within the hose relative to the mixing length is critical, as premixing of the gases reduces the benefit gained from alternating between gases.

The benefits of alternating shielding gases can be attributed to the constriction of helium in the arc region, and so it would be expected that this effect is maximised with increasing alternating frequencies. However, the degree of premixing in the gas line highlights the need for an optimised gas delivery system, possibly dispersing helium directly onto the weld region.

8.6 References

[8.1] May, T., Rein, M., Großmann, P. and Mann, K., 'Brilliance improvement of laser-produced soft x-ray plasma by a barrel shock', *New Journal of Physics*, Vol. 14, Article No. 073045 (14pp), 2012.

[8.2] Hosch, J. W. and Walters, J. P., 'High spatial resolution Schlieren photography', *Applied Optics*, Vol. 16, No. 2, pp. 473-482, 1977.

[8.3] Settles, G. S., 'Schlieren and shadowgraph techniques', New York: Springer-Verlag Berlin Heidelberg, 2001.

[8.4] Schnick, M., Dreher, M., Zschetzsche, J., Füssel, U. and Spille-Kohoff, A., 'Visualization and optimization of shielding gas flows in arc welding', *Welding in the World*, Vol. 56, No. 1-2, pp. 54-61, 2012.

[8.5] Dreher, M., Füssel, U., Schnick, M. and Hertel, M., 'Numerical simulation of the shielding gas flow with GMA welding and options of validation by diagnostics', *Materials Science and Technology*, Vol. 2, pp. 39-49, 2009.

[8.6] Siewert, E., Wilhelm, G., Hässler, M., Schein, J., Hanson, T., Schnick, M. and Füssel, U., 'Visualization of Gas Flows in Welding Arcs by the Schlieren Measuring Technique', *Welding Journal*, Vol. 93, No. 1, pp. 1s-5s, 2014.

[8.7] Schardin, H., ‘Toepler’s schlieren method: basic principles for its use and quantitative evaluation’, Washington: United States Navy, 1947.

[8.8] Schwass, D., Wittlich, M., Schmitz, M. and Siekmann, H., ‘Emission of UV radiation during welding’, Bonn: Institut fuer Arbeitsschutz der Deutschen Gesetzlichen Unfallversicherung (IFA), 2011.

[8.9] Weinstein, L. M., ‘Review and update of lens and grid schlieren and motion camera schlieren’, *The European Physical Journal Special Topics*, Vol. 182, No. 1, pp. 65-95, 2010.

[8.10] Tanaka, M. and Lowke, J. J., ‘Predictions of weld pool profiles using plasma physics’, *Journal of Physics D: Applied Physics*, Vol. 40, No. 1, pp. R1-R23, 2007.

[8.11] Lancaster, J. F., ‘The physics of welding’, Oxford: Pergamon Press, 1986.

[8.12] Okada, T., Yamamoto, H. and Harada, S., ‘Observation of the shielding gas flow pattern during arcing by the use of a laser light source’, in ‘Arc Physics and Weld Pool Behaviour’, Lucas, W. (ed), Vol. 1, pp. 203-213, Cambridge: The Welding Institute, 1980.

[8.13] Rao, Z. H., Liao, S. M. and Tsai, H. L., ‘Effects of shielding gas compositions on arc plasma and metal transfer in gas metal arc welding’, *Journal of Applied Physics*, Vol. 107, No. 4, Article No. 044902 (11pp), 2010.

[8.14] Jönsson, P. G., Eagar, T. W. and Szekely, J., ‘Heat and metal transfer in gas metal arc welding using argon and helium’, *Metallurgical and Materials Transactions B*, Vol. 26, No. 2, pp. 383-395, 1995.

[8.15] Murphy, A. B., Tanaka, M., Yamamoto, K., Tashiro, S., Sato, T. and Lowke, J. J., ‘Modelling of thermal plasmas for arc welding: the role of the shielding gas properties and of metal vapour’, *Journal of Physics D: Applied Physics*, Vol. 42, No. 19, Article No. 194006 (20pp), 2009.

[8.16] Cussler, E. L., ‘Diffusion: mass transfer in fluid systems’, Cambridge: Cambridge University Press, 2007.

9 Concluding remarks

This thesis focussed on shielding gas optimisation in gas shielded arc welding processes, and has been conducted along two themes; deriving conditions in which the shielding gas flow rate can be safely reduced, and through the highly novel process of alternating shielding gases.

9.1 Shielding gas flow rate optimisation

Experimental trials have shown that the shielding gas flow rate can be reduced, in a draft-free environment, to 6 l/min, resulting in approximately 60% savings in gas cost in comparison to the 15 l/min base case, and without detriment to quality.

In addition to the savings produced by reducing the shielding gas flow rate, a lower flow rate has been shown to increase penetration, which compounded with the increased distortion and peak temperature, as a result of lower convective cooling for lower shielding gas flow rates. This suggests that for lower shielding gas flow rates, the welding travel speed could be increased whilst producing equivalent levels of penetration.

Shadowgraphy was successfully applied to GMAW to measure the shielding gas flow profile and regions of turbulence. Measurements without the welding arc (cold measurements) showed that the impingement distance of the shielding gas flow, and the cross draft to shielding gas velocity ratio provide reliable indicators of the effect of cross drafts on the weld quality before welding. A pixel-wise Fourier analysis of the intensity fluctuation with time of a sequence of shadowgraphy images was proposed as a qualitative measure of turbulence in the flow, enabling prediction of weld quality from shadowgraphy during the welding process.

A simplified CFD model was developed to determine the effects that welding nozzle geometry changes, and cross drafts, have on the shielding gas flow coverage during GMAW. An economic benefit to industry of modifying the nozzle geometry has been identified allowing for a lower shielding gas flow rate to be implemented whilst maintaining cross draft resistance.

This series of work has shown the minimum shielding gas flow rate necessary for acceptable weld quality in the presence of cross drafts, which is being applied on a practical basis. In a typical shipyard, BAE Systems Naval Ships were using an average gas flow of 24–26 l/min for the 16 mm weld nozzle tested in this study, against the process norm of 18 l/min. The shadowgraphy results established that there was no loss of shielding gas coverage, and hence no degradation in the weld quality, at shielding gas flow rates of 10 l/min and above for the worst draft conditions measured in a typical shipyard fabrication hall.

On the basis of this study, shielding gas flow controllers, preset at 12 l/min have been fitted in a large shipyard environment, removing the welding operatives ability to increase the shielding gas flow rate. These changes were initially introduced in a workplace area where a high number of radiographs are taken, and then extended into a steel workshop and the pipe shop. To date, no defects have been found, and the next areas to be targeted are a panel line and a subassembly manufacture area. The 50% reduction in shielding gas consumption (compared to previous actual usage) will yield a predicted cost saving of approximately £300k per annum (based on 2014 data).

A further reduction to 10 l/min is possible, and a reduced nozzle diameter could be introduced as a result of this study. Spatter build-up on an 11 mm diameter nozzle may be a limiting factor, in which case a 14 mm diameter nozzle would seem to be reasonably practical. If a move to 14 mm diameter is judged viable, then a further reduction in flow rate to 9 l/min is also practical.

9.2 Alternating shielding gases

The application of alternating shielding gases offers clear manufacturing cost reduction benefits which arise from measurable increases in productivity, improved distortion control and re-work reduction, and overall improvements to the mechanical properties of the weld.

Although helium containing shielding gases are often disregarded due to their high unit cost. An economic evaluation of the process has shown that the gas contribution

to the total cost of the weld is relatively low in comparison to the labour costs and filler wire costs, that it is in fact the travel speed that has a major bearing on the weld cost. Therefore, by increasing the travel speed, the weld cost can be reduced in spite of the higher gas costs. The increase in travel speed permitted through the use of alternating shielding gases has resulted in higher productivity, generating savings of approximately 17%.

ANN is a computational modelling technique that has the ability to develop patterns and detect subtle link/trends in data, making them ideal for the implementation to a welding process, which exhibits extremely complex interactions between several nonlinear welding variables. Due to their bi-directionality, ANNs are able to calculate an output for a given set of input variables and vice versa.

An ANN model was developed to predict key weld geometries, and highlighted the influence of the alternating frequency on the weld penetration. In doing so, this has shown that there is an inherent relationship between the frequency of alternation and the travel speed. Training the ANN model in reverse, determined that for an equivalent level of penetration, the travel speed for alternating shielding gases could be increased by, on average, 28% when compared to the argon / 20% carbon dioxide base case, producing a noticeable economic benefit.

In addition to the productivity benefits, the faster travel speed used when implementing alternating shielding gases has also been shown to have a positive benefit in reducing the distortion induced in the workpiece, and consequently the rework required to rectify it.

It has also been shown that the application of alternating shielding gases has no detrimental effect on the mechanical properties of the weld and HAZ. In fact, marginal improvements in yield and tensile strength, Charpy impact toughness, and hardness have been achieved as a consequence of the refined microstructure associated with the use of the alternating gases. Again, this can be related back to the increased travel speed, reducing the heat input and subsequently the degree of grain migration and coarsening.

The addition of helium to the shielding gas has shown a reduction in the percentage inclusion present within the solidified weld. The reduction in porosity can be

attributed to the increased weld pool fluidity as a result of the addition of helium, thus encouraging the gas bubbles to escape from the molten metal. It has also been shown that the application of alternating shielding gases can further reduce the level of inclusions present within the weld when compared to premixed shielding gases. This is mainly attributed to a combination of the variation in weld pool fluidity and the dynamic action that the weld pool experiences owing to the fluctuation between different shielding gas environments.

Considering the forces acting on the liquid weld metal, it can be observed there is a definite magnitude change, with the potential that the flow vectors for helium and argon being in the opposite direction, creating the aforementioned dynamic action within the weld pool when using alternating shielding gases. Although GTAW-P produces arc pressure variations similar in form to alternating shielding gases, their magnitude is comparable to the respective steady state values. The GTAW-P process would exhibit similar effects due to the varying magnitude of the forces acting on the weld metal but all flow would be in the same direction causing a 'jerking' motion.

The magnitude and direction of the fluid flow in the liquid weld metal is an important characteristic for the determination of the final solidified weld geometry. Hence, by controlling the shielding gas present in the arc plasma, the flow vectors can be manipulated in such a way as to provide the desired weld profile.

The thermal property assessment has highlighted the influence that the shielding gas parameters have on the weld metal properties, and therefore each set of welding parameters will exhibit unique aspects. Therefore, the accuracy of computational simulations to predict the temperature field, and consequently residual stresses and deformation can be improved through the use of temperature dependent thermal properties for the parent plate and weld metal.

It has been determined that the shielding gas flow rate has a significant effect on the thermal properties of the solidified weld. A lower shielding gas flow rate was found to reduce the linear thermal expansion coefficient, whilst increasing the specific heat capacity and thermal conductivity, with the thermal diffusivity being independent of the shielding gas flow rate. It can therefore be inferred that a lower shielding gas flow rate will result in less weld-induced distortion as a result of lower degree of

weld metal contraction, and quicker dissipation of the heat to the surrounding plate, resulting in quicker thermal equilibrium with the surrounding material. In addition, the higher specific heat capacity associated with the lower shielding gas flow rate results in a faster weld metal cooling rate, which produces a finer microstructure.

There were no real trends in the data produced when varying the frequency of alternating shielding gases, although the results were generally found to be within the upper and lower limits imposed by the argon / 20% carbon dioxide and helium cases.

The systematic cross draft study conducted found that the alternating shielding gas process does not provide the same level of resistance when compared to a conventional argon / 20% carbon dioxide mixture. This is primarily due to the density of the helium being considerably lighter that air; thus, the gas is far more susceptible to drifting from the weld pool. Conversely, argon has a higher density than air, creating a blanket effect over the weld region.

The development of an ANN model to predict the quality of a weld using a specified set of inputs improves the efficiency of the GMAW process, enabling the operator to predict the weld quality prior to performing the weld itself. For example, should a higher cross draft be detected, the software can predict the weld inputs (nozzle diameter, shielding gas flow rate, etc.) required to produce a high quality weld.

The ability to predict the weld quality for lower shielding gas flow rates leads to obvious benefits on an industrial scale. Investment in an ANN model, which has been thoroughly developed and validated for the specific process it is to predict, would lead not only to time and material saving, but also help reduce wastage of gas in the process itself.

CFD models have been developed to simulate MHD effects, i.e. electromagnetism and fluid flow, in the electrical arc produced in GTAW for different shielding gas compositions.

The simulations have shown that helium produces a considerably higher peak temperature (~19,800 K) than argon (~13,800 K), with a velocity in the arc region approximately 3 times greater.

The total heat flux to the workpiece was approximately 3.5 times greater for the helium arc than the argon arc, primarily due to an increased arc voltage, which would consequently result in higher weld pool fluidity. The heat intensity at the axis of the arc plasma is approximately 4 times greater for helium than it is for argon, indicating that a higher proportion of the arc energy is concentrated at the core of the plasma. Hence, the helium arc plasma is more constricted than argon as a result of an increased current density in the central portion of the arc plasma due to the electrical conductivity of the plasma medium.

The ability to simulate the effect of different shielding gas compositions would potentially lead to shielding gases being tailored to produce a weld of a specific requirement, i.e. penetration, based on the arc characteristics.

The highly novel schlieren visualisations of the alternating shielding gas process have shown that there is a greater degree of helium entrainment in the primary jet due to a constriction of its flow in the secondary jet. Through this mechanism, it would be expected that a greater proportion of helium is present in the arc plasma, influencing the arc's behaviour and inferring more of the associated benefits.

The theoretical analyses of the degree of premixing conducted, and experimental observations indicated that a lower degree of premixing was present for a lower alternating frequency. It was found that maximising the length of the pulses within the hose relative to the mixing length is critical, as premixing of the gases reduces the benefit gained from alternating between gases.

The benefits of alternating shielding gases can be attributed to the constriction of helium in the arc region, and so it would be expected that this effect is maximised with increasing alternating frequencies. However, the degree of premixing in the gas line highlights the need for an optimised gas delivery system, possibly dispersing helium directly onto the weld region.

9.3 Recommendations for future work

The techniques implemented, and the subsequent results generated, throughout this body of research have significantly enhanced the state of the art in the research field

of shielding gas optimisation for advanced manufacturing. However, there are various new challenges that have been identified and aspects where further research is required to increase scientific knowledge:

- How much lower can the shielding gas be reduced whilst maintaining weld quality in a draft free environment? How does the optimum flow rate vary for different welding orientations and configurations, and parent materials?
- It has been shown in this study that the shielding gas flow rate influences the convective cooling and, consequently, a lower shielding gas flow rate results in increased temperature within the workpiece. Investigations should therefore be conducted to quantify the cooling effect, characterise the effect of shielding gas flow rate on the microstructure, and the subsequent mechanical properties of the welded joint.
- Investigations should be conducted to determine why there is a pressure surge at arc initiation, and why it takes 3-5 seconds to stabilise. Is this a thermal effect? Is this a function of welding current, i.e. will a higher welding current take longer to stabilise (or vice versa)?
- The literature available on the application of alternating shielding gases has been limited to argon (or an argon based mixture) and helium. Therefore, additional studies are required to examine this supply method for different shielding gas combinations, and to tailor the shielding gas configuration for the parent material being used.
- Detailed investigations should be conducted to characterise any microstructural effects of implementing an alternating shielding gas supply, and relate this back to the mechanical and thermal property effects.
- Various mechanical property data has been generated for an alternating shielding gas method, however its affect on fatigue life is relatively unknown.
- Advances need to be made on the imaging aspect of alternating shielding gases. In particular, real-time observations of the weld pool behaviour, or the use of tracer particles, would lead to a better understanding of the physical phenomena and should correlate with the arc pressure measurements and force derivation in this study.

- This study has primarily focussed on the alternating frequency, it would be interesting to study this novel shielding gas supply technique with various mark space ratios (i.e. the time ratio of argon to helium), so as to optimise the parameter selection.
- Spectrometry could be conducted to determine the metal vapour content for different shielding gas configurations.
- A number of advancements could be made to the numerical simulation of the arc characteristics:
    - Multi-species in order to predict the shielding gas – air boundary, whilst accounting for the MHD effects.
    - Include the effect of metal vapour based on spectrometry measurements.
    - Develop a transient model to simulate the effect of alternating shielding gases on the arc characteristics, and expand the model to predict the fluid flow in the liquid weld metal.

Appendix A – Alternating gas control unit

Nomenclature

C_1	- Capacitor
f	- Frequency
K_v	- Flow coefficient
P_1	- Inlet pressure
Q_v	- Volume flow rate
ρ_a	- Air density
ρ_g	- Gas density
R_1, R_2	- Resistor
R_a, R_b	- Resistor components of variable resistor
t	- Time
t_m	- Mark time
t_s	- Space-time
T	- Temperature

Introduction

The basis of the alternating gas control unit was two, eight pin, triple five (555) timing circuits that supplied a control signal to a solenoid valve on each gas supply line, thus regulating the flow of each gas.

Circuit design

The 555 integrated circuit (IC) is commonly utilised in a timer circuit due to their ease of use and low cost. Although the 555 IC relies upon both analogue and digital techniques, the output signal is digital and is either high (supply voltage) or low (0V). 555 timer chips have two common operational modes: astable and monostable. Astable mode produces a continuous square wave at a specified frequency, whereas monostable mode produces an output of set length depending upon the triggering input. Astable mode is used in the gas control unit. In order to operate in astable

mode, the 555 timer chip is compiled with three external components, two resistors and a capacitor. The circuit diagram of the chip configured for astable mode is often drawn as shown in Figure A.1 as it is easier to recognise the function of each pin. The values of the resistors and capacitor can be changed to alter the alternating frequency and the mark space ratio.

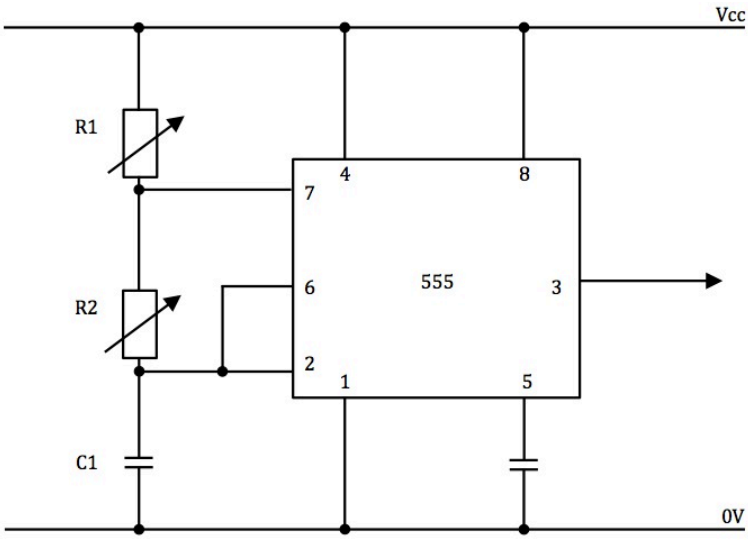

Where:

1: Ground
2: Trigger
3: Output
4: Reset
5: Control
6: Threshold
7: Discharge
8: Supply voltage
R1: Resistor 1
R2: Resistor 2
C1: Capacitor 1

Figure A.1: 555 timer chip with external components

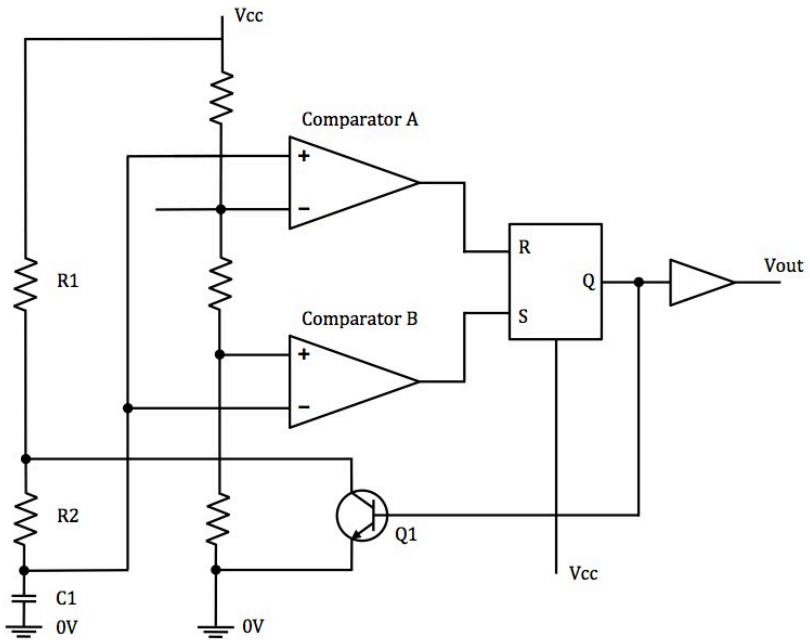

Figure A.2: Internal configuration of the 555 timer chip

The output from the 555 timer chip (Figure A.2) is dependent upon the charge/discharge state of the external capacitor, C1. When the power supply is initially turned on, C1 is discharged; thus the trigger voltage (pin 2) is zero. As a result, the output from comparator A will be low and the output of comparator B will be high. The capacitor, C1, will then start to charge through the series of resistors, R1 and R2, and once it reaches 1/3 Vcc, the comparator B switches to low. When the capacitor, C1, reaches 2/3 Vcc, the comparator A switches to high. As a result, the latch at the transistor, Q1, is reset, switching on the transistor. This changes the direction of the current flow, enabling the capacitor, C1, to discharge through resistor, R2, and the transistor. As the capacitor, C1, discharges to 2/3 Vcc, comparator A will change state to low, and once it discharges to 1/3 Vcc, comparator B will change state to high, thus changing the state of the latch at Q1, turning off the transistor and completing the cycle.

The values of the resistors and capacitor affect the timing of the cycle, and the waveform can be expressed through the mathematical equations:

$$t = In(2).(R_1 + 2R_2)C_1 \tag{A.1}$$

$$f = \frac{1}{In(2)(R_1 + 2R_2)C_1} \tag{A.2}$$

Where t is the period and f is the frequency of the output oscillation. In addition, the oscillation is split into two parts; mark time (high) and space-time (low), and can be defined as follows:

$$t_m = In(2)(R_1 + R_2)C_1 \tag{A.3}$$

$$t_s = In(2)R_2C_1 \tag{A.4}$$

As can be noted from the above equations, there is no independent means of changing the mark space ratio, i.e. the ratio of mark time to mark space. The resistor,

R2, varies both the mark time as well as the space-time, while resistor, R1, can only influence the mark time.

In order to create a setup in which the mark space ratio can be changed by varying only one resistor, a more complex circuit is required, as depicted in Figure A.3. The amended circuit works on the same principal as the original, i.e. the charging/discharging of the capacitor, C1. However, in this case, the output (pin 3) is connected to resistor, R1, and then a variable resistor, RV1. The variable resistor is split into two components; Ra and Rb, and the direction of the current flow controlled by two diodes. In this setup, the Ra value controls the mark time and the Rb value controls the space-time, thus the setup can be expressed through the revised equations:

$$t_m = In(2)(R_a + R_1)C_1 \tag{A.5}$$

$$t_s = In(2)(R_b + R_1)C_1 \tag{A.6}$$

$$t = In(2)(R_a + R_b + 2R_1)C_1 \tag{A.7}$$

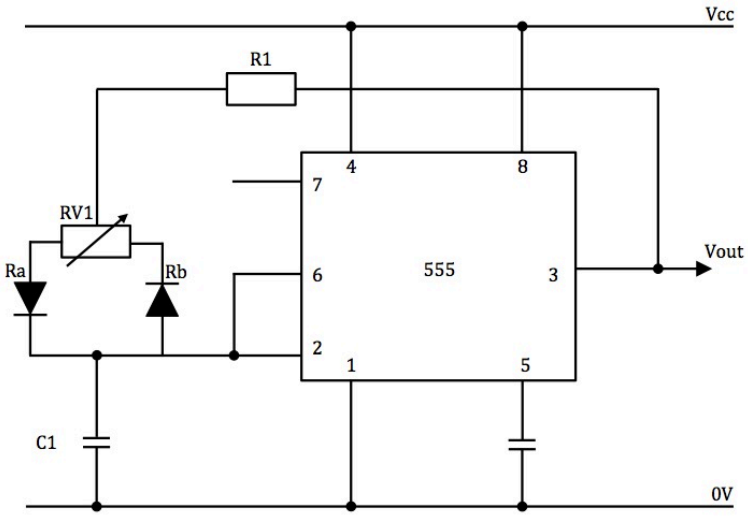

Figure A.3: Amended circuit for mark space ratio variation

In addition to having the ability to adjust the frequency of alternation and the mark space ratio, an override and invert function were added to the control circuit.

The override function was controlled using a three way rotary switch for each gas (red and green dials, Figure 2.7). The first pole was connected to 0V (off), the second pole connected to the output from the 555 timing circuit (pulsed), and the third pole connected directly to the supply voltage (on).

The outputs from the two timing circuits in the control unit govern the flow of each shielding gas. The invert function mirrors the output from one circuit to the second, thus allowing for the exact alternation of the two gases. The invert function is a two way rotary switch and through a series of logic gates replicates and inverts an incoming wave.

The frequency of alternation and the mark space ratio were validated through the use of a Tektronix TDS 210 oscilloscope.

Solenoid valves

A solenoid valve on each gas line is controlled by the output signal from the electronic gas control unit. A solenoid valve is an electromechanical device that converts an electrical signal to a mechanical force, which changes the state of the valve.

There are many different variations of the solenoid valve, however they all operate according to the principles of electromagnetism. A solenoid valve consists of two main parts; the electromagnet coil and a valve connected to a core, known as the armature. The solenoid valves used in alternating gas unit operate on an on/off basis, and do not have the capability to vary the shielding gas flow rate. Flow rates and subsequent pressure build up are defined by the geometry and nature of the valve. The shielding gas flow rate was controlled using dedicated flow meters and the volume flow rate set when flowing continuously.

On/off solenoids come in two configurations: normally open and normally closed, referring to the de-energised state of the solenoid. The solenoid valves used in the alternating gas unit are of the normally closed state. When in the de-energised state,

the return spring exerts a force on the spool valve closing the valve and preventing flow from A to B, Figure A.4 (a). When the solenoid coil is energised, the armature is attracted to the pole, moving the push rod downwards opposing the retaining force of the return spring, thus opening the valve and allowing flow from A to B, Figure A.4 (b).

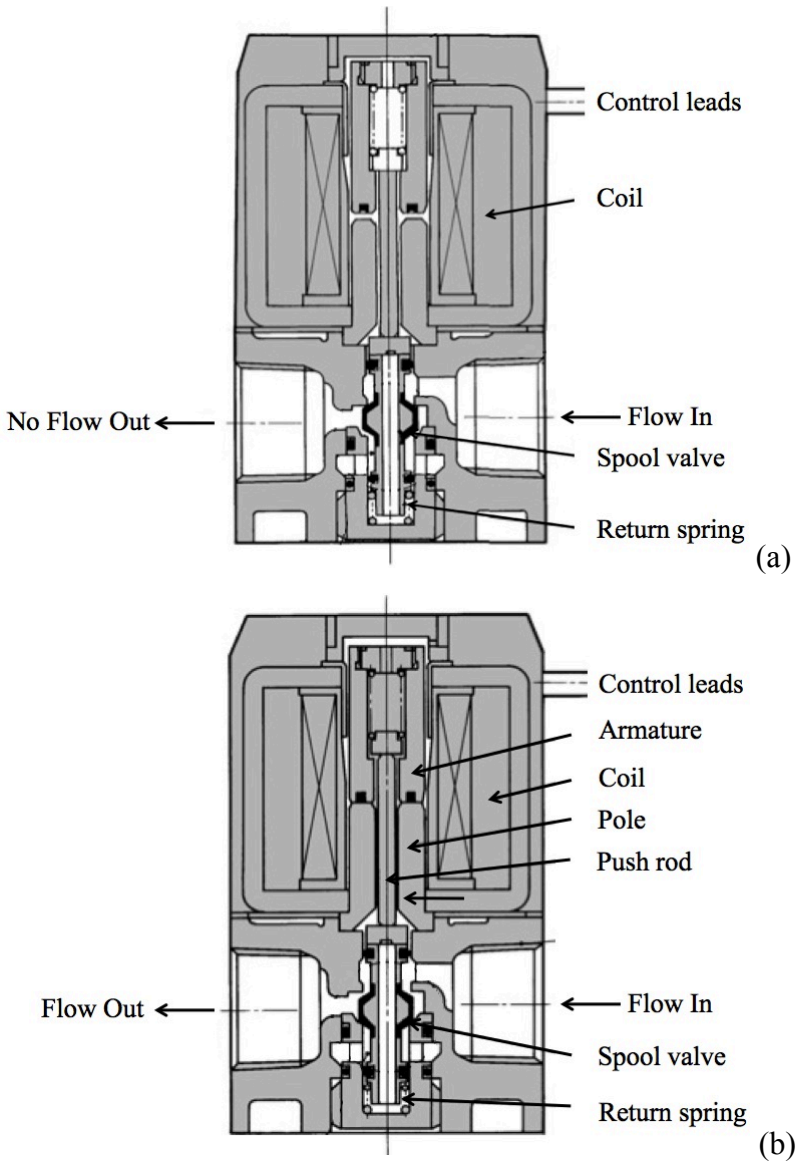

Figure A.4: Solenoid valve in (a) de-energised state and (b) energised state

The correct valve selection is essential to ensure that any pneumatic system is reliable, operates efficiently, and provides the correct system performance. It is therefore necessary to establish the required flow rate through the valve, the gas

density and the operating pressure differential across the valve, in order to calculate the coefficient of flow for the solenoid valve:

$$K_v = \frac{Q_v}{257}\left(\frac{\sqrt{(\rho_g/\rho_a)\,T}}{P_1}\right) \tag{A.8}$$

Therefore, the maximum value for the flow coefficient will be for the highest potential flow rate (18 l/min = 1.08 m^3/h) and when the gas with the highest specific gravity at room temperature is being used (argon = 1.482). In addition, a pressure differential of 4 bar across the valve and the temperature was assumed to be 293 K, thus a value of 0.022 was calculated for K_v.

Solenoid valve manufacturers also specify the maximum flow, C (dm^3/(s.bar)), and the pressure differential for a solenoid valve. The values previously presented, 18 l/min flow rate and 4 bar pressure differential, correlate to a C value of 0.075.

The solenoid valves selected for the alternating gas unit have a K_v value of 0.18, C value of 0.71 dm^3/(s.bar) and a pressure differential of 9 bar, thus ensuring the capability of the valve for the setup.

Appendix B – Optical visualisation theory

Nomenclature

a_1 - Unobstructed height of the light source

Δa - Light ray refraction distance

b - Breadth of the source slit

B - Light source illuminance

C - Contrast/sensitivity of the schlieren system

d - Schlieren object size

d' - Projected schlieren object size

D - Light source diameter

ε - Refraction angle

E - Illuminance

E_0 - Background illuminance

f - Focal length of the optical setup

f_1, f_2 - Focal length of mirror 1 and 2

g - Distance from the light source to the screen

h - Distance from the schlieren object to the screen

h_1 - Height of the source slit

m - Magnification factor

λ - Wavelength

S - Contrast sensitivity

Introduction

Many fluids are transparent in nature and therefore require special visualisation methods in order to make the flow regimes visible. Optical visualisation techniques operate on the principle that the path of the light source is distorted due to variations in the refractive indexes of the fluids.

Shadowgraphy

There are three main shadowgraphy setups; direct shadowgraphy in divergent light, direct shadowgraphy in parallel light, and 'focussed' shadowgraphy.

Direct shadowgraphy in divergent light

Direct (or simple) shadowgraphy in its simplest form (i.e. diverging light source) requires only a small bright light, L, a schlieren object, S, and a suitable surface to project the shadowgram, as illustrated in Figure B.1.

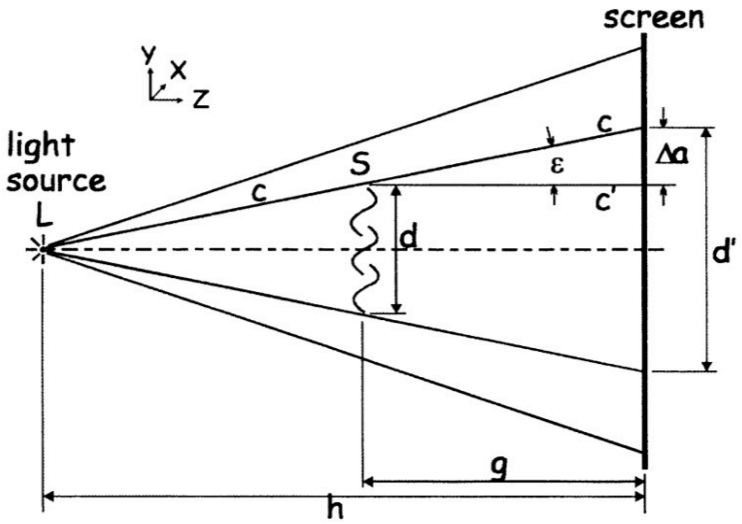

Figure B.1: Schematic diagram of direct shadowgraphy in diverging light [B.1]

The magnification of the shadowgram with respect to the schlieren object can be determined through:

$$m = \frac{h}{(h - g)} \tag{B.1}$$

Shadowgraphy is based on the principle that a light ray, c, will refract through an angle, ε, at the edge of the schlieren object and impact the screen at position c', at a distance Δa from its original position, i.e.

$$\varepsilon \cdot g = \Delta a \tag{B.2}$$

The contrast (or sensitivity) of any system can be defined as the ratio of the change in illuminance to the back illuminance:

$$C = \frac{\Delta E}{E_0} \tag{B.3}$$

Applied to the direct shadowgraphy setup this becomes [B.2]:

$$C = \frac{\Delta E}{E_0} = \frac{\Delta a}{d'} = \frac{\varepsilon}{d} \cdot \frac{g(h-g)}{h} \tag{B.4}$$

However, since ε/d is a characteristic of the schlieren object, $g\ (h-g)/h$ represents the optical geometry effect on sensitivity. Thus, the maximum sensitivity of the optical setup can be achieved by differentiating $g\ (h-g)/h$ with respect to g, i.e. when $g/h\ =\ 1/2$.

Geometric blur occurs because the 'point' source can never be exactly zero, it can tend to zero with respect to g and h but it will always have a finite diameter, D, as shown in Figure B.2. This leads to a 'circle of confusion', the size of which can be determined by combining the aperture angle, D/h, with the optical geometry effect on sensitivity, $g\ (h-g)/h$, yielding $gD/(h-g)$. Thus, when a system is setup to achieve maximum sensitivity, the 'circle of confusion' is equal to the diameter of the light source [B.3].

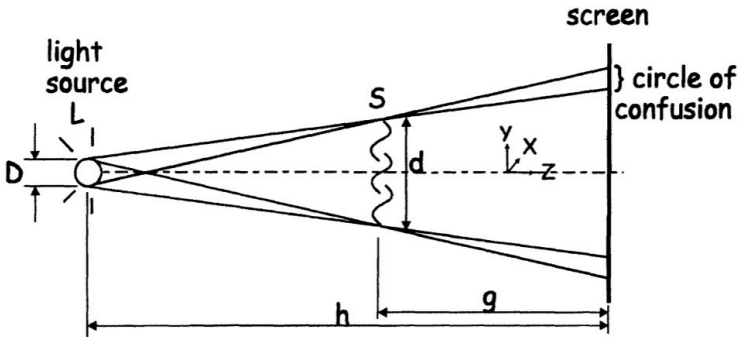

Figure B.2: Schematic diagram illustrating geometric blur in direct shadowgraphy in diverging light [B.1]

It has been recognised [B.1, B.3], that the maximum tolerable level of blur in a shadowgram is dependent upon the size of the smallest feature in the schlieren. The relative blur size, gD/h, can be obtained by dividing the geometric 'circle of confusion' by the shadowgram magnification. Thus the corresponding maximum usable sensitivity is [B.3]:

$$\frac{\Delta E}{E_0} = \frac{\delta \varepsilon}{\delta y} \cdot \frac{\delta h}{2D} \tag{B.5}$$

This implies that the resolution and sensitivity can be increased indefinitely by reducing the light source diameter, D. However, it has been shown [B.1] that there is a limit, beyond which, further reduction does not yield improvements in resolution. In order for an object to be visible, its' refraction angle must exceed the unsharpness angle associated with it; Weinberg [B.3] derived the following equations that govern the minimum refraction angle, smallest resolvable object and the minimum light source diameter, respectively, for a divergent light source.

$$\varepsilon_{min} = 1.33\sqrt{\lambda h/g(h-g)} \tag{B.6}$$

$$\delta_{min} = 1.33\sqrt{\lambda g(h-g)/h} \tag{B.7}$$

$$D_{min} = 1.33\sqrt{\lambda h(h-g)/g} \tag{B.8}$$

The illuminance of a shadowgram in divergent light is inversely proportional to the shadowgraph magnification:

$$E_0 = \frac{\pi B D^2}{4m^2 h^2} \tag{B.9}$$

Direct shadowgraphy in parallel light

If the distance between the light source and shadow plane approaches infinity, the magnification factor (equation (B.1)) tends to unity, and the light source is essentially parallel. This can be transferred to a laboratory setup by means of an optical system, either using a lens or mirror, as illustrated in Figure B.3.

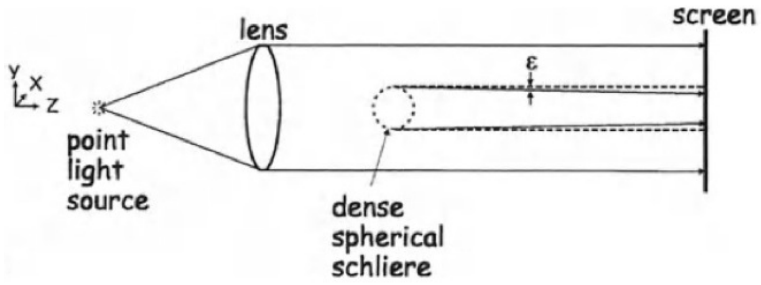

(a)

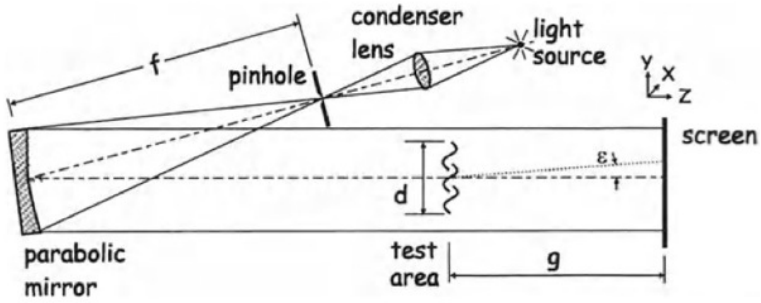

(b)

Figure B.3: Schematic diagram of direct shadowgraphy in parallel light using (a) an optical lens, and (b) a parabolic mirror [B.1]

The shadowgram contrast in parallel light becomes [B.1]:

$$C = \frac{\Delta E}{E_0} = \frac{\Delta a}{d} = \frac{\varepsilon \cdot g}{d} \tag{B.10}$$

Thus, remembering that ε/d is a characteristic of the schlieren object, the maximum sensitivity of the shadowgram in parallel light is g, i.e. the parallel light system produces twice the sensitivity as the equivalent divergent light system.

The aperture angle, D/h for a divergent light source, becomes D/f for a parallel light source, where f is the focal length of the optical setup.

The corresponding 'circle of confusion' for a parallel light source is gD/f. Thus to minimise geometric blur, the focal length must be increased or the diameter of the light source decreased. However, since maximum tolerable level of blur in a shadowgram is dependent upon the size of the smallest feature in the schlieren, the maximum usable sensitivity is [B.3]:

$$\frac{\Delta E}{E_0} = \frac{\delta \varepsilon}{\delta y} \cdot \frac{\delta f}{D} \tag{B.11}$$

Weinberg [B.3] derived the following equations that govern the minimum refraction angle, smallest resolvable object and the minimum light source diameter, respectively, for a parallel light source.

$$\varepsilon_{min} = 1.33\sqrt{\lambda/g} \tag{B.12}$$

$$\delta_{min} = 1.33\sqrt{\lambda g} \tag{B.13}$$

$$D_{min} = f\sqrt{\lambda/g} \tag{B.14}$$

The illuminance of a shadowgram in parallel light is the same as the illuminance incident upon the mirror/lens:

$$E_0 = \frac{\pi B D^2}{4f^2} \tag{B.15}$$

‘Focussed’ shadowgraphy

‘Focussed’ shadowgraphy is similar in form to a parallel light source, but with the addition of one or more optical elements between the test object and shadowgraph, as depicted in Figure B.4.

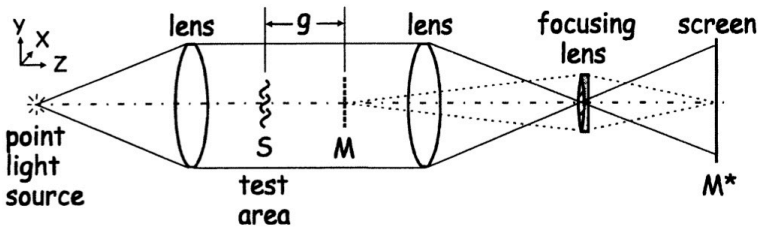

Figure B.4: Schematic diagram setup for ‘focussed’ shadowgraphy [B.1]

With a parallel light source, the shadowgram for the schlieren object, S, would appear at location M, a distance, g, beyond the object if a screen was placed there. However, a second lens brings the light source to a focal point, where a third lens is used to image the shadowgram, M, onto a screen at location M^*. Thus the two imaging planes are conjugates, and the original shadowgram is formed at the new location.

If the shadowgram is imaged at the same size as the original, i.e. the magnification is unity, then the ‘focussed’ shadowgraphy setup follows the same governing equations as the parallel light source. However, if the magnification is not unity, then the illumination of the shadowgraph is similar to that of the divergent light source:

$$E_0 = \frac{\pi B D^2}{4m^2 f^2} \tag{B.16}$$

Therefore, if the image obtained has a magnification factor less than unity, then the image at location M^* will be brighter than the original at location M.

‘Focussed’ shadowgraphy is therefore particularly important for imaging, due to its ability to demagnify the original shadowgram to a size convenient for the optical sensor of a digital camera.

Schlieren

There are two main schlieren setups; a simple lens-type schlieren setup and Toepler's schlieren setup, which can be constructed using a lens or mirror setup.

Simple lens-type schlieren

The simple lens-type schlieren setup is similar to that of 'focussed' shadowgraphy, with the addition of a knife-edge, and a focussing lens for an extended light source, as shown in Figure B.5.

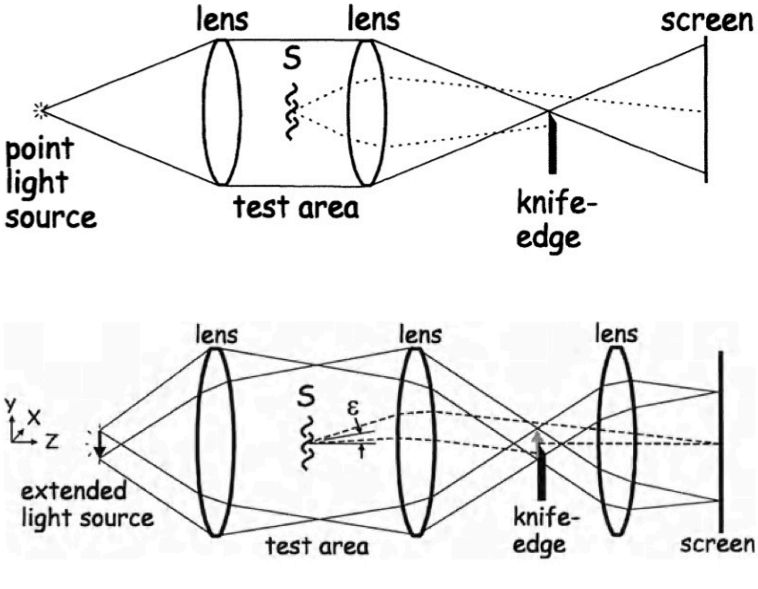

Figure B.5: Schematic diagram of simple lens-type schlieren system, with (a) point light source, and (b) extended light source [B.1]

As was the case for 'focussed' shadowgraphy, the first lens collimates the light source, and the second lens refocuses the beam to an image of the point source and proceeds to produce an inverted image at the screen.

The knife-edge is positioned at the focal distance of the optical system; indicated by the uniform distribution of light intensity over the screen. Conversely, if the knife-edge is too close or too far away from the second lens, the light intensity distribution is non-uniform. It is important to adjust the percentage cutoff in order to produce the desired level of sensitivity; too small a cutoff results in a large amount of light

reaching the screen producing poor contrast and possible oversaturation, whereas too much cutoff results in high contrast but with the loss of information in the regions of low density gradients.

Considering the point source setup shown in Figure B.5, the schlieren object distorts two light rays (as indicated by a dashed lines); one distorts upwards and the other downwards. The ray deflected upwards brightens a point on the screen, whereas the ray deflected downwards is intercepted by the knife-edge and results in a dark point on the screen. The knife-edge affects only rays moving perpendicular to the schlieren object; a horizontal knife-edge will result in the vertical components of the schlieren object being detected, whereas a vertical knife-edge will result in the horizontal components being detected. Therefore, for a finite schlieren object there will be multiple rays distorted, which for a horizontal knife-edge will generate the phase difference plot of $\delta n/\delta y$.

A point light source results in infinite sensitivity over zero measuring range, thus an extended light source is required.

For extended light source setup, the first lens collimates the light rays, and the second lens refocuses the light to an inverted image at the knife-edge. However, as the light source is a no longer a point source, the light rays are not exactly parallel. Beyond the knife-edge, a third lens focuses the image onto a screen.

Due to the light source being of finite size, it is essentially a series of point sources, each producing a schlieren beam that focuses to a corresponding point on the screen. This allows a depth of focus for the setup, which allows the sensitivity and measuring range to be tailored to produce the desired image.

Toepler's schlieren setup

The Toepler schlieren setup implements a condenser lens and slit prior to the collimating lens/mirror, Figure B.6. High quality lenses are favoured for schlieren work, however lens imperfections can mask schlieren images, and high quality lenses are expensive in comparison to parabolic mirrors.

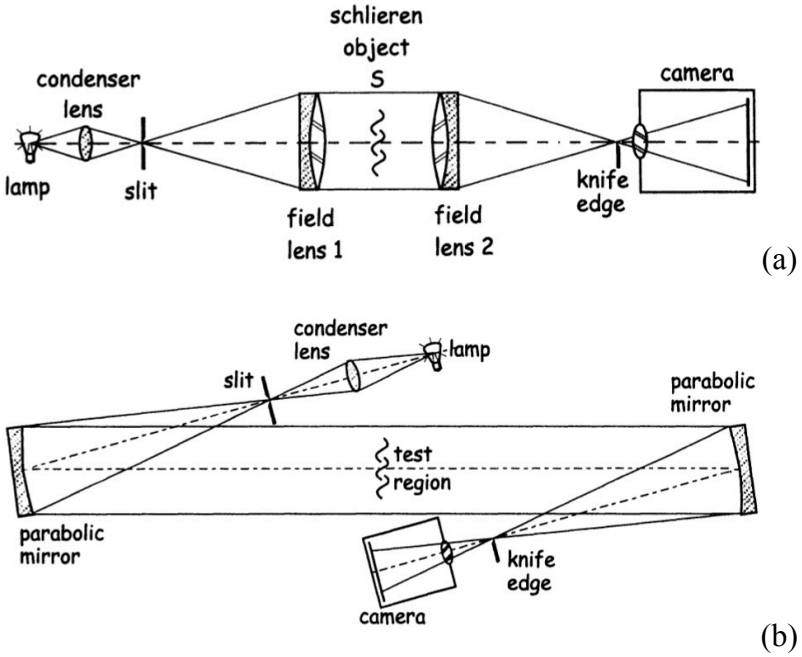

Figure B.6: Toepler's schlieren setup using (a) in-line lens, and (b) z-type mirror, configurations [B.1]

The most popular configuration is the z-type mirror setup, Figure B.6 (b), which uses two, on-axis, oppositely tilted parabolic mirrors. The minimum distance between the mirrors is $2f$, where f is the focal length of the mirrors. Lens optical aberrations, i.e. coma and astigmatism caused by the geometrical and optical axes not being coincident, are proportional to the offset angle of the mirror and the inverse square of the $\mathrm{f}/no.$ for a given angle. Therefore, aberrations can be minimised by reducing the offset angle and by using long focal length mirrors. The z-type setup, assuming the mirrors are perfectly aligned allow for the elimination of coma aberrations from the image [B.4].

For the z-type schlieren setup with a horizontal source slit, the illuminance incident upon the first mirror is:

$$E_0 = \frac{Bbh_1}{f_1^2}$$

(B.17)

Neglecting any losses, this is also the illuminance level present at the schlieren object, and the second mirror.

If a horizontal knife-edge blocks some of the source light at the second mirror focus point, and accounting for a magnification factor, the illuminance becomes:

$$E = \frac{Bba_1}{m^2 f_1 f_2}$$

(B.18)

If a schlieren object in the test region refracts a light ray through an angle, ε, having a y-component, ε_y, then the light ray will distort a distance, $\Delta a = \varepsilon_y f_2$. Therefore, the change in illuminance is:

$$\Delta E = \frac{Bb\varepsilon_y}{m^2 f_1}$$

(B.19)

The contrast (or sensitivity), is defined as the ratio of the change in illuminance to the back illuminance:

$$C = \frac{\Delta E}{E_0} = \frac{f_2 \varepsilon_y}{a_1}$$

(B.20)

Another technique metric is the contrast sensitivity, which characterises how easily the luminance differences within a captured image are discernible. This may be taken as the rate of change of contrast with respect to the refraction angle:

$$S = \frac{dC}{d\varepsilon} = \frac{f_2}{a_1}$$

(B.21)

It can therefore be concluded that since the focal length is fixed for a particular system, the primary factor influencing sensitivity is the unobstructed height of the source image.

The system's measuring range is defined as the range of angles ε over which a definite, gradual change in illumination compared to the background occurs. If the entire source image is on or off the knife-edge, then the corresponding image point has reached its darkest value (over-ranged above the bright limit) or its brightest value (under-ranged below the dark limit). Thus larger deflection angles no longer produce a change in illuminance, losing detail in the respective regions. A knife-edge cutoff of 50% would result in an equal range in both directions, with a maximum range:

$$\varepsilon_{y_{max}} = \frac{\Delta E}{E}\frac{h_1}{2f_2} \tag{B.22}$$

A knife-edge cutoff of 50%, although having the highest equal range, is not very sensitive. Therefore, to increase sensitivity, the source slit must be narrowed. Hence, the sensitivity and measuring range are inversely proportional.

References

[B.1] Settles, G. S., 'Schlieren and shadowgraph techniques', New York: Springer-Verlag Berlin Heidelberg, 2001.

[B.2] Schardin, H., 'Die Schlierenverfahren und ihre Anwendungen. Ergebnisse der Exakten Naturwissenschaften, Vol. 20, pp. 303-439, 1942. (English translation: NASA TT F-12731, (N70-25586), 1970).

[B.3] Weinberg, F. J., 'Optics of flames: including methods for the study of refractive index fields in combustion and aerodynamics', London: Butterworths, 1963.

[B.4] Hosch, J. W., and Walters, J. P., 'High spatial resolution Schlieren photography', Applied Optics, Vol. 16, No. 2, pp. 473-482, 1977.

Appendix C – Peer-reviewed journal articles (2011-2015)

Campbell, S. W., Galloway, A. M. and McPherson, N. A., 'Techno-economic evaluation on the effects of alternating shielding gases for advanced joining processes', *Proceedings of the Institution of Mechanical Engineers, Part B: Journal of Engineering Manufacture*, Vol. 225, No. 10, pp. 1863-1872, 2011.

Campbell, S. W., Galloway, A. M., McPherson, N. A. and Gillies, A., 'Evaluation of gas metal arc welding with alternating shielding gases for use on AA6082T6', *Proceedings of the Institution of Mechanical Engineers, Part B: Journal of Engineering Manufacture*, Vol. 226, No. 6, pp. 992-1000, 2012.

Campbell, S. W., Galloway, A. M. and McPherson, N. A., 'Artificial neural network prediction of weld geometry performed using GMAW with alternating shielding gases', *Welding Journal*, Vol. 91, No. 6, pp. 174s-181s, 2012.

Ramsey, G. M., Galloway, A. M., **Campbell, S. W.**, McPherson, N. A. and Scanlon, T. J., 'A computational fluid dynamics analysis of the effect of side draughts and nozzle diameter on shielding gas coverage during gas metal arc welding', *Journal of Materials Processing Technology*, Vol. 212, No. 8, pp. 1694-1699, 2012.

Campbell, S. W., Galloway, A. M. and McPherson, N. A., 'Techno-economic evaluation of reducing shielding gas consumption in GMAW whilst maintaining weld quality', *International Journal of Advanced Manufacturing Technology*, Vol. 63, No. 6-9, pp. 975-985, 2012.

Barclay, C. J., **Campbell, S. W.**, Galloway, A. M. and McPherson, N. A., 'Artificial neural network prediction of weld distortion rectification using a travelling induction coil', *International Journal of Advanced Manufacturing Technology*, Vol. 68, No. 1-4, pp. 127-140, 2013.

Campbell, S. W., Galloway, A. M., Ramsey, G. M. and McPherson, N. A., 'A computational fluid dynamic analysis of the effect of weld nozzle geometry changes on shielding gas coverage during gas metal arc welding', *Journal of Manufacturing Science and Engineering*, Vol. 135, No. 5, Article 051016, 2013.

Campbell, S. W., Galloway, A. M. and McPherson, N. A., 'Arc pressure and weld metal fluid flow while using alternating shielding gases. Part 1: arc pressure measurement', *Science and Technology of Welding and Joining*, Vol. 18, No. 7, pp. 591-596, 2013.

Campbell, S. W., Galloway, A. M. and McPherson, N. A., 'Arc pressure and fluid flow during alternating shielding gases. Part 2: arc force derivation', *Science and Technology of Welding and Joining*, Vol. 18, No. 7, pp. 597-602, 2013.

Beyer, V., **Campbell, S. W.**, Ramsey, G. M., Galloway, A. M., Moore, A. J. and McPherson, N. A., 'Systematic study of the effect of cross-drafts and nozzle diameter on shield gas coverage in MIG welding', *Science and Technology of Welding and Joining*, Vol. 18, No. 8, pp. 652-660, 2013.

Baillie, P., **Campbell, S. W.**, Galloway, A. M., Cater, S. R. and McPherson, N. A., 'A comparison of double sided friction stir welding in air and underwater for 6mm S275 steel plate', *International Journal of Chemical, Nuclear, Metallurgical and Materials Engineering*, Vol. 8, No. 8, pp. 651-655, 2014.

Campbell, S. W., Ley, F. L., Galloway, A. M. and McPherson, N. A., 'Artificial neural network optimization of shielding gas flow in gas metal arc welding subjected to cross drafts when using alternating shielding gases, *Proceedings of the Institution of Mechanical Engineers, Part B: Journal of Engineering Manufacture*, Vol. 229, No. 1, pp. 122-129, 2015.

Ley, F. H., **Campbell, S. W.**, Galloway, A. M. and McPherson, N. A., 'Effects of shielding gas parameters on weld metal thermal properties in gas metal arc welding', *International Journal of Advanced Manufacturing Technology*, In Press.

Baillie, P., **Campbell, S. W.**, Galloway, A. M., Cater, S. R. and McPherson, N. A., 'Friction stir welding of 6mm thick carbon steel underwater and in air', *Science and Technology of Welding and Joining*, In Press.

Appendix D – Conference articles (2011-2015)

McPherson, N. A., MacPherson, M. J., Galloway, A. M., Gillies, A., **Campbell, S. W.**, Scanlon, T., Moir, A., Moore, A. J. and Wu, T., 'MIG gas shielding – economic savings without detriment to quality', Presented at the International Conference on Materials Science, Metal & Manufacturing (M3), December 2011, Singapore.

Campbell, S. W., Galloway, A. M., Ramsey, G. M. and McPherson, N. A., 'A potential solution to GMAW gas flow optimisation', Presented at the 9th International Conference on Trends in Welding Research, June 2012, Chicago, USA.

Campbell, S. W., Galloway, A. M. and McPherson, N. A., 'Derivation of forces acting on the liquid weld metal based on arc pressure measurements produced using alternating shielding gases in the GTAW process', Presented at the 8th Pacific Rim International Congress on Advanced Materials and Processing, August 2013, Hawaii, USA.

Campbell, S. W., Galloway, A. M. and McPherson, N. A., 'GMAW shielding gas flow optimisation by refinement of nozzle geometry', Presented at the 8th Pacific Rim International Congress on Advanced Materials and Processing, August 2013, Hawaii, USA.

Baillie, P., **Campbell, S. W.**, Galloway, A. M., Cater, S. R. and McPherson, N. A., 'A comparison of double sided friction stir welding in air and underwater for 6mm S275 steel plate', Presented at the International Conference on Materials and Product Technology (ICMPT14), August 2014, Vancouver, Canada.

Campbell, S. W., Galloway, A. M., McPherson, N. A., Camilleri, D. and Micallef, D., 'Modelling magnetohydrodynamics to investigate variation of shielding gases on arc characteristics in the GTAW process', Presented at the International Conference on Materials and Product Technology (ICMPT14), August 2014, Vancouver, Canada.